Technical Report

LABORATORY SIMULATION AND FIELD ESTIMATES OF ATMOSPHERIC TRANSPORT-DISPERSION OVER MOUNTAINOUS TERRAIN

by

M. M. Orgill
J. E. Cermak
L. O. Grant

Prepared Under
Atmospheric Water Resources Research
Division of the Bureau of Reclamation
Contract Nos. 14-06-D-6455 and
14-06-D-6842
Denver Federal Center
Denver, Colorado

Fluid Dynamics and Diffusion Laboratory
College of Engineering
Colorado State University
Fort Collins, Colorado

May 1971 CER70-71MMO-JEC-LOG40

ABSTRACT

LABORATORY SIMULATION AND FIELD ESTIMATES OF
ATMOSPHERIC TRANSPORT-DISPERSION OVER MOUNTAINOUS TERRAIN

In many weather modification programs in the Western United States, ground-based silver-iodide generators are used to produce silver-iodide plumes for the purpose of artificially nucleating orographic cloud systems to increase snowfall production. To assist in evaluating the potential success of the seeding operations it is important to estimate accurately the horizontal direction of the plume, the vertical and horizontal dispersion, and the relative concentration of seeding material at any region in the lower atmosphere.

This problem, the transport and dispersion of a particulate material plume over mountainous terrain, was studied by physical simulation in a meteorological wind tunnel. Both a neutral and barostromatic* atmospheric boundary-layer were simulated to estimate the airflow and transport-dispersion characteristics over a scaled (1:9,600) topographic model of the Eagle River Valley-Climax region in central Colorado for northwest winds parallel to the river valley.

Field data were used to verify laboratory predictions for the prototype and to evaluate the application of modeling techniques to weather modification operations and other phenomena in mountainous areas dependent upon dispersion of mass. These data were obtained from rawinsondes, pilot balloons, constant-volume balloon flights, aircraft and surface sampling of silver-iodide nuclei.

*Defined for the purpose of this paper as airflow with stable thermal stability in the upper levels and near-neutral thermal stability in the lower levels.

The laboratory and field data revealed that near-neutral stability conditions within the valley, orographically induced eddies, directional wind-shear and convection during orographic storm events dispersed the seeding material in the vertical and cross-valley. The observed vertical dispersion was approximately 1,000 to 1,200 m/5 km of horizontal transport. This exceeded the natural slope of the terrain which is approximately 140 m/5 kms.

Comparison of model and field data similarity criteria showed that approximate geometric, kinematic, thermal, and dynamic similitude was achieved by the two laboratory airflow models. The barostromatic model results compared more favorably with field results than the neutral model results. The concentration field of the models and prototype were dependent strongly on the topography and the thermal stratification.

The results indicated that studies of transport-dispersion over scaled topographic models will be of direct value to field programs by providing general pre-operational information on the direction of seeding plumes, estimates on the cloud volume occupied by seeding material, vertical and horizontal dispersion estimates and information on the location of seeding generator sites. The laboratory modeling of transport and dispersion attain their greatest potential value when conducted before or during the planning stages of proposed field programs.

Montie M. Orgill
Fluid Mechanics Program
Department of Civil Engineering
Colorado State University
Fort Collins, Colorado 80521
May 1971

TABLE OF CONTENTS

TABLE OF CONTENTS - Continued

TABLE OF CONTENTS - Continued

TABLE OF CONTENTS - Continued

LIST OF TABLES

LIST OF TABLES - Continued

LIST OF FIGURES

LIST OF FIGURES - Continued

LIST OF FIGURES - Continued

LIST OF FIGURES - Continued

LIST OF FIGURES - Continued

LIST OF FIGURES - Continued

LIST OF FIGURES - Continued

LIST OF SYMBOLS

Symbol	Definition	Dimension
A	Experimental determined constant	--
B	Experimental determined constant	--
C	Concentration of a diffusing material e.g. silver iodide and krypton-85	AL^{-3}
$\overline{C}$	Average concentration	AL^{-3}
C'	Concentration fluctuation	AL^{-3}
c	Hot wire constant depending on yaw angle of wire	--
C_D	Drag coefficient	--
C_{max}, C_m	Centerline, axial or maximum concentration	AL^{-3}
C_p, C_{pd}	Specific heat at constant pressure (dry air)	$HM^{-1}\theta^{-1}$
$\mathcal{D}$	Depletion and deposition mechanisms acting on a tracer plume	--
E	Voltage output across a hot wire	V
e_1', e_2'	Fluctuating voltage signals	V
$F(k)_m$,$F(k)_p$	Three-dimensional spectrum-function with respect to wave number k	L^3T^{-1}
f	Coriolis parameter $2\Omega \sin\phi$	T^{-1}
$\vec{g}$,g	Acceleration of gravity	LT^{-2}
$\vec{g}_a$	Pure gravitational attraction of the earth	LT^{-2}
H	Planetary boundary layer thickness	L
h	Height of source above the ground	L
I_x,I_y,I_z;I_i	Longitudinal, lateral, and vertical intensity of turbulence	--

---

Symbols used to indicate dimension are:
M - Mass, L - Length, T - time, θ - temperature, A - activity,
H - Heat, V - Volts, R - Radians or degrees.

LIST OF SYMBOLS - Continued

Symbol	Definition	Dimension
K_H	Coefficient of exchange of heat	L^2T^{-1}
K_M	Coefficient of exchange of momentum	L^2T^{-1}
$K_x, K_y, K_z; K_i$	Coefficients of eddy viscosities in the x, y, z directions	L^2T^{-1}
$K_{xx}, K_{yy}, K_{zz}; K_{ii}$	Coefficients of turbulent diffusivities for mass in x, y, and z directions	L^2T^{-1}
K	Constant eddy-diffusivity coefficient	L^2T^{-1}
k	Coefficient of thermal conductivity	$HL^{-1}T^{-1}\theta^{-1}$
k_m	Molecular diffusivity	L^2T^{-1}
k_r, k_t	Geometric heights of roughness features	L
L	Reference length	L
L	Stability-dependent length	L
m	Exponent in King's law relationship between voltage and velocity	--
N	Number of observations	--
P	Atmospheric pressure	$ML^{-1}T^{-2}$
p	Power index or exponent	--
p,q	Stability dependent diffusion coefficients	--
Q, Q_s	Source strength; time rate of material emission from a continuous point source	MT^{-1}
Q_E	Latent heat of evaporation and evapo-transpiration	$HL^{-2}T^{-1}$
Q_G	Transfer of heat through the ground	$HL^{-2}T^{-1}$
Q_H	Turbulent transfer of sensible heat to the atmosphere	$HL^{-2}T^{-1}$
$Q_{L\uparrow}$	Long-wave radiation emitted by the surface	$HL^{-2}T^{-1}$
$Q_{L\downarrow}$	Long-wave radiation received by the surface from the atmosphere	$HL^{-2}T^{-1}$

LIST OF SYMBOLS - Continued

Symbol	Definition	Dimension
Q_R	Short-wave radiation reflected from the earth	$HL^{-2}T^{-1}$
Q_T	Short-wave radiation from sun and sky	$HL^{-2}T^{-1}$
q, q_{sa}	Source or sampling flow rate	L^3T^{-1}
$\vec{R}$	Vector from axis of earth extending normal to the axis	L
$R(\xi)$	Lagrangian autocorrelation coefficient	--
R_d	Specific gas constant for dry air	$L^2T^{-2}\theta^{-1}$
$\overline{R}$	Counts min^{-1} of ice nuclei as registered on a Rustrak recorder	T^{-1}
$R(x, y, z)$	Three-dimensional separation distance of dual constant-volume balloons	L
R_{s+b}	Observed sample-plus-background rate	T^{-1}
R_b	Background rate	T^{-1}
$\vec{r}$	Three-dimensional vector for position	L
S	Steadiness of the wind	--
$\overline{s}$	Mean scalar wind speed	LT^{-1}
S_u	Hot-wire sensitivity w.r.t. velocity	$VL^{-1}T$
T	Local temperature	θ
$\overline{T}$	Ambient or average temperature	θ
T_s	Temperature of source material	θ
T_m,T_p	Travel times, model and prototype	T
t	Time	T
t_f	Period or frequency of turbulent eddies	T
t_s	Sampling time	T
t_s,t_b	Measurement time for sample and background, respectively	T
t_R	Residence time	T

LIST OF SYMBOLS - Continued

Symbol	Definition	Dimension
U	Reference velocity; air velocity as measured by pitot tube	LT^{-1}
$\overline{U}$	Mean wind speed effecting a dispersing tracer plume	LT^{-1}
U_∞	Free stream velocity	LT^{-1}
$\overline{U},\overline{V},\overline{W};\overline{U}_i$	Mean velocity components in x,y,z directions; for field, east-west, north-south and vertical directions	LT^{-1}
$u,v,w;u_i$	Instantaneous velocity components in x,y,z directions; for field, east-west, north-south and vertical directions	LT^{-1}
$u',v',w';u_i'$	Velocity fluctuations in x,y,z directions for field, east-west, north-south and vertical directions	LT^{-1}
u_*	Friction velocity	LT^{-1}
u_s	Stream-wise velocity	LT^{-1}
$\vec{V}$	Total velocity vector	LT^{-1}
$\vec{V}_g,V_g$	Geostrophic or freestream velocity	LT^{-1}
$\vec{V}(z)$	Total wind velocity as a function of height	LT^{-1}
V_{sa}	Sampling velocity	LT^{-1}
w_s	Source efflux velocity	LT^{-1}
x,y,z	Distances along longitudinal, lateral and vertical directions; for field east-west, north-south and vertical directions	L
X,Z	Reference lengths	L
Y	Width of valley	L
$Z_m,Z_p,\vec{Z}$	Height of terrain; model or prototype	L
z_o	Surface roughness length	L

LIST OF SYMBOLS - Continued

Symbol	Definition	Dimension
α_o	Angle between the direction of the wind near the surface and the direction of the geostrophic wind	R
$\overline{\alpha}$	Mean resultant wind direction	R
β	Stability parameter $\equiv \frac{1}{\theta} \frac{\partial \theta}{\partial z}$	L^{-1}
δ	Thickness of the local momentum boundary layer	L
$\Delta x, \Delta y, \Delta z$	East-west, north-south, and vertical separation distances between dual launched constant-volume balloons	L
$\Delta \overline{T}$	Vertical temperature change	θ
Δp	Differential pressure from pitot static tube ~ $1/2\ \rho U^2$; also pressure change with distance	$ML^{-1}T^{-2}$
ϵ	Eddy energy dissipation	L^2T^{-3}
θ	Potential temperature	θ
θ_e	Equivalent potential temperature	θ
κ	Von Karman's constant ~0.4	--
λ	Height of roughness features e.g. trees, large rocks, etc.	L
μ	Coefficient of dynamic viscosity	$ML^{-1}T^{-1}$
ν	Coefficient of kinematic viscosity	L^2T^{-1}
ξ	Time interval	T
π	Constant $\equiv$ 3.14159.....	--
ρ	Air density	ML^{-3}
$\sigma_i^2(t)$	Variance of a distribution of particles	L^2
σ_{RS}	Standard deviation in the net rate for a sample	T^{-1}
$\sigma_u, \sigma_w, \sigma_v$	Standard deviations of the velocity components	LT^{-1}

LIST OF SYMBOLS - Continued

Symbol	Definition	Dimension
σ_θ	Standard deviation of lateral (horizontal) wind-direction distribution	R
σ_y, σ_z	Lateral and vertical standard deviations of plume concentration distribution	L
τ	Shear stress	$ML^{-1}T^{-2}$
τ_o	Surface shear stress	$ML^{-1}T^{-2}$
ϕ	Latitude	R
Φ	Energy dissipation function	$ML^{-1}T^{-3}$
$\vec{\Omega}$	Angular rotation of the earth	RT^{-1}
Ω_{im}, Ω_{ip}	Size of mean eddies, model and prototype (field)	L
δ_{ij}	Kronecker delta $\delta_{ij} = \begin{cases} 1 & i=j \\ 0 & i \neq j \end{cases}$	
ε_{ijk}	Permutation symbol $\varepsilon_{123} = \varepsilon_{231} = \varepsilon_{312} = +1$ $\varepsilon_{321} = \varepsilon_{213} = \varepsilon_{132} = -1$ all others = 0	
$)_m$	Pertains to model	
$)_{p \text{ or } f}$	Pertains to prototype or field	
$'$	Indicates fluctuation quantity	
$\overline{\ }$	Indicates average quantity	
$\hat{\ }$	Nondimensional variable	
$*$	Characteristic variable e.g. length, velocity, etc.	
$\rightarrow$	Vector quantity	

Chapter I

INTRODUCTION

1.1 General Statement of the Problem

The majority of classical atmospheric diffusion models have been developed for the special case of relatively flat lower boundary configurations. The problem of diffusion over large irregular roughness elements such as complicated mountain topography has proven too complicated for classical analytical methods. The relatively small amount of research that has been done on this problem originates with special field programs instituted in the past twenty years and with some contributions from numerical and laboratory studies.

The present theoretical, operational, and ecological problems of air pollution, chemical and biological warfare, radioactive fallout, and weather modification indicate a continuing need for a complete understanding of the transport and dispersive properties of the lower atmosphere, particularly over irregular terrain.

The present weather modification program for the Colorado River Basin instituted by the Bureau of Reclamation for augmenting the snowpack in mountainous regions in the Western United States offers a unique opportunity to study the diffusion problem over mountainous terrain. Generally, this pilot program is to form the basis for field programs in seeding orographic clouds within the Western Rockies. The pilot program is intended to serve as a transition from experimental to fully applied programs (Ref. 41). Many private and university research groups are now involved with various aspects of the precipitation augmentation problem.

The general purpose of this study was to investigate the problem of transport and dispersion over irregular terrain. Three methods are available for studying this problem, field measurement programs, numerical simulation, and laboratory simulation. At this juncture all three methods are necessary because of the complexity of the problem and due to the fact that no single method appears capable of providing a complete solution to the problem. However, the task of conducting studies with all three methods proved to be a research program larger than could be handled efficiently. Since laboratory simulation has not been fully developed for the study of diffusion on such a scale, but has promise of being a versatile and inexpensive tool, the laboratory approach was selected as one of the two principal methods. The other method adopted was a field study.

1.2 Objectives of Research

The principal objectives of this work may be summarized as the following:

1) To develop a laboratory airflow model which would be adequate for estimating the airflow and transport-dispersion characteristics during winter storms over the Eagle River Valley-Climax topographic area in central Colorado.

2) To compare the model data with the field data through the principles of similarity and dimensional analysis and to determine how well the physical models can simulate actual atmospheric airflow and transport-dispersion.

3) To determine the transport-dispersion mechanisms and characteristics over the Eagle River Valley-Climax region during storm periods typical for cloud seeding by use of both the model and field data.

4) On the basis of field and model results examine the feasibility of utilizing model studies of atmospheric transport-dispersion over scaled topographic models for application to weather modification dispersion problems.

1.3 Procedures for Completing Objectives

In order to fulfill these objectives the following procedures were completed. First, since the problem is very complex, a brief review of the various aspects of the problem, such as, weather modification, airflow over mountains, diffusion theories, and laboratory simulation are presented in Chapter II.

Second, in Chapter III, the required assumptions, equations, and similitude parameters which govern the airflow and transport-dispersion characteristics of the laboratory models are established by examining and reducing the basic equations governing the atmosphere in the planetary boundary layer.

Third, to satisfy the basic requirement of geometric similarity a scaled (1:9,600) topographic model of the Eagle River Valley and Climax-Leadville area was constructed and arranged in a wind-tunnel for the necessary laboratory work.

Fourth, several laboratory experiments were conducted on the simulation of the atmospheric planetary boundary layer and transport-dispersion of a passive tracer over the scaled topographic model. Two model airflow types were explored, a neutral and barostromatic.

Fifth, field observations of temperature, wind velocity with height, surface concentrations, dispersion and transport estimates

from constant-volume balloons and aircraft sampling of silver-iodide were obtained, analyzed and interpreted to provide information on the weather conditions and how these conditions effected the transport-dispersion process in the field. This information is presented in Chapter IV.

Sixth, the crux of this work is presented in Chapters V and VI. The model results are compared with the field for geometric, kinematic, thermal, and dynamic similarity. For the most part, this was accomplished by utilizing the relevant similitude criteria derived in Chapter III. The model transport and dispersion results are also compared with the available field data to evaluate how well the models approximate actual field conditions. In addition, the model and field results were used to assess the value of the laboratory experiments for assisting weather modification field programs in cloud seeding.

Chapter II

BACKGROUND LITERATURE

2.1 Weather Modification Problem

The physical basis for weather modification studies involves the subject of cloud physics, especially precipitation development within clouds. Since this information is basic for a clear understanding of our problem a brief review of the weather modification problem will follow.

Artificial stimulation of precipitation was first believed possible under certain atmospheric conditions when in 1911 Wegner pointed out the rapid growth of ice crystals within supercooled water clouds. Attempts at precipitation augmentation began in earnest after 1946-47 when Schaefer demonstrated the conversion of a supercooled water cloud to ice in a cold chamber utilizing dry ice and Vonnegut discovered the great efficiency of silver iodide as an ice-crystal nucleus.

The physical basis for treating cold orographic clouds by seeding was first discussed by Bergeron in 1949. In 1955 Ludlam extended this work. During the past ten years this work has been further extended by Grant and colleagues (Ref. 41) for the Western Rockies. Much of what follows next is a condensed summary of their ideas.

The orographic induced clouds along and windward of the mountain ranges over the Western United States are frequently composed of supercooled liquid droplets. The temperature activation spectrum of natural nuclei is such that the number of effective natural ice nuclei may not meet cloud requirements for converting the cloud water to ice form at the warmer cloud temperatures and higher condensation rates. In such

cases snow may not develop, or the precipitation process may be inefficient. If artificial ice nuclei can be activated in the saturated orographic stream far enough upwind of the mountain barrier, a more efficient conversion of cloud water to ice crystals should result in increased snowfall. Otherwise, the unconverted cloud water evaporates to the lee of the mountain barrier. Another type of modification exists if, by treating the cloud system, an additional latent heat release can affect a change in the condensation rate itself by altering the vertical motion field (Ref. 41).

Successful cloud seeding depends upon the introduction of sufficient artificial nuclei, e.g., silver iodide, into supercooled clouds to obtain optimum crystal concentrations. If the concentrations of crystals in the cloud should be less than the optimum concentration, then not all of the vapor provided by the orographic updraft can be readily condensed upon the snow crystals. When the concentration of crystals is above the optimum number overseeding may occur and the resultant precipitation may be less than would have occurred naturally. Ludlam (Ref. 64) calculated a mean requirement of approximately 20 crystals per liter as the optimum number in orographic clouds.

Grant and colleagues (Ref. 40) have developed a simple model for showing the variation of optimum ice nuclei concentration as a function of cloud system temperatures. The optimum ice nuclei concentration was defined as that which enabled the cloud system to grow ice by diffusion at a given condensation rate. On the basis of this model Grant has estimated the optimum concentration of crystals needed to insure an efficient precipitation process in the Climax-Leadville, Colorado area as 5 to 100 per liter depending on the range of

temperatures (-13°C to -35°C) and vertical velocities (0.1 to 1.5 m/sec) that occur at this location. A more refined and improved model has been derived by Chappell (Ref. 19) that is tailored for existing cloud conditions at Climax and Wolf Creek Pass, Colorado.

Studies have indicated that orographic cloud systems in which systematic condensation is caused by geographical features are most suitable for seeding. However, the obtaining of optimal distribution of seeding material in orographic cloud systems presents a complex theoretical and operational problem.

A pertinent discussion of the optimization seeding problem for orographic clouds is well described by McDonald (Ref. 66):

> From the standpoint of optimizing cloud seeding, one wishes to be able to predict what flux of nuclei should be released at the generator site in order to insure a specified concentration at a given level within clouds at a roughly given distance. An error of much more than one order of magnitude in concentration may, on existing theory, spell the difference between seeding success and failure, yet such a precision places demands on turbulence theory that cannot at present be met, above all under conditions of airflow over orographic barriers of complex form. Since seeding of orographic clouds holds, in many ways, better promise than seeding of any other cloud type, this difficulty is not a trivial one.

Several techniques such as aircraft, ground generators, balloons, rockets, anti-aircraft guns and natural rising air currents have been employed in an attempt to place the seeding material within the clouds. For storm situations in the Rocky Mountains, ground-based generators are usually used due to their continuous seeding capability, low cost, and safety features. However, aerial line sources are sometimes employed when atmospheric conditions are not too severe.

2.2 General Review of the Effects of Mountains on Airflow

Mountains may alter atmospheric airflow characteristics and motion in a number of different ways. These can be classified broadly as follows:

a) small- and medium-scale turbulent motion thickening the planetary boundary layer,

b) medium- and large-scale dynamic effects,

c) gravity oscillations,

d) dynamic-thermal effects,

e) oscillations about geostrophic equilibrium, and

f) quasi-geostrophic motions.

Since the quasi-horizontal oscillations of air about geostrophic equilibrium occur with time and dimension scales larger than 12 hrs and 100 km, respectively, these affects will be neglected because they will be larger than the orographic affects to be considered in this study.

2.2.1 Planetary boundary layer - It is well known, that the planetary boundary layer is defined as that depth of the troposphere through which the air is significantly affected by the surface roughness or topography. For level terrain there are now many formulae and models for estimating the thickness of the planetary boundary layer. Hanna (Ref. 47) has summarized the various techniques for determining the planetary boundary-layer thickness over level terrain and implies that

$$H = f(u_* , f , V_g , \alpha_o , \Delta\theta/\Delta z) \qquad 2.1$$

where different combinations of the preceding variables may give good results depending upon the stability conditions.

Few formulae or models exist for estimating the thickness of the planetary boundary layer over mountains. Sawyer (Ref. 90) and Cressman (Ref. 25) have described the various methods which are used to incorporate the frictional effects of the planetary boundary layer over mountains into hemispherical forecasting numerical models. Generally, these methods attempt to estimate the vertical velocity at the top of the friction layer from the wind drift across the isobars in the friction layer. Estimates of the skin drag coefficient or surface shear stress are also required for the estimates of the vertical motion.

2.2.2 Dynamic effects - The dynamic effects of mountains on airflow can be generally classified according to the perturbed airflow as follows:

quasi-laminar airflow,
separation airflow,
blocking and stagnation airflow and
channel and gap airflow.

a) Quasi-laminar airflow

This type of airflow comprises of a smooth shallow wave over a mountain, producing weak vertical currents and downstream phenomena (Fig. 1a). These conditions are approximated in stably stratified airflow in wind tunnels and for very stable conditions in the actual atmosphere.

b) Separation airflow

When the static stability is near neutral, airflow over mountains may create pressure gradients in the direction of the flow. These pressure gradients are also experienced by the air close to the surface which is more retarded by friction than the airstream above.

If friction together with the adverse pressure gradient produces stagnation, then reversed flow may develop downstream from that point. These events usually produce a large semi-permanent eddy to the lee of a mountain; this implies reversed flow up the lee slope (Fig. 1b). The presence of such eddies have important repercussions on the flow at greater heights, since the effective shape of the mountain is modified by the presence of the eddy.

Scorer (Ref. 94) and Davidson (Ref. 27) have studied separation phenomena in the field. Halitsky et al. (Refs. 44, 45, 46), Plate and Lin (Ref. 84) and Chang (Ref 17) have studied this particular phenomena in the wind tunnel with model hills.

c) Blocking and stagnation airflow

Many of the mountain airflow studies have been directed toward the many interesting leeside wind airflows with relatively few studies of the windward side motions (Fig. 1c). Pioneer investigations of this phenomenon have been launched by Scorer (Ref. 94), Myers (Ref. 73), and Kao (Ref. 54). Studies on the blocking action of relatively isolated mountains are currently in progress at the University of Wyoming (Ref. 74).

d) Channel and gap airflow

One of the most neglected aspects of mass transport across mountainous terrain is the phenomenon of gap winds (Fig. 1d). Each real mountain range is far from being an idealized infinite ridge, usually there are a number of well defined gaps; the mountain passes running along the ridge. At lower levels, winds exceeding 25 m/s may occur for extended periods of time. Good examples have been observed in Hawaii, California, Colorado, Gibraltar and many other places.

2.2.3 Dynamic-thermal effects - The dynamic-thermal effects of mountains can be generally classified as follows:

horizontal eddying airflow and

slope and valley airflow

a) Horizontal eddying airflow

Recent data provided by weather satellites have revealed the existence of mesoscale eddies, which are on a scale too small to be delineated by the standard weather observation network. Chopra and Hubert (Ref. 21) have described the characteristic properties of mesoscale eddies formed in the wakes of islands that are steep-sided and extend far above the low-lying temperature inversion. These eddies are made visible by patterns in stratocumulus clouds lying beneath a strong inversion about 0.5 to 2.0 Km above the ocean surface and have been observed to persist several hundred kilometers downstream. The bandwidth of the eddies is of the order of the cross-stream diameter of the island.

Under favorable conditions, the pattern of the eddies shows a strong resemblance to the classical Kármán vortex street pattern observed in laboratory studies of wakes behind obstacles (Fig. 1e).

b) Slope and valley airflow

The literature on slope and valley airflow is very extensive. Several analytical solutions are now available and a few numerical solutions have been attempted. Two numerical studies examined different aspects of the problem. Thyer (Ref. 104) utilized the basic equations of motion and heat conduction to construct a mathematical model that succeeded in producing a system of simultaneous slope winds, valley winds, and anti-valley winds by simulating heating at appropriate parts

of the boundary of a three-dimensional valley, in which the air was initially at rest (Fig. 1f).

Orville (Ref. 78) used equations developed by Ogura to model convective motions over a two-dimensional mountain ridge, including both thermal and evaporation effects. One object of this study was to separate the hydro-thermal effects and the mountain wave effects on vertical motions over ridges.

No extensive laboratory study has been accomplished on this problem although Thyer conducted some preliminary experiments before conducting his numerical study. An unpublished literature survey and feasibility study has been done by Orgill (Ref. 77).

2.2.4 Gravity oscillations - It is well known that under appropriate conditions mountains may initiate gravity oscillations in the overlying airflow. Generally, the gravity oscillations can be classified as:

lee waves,

lee vortices (rotors) and

hydraulic (analog) airflow.

a) Lee waves

Mountain lee waves develop when the air mass flowing over a topographic obstacle has three principal characteristics: 1) stable stratification, 2) wind direction changes little with height, and 3) airspeed increases upward through the troposphere (Fig. 1g).

The literature on mountain lee waves is very extensive, some good summaries on the earlier work is available through Corby (Ref. 23), Queney et al. (Ref. 86), and Krishnamurti (Ref. 56). This phenomenon was studied in a wind tunnel by Lin and Binder (Ref. 61) and in a water

channel by Long (Ref. 63). Several researchers are working on analytical, laboratory, and computer solutions to this problem.

b) Lee vortices (rotors)

This type of airflow arises when the wind is very strong and extends through a restricted vertical depth, comparable with the height of the mountain. Such an airflow can occur when there is a strong reversed thermal wind or when the wind direction varies markedly with height. Förchtgott (Ref. 33) frequently found severe turbulence to the lee of the mountain and from its nature concluded that the flow comprised a system of quasi-stationary vortices rotating in opposite directions (Fig. 1h).

These vortices are quasi-stationary, having axes parallel to the mountain ridge and whose influence often extends up to the level of the mountain crest or even higher in some cases (e.g., Sierra Nevada). Remarkable variations of wind speed and direction are often observed beneath rotors. The theory of rotors has been considered by Lyra, Queney, and Kuettner (Ref. 86).

c) Hydraulic (analog) airflow

Areas along the eastern slope of the Rocky Mountains are struck from time to time during winter and spring by strong and relatively warm winds which suddenly flow down the leeside of the mountains. This phenomenon is commonly known as the Chinook, the North American counterpart of the European foehn. Some investigators suggest that these strong winds may be connected with atmospheric hydraulic "jumps" analogous to the hydraulic phenomenon (Fig. 1i).

Long (Ref. 62) has studied this phenomenon in a water channel. Houghton and Kasahara (Ref. 51) studied the nature of hydraulic airflow

using the one-dimensional time-dependent "shallow water" equations. Several investigators have observed and studied similar phenomena in the atmosphere such as Beran (Ref. 9).

2.3 Present Turbulent Diffusion Theories and Limitations

The problem of turbulent diffusion* in the atmosphere has not been uniquely formulated in the sense that a single basic physical model has been proposed which seems capable of explaining all the significant aspects of the problem. Instead there are basically three alternative approaches, neither of which can be categorically eliminated from consideration since each has areas of utility not overlapping the others. The four approaches can be generally summarized as follows;

1. Gradient transport theory
    - A. Fickian diffusion
    - B. "K" theory
        - 1) Gaussian plume diffusion model
        - 2) Fluctuating plume model
        - 3) Non-Gaussian diffusion models
2. Statistical theories
    - A. Taylor's theorem
    - B. Sutton's diffusion model
    - C. Lagrangian similarity theory
    - D. Relative atmospheric diffusion

---

*Some authors prefer the word dispersion in the case where small particles are released into the atmosphere. Diffusion and dispersion are closely related, differing only in that for dispersion the possibility exists of effects arising from the size and inertia of the particles involved. In this paper, dispersion will be favored.

3. Practical schemes

A. Cramer's method

B. Pasquill's method

C. Gifford's modification of Pasquill's method.

2.3.1 Gradient transport theory - The gradient transport theory or "K" theory uses the simple parabolic diffusion equation and the assumption that the transport of particulate material is proportional to the gradient of concentration of the passive material. The parabolic diffusion equation can be derived from conservation of mass concepts and when applied to turbulent quantities may be written as,

$$\frac{\partial \overline{C}}{\partial t} + \frac{\partial}{\partial x_i}(\overline{C}\,\overline{U}_i) = \frac{\partial}{\partial x_i}(-\overline{c'u'}_i) + k_m \frac{\partial^2 \overline{C}}{\partial x_i \partial x_i} \quad . \tag{2.2}$$

This equation can be changed into the more familiar form by using Boussinesq's exchange coefficient method where,

$$\begin{aligned} -\overline{c'u'} &= K_{xx}\frac{\partial \overline{C}}{\partial x} + K_{xy}\frac{\partial \overline{C}}{\partial y} + K_{xz}\frac{\partial \overline{C}}{\partial z} \\ -\overline{c'v'} &= K_{yx}\frac{\partial \overline{C}}{\partial x} + K_{yy}\frac{\partial \overline{C}}{\partial y} + K_{yz}\frac{\partial \overline{C}}{\partial z} \\ -\overline{c'w'} &= K_{zx}\frac{\partial \overline{C}}{\partial x} + K_{zy}\frac{\partial \overline{C}}{\partial y} + K_{zz}\frac{\partial \overline{C}}{\partial z} \end{aligned} \tag{2.3}$$

and assuming that the x,y,z axes are the principal axes of the diffusion tensor then all the components except those on the diagonal are equal to zero, therefore,

$$\frac{\partial \overline{C}}{\partial t} = \frac{\partial}{\partial x_i}(\overline{C}\,\overline{U}_i) = \frac{\partial}{\partial x_i} K_{ii}\frac{\partial \overline{C}}{\partial x_i} + k_m \frac{\partial^2 \overline{C}}{\partial x_i \partial x_i} \tag{2.4}$$

where the first term, represents the local temporal variation of concentration, the second, convective transport, the third, turbulent diffusion exchange, and the fourth, molecular diffusion, which is neglected in turbulent airflow. Much of the earlier diffusion work was based upon simplifications of this equation (Ref. 103).

2.3.2 Statistical theories - The gradient transport theory, in some cases, has been supplanted by the statistical methods of Taylor, Sutton and others. The basic theorem of Taylor relates the standard deviation of a cluster of particles to the correlation coefficient of velocity fluctuations. In the case of diffusion in an isotropic, homogeneous, stationary turbulent flow field, the standard deviation is given by the formula,

$$\sigma_i^2(t) = \overline{x_i^2(t)} = 2\overline{u_i'^2} \int_0^T \int_0^t R_i(\xi) d\xi dt \qquad 2.5$$

where $T = x/\overline{U}$ and $R_i(\xi)$ is the Lagrangian autocorrelation coefficient.

$$R_i(\xi) = \frac{\overline{u_i'(t) u_i'(t+\xi)}}{\overline{u'^2}} \quad . \qquad 2.6$$

From these two theories, the gradient transport and statistical, formulae have been derived which are used to study the diffusion of passive materials up to one kilometer or more. Much of this work has been well summarized by Sutton (Ref. 103), U.S. Weather Bureau (Ref. 107), Pasquill (Ref. 83), and U.S. Atomic Energy Commission (Ref. 106).

In general, these two theories on diffusion are only reliable for specifying the average distribution of concentration, over a kilometer or so downwind of a source operating for a few minutes on level

unobstructed terrain, with a steady wind direction, neutral conditions of atmospheric stability and usually isotropic, homogeneous, stationary turbulence.

2.3.3 Practical schemes - In an attempt to improve this situation Cramer (Ref. 24), Pasquill (Refs. 82, 83), Gifford (Ref. 36) and Slade (Ref. 97) have derived practical systems for estimating diffusion in a wide range of meteorological conditions and distances up to 100 kilometers. Turner (Ref. 105) has presented a Pasquill-Gifford practical system in form of a workbook method. Yet, none of these methods have attempted so far to incorporate rough terrain.

2.4 Present Status of Knowledge Concerning Transport-Dispersion in Mountainous Terrain

2.4.1 Field experiments - The complexity of dispersion and transport in irregular terrain has limited many field experiments to relatively flat or undulating terrain. The U.S. Atomic Energy Commission (Ref. 106) has reviewed the majority of field experiments under this category.

Serious attempts at conducting field experiments over relatively nonhomogeneous terrain probably started with the work of Braham (Ref. 11) and Crozier and Seely (Ref. 26) in New Mexico. Some additional preliminary work was accomplished by Smith and Heffernan (Refs. 99, 100), MacCready (Ref. 65), Schaefer (Ref. 91) and Kassander (Ref. 55). Some of these studies used silver iodide as a tracer.

In the early 1960's some important experiments were conducted over a variety of irregular terrain by Meteorology Research, Inc. and Metronics Associates. This work was summarized by Smith and Kauper (Ref. 101), McMullen and Perkins (Ref. 67), Smith and Wolf (Ref. 102)

and Smith (Ref. 98). Smith and Kauper were able to generalize some of their results schematically as shown by Fig. 2.

In the mid-1960's weather modification groups started to express interest in the dispersion problem. DePena (Ref. 28) in France considered the problem of silver-iodide dispersion as well as Henderson (Ref. 48), E. Bollay Associates (Ref. 30), Willis (Refs. 108, 109), Langer et al. (Ref. 58), and Auer (Ref. 4).

A study of particular interest, since it was done in typical irregular terrain, was the research accomplished by EG and G (Ref. 88) within the Park Range located in Northern Colorado. Fifty-two aircraft-tracked ground releases were made in this study as well as a number of air borne releases.

This study concludes its findings with these general observations:

(1) The horizontal dispersion was related to the horizontal wind fluctuations in neutral and unstable stability. Plume widths were either very narrow or very wide under stable conditions.

(2) Significant vertical dispersion was completely stopped by any inversion above the release level and slowed by any stable layer. From some 13 case studies, the observed vertical dispersion was as great as 1000 meters/5 Kms during neutral or unstable conditions. For very stable conditions the vertical dispersion was as small as 100 meters/8 Km.

(3) Under neutral stratification through a deep layer above the release point with a simple wind profile, the method of Pasquill-Gifford was adequate for predicting the distribution of nuclei.

(4) Seeding plumes were tracked as far as 33 Km from the source.

Many of the field experiments indicated that the particulate plume can be detected at distances greater than 15 Km but the symmetrical structure of the plume with a marked central peak is replaced by a more diffuse structure having minor increases of high concentration dispersed at random through the plume (Ref. 11, 58, and 4).

2.4.2 Numerical models - The many complicated, interacting, non-linear effects such as surface roughness, wind shear, advection, and stratification of potential temperature make numerical modeling of dispersion over irregular terrain an attractive method to apply to the problem. Serra (Ref. 95) and Milly et al. (Ref. 70) have used Sutton's development and solutions in order to study the effect of multiple sources, atmospheric stability, and wind speed on the diffusion over flat terrain.

Buettner (Ref. 13) and Hino (Ref. 49) have used the parabolic diffusion equation and numerically generated airflow over various simplified terrain models to study the problem of dispersion over irregular terrain.

2.4.3 Laboratory simulation - Laboratory simulation, although not new, has not been utilized extensively by meteorologists and has not been developed as a tool for estimating dispersion patterns over irregular terrain. Part of the lack of utilization is due to the scarcity of laboratory facilities which are capable of achieving similitude, i.e., equality of Reynold's number, Richardson number, etc., for the model flow and the actual prototype airflow. Some exploratory investigations of dispersion over model terrain have been accomplished by Plate and Sheih (Ref. 85), Cermak and Peterka (Ref. 16), and Meroney and Cermak (Ref. 69).

2.5 Laboratory Simulation of Atmospheric Transport and Dispersion Over Irregular Terrain

2.5.1 Transport and dispersion over irregular terrain - The problem of atmospheric transport and dispersion of fine particulate material (e.g., silver iodide) and gaseous material is most easily approached by considering the factors that influences the transport and spread of the material from the source. These factors are (1) source characteristics, (2) depletion mechanisms, (3) atmospheric motions, and (4) lower boundary conditions.

The source characteristics consider the strength, height, efflux velocity and temperature, and dissemination time of the source. These characteristics as well as the source location can be varied in an effort to obtain specific operational objectives. The depletion mechanisms enhance the fall in concentration of suspended matter with downwind distance.

Atmospheric motions can be separated into two components, turbulence and mean motion. An examination of the turbulent diffusion equation (Eq. 2.4) indicates the manner which these two motions enter into the transport mechanism. For material with negligible fall velocity the time averaged diffusion equation may be written as follows:

$$\frac{\partial \overline{C}}{\partial t} + \overline{U}_i \frac{\partial \overline{C}}{\partial x_i} = k_m \frac{\partial^2 \overline{C}}{\partial x_i^2} - \frac{\partial (\overline{u_i' c'})}{\partial x_i} \quad . \qquad 2.7$$

The various terms may be interpreted as follows:

$\overline{U}_i \frac{\partial \overline{C}}{\partial x_i}$ --- convective transport by mean flow

$k_m \frac{\partial^2 \overline{C}}{\partial x_i^2}$ --- molecular diffusion

$$-\frac{\partial(\overline{u_i' c'})}{\partial x_i}$$ --- turbulent diffusion.

In the field, molecular diffusion is neglected since the turbulent diffusion is much larger. Turbulence governs the diffusion of airborne material and is a function of atmospheric stability, directional and speed wind shear, and surface roughness. The large-scale mean motions govern the direction in which the diffusing cloud of airborne material will be transported. Motions of the convective (advective) transport scale are governed by general synoptic flow patterns, mesoscale circulations, and the nature of the terrain.

The lower boundary conditions, especially if they are irregular, may act to enhance the effects of depletion of a plume and increase the effects of turbulence and mean motion. Irregular terrain is difficult to generalize but nevertheless three types can be recognized; blocking ridge or mountain range, where the obstacle acts to impede or block the airflow. The only avenue for the oncoming airflow is to ascend the blocking topography. A plume of seeding material approaching the ridge may have portions of its material trapped in the lower layers while other portions are caught in the ascending airflow and transported over the ridge; valley, where the oncoming airflow may be channeled by the surrounding walls of the main valley, yet, interacting with the airflow from minor tributary valleys. In this case, a plume of seeding material may be trapped and channeled in the valley but with portions of it escaping the top of valley due to mechanical and convective turbulence and stability; singular mountain, where a substantial portion of the oncoming airflow is forced to diverge and flow around the obstacle

instead of over it. A plume of seeding material may be effected in the same manner but with portions of the material ascending the summit of the mountain.

It is not difficult to find examples of all three terrain types in the Western United States. In Colorado, the Eagle River Valley and Climax-Leadville area located in the Central Rocky Mountains exhibit all three types. It is this area that was chosen for the field and laboratory study of transport and dispersion over irregular terrain.

2.5.2 Laboratory simulation problems and advantages - The laboratory simulation of transport and dispersion over irregular terrain such as the Eagle River Valley and Climax-Leadville area presents many problems which may be generalized as follows,

(1) the physical limitations of the laboratory apparatus necessitates adopting several restrictive assumptions,

(2) the problem of similitude between model and prototype,

(3) the problem of obtaining proper measurements of the pertinent parameters,

(4) and the necessity of verifying the model results with actual field measurements.

At the present time only three general types of airflow can be generated in a wind tunnel;

Neutral airflow, where static stability is assumed neutral and the pressure field is determined by the geometry of the terrain features. If the terrain features are sharp, the flow patterns are not influenced by viscous forces and Reynold's number differences between the model and prototype. Irreversibility in the flow is usually due to the

production of separation eddies, which appear on the lee side of obstacles (Fig. 1b).

Barostromatic* airflow, where the air is stably stratified due to density or temperature stratification. This type of airflow is generally quasi-laminar and with proper density stratification gravity waves and hydraulic "jumps" occur. Large vertical temperature gradients and low flow velocities are required in order to produce this type of flow in the wind tunnel (Figs. 1g and 1i).

Unstable airflow, where the air is heated from below producing thermal convection cells throughout the flow medium.

Most topographic model studies have been made with neutral flow while barostromatic airflow has just recently been investigated in the wind tunnel. However, an effort was made in 1941 by Abe to study flow over Mt. Fuji with an air stream stratified by solid carbon dioxide. Table 1 gives a listing of terrain models which have been studied and the type of flow used.

A neutral airflow, although the most convenient to simulate, may only apply to the actual field conditions in very special atmospheric conditions, i.e., during periods of neutral stability through deep layers of the atmosphere. A barostromatic airflow attempts to simulate the normal temperature stratification one observes in the atmosphere, i.e., an increase of potential temperature with height. This type of airflow is difficult to produce realistically because of the required temperature or density stratification.

---

*Word derived from Greek and adopted by R. S. Scorer (Ref. 93) as representing an airflow which exhibits density stratification. For the purpose of this study it represents airflow with stable thermal stability in the upper levels and near-neutral thermal stability in the lower levels.

A critical appraisal is needed of the laboratory method to determine how well it can duplicate certain aspects of the actual atmosphere. In the past there has been doubt that a laboratory model, particularly a wind tunnel model, could reproduce the essential characteristics of the atmosphere in the planetary boundary layer. Queney et al. (Ref. 86) states the following in reference to modeling airflow over a mountain obstacle in a wind tunnel,

> .... Now, even if it were possible to maintain the very large temperature gradient of $1°C\ cm^{-1}$ in the model, we should require a flow speed of only 9 cm sec^{-1}. For smaller temperature gradients, even slower flow speeds in the model would be necessary. Such flows with large temperature gradients and very low flow speeds cannot be accomplished, at least in conventional wind tunnels. .... the above considerations indicate that model experiments in a wind tunnel using air as the streaming medium would be useless if it is desired to accomplish quantitative similarity.

Buettner et al. (Ref. 13) states the following in relation to this problem,

> .... It would seem natural that scale models with the desired geometric properties should be constructed and studied in a low speed wind tunnel, but there are a number of serious drawbacks to such a procedure. In the first place, there exists a serious problem of scaling, that is, trying to reduce dimensions and speeds in the ratio of 10^3-10^4:1. .... Furthermore, it is difficult to completely represent each aspect of the meteorological dynamics, ... Generally, when using models for study, only part of the problem may be investigated at one time, and many simplifying assumptions are made by necessity.

Scorer (Ref. 93) and Corby (Ref. 23) have also noted similar drawbacks of wind-tunnel modeling. Generally, the concensus is that the exact conditions for similitude between model and field may not be achieved. However, it should be noted that some of the drawbacks mentioned by the above authors apply to any method of modeling.

Another problem, related to the similitude problem, is that quite often adequate field data are not available in order to check the model results. In this work, the second method of research, the field program was necessary in order to provide certain pertinent observations that would assist in checking the laboratory simulation. Also, these same observations were used to extend our knowledge on the actual transport - diffusion processes in the field.

Certain advantages or benefits of laboratory simulation may be realized when similarity conditions are partially or actually satisfied between field and model. These are:

(1) The problem may be studied in the three space dimensions.

(2) A certain latitude is available for controlling the essential variables in the problem.

(3) The inherent possibility for defining and locating particular problems which might exist on proposed weather sensitive field projects.

(4) Determination of the location of sites for meteorological instruments and towers, cloud seeding generators, etc., in the actual field for the purpose of obtaining representative observations pertinent to a particular project.

(5) Obtaining relevant data that may be used in guiding field programs toward their proposed goals.

(6) The reduction in time and expense of extensive field programs or studies.

In the case of proposed weather modification projects laboratory simulation could possible provide information to such questions as the following:

(1) Under given storm conditions will artificial freezing nuclei reach the target area?

(2) How much of the target volume will be covered (i.e., horizontal and vertical dimensions of seeding plume) and in what concentrations?

(3) What are the effects of stability, wind shear, orographic features and other natural factors on dispersion of the seeding material.

Chapter III

THEORY AND SIMILITUDE

3.1 Basic Equations and Assumptions

In this chapter we will consider the relevant equations and assumptions required to define the two wind-tunnel models and related similarity criteria. The equations will be expressed in terms of the actual atmosphere, then later modified by the various assumptions to correspond to the neutral and barostromatic models.

3.1.1 Basic equations - The basic equations necessary for considering atmospheric motions are the following:

equation of motion,

continuity equation,

equation of state,

poisson's equation,

equation of turbulent heat transfer, and

equation of heat transfer from the surface boundary.

a) Equation of motion

The principal forces governing motions in the atmosphere are the pressure gradient, the Coriolis, buoyancy, and the frictional forces. That is,

$$\frac{D\vec{V}}{Dt} = -\frac{1}{\rho}\vec{\nabla}p - 2\vec{\Omega} \times \vec{V} + \vec{g} + \vec{F} \qquad 3.1$$

where $\vec{g} = \vec{g}_a + \Omega^2 \vec{R}$. Equation 3.1 expresses the fundamental law of motion with respect to the noninertial or relative frame of reference.

The actual wind is sometimes expressed as the sum of the geostrophic wind and the ageostrophic component, or

$$\vec{V} = \vec{V}_g + \vec{V}_{ag} \qquad 3.2$$

where

$$\vec{V}_g = \frac{1}{\rho f} \vec{\nabla} p \qquad 3.3$$

and the resultant ageostrophic wind is the vector sum of several components, such as,

$\vec{V}_{ai}$ - isallobaric wind

$\vec{V}_{aa}$ - advective ageostrophic wind

$\vec{V}_{ca}$ - convective ageostrophic wind

$\vec{V}_{af}$ - frictional and topographic ageostrophic wind

$\vec{V}_{aag}$ - component due to ageostrophic acceleration.

If we take the atmosphere as a turbulent fluid, then we can express the actual or instantaneous wind as

$$\vec{V} = \overline{\vec{V}} + \vec{V}' \qquad 3.4$$

or $u = \overline{u} + u' (\overline{u}' = 0)$, etc. Note that there may be some correspondence between Eqs. 3.2 and 3.4 in that the steady component of the wind, over a certain period of time, may be the result of the geostrophic component while the fluctuating component may be the result of the ageostrophic components.

If we express Eq. 3.1 in terms of expressions like Eq. 3.4 then we obtain Reynolds equation for the average motion, such as,

$$\frac{\partial \overline{U}_i}{\partial t} + \overline{U}_j \frac{\partial \overline{U}_i}{\partial x_j} + 2\varepsilon_{ijk}\Omega_j \overline{U}_k = - \frac{1}{\rho} \frac{\partial \overline{p}}{\partial x_i} + \frac{1}{\rho} \frac{\partial \overline{\sigma}_{ij}}{\partial x_j} + \frac{1}{\rho} \frac{\partial \sigma_{ij}}{\partial x_j} - g\delta_{i3} \qquad 3.5$$

where

$$\overline{\sigma}_{ij} = \mu \left(\frac{\partial \overline{U}_i}{\partial x_j} + \frac{\partial \overline{U}_j}{\partial x_i} \right) - \frac{2}{3} \mu \delta_{ij} \frac{\partial \overline{U}_k}{\partial x_k} \quad \text{(viscous stresses)} ,$$

$$\sigma_{ij} = \begin{bmatrix} \rho\overline{u'^2} & \rho\overline{u'v'} & \rho\overline{u'w'} \\ \rho\overline{u'v'} & \rho\overline{v'^2} & \rho\overline{v'w'} \\ \rho\overline{u'w'} & \rho\overline{v'w'} & \rho\overline{w'^2} \end{bmatrix} \equiv \text{(Reynolds stresses)},$$

$$2\,\varepsilon_{ijk}\,\Omega_j\,\overline{U}_k \equiv \text{(Coriolis accelerations)}$$

and

$$\frac{\partial \overline{U}_k}{\partial x_k} = \nabla\cdot\vec{V} \equiv \text{(dilatation)}.$$

The last term, the body or buoyancy force, can be written as $-(\Delta\overline{T}/\overline{T})g\delta_{i3}$ using the Boussinesq approximation which expresses the effect of temperature stratification upon the body force. Equation 3.5 neglects such small terms as horizontal components of gravity and terms involving the curvature of the earth.

b) Continuity equation

$$\frac{\partial \rho}{\partial t} + \frac{\partial (\rho \overline{U}_i)}{\partial x_i} = 0 \qquad 3.6$$

c) Equation of state

$$p\,\frac{1}{\rho} = R_d\,T \qquad 3.7$$

d) Equation of Poisson

$$\theta = T\left(\frac{1000}{p}\right)^{R_d/c_{p_d}} \qquad 3.8$$

e) Equation of turbulent heat transfer

$$\rho c_p\left(\frac{\partial \overline{T}}{\partial t} + \overline{U}_j\,\frac{\partial \overline{T}}{\partial x_j}\right) - \frac{\partial \overline{p}}{\partial t} - \overline{U}_j\,\frac{\partial \overline{p}}{\partial x_j} - \overline{u_j'\,\frac{\partial p'}{\partial x_j}}$$

$$= \frac{\partial}{\partial x_j}\left(k\,\frac{\partial \overline{T}}{\partial x_j}\right) - c_p\rho\,\frac{\partial}{\partial x_j}\left(\overline{T'u_j'}\right) + \overline{\Phi}\ . \qquad 3.9$$

Terms involving internal heat generation and radiation have been neglected.

f) Equation of heat transfer from the surface boundary

The principle of conservation of energy states that all gains and losses of energy at the surface of the earth must balance. The conservation principle (Ref. 72) can be expressed as a very general equation applicable at any instant in time:

$$Q_T - Q_R + Q_{L\downarrow} - Q_{L\uparrow} = \pm Q_G \pm Q_H \pm Q_E \quad . \tag{3.10}$$

For the set of equations to be complete, equations dealing with the physics of clouds should be included, but this aspect of the problem cannot be considered in a wind-tunnel model at the present time.

3.1.2 General assumptions - In order that the flow in any laboratory model should be of value in interpreting or predicting the observed flow in the atmosphere, it is essential that the two systems should be dynamically, thermally, and geometrically similar. This means that it must be possible to describe the flow in the two systems by the same equations after appropriate adjustment of the units of length, time, and other variables have been made.

Several difficulties arise in attempting to devise a wind-tunnel model which will be similar to the atmosphere. The difficulties are principally due to the limitations of the laboratory apparatus in reproducing a scaled-down model atmosphere. These problems require a simplification of the basic equations of the atmosphere by a set of restrictive assumptions. The following restrictions must be placed upon the atmospheric flow in order to make laboratory simulation possible:

a) Coriolis forces

The effects of Coriolis acceleration on air motion can be neglected due to the relatively small prototype region of 40 to 50 km. A justification for such an assumption follows:

If the Coriolis term in Eq. 3.5 is non-dimensionalized one obtains a non-dimensional ratio of the inertial force to the Coriolis force called the Rossby number,

$$R_o = \frac{U^{*2}/L^*}{fU^*} \qquad 3.11$$

If we select a characteristic length $L^* = 50$ km, a characteristic velocity $U^* = 10$ m/sec and let $f = 9 \times 10^{-5}$ sec^{-1} at $\phi = 37$ deg latitude, a comparison between the inertial and Coriolis term yields,

$$U^{*2}/L^* = 2.0 \times 10^{-3}$$

and

$$fU^* = 9.0 \times 10^{-4}$$

The inertial term is nearly an order of magnitude greater than the Coriolis term, therefore, the inertial effects would be expected to predominate over the Coriolis effects. The local terrain effects should increase the magnitude of the inertial terms and thus decrease further the effect of the earths rotation.

b) Steady-state conditions

In the model it was assumed that velocity, temperature or density fields were in steady-state. This was a good approximation for the neutral airflow model but in the case of the barostromatic airflow model the temperature field over the model was unsteady with time.

c) Uni-directional freestream

In the model airflows the freestream or geostrophic flow was considered essentially uni-directional or that little directional wind shear occurs due to a thermal wind or horizontal temperature gradients. However, directional wind shear may occur due to irregular terrain and resultant secondary flows.

d) Cloud system effects

All physical effects from a cloud system are neglected in the wind-tunnel models. This limitation means that the model airflows do not experience any large thermodynamic or compressibility effects and that the airflow patterns are primarily determined by topography and thermal stratification.

3.1.3 Neutral airflow model - The principal assumptions for the neutral prototype and model airflow are the following:

a) Atmospheric stability

The atmospheric stability is assumed to be in a neutral state or adiabatic equilibrium. Under these conditions an air parcel displaced adiabatically will continue to possess the same temperature and pressure as its surroundings, so that no restoring force acts on a parcel displaced vertically. The state of adiabatic equilibrium is approached in a layer of air in which there is strong vertical mixing, e.g., when the sky is thickly covered with cloud and there is a moderate or high wind.

In a neutral state the environmental lapse rate of temperature is equal to the dry-adiabatic lapse rate or the saturation-adiabatic lapse rate. When expressed in terms of the potential temperature one can write,

$$\theta = T\left(\frac{1000}{p}\right)^{R_d/c_{p_d}} \qquad 3.12$$

or when Eq. 3.12 is expressed in terms of a logarithmic derivative with respect to z,

$$\frac{1}{\theta}\ \frac{d\theta}{dz} = \frac{1}{T}\ \frac{dT}{dz} - \frac{R_d}{c_{p_d}}\ \frac{1}{p}\ \frac{dp}{dz} \quad .$$

In the neutral state, the temperature and pressure terms balance to give,

$$\frac{1}{\theta}\frac{\partial\theta}{\partial z} = 0 \quad . \qquad 3.13$$

The above derivations are based on the quasi-hydrostatic approximation which assumes that,

$$\frac{\partial p}{\partial z} = -\rho g \quad . \qquad 3.14$$

In the neutral airflow model although the pressure may be governed by the hydrostatic approximation the present laboratory equipment does not permit scaling the hydrostatic pressure exactly. In fact for the vertical thickness considered in the model the vertical pressure gradient is assumed to be,

$$\left.\frac{\partial p}{\partial z}\right)_m \sim 0 \quad . \qquad 3.15$$

This restriction means that atmospheric compressibility effects related to vertical motion are neglected, i.e., the model airflow is essentially incompressible in respect to vertical displacements. As a consequence Eq. 3.6 is written,

$$\frac{1}{\rho}\ \frac{D\rho}{Dt} = -\left(\frac{\partial\overline{U}}{\partial x} + \frac{\partial\overline{V}}{\partial y} + \frac{\partial\overline{W}}{\partial z}\right) = 0 \quad . \qquad 3.16$$

With the assumption of Eq. 3.15 the model airflow stability relation is,

$$\frac{1}{\theta}\frac{\partial\theta}{\partial z} = \frac{1}{T}\frac{\partial T}{\partial z}$$

or in the case of the neutral stability in the atmosphere the model stability is,

$$\left.\frac{1}{\theta}\frac{\partial\theta}{\partial z}\right)_{\text{field}} \equiv \left.\frac{1}{T}\frac{\partial T}{\partial z}\right)_{\text{model}} = 0 \qquad 3.17$$

The main limitation in these approximations is that it must be possible to treat the atmosphere like an incompressible fluid. It is well known that potential temperature in the atmosphere behaves almost exactly like density in a stratified incompressible fluid so that the limitation is generally acceptable (Ref. 23). However, the full consequences of such an assumption have not been fully explored for modeling especially on the planetary boundary-layer scale.

Another consequence of neutral stability conditions is the absence of gravitational instability or the production of gravity waves. Also, Eqs. 3.9 and 3.10 are not relevant for these conditions.

b) Turbulent airflow

The prototype and model airflow are assumed to be turbulent because of the irregular terrain features. Molecular viscosity is negligible in both flows except perhaps in certain local regions near the surface of the model. Since turbulent eddy viscosity predominates, the molecular viscosity terms in the equation of motion are neglected.

c) Basic equations

With the above assumptions, the basic equations for the neutral prototype and model airflow can be written as,

1) Equation of motion

$$\overline{U}_j \frac{\partial \overline{U}_i}{\partial x_j} = - \frac{1}{\rho} \frac{\partial \overline{p}}{\partial x_i} - \frac{\partial}{\partial x_j} (\overline{u_i' u_j'}) \qquad 3.18$$

2) Continuity equation

$$\frac{\partial \overline{U}}{\partial x} + \frac{\partial \overline{V}}{\partial y} + \frac{\partial \overline{W}}{\partial z} = 0 \qquad 3.19$$

3) Equation of state

$$\overline{p} \frac{1}{\rho} = R_d \overline{T} \qquad 3.20$$

4) Modified Poisson's equation

$$\frac{1}{\overline{\theta}} \frac{\partial \overline{\theta}}{\partial z}\bigg|_{field} \equiv \frac{1}{\overline{T}} \frac{\partial \overline{T}}{\partial z}\bigg|_{model} \equiv - \frac{1}{\overline{\rho}} \frac{\partial \overline{\rho}}{\partial z}\bigg|_{model} \qquad 3.21$$

3.1.4 Barostromatic airflow model - Many of the assumptions of the neutral airflow model apply to this model although the following significant differences do occur:

a) Temperature or density stratification

Temperature or density stratification exists in this type of airflow so gravitational instability or gravity waves maybe present. It is necessary to consider the buoyancy term in Eq. 3.5.

b) Quasi-laminar airflow

A quasi-laminar model airflow with molecular transport properties is assumed to approximate a turbulent prototype airflow with constant eddy viscosity K_M and eddy conductivity K_H .

c) Heat fluxes

The weather situation of interest is storm periods with fairly extensive cloud cover over the region, therefore, Q_T, Q_R, $Q_{L\downarrow}$

and $Q_{L\downarrow}$ in Eq. 3.10 remain negligible. Although condensation and evaporation occur in the field flow Q_E is not included in the model. Q_H and Q_G are of some importance since the airflow near the surface could be warmer or colder than the underlying surface, both for model and prototype.

d. Basic equations

With these assumption, along with others (incompressibility, steady state, etc.) stated previously, the basic equations for the mean airflow can be written as follows:

1) Equations of motion

$$\overline{U}_j \frac{\partial \overline{U}_i}{\partial x_j} = -\frac{1}{\rho} \frac{\partial \overline{p}}{\partial x_i} + \nu \frac{\partial^2 \overline{U}_i}{\partial x_j \partial x_j} + K_M \frac{\partial^2 \overline{U}_i}{\partial x_j \partial x_j} - \frac{\Delta \overline{T}}{\overline{T}} g\delta_{i3} \qquad 3.22$$

(small)

2) Continuity equation

$$\frac{\partial \overline{U}}{\partial x} + \frac{\partial \overline{V}}{\partial y} + \frac{\partial \overline{W}}{\partial z} = 0 \qquad 3.23$$

3) Modified Poisson's equation

$$\frac{1}{\overline{\theta}} \frac{\partial \overline{\theta}}{\partial z} \equiv \frac{1}{\overline{T}} \frac{\partial \overline{T}}{\partial z} \qquad 3.24$$

4) Equation of turbulent heat transfer

$$\rho c_p \left(\frac{\partial \overline{T}}{\partial t} + \overline{U}_j \frac{\partial \overline{T}}{\partial x_j} \right) = k \frac{\partial^2 \overline{T}}{\partial x_j \partial x_j} + K_H c_p \frac{\partial^2 \overline{T}}{\partial x_j \partial x_j} + \overline{\Phi} \qquad 3.25$$

(small)

where

$$\Phi = \frac{\mu}{2} \left(\frac{\partial \overline{U}_i}{\partial x_j} + \frac{\partial \overline{U}_j}{\partial x_i} \right)^2$$

5) Equation of heat transfer from the surface boundary

$$0 \sim \pm Q_G \pm Q_H \quad . \tag{3.26}$$

In Eqs. 3.22 and 3.25 the turbulent terms are considered small since the airflow is quasi-laminar.

3.2 Similitude Criteria

For complete flow similarity in two systems of different length scales, geometrical, kinematical, dynamical and thermal similarity must be achieved. In addition, boundary conditions upstream, in the upper atmosphere, and downstream should also be similar.

Geometrical similitude exists between model and prototype if the ratios of all corresponding dimensions in model and prototype are equal. This is realized by using an undistorted scale model of the prototype geometry. Kinematic similitude exists between model and prototype if the paths of homologous moving particles are geometrically similar and if the ratio of the velocities of homologous particles are equal. Dynamic similitude exists between geometrically and kinematically similar systems if the ratios of all homologous forces in model and prototype are the same. Thermal similitude exists if the temperature or density stratification are similar.

The proper similitude parameters governing the phenomena of interest may be established by dimensional analysis, similarity theory or inspectional analysis. No attempt will be made here to give a comprehensive description of each of these methods since several good discussions are available in various textbooks and publications, e.g., McVehil *et al.* (Ref. 68), Cermak *et al.* (Ref. 14) and Nemoto (Ref. 75, 76).

The technique used in this section for determining the similitude parameters will be a combination of dimensional analysis and inspectional analysis. For the latter method this will mean selecting characteristic values of the dependent and independent variables and writing the relevant equations governing the problem in non-dimensional form. With some mathematical rearrangement the appropriate non-dimensional groupings will appear with the various terms of the non-dimensional equations. Next, it will be necessary to examine the most relevant non-dimensional groupings to see whether it is possible to satisfy each one for the model and prototype airflow.

3.2.1 Neutral airflow model -

a) Thermal similarity

One of the principal assumptions of this type of model airflow as stated in Sec. 3.1.3 is that the atmospheric stability is assumed to be in a neutral state. This implies $\left.\frac{\partial\theta}{\partial z}\right|_{field} \equiv \left.\frac{\partial T}{\partial z}\right|_{model} = 0$ for the temperature distribution in the field and wind tunnel. How valid this assumption was for the prototype area will be discussed in Chapter V.

b) Geometric, dynamic, and kinematic similarity

In the case of neutral flow the variables relevant to flow in the planetary boundary layer in the atmosphere are $V(z)$, V_g, ρ, f, τ, τ_o, H, Z and z_o. According to the assumption in section 3.1.2a it will be permissible to neglect the Coriolis parameter f as a variable.

Now in dimensional analysis one assumes that a functional relationship exists of the form,

$$f(V(z), V_g, \rho, \tau, \tau_o, H, z_o, Z) = 0 \qquad 3.27$$

from which an appropriate set of independent dimensionless combinations can be derived. The physical dimensions of the variables are,

$$[V] = [V_g] = LT^{-1}$$

$$[\tau] = [\tau_o] = ML^{-1}T^{-2}$$

$$[H] = [z_o] = [Z] = L$$

$$[\rho] = ML^{-3}$$

and these eight variables in three dimensions yield five independent dimensionless combinations,

$$f\left[\frac{V_g}{(\tau_o/\rho)^{\frac{1}{2}}}\ ,\ \frac{V}{V_g}\ ,\ \frac{Z}{H}\ ,\ \frac{z_o}{H}\ ,\ \frac{\tau}{\tau_o}\right] = 0 \quad . \qquad 3.28$$

The dimensionless groups Z/H , z_o/H and other similar ratios which could be formed from additional dimensions require geometric similarity. The dimensionless group $V(z)/V_g$ indicates that velocity profiles or flow field should be similar. The other two groups require certain aspects of the turbulent flow to be similar.

Another approach to the similarity problem is to consider the equations which describe the mean flow in the planetary layer. At this point it is important to note a basic distinction between the layer immediately above the surface and the remainder of the planetary boundary layer above it.

Very near the surface (~100 m), the wind, wind shear, and stress all lie in the same direction, and the mean wind under neutral conditions in quite often given by,

$$\bar{u} = \frac{u_*}{\kappa}\ \ell n\ \frac{z}{z_o} \quad . \qquad 3.29$$

However, above the surface layer several other factors enter into the problem as indicated in Sec. 3.1.1 and the mean flow is described by the equations of motion as derived by Reynolds.

To find the relevant scaling parameters for dynamic and kinematic similarity Eqs. 3.18, 3.19 and 3.20 are required. However, Eqs. 3.19 and 3.20 do not give any pertinent scaling parameters and can be neglected.

Inspectional analysis of Eq. 3.18 will give the proper scaling parameters. If one expresses the Reynolds stresses in Eq. 3.18 by the Boussinesq approximation,

$$
\begin{aligned}
-\overline{u'v'} &= K_y \frac{\partial \overline{U}}{\partial y} \quad \text{or} \quad K_x \frac{\partial \overline{V}}{\partial x} \\
-\overline{u'w'} &= K_z \frac{\partial \overline{U}}{\partial z} \quad \text{or} \quad K_x \frac{\partial \overline{W}}{\partial x} \\
-\overline{v'w'} &= K_z \frac{\partial \overline{V}}{\partial z} \quad \text{or} \quad K_y \frac{\partial \overline{W}}{\partial y}
\end{aligned}
\qquad 3.30
$$

Then Eq. 3.18 can be written,

$$
\begin{aligned}
\overline{U}\frac{\partial \overline{U}}{\partial x} + \overline{V}\frac{\partial \overline{U}}{\partial y} + \overline{W}\frac{\partial \overline{U}}{\partial z} &= -\frac{1}{\rho}\frac{\partial \overline{p}}{\partial x} - \frac{\partial}{\partial x}(\overline{u'u'}) + \frac{\partial}{\partial y}\left(K_y \frac{\partial \overline{U}}{\partial y}\right) + \frac{\partial}{\partial z}\left(K_z \frac{\partial \overline{U}}{\partial z}\right) \\
\overline{U}\frac{\partial \overline{V}}{\partial x} + \overline{V}\frac{\partial \overline{V}}{\partial y} + \overline{W}\frac{\partial \overline{V}}{\partial z} &= -\frac{1}{\rho}\frac{\partial \overline{p}}{\partial y} - \frac{\partial}{\partial y}(\overline{v'v'}) + \frac{\partial}{\partial x}\left(K_x \frac{\partial \overline{V}}{\partial x}\right) + \frac{\partial}{\partial z}\left(K_z \frac{\partial \overline{V}}{\partial z}\right) \\
\overline{U}\frac{\partial \overline{W}}{\partial x} + \overline{V}\frac{\partial \overline{W}}{\partial y} + \overline{W}\frac{\partial \overline{W}}{\partial z} &= -\frac{1}{\rho}\frac{\partial \overline{p}}{\partial z} - \frac{\partial}{\partial z}(\overline{w'w'}) + \frac{\partial}{\partial x}\left(K_x \frac{\partial \overline{W}}{\partial x}\right) + \frac{\partial}{\partial y}\left(K_y \frac{\partial \overline{W}}{\partial y}\right)
\end{aligned}
\qquad 3.31
$$

If we let L^* , U^* and ρ^* denote a characteristic length, velocity, and density then the above equations may be expressed in non-dimensional form by scaling all the variables as follows:

$$\hat{X}_i = \frac{x_i}{L^*} \quad ; \quad \hat{U} = \frac{\overline{U}_i}{U^*} \quad ; \quad \hat{p} = \frac{p}{\rho^* U^{*2}} \quad .$$

After considerable mathematical rearranging of the non-dimensional equations the following dimensionless parameters can be found,

$$\mathrm{Re}_{T_i} \text{ (Turbulent Reynolds number)} = \frac{L^* U^*}{K_i} \qquad 3.32$$

$$I_i \text{ (Turbulent intensities)} = \frac{\overline{u_i' u_i'}}{U^{*2}} \quad . \qquad 3.33$$

Similitude requires each turbulent Reynolds number with respect to each direction x, y, z at any corresponding location of the model and prototype flow be identical with each other. A similar statement can be made for the turbulent intensities. If this type of similarity could be achieved it would be a large step for laboratory simulation. Unfortunately, these requirements are difficult to satisfy as well as check because complete model and field data are seldom available.

The above similitude criteria have been expanded by Nemoto (Ref. 75) for flow conditions within the planetary boundary layer. From Eqs. 3.32 and 3.33, Nemoto derives the following similarity criteria for the airflow,

$$\frac{U_{\infty_m}}{U_{\infty_p}} = \left(\frac{\varepsilon_m}{\varepsilon_p}\right)^{\frac{1}{3}} \left(\frac{L_m}{L_p}\right)^{\frac{1}{3}} \quad . \qquad 3.34$$

Nemoto reduces the above relation by assuming $\varepsilon_m = \varepsilon_p$ or

$$\frac{U_{\infty_m}}{U_{\infty_p}} = \left(\frac{L_m}{L_p}\right)^{\frac{1}{3}} \quad . \tag{3.35}$$

The above relations are based on the following conditions:

1) Intensities of turbulence at corresponding locations for model and prototype are equal, i.e., Eq. 3.33.

2) Each size of mean eddy in the x,y,z direction of the model flow at each location corresponding to the location of the natural flow decrease according to the reduced scale of the model,

$$\frac{\Omega_{i_m}}{\Omega_{i_p}} = \frac{L_m}{L_p} \quad .$$

3) Spectrum function of the turbulent energy with respect to wave number are similar for both cases,

$$\int_{k_{im}}^{\infty} F(k)_m dk = \int_{k_{ip}}^{\infty} F(k)_p dk \quad .$$

4) Turbulence is isotropic.

5) Criteria are restricted to short time periods.

Another point of view which has been the most commonly applied in model neutral flows is based on the concept of aerodynamically rough surfaces (Refs. 16, 32, and 12). An aerodynamically rough surface is one in which the roughness elements are large enough to prevent the formation of any laminar sublayer, so that the motion is turbulent down to the surface itself. Since the depth of the laminar sublayer depends on the magnitude of the Reynolds number, the classification of a surface according to the above definition involves not only the geometrical

characteristics of the boundary but also the magnitude of the mean velocity, so that a surface which is "smooth" at low velocities may become "rough" as the mean velocity increases (Ref. 103).

If a surface is fully rough, the direct influence of viscosity is negligible and the Reynolds number does not enter into the similarity criteria. Generally, the requirement for fully rough flow is

$$\frac{u_* \lambda}{\nu} > 100 \quad \text{(Sutton)}$$

or 3.36

$$\frac{U_\infty x}{\nu} > 10^4 \text{ to } 10^6 \quad \text{(Schlichting)} \ .$$

One consequence of this concept is that the local skin friction of a rough surface is almost exactly proportional to the square of the reference velocity.

c) Similarity requirements for transport and dispersion

The average concentration $\overline{C}$ at a particular location in a particulate plume over mountainous terrain is affected by numerous variables, e.g.,

$$\overline{C}(\vec{r}) = f(Q, w_s, T_s, \mathcal{D}, \vec{Z}, \lambda, \vec{V}(z), \beta, \frac{\partial \vec{V}}{\partial z}, K_{ii}, t) \qquad 3.37$$

where Q, w_s, T_s are parameters depending on the source characteristics. $\mathcal{D}$ represents various mechanisms causing deposition or depletion of the particulate material in transit to the target site. $\vec{Z}$ and λ describes the topographic terrain. $\vec{V}(z)$ represents the transport by geostrophic and ageostrophic winds. β, $\frac{\partial \vec{V}}{\partial z}$, K_{ii}, are parameters which influence turbulent mixing or dispersion. t is time or sampling time.

1) Source characteristics

A particulate plume, e.g., silver-iodide particles, quickly attains the wind speed in the horizontal plane, while its rise is determined by its vertical momentum and buoyancy due to heat and molecular-weight difference. Rise of the plume is impeded by entrainment with air, which at first is due to turbulence generated by the relative motion of the plume. As this dies out, atmospheric turbulence dominates the mixing. Buoyancy of the plume may be altered by the atmospheric stability. Stable air acts as a restoring force on the plume, but in unstable air the plume may rise to large heights.

The sources in the field are generated by Colorado State University modified Sky-Fire Acetone generators which burn approximately 20 gms of silver iodide per hour (Q) at a flame temperature (T_s) around 1000°C. The material emits at a few meters per sec (w_s) from the orifice.

For a wind-tunnel model of 1:9600 scale ratio it is not feasible to scale or simulate Q , T_s and w_s for prototype silver-iodide generators. The source or sources on the model correspond approximately to a field virtual source elevated some 50 meters from the surface. For the neutral airflow it was assumed that the effects of dissimilarity due to T_s , Q and w_s are quickly masked by the effects of turbulent mixing as the material moves downstream after release.

2) Deposition and depletion mechanisms

The mechanisms causing deposition and depletion are numerous and often not well understood. These include gravitational settling (fallout), precipitation scavenging (washout, snowout, and rainout), surface impaction (storage), electrostatic attraction, adsorption (coagulation) and chemical interaction. A further complication is the

possibility of ultraviolet decomposition of the silver-iodide crystals. A third process is the possibility of resuspension and redeposition of the material.

No attempt was made to model any of the deposition variables on the model scale. Some of the variables such as the fallout velocity of silver iodide particles ($d \sim .02\mu$) is very small and can be neglected. Grant et al. (Ref. 39) suggests that precipitation scavenging, coagulation, ultraviolet decomposition and electrostatic attraction have a small effect in depleting the seeding materials in the Eagle River Valley and Climax area.

The problem of resuspension and redeposition exists for the field as discussed by Grant (Ref. 38) but it appears that the time scale for this mechanism is somewhat longer than the one of interest in this study. Surface impaction may be an important deposition variable in the case of ground-based sources because of the possible interception by dense stands of trees.

3) Turbulent dispersion

If the source and depletion variables are neglected Eq. 3.37 may be written as,

$$\overline{C}(\vec{r}) = f(Q, \vec{Z}, \lambda, \vec{V}(z), \beta, \partial\vec{V}/\partial z, K_{ii}, t) \qquad 3.38$$

The first six variables do not require additional treatment since they are directly involved in geometric, dynamic, and thermal similarity, however, the last two parameters need further consideration.

The proper scaling parameters for the eddy diffusivity K_{ii} can be obtained by expressing the parabolic diffusion equation,

$$\frac{\partial \overline{C}}{\partial t} + \frac{\partial}{\partial x_i} (\overline{C}\,\overline{U}_i) = \frac{\partial}{\partial x_i} (K_{ii} \frac{\partial \overline{C}}{\partial x_i}) \qquad 3.39$$

in non-dimensional form by using the following scaling quantities,

$$\hat{x}_i = \frac{x_i}{L^*} \;;\; \hat{\overline{U}}_i = \frac{\overline{U}_i}{U^*} \;;\; \hat{\overline{C}} = \frac{\overline{C}}{C^*} \;;\; \hat{K}_{ii} = \frac{K_{ii}}{K^*_{ii}} \;;\; \hat{t} = t \frac{U^*}{L^*} \;.$$

With substitution of the scaling quantities the diffusion equation may be written,

$$\frac{\partial \hat{\overline{C}}}{\partial \hat{t}} + \frac{\partial}{\partial \hat{x}_i} (\hat{\overline{C}}\,\hat{\overline{U}}_i) = \frac{1}{(Pe)^i_t\big]_m} \frac{\partial}{\partial \hat{x}_i} \left[(\hat{K}_{ii} \frac{\partial \hat{\overline{C}}}{\partial x_i}) \right] \qquad 3.40$$

where $(Pe)^i_t = \frac{U^*L^*}{K^*_{ii}}$ and represents a three-dimensional turbulent Péclét number since the characteristic eddy diffusivity coefficients vary depending upon the direction (Ref. 53). Similarity between model and field requires that

$$(Pe)^i_t\big]_m = (Pe)^i_t\big]_p \;. \qquad 3.41$$

4) Time

If the time is included as another variable relevant to the flow in the planetary boundary layer along with the others in Eq. 3.27, then it is possible to arrive at another dimensionless variable,

$$\frac{t\,\vec{V}_g}{\vec{Z}} \;. \qquad 3.42$$

This dimensionless variable gives the simplest relation connecting the time-scale of the model t_m to that of the real flow t_p, i.e.,

$$t_m = \frac{L_m}{L_p} \frac{U_p}{U_m} t_p \quad . \tag{3.43}$$

A specific mathematical relation for the sampling time for diffusion problems have been derived by Hino (Ref. 50).

5) Concentration parameter

Concentration measurements on the model scale occur in radioactive units of $\mu\mu$ curie/cc while for the field measurements concentration was measured in terms of particles per liter. These two different units of concentration can be made compatible by use of the dimensionless concentration parameter,

$$\frac{\overline{C}\,\overline{U}X^2}{Q} \quad . \tag{3.44}$$

$\overline{C}, \overline{U}, X$ and Q are defined in the list of symbols.

3.2.2 Barostromatic airflow model

a) Dynamic, kinematic and thermal similarity

When a vertical gradient of potential temperature exists in the atmosphere, buoyancy forces develop which necessitate the use of additional similitude parameters. In addition to the variables in Eq. 3.27, β and g or some other equivalent variables would have to be included in the functional relationship describing the flow in the planetary boundary layer. Dimensional or inspectional analysis would generate additional similitude parameters such as the Froude or Richardson number as well as the Reynolds number.

At the present time it is not possible to generate a thermally stratified turbulent-boundary layer within a wind tunnel in which the

Froude number similarity can be satisfied at the same time as the turbulent Reynolds number. The energy requirements for such an experiment on the scale of a 6 ft x 6 ft wind tunnel are generally too large to be maintained in the present wind tunnel facilities.

In order to satisfy the wind shear and temperature stability conditions for Froude number similarity the laboratory flow speeds must be reduced to where the airflow approaches a quasi-laminar state. When this is the case the similarity criteria must be relaxed to obtain partial similitude between model and field. The possible approaches for achieving similitude under these conditions will be considered next.

1) Approach of Abe and Cermak

In the case of model airflows over irregular terrain with thermal stratification, Cermak (Ref. 16) proposed that partial similarity may be achieved by comparing a laminar laboratory airflow model to a turbulent atmospheric prototype airflow.

This approach to similarity can be illustrated by the following development. Criteria for dynamic and kinematic similarity for model and field are given by the momentum conservation equations --

Field

$$\frac{\partial \overline{U}_i}{\partial t} + \overline{U}_j \frac{\partial \overline{U}_i}{\partial x_j} = -\frac{1}{\rho} \frac{\partial \overline{p}}{\partial x_i} - \frac{\Delta \overline{T}}{\overline{T}} g\delta_{i3} + K_m \frac{\partial^2 \overline{U}_i}{\partial x_j \partial x_j} \qquad 3.45$$

Model

$$\overline{U}_j \frac{\partial \overline{U}_i}{\partial x_j} = -\frac{1}{\rho} \frac{\partial p}{\partial x_i} - \frac{\Delta \overline{T}}{\overline{T}} g\delta_{i3} + \nu \frac{\partial^2 \overline{U}_i}{\partial x_j \partial x_j} \qquad 3.46$$

Equation 3.45 neglects effects due to the rotation of the earth and viscous effects. Equation 3.46 neglects time dependent variables, rotation effects, and the Reynolds shear stresses.

Criteria for thermal similarity for model and field are given by the statement for conservation of energy,

Field

$$\rho c_p \left(\frac{\partial \overline{T}}{\partial t} + \overline{U}_j \frac{\partial \overline{T}}{\partial x_j} \right) = \rho c_p K_H \frac{\partial^2 \overline{T}}{\partial x_j \partial x_j} + \overline{\Phi} \qquad 3.47$$

Model

$$\rho c_p \left(\frac{\partial \overline{T}}{\partial t} + \overline{U}_j \frac{\partial \overline{T}}{\partial x_j} \right) = k \frac{\partial^2 \overline{T}}{\partial x_j \partial x_j} + \overline{\Phi} \qquad 3.48$$

Inspectional analysis of Eqs. 3.45, 3.46, 3.47 and 3.48 will give the following dimensionless parameters,

	Model	Field	
Reynolds number	$Re = \frac{U^*L^*}{\nu}$	$Re_t = \frac{U^*L^*}{K_i}$	3.49
Prandtl number	$Pr = \frac{\mu c_p}{k}$	$Pr_t = \frac{K_m}{K_H}$	3.50
Froude or Richardson number	$Ri = \frac{g^*}{T^*} \frac{\Delta T^* L^*}{U^{*2}}$		3.51
Euler number	$Eu = \frac{\Delta p^*}{\rho U^{*2}}$		3.52
Eckert number	$Ek = \frac{U^{*2}}{c_p \Delta T^*}$.		3.53

Similitude as proposed by Cermak requires that these dimensionless numbers be the same for model and field.

The similitude criteria can be relaxed somewhat by neglecting Eckert and Euler number requirements. The Eckert number is closely related to the Mach number and since in low speed flows the compressibility effects, of which the Mach number is a measure, is unimportant this parameter is of little significance to the problem.

In the type of airflow being studied local pressure differences are, as for an ideal flow, assumed dependent essentially on the geometry. Therefore, the Euler numbers are assumed to be nearly equal for model and prototype but measurements are usually not available to verify this equality.

If Richardson number and Prandtl number similarity is assumed to be satisfied then the Reynolds number similarity can be closely matched by using a concept proposed by Abe (Ref. 1) several years ago. He proposed that a turbulent prototype fluid with an average turbulent eddy viscosity K_m could be approximated by a quasi-laminar fluid with a molecular kinematic viscosity ν .

A comparison of the model and field Reynolds numbers may be made for estimating the degree of dynamic similarity. The ratio of these two Reynolds numbers,

$$\frac{Re_m}{Re_p} = \left(\frac{U^*_m}{U^*_p}\right)\left(\frac{L^*_m}{L^*_p}\right)\left(\frac{K_{mp}}{\nu_m}\right) \qquad 3.54$$

can be estimated by selecting typical values for the speed, length, and viscosity ratios.

Similar reasoning is applied to finding the relevant scaling parameters for transport and dispersion similarity. The turbulent diffusion equation for model and field can be expressed as,

Field

$$\frac{\partial \overline{C}}{\partial t} + \overline{U}\frac{\partial \overline{C}}{\partial x} + \overline{U}\frac{\partial \overline{C}}{\partial y} + \overline{W}\frac{\partial \overline{C}}{\partial z} = K\left(\frac{\partial^2 \overline{C}}{\partial x_i^2}\right) \qquad 3.55$$

Model

$$\frac{\partial \overline{C}}{\partial t} + \overline{U}\frac{\partial \overline{C}}{\partial x} + \overline{V}\frac{\partial \overline{C}}{\partial y} + \overline{W}\frac{\partial \overline{C}}{\partial z} = k_m\frac{\partial^2 \overline{C}}{\partial x_i^2} \qquad 3.56$$

where molecular and turbulent diffusivities are neglected in Eqs. 3.55 and 3.56, respectively. When Eqs. 3.55 and 3.56 are expressed in dimensionless form, the additional scaling parameters are a turbulent and molecular Péclét number,

	Model	Field	
Péclét number	$Pe_{turb} = \frac{U^*L^*}{K}$	$Pe_{mol} = \frac{U^*L^*}{k_{mol}}$	3.57

The ratio of the two Péclét numbers can be estimated by selecting typical values for U^*, L^*, K and k_{mol} and assuming that the mass diffusivity k_m is equivalent to the eddy diffusivity K.

2) Richardson number similarity

One of the most commonly used similitude parameters when buoyancy forces are present is the Richardson number, which is the ratio of the rate of work done by buoyancy forces to the rate of work done by inertia forces. Batchelor (Ref. 8) has established that if the flow fields are such that the pressure and density everywhere depart by small fractional amounts only from the values for an equivalent atmosphere in adiabatic equilibrium and if the vertical length scale of the velocity distribution is small compared with the scale height of the atmosphere, the Richardson number is the sole parameter governing dynamical similarity. Unfortunately, these conditions are only normally satisfied in the first 100 m of the planetary boundary layer.

Another widely used parameter to describe the state of the atmospheric surface layer under nonadiabatic conditions is the Monin-Obukhov length. Monin and Obukhov (Ref. 71) assumed that when buoyancy forces exist, the character of the flow depends no longer upon the Reynolds number but

upon u_*, Q_H, ρ, c_p, g and T. These may be combined dimensionally to yield a length L defined as,

$$L = - u_*^3 \, T \, \rho \, c_p / \kappa g Q_H \qquad 3.58$$

The Monin-Obukhov similarity statement is valid only if several conditions are fulfilled such as,

a) fractional changes in the potential temperature must be small,

b) the ratio of the eddy transport coefficients of momentum and heat must be a constant independent of both height and stability,

c) a change in z_o should not alter the detailed turbulent structure of the flow,

d) u_* and $Q_H/\rho c_p$ must be independent of height,

e) the flow must be fully aerodynamically rough and have planar homogeneity.

The Monin-Obukhov stability length was derived for the surface layer and not for the entire planetary boundary layer. Its many restrictions does not permit application to the total boundary layer. Also, another disadvantage of the Monin-Obukhov length is that the flux of heat Q_H and u_* are very seldom known in the atmosphere. Other stability parameters such as the flux Richardson number or Panofsky's length have the same difficulties (Ref. 68).

The discussion indicates that although the gradient Richardson number may not be the only sole similarity parameter governing the flow it still remains a parameter for checking similitude between model and field. The Richardson number expressed as a local parameter is defined by,

$$Ri = \frac{g}{\bar{\theta}} \frac{\left(\frac{\partial \bar{\theta}}{\partial z}\right)}{\left(\frac{\partial u}{\partial z}\right)^2} \qquad 3.59$$

Batchelor has emphasized that no local, variable quantity can be used as a similarity parameter. Similarity parameters can have meaning only when they characterize the gross features of the flow.

When a gross or bulk Richardson number is desired to describe the thermal influence over a layer of thickness Δz , the following form is convenient,

$$Ri = \frac{g}{\bar{\theta}} \frac{\Delta \bar{\theta}}{(\Delta u)^2} \Delta z \quad . \qquad 3.60$$

In the case of the model airflow the potential temperature may be replaced by temperature or density.

B. Similarity through surface geometry

In the case of irregular terrain combined with thermal stratification the similarity of transport and dispersion may depend strongly on geometric similarity. This means that the transport and, perhaps the dispersion to a lesser extent, may be predominately influenced by the convective transport by the mean motion (see equation 2.7 and Ref. 16).

Another way to examine this type of similarity would be through the continuity equation in the form,

$$\nabla_H \cdot \vec{V} = \frac{\partial u}{\partial x} + \frac{\partial v}{\partial y} = - \frac{\partial w}{\partial z} \quad . \qquad 3.61$$

Since the horizontal divergence would be governed by the geometry or terrain features this would effectively determine the local vertical velocity distributions. As a result, the vertical and horizontal distributions of a tracer material would depend strongly on the local influence of the terrain. However, Richardson number similarity would still exert an influence on the vertical distribution of the tracer material.

This type of similarity reasoning would only hold for prototype regions where secondary horizontal velocity fields, e.g., antivalley, slope or drainage winds were not well organized.

Chapter IV

EXPERIMENTAL PROGRAM

4.1 Laboratory Simulation

The laboratory or wind tunnel part of the experimental program is divided into two phases. The first phase considers the problems and eventual measurements for the neutral airflow model, i.e., the airflow as generated by the wind tunnel over the topographic model with the aid of necessary artificial obstructions for creating an acceptable turbulent boundary layer. The second phase considers the problems and measurements for the barostromatic airflow model i.e., the airflow as generated by a cold source of dry ice upstream of the model and the wind tunnel.

4.1.1 Neutral airflow model

4.1.1.1 Simulation of boundary layer - In the case of a neutral atmosphere in which the change in direction of the wind with height is neglected the modeling problem is to produce a thick turbulent boundary layer over the topographic relief within the limits of the tunnel test section length. An important question is whether the shear flow, and the Reynolds stresses can be simulated at the same time.

The structure of the atmospheric planetary boundary over irregular terrain is extremely complex even for neutral stability conditions, and in principle a large number of parameters are required for a complete description of the flow. An adequate description of flow would require, at least, a knowledge of the following parameters:

a) mean velocity distribution as a function of height;

b) intensity of each component of turbulence as a function of height;

c) the spectra of turbulence;

d) the Reynolds stresses $\overline{u'w'}$, etc.;

e) integral scales of turbulence;

f) micro-scales of turbulence (energy dissipation scale).

To measure each of these parameters would require a lengthy experimentation program, and usually a compromise must be made to decide what properties of the flow should be attempted for simulation.

The shear flow and turbulence in the atmosphere has been simulated in the wind tunnel by using various forms of screens or honey combs, rods, flat plates, obstructions, and roughness located in long wind tunnel test sections (Ref. 60). These methods rely on local energy extraction from the mean flow for the production of a shear flow.

Once an artificial boundary layer has been produced the turbulence will decay, particularly, at the low frequency end of the spectrum which will have its energy passed to higher frequencies, unless there is some mechanism for the continued production of turbulence as the flow proceeds downstream. In the natural boundary layer this is provided by the action of the Reynolds stresses on the mean velocity profile. Therefore, it is evident that the continued production of turbulence requires the Reynolds stresses and the velocity profile to be simulated.

A preliminary attempt was made toward simulating the shear flow but with no direct attempt in simulating the Reynolds stresses. Initial experiments were made with roughness elements, screens, and a vortex generator upstream from the model in various combinations. These initial results were not totally satisfactory due to the following reasons. One, the artificial devices could not produce a self-preserving shear flow over the length of the model. Two, the apparent dominating influence of

the Red and White mountain ridge on the initial airflow and turbulence in the Eagle River Valley. Then, at this stage, inadequate field data on velocity profiles in the Eagle River Valley area.

An intensive program for shear flow simulation could not be followed through because of experimental and time limitations. Therefore, on the basis of experiments and later field data the best experimental arrangement found for producing an acceptable turbulent boundary layer and shear flow was a set of screens (Appendix B) placed just upstream from the model and the model topography itself.

4.1.1.2 Experimental procedure - Proper simulation of the momentum boundary layer depends strongly on geometric similitude between field and model. To assure this type of similarity a 1:9600 scale topographic model of the Eagle River Valley-Climax region was constructed and arranged in the Colorado State University low-speed wind tunnel. Details of the construction of the model is presented in Appendix A.

The experimental wind tunnel and equipment used in this particular experiment is also discussed in Appendix A. The wind-tunnel arrangement for the neutral airflow experiments and description of the procedures for obtaining measurements of velocity, turbulence, concentration, etc. are discussed in Appendix B.

4.1.1.3 Discussion - Six experimental periods in the wind tunnel were required in order to obtain data on the static pressure distribution, surface streamlines, velocity, turbulence, and concentration for the neutral case.

Since significant aspects of the results will be discussed thoroughly in relation to the field data in Chapter V only an abbreviated review of the results will be presented in this section.

a) Mean velocity field

The free stream velocity in this case was V_g = 15 m/s. However, due to the blockage of the model and the fixed roof of the tunnel the local free-stream velocity increased, in some cases, to approximately 17 m/s over the model. With the fixed roof the longitudinal pressure gradient was not adjusted to zero, consequently, the static pressure distribution in the free stream region (not shown) increased negatively along the model.

Figure 3 shows the near surface streamline pattern as determined by pivoting directional vanes mounted on the model. The wall boundary layer extended approximately 1 ft on each side of the tunnel effectively limiting the area of reliability to 4 ft. Consequently, some of the streamlines near the wall boundary layers were noticeable influenced.

One of the most interesting features of the surface flow pattern was the diverging flow upstream from Chicago Ridge where part of the airflow was diverted through the East Fork of the Eagle River and the other through the Tennessee Pass area.

Figure 4 shows the longitudinal velocity field over the model and the development of the boundary layer. The thickness of the boundary layer on the model scale varied from 30 cm to 60 cm. Separation phenomena were indicated by the low velocity zones downstream from major terrain features.

The model velocity data for six different locations on the model, viz, Minturn, Bolts Lake, Gilman, Redcliff, Camp Hale and Chalk Mountain were plotted with respect to height on semi-logarithmic and logarithmic graph paper, an examined for logarithmic and power-law profiles. All of the velocity profiles showed a power-law form viz.

$$\frac{U}{U_\infty} = \left(\frac{z}{\delta}\right)^p \qquad 4.1$$

but none indicated a logarithmic form (Eq. 3.29).

The power index p for these six different velocity profiles varied from 0.25 to 0.72. These values can be compared with the power index value of $\frac{1}{7}$ (=0.142) which occurs in the generally accepted power-law profile for the turbulent boundary layer over a flat plate. The higher index values for the model velocity profiles indicated that the airflow was fully rough or very turbulent.

Six lateral cross-sections of the longitudinal velocity were plotted to check the uniformity of the velocity field over the model. Figure 5 shows three selected lateral cross-sections of the velocity. The velocity was generally uniform across the model except near the surface features. Farther downstream where the terrain features were more prominent the horizontal gradients increased above the model surface. Horizontal velocity shears of 10 sec^{-1} model scale or 10^{-3} sec^{-1} field scale were observed 10 cm above the model. These shears may be due in part to the irregularity of the terrain.

b) Turbulence measurements

1) Turbulent intensities

Figures 6, 7 and 8 shows the longitudinal I_x, lateral I_y, and vertical turbulent intensities I_z as a function of height over the first half of the model. The patterns for I_x, I_y and I_z approach similarity but differences do exist especially in magnitude. Isotropy can not be expected in this model shear flow.

The turbulent field upstream from Red and White Mountain was artificial since it was produced by the screen set across the tunnel. This turbulence decayed as it approached the model.

Turbulence patterns near the model surface were directly related to separation phenomena found in the downwind sides of terrain features. Two major separation regions were observed downwind of the Red and White Mountain and over the town of Redcliff. Maximum values of I_x, I_y, and I_z occur in these regions of separation.

A feature of interest was the relative positions of the I_x, I_y, and I_z maximum regions to the first model feature, Red and White Mountain. These centers are displaced from each other and comparisons with other turbulence data associated with model ridges (Refs. 45 and 46) suggest that this feature may be a real effect of the model ridge orientation on the turbulent character of the flow.

2) Shear stress parameters

The turbulent stress $-\overline{u'w'}$ was determined for only two locations on the model, i.e., Minturn and Redcliff. Measurements of $-\overline{u'w'}$ were taken twice at the same location by rotating the hot-wire probe. The measurements from these two readings were then averaged and plotted with respect to height. The results are tabulated in Table 2.

A number of parameters can be computed from the turbulent stress $-\overline{u'w'}$ and the wind shear $\partial u/\partial z$ which will be of importance to the modeling criteria. The parameters computed were the following:

vertical flux of the longitudinal momentum or shearing stress

$$\tau = -\rho\,\overline{u'w'}\,, \qquad 4.2$$

friction velocity

$$u_* = \sqrt{(|\overline{u'w'}|)} \quad , \qquad 4.3$$

coefficient of eddy viscosity

$$K_M = - \frac{\overline{u'w'}}{\partial \overline{u}/\partial z} \quad , \qquad 4.4$$

and rate of production of eddy kinetic energy due to the vertical shear of the mean longitudinal wind or in some restricted cases, the eddy energy dissipation

$$\varepsilon = - \overline{u'w'} \frac{\partial \overline{u}}{\partial z} \qquad 4.5$$

Table 2 shows the variation of these parameters with respect to height for the two locations on the model. The wind shear $\partial u/\partial z$ was obtained from the local velocity profiles at the two locations (Fig. 4).

The general character of all parameters was to increase in magnitude with height to a maximum near the ridge heights and then to decrease gradually with increasing height.

The Reynolds stresses observed should not be accepted as typical for the whole model since they were measured at only two locations and these were immediately downstream from regions of separation. The steep gradients of the Reynolds stresses near the lower regions of the model boundary indicated that the flow was still quite turbulent at these locations.

c) Concentration measurements

Two sets of data were obtained; one, simulating a single source at the location of Minturn and two, simulating a dual source at the location of Minturn and Redcliff.

1) Minturn source - Lateral and vertical cross-sections of the concentration parameter $\overline{C}\,\overline{U}/Q$ are presented in Figures 9 and

10. A hypothetical cloud system has been added to the figures to show how the tracer material may enter a cloud and, also, depict how much of the cloud system may be affected by the tracer material.

The upper boundary of the tracer plume was set a $\overline{C}\,\overline{U}/Q = 10 \times 10^{-9} m^{-2}$. This value was chosen on the basis of the accuracy of counts from the Geiger-Mueller tubes which was based on Eq. B.12 (Appendix B). According to this equation, the upper limit of the tracer plume would fall between 0 and $10 \times 10^{-9} m^{-2}$ due to the accuracy of the radioactive measurements.

Figure 11 shows a plot of the surface concentration downstream from the Minturn source. The effect of the upstream ridge on the direction of the plume was quite evident in this case.

2) Minturn and Redcliff sources - Lateral and vertical cross-sections of $\overline{C}\,\overline{U}/Q$ are presented in Figs. 12, 13 and 14.

The values of the concentration parameter from Minturn to Redcliff were interpolated because the source strength (Table 12) used in this experiment was increased for both sources to assure that the radioactive material would be detected far from the sources. No measurements were made between Minturn and Redcliff.

The upper boundary of the tracer cloud was between $\overline{C}\,\overline{U}/Q = 0$ to $5 \times 10^{-9} m^{-2}$ according to Eq. B.12.

Figure 15 shows a plot of the surface concentration downstream from the two sources. The effects of topography on the concentration pattern were not as obvious and was partly due to the high free stream velocity.

4.1.2 Barostromatic airflow model

4.1.2.1 Experimental procedure - In the case of a thermally stratified airflow the important features of the atmosphere to model is the shear flow and the temperature stratification. The problem is just as difficult or more so than the neutral case since large vertical temperature gradients and low flow velocities are required to satisfy similarity conditions.

At the present time only three methods are available for producing the required airflow conditions--a) metal plates constituting the test section of a wind tunnel and cooled by a circulating brine solution (Ref. 22), b) horizontal rods placed in the upstream section of a wind tunnel and heated differentially from bottom to top (Ref. 110), and c) solid carbon dioxide (dry ice) placed in the upstream section of a wind tunnel (Ref. 35). Of the three methods only the third method was readily available for conducting the required experiments for such a large topographic model.

The procedures for arranging the dry ice in the wind tunnel, the set-up of experimental equipment and procedures for obtaining measurements of velocity, temperature, concentration, etc., are discussed in Appendices A and C.

4.1.2.2 Discussion - One problem with the dry ice method for providing a temperature stratification and shear flow was that the duration of effective measurement time was usually limited to 6 to 8 hours. This limitation of the method required conducting a series of experimental programs to obtain data on velocity, temperature, density, and radioactive concentration measurements. Altogether, approximately eight separate dry-ice experiments were conducted in

order to obtain acceptable measurements of the above quantities. Laboratory set-up and conditions were kept the same as much as possible.

Measurements of most quantities were generally restricted in the principal valley of the model or on ridges near the centerline of the model. This means that the three dimensional properties of most of the variables were not explored extensively except for the radioactive concentration measurements which were obtained in the three space dimensions.

a) Mean velocity field

Figures 16 and 17 shows the mean resultant and lateral velocity distribution over the model as measured by means of the smoke-wire method (Appendix C).

The velocity field was not typical of classical wind tunnel airflows in that a marked decrease in the horizontal velocity occurred some 15 cm above the model. In addition, a nontypical lateral shear of complex nature was observed over the model. This was detected by observing the horizontal shear of the smoke-wire plumes.

The proposed origin of the wind-tunnel flow field over the model is shown in schematic in Figure 18. The dry ice acts as a cold source creating a high pressure zone. This high pressure zone establishes a pressure gradient in the lower levels down the wind tunnel which drives the cold lower air over the model cooling it in time and space. The volume of dry ice, evidently, was not efficient enough to cool the complete model to a equilibrium temperature since a horizontal temperature gradient was established along the model (Fig. 20).

A reversed compensation current developed over the lower cold airflow as a consequence of the baroclincity associated with the

pressure and temperature gradient imposed over the model. The elevated regions of the model on the far end may augment this circulation scheme by blocking action and as a potential heat source. This was the character of the flow field before the wind tunnel was operating.

The problem at this stage was to eliminate the reversed compensation current in order to make the velocity profile more realistic, i.e., with the wind direction from the northwest through the whole layer. The wind tunnel was set at a low-speed setting in order to move enough air against the reversed airflow to cancel its effect. Only one critical speed setting was found where this could be accomplished without disturbing the complete airflow in the tunnel. A speed setting greater than the critical one produced unstable gravity waves as a result of the interaction between wind tunnel airflow and reversed flow.

The origin of the lateral airflow near the surface may be explained in part by the orientation of model topography and its effect on the airflow. In the higher levels, the answer is not so obvious but the lateral currents may be a combination of compensation currents for the lower levels and secondary flows peculiar to this wind tunnel arrangement.

Figure 19 shows the results from computing the unsteadiness factors for this airflow (Appendix C, Sec. C). The high values of the unsteadiness factors occurred at the level where the reversed flow was observed. The unsteadiness of the airflow decreased downstream especially in the longitudinal component.

b) Mean temperature and density field

The mean temperature field over the model as the result of the dry ice airflow is shown in Figure 20. An apparent heat flux

from the model caused a thin unstable layer near the model surface and a slightly deeper neutral layer above it. A more stable regime begins 6 cm above the near-neutral layer.

The thermal boundary layer was approximately 30 cm above the model and was depicted better in the density field which is shown in Figure 21.

Calculations show that the additional CO_2 vapor increased the density by 11% in the lower levels of the model atmosphere. The effect of this density distribution on stability will be considered in Chapter V.

c) Concentration measurements

Two sets of concentration measurements were made over the model. In one case, a single source at the location of Minturn was simulated while the second, simulated a single source at the location of Redcliff.

1) Minturn source - A lateral cross-section of the concentration parameter $\overline{C}\,\overline{U}/Q$ at selected locations for the Minturn source is shown in Figure 22. A vertical cross-section of $\overline{C}\,\overline{U}/Q$ over the model is shown in Figure 23.

The lateral and vertical distribution of the concentration nearest to the Minturn source, which was approximately over Gilman, showed maximum concentrations somewhat elevated from the ground. It was not possible to ascertain whether this feature was caused by topographic effects or possible buoyancy effects of the radioactive gas or both. The radioactive gas was cooled twice before entering the wind tunnel (Fig. 70) but the source gas temperature was not monitored. Therefore, quantitative information on possible buoyancy effects are not known.

2) Redcliff source - Lateral and vertical cross-sections of the concentration parameter for a Redcliff source are presented in Figs. 24 and 25. A plot of the surface concentration downstream from the Redcliff source is shown in Fig. 26.

A tentative examination of the preceding figures indicate that with the barostromatic airflow generated by dry ice, that valley orientation and topography had a noticeable effect on the direction of the tracer plume. The full implications of these features will be discussed in Chapter V.

4.2 Field Measurements

The field study of the experimental program is divided into three phases. The first phase describes the measurements obtained of upper level winds, vertical motion and temperature distributions during synoptic events which were selected for seeding operations. The second phase describes the constant-volume balloon measurements obtained for dispersion estimates. The third phase discusses the aircraft sampling of silver-iodide plumes as released from ground-based generators in the Eagle River Valley.

4.2.1 Description of Topographic Area

A description of the field experimental region is given in Appendix A.

4.2.2 Climatology

The material presented in this section summarizes certain natural climatic characteristics of the Climax-Eagle River Valley area. They include a brief description of certain characteristics of the precipitation and storm periods, snowfall accumulations, temperature regimes, and of the upper-air conditions associated with storm periods. Certain

portions of this information will be important for model and field similitude verification.

4.2.2.1 Storms and winter precipitation - During the winter months (November through April) the Climax area is affected by traveling extratropical cyclones which occasionally penetrate the seasonal long-wave ridge position. These storms occur more frequently during the late winter and early spring months. Most storm periods are 3 days or less.

The important characteristics of the snow season precipitation have been summarized by Grant and Schleusener (Ref. 43), Chappell (Ref. 18) and Grant et al. (Ref. 41). The average wintertime (November-April) precipitation at Climax is approximately 14.14 inches. The average number of days with precipitation is 85 which is almost half of the 181 days during the November-April period. Daily precipitation amounts in general are light, with daily averages being under 0.50 inch on some 80% to 90% of all days. While Climax is representative of much of the area that accumulates snowpack in the northern Colorado Rockies, many higher elevations and areas exposed to stronger orographic influences receive total winter snowfall of nearly double the Climax amount.

A definite diurnal cycle has been observed in the precipitation at Climax and other stations located in the north portion of the Colorado River Basin. A marked peak in the occurrence of snow occurs at around 0300 MST and a pronounced minimum occurs at 1100 MST. The probability of precipitation at 0300 MST at Climax is almost three times that for the period from 0700 to 1100 MST.

4.2.2.2 Orographic clouds and snowfall - Orographic influence at Climax result in greater amounts of snowfall with northwest flow and a damping of snowfall activity when southwest flow is present. About 50%

of the total snow occurs with the 700 mb wind between 280 and 330 degrees while only about 12% of the total snow occurs with the flow from 180 to 250 degrees.

Airflow from the northwest is perturbed by a number of mountain ridges before entering the Eagle River Valley. The steep slope of the valley floor, in addition to the blocking effect of Chicago Ridge and Tenmile-Mosquito Range, produces a strong orographic effect along the Valley.

The relative deficiency of snowfall with southwest flow is apparently related to the presence of the San Juan and Sawatch Mountains to the southwest of Climax (Ref. 41). Airflow from the southwest must pass over the Sawatch Range before reaching Chalk Mountain. Under these conditions a substantial amount of precipitation may be deposited on the windward side of the Divide before it reaches Chalk Mountain.

Furman (Ref. 34), using horizontal and vertical scanning 3 cm radar data, has studied the physical features of the orographic clouds in the Climax area. He has concluded that,

(a) mean cloud depth ranged from 4,000 ft to 9,000 ft,

(b) cloud bases were 12,500 ft to 13,000 ft,

(c) mean cloud tops occurred from 16,000 ft to 21,000 ft with occasional tops reaching to 27,000 ft msl,

(d) movement of cloud echoes were steered by 500 mb wind velocity,

(e) cloud elements were thought to be organized into lines with spacing of cloud elements approximately 110 miles between centers,

(f) and most intense precipitation and dense clouds were found in the vicinity of the tops of mountains and ridges.

Snowfall at Climax occurs from cloud systems that average slightly colder and drier than those observed at Wolf Creek Pass in the San Juan Mountains.

4.2.2.3 Vertical temperature distribution - The first study on the temperature distribution or stability over the Eagle River Valley was reported by Chappell (Ref. 18). This statistical study relates the 500 MB-cloud top winds to the mean lapse-rate stability between the 500 and 700 MB levels. In general, this investigation concluded that larger stabilities (more stable) were associated with higher wind speeds (>10 mps) and northwest winds. Yet, the percentage of events with wet adiabatic-lapse conditions had a maximum value for northwest wind flow.

Mean stabilities accompanying winds from the west and southwest were approximately equal, and less than those from the northwest. The percentage of events with wet adiabatic lapse conditions were also less frequent.

A radiosonde program was started at Chalk Mountain during the winter of 1967 and has provided vertical temperature and humidity data for many of the winter storm situations. Also, since the winter of 1968 five special but limited field programs (Table 3) were planned and carried out to provide additional data within the Eagle River Valley.

The special field programs were planned for days with northwest flow. Radio-or rawinsondes were obtained whenever possible during these days. All the data, though limited, gives a little better understanding of the temperature distribution during storm periods accompanied with northwest winds.

Some eighty morning and afternoon radiosonde soundings at Chalk Mountain were examined and classified. Thirty four of the eighty soundings were taken during snow events. Eighteen of the thirty-four

were obtained during snow events with northwest winds and the other sixteen were taken during west and southwest winds. A mean temperature and potential temperature sounding (Fig. 27) as derived from the above observations show small but significant differences between the two soundings.

The mean soundings show that stability conditions were typically stable with respect to the dry adiabat. However, examination of individual soundings point out that the stability conditions may vary considerably depending on the particular storm.

Temperature inversions particularly elevated ones were not a rare occurrence over Chalk Mountain. An examination of the 80 soundings showed that 35% had some type of temperature inversion. Information on the duration of these inversions was lacking but this is an important aspect of the transport and dispersion problem since it is well known that elevated temperature inversions inhibit the vertical dispersion of particulate material released from ground sources.

The radio- and rawinsonde data for the special field programs were reduced from the analog form to digital data by utilizing computer program MIXRAT (Appendix G). Temperature, relative humidity, mixing ratio, equivalent potential temperature, and potential temperature were computed in relation to pressure or height.

These data are summarized for Minturn and Camp Hale in Table 4 by computing potential and equivalent potential temperature lapse-rates for two layers, the first, from the valley floor to the tops of surrounding mountains and the second, in the free atmosphere above the mountains. To assist in understanding the temperature distribution in the Climax area simultaneous radiosonde and rawinsonde flights were conducted at three

stations in the area, Minturn, Camp Hale and Fairplay. Soundings were taken at frequent intervals. These soundings were taken on January 15 during a brief northwest snow event. The temperature distribution during this event is illustrated by the mean potential temperature cross-section from Minturn to Fairplay in Fig. 28.

An examination of the present information show that stability conditions vary considerably during a storm period. In general, snow events within the valley were accompanied with near-neutral or unstable (with respect to the moist adiabat) stability conditions which at times may exceed the depth of the valley. These conditions were found more often in the afternoon and may stabilize in a few hours depending upon the storm system and the moisture supply.

Some additional stability parameters will be computed in Chapter V using these data, and portions of the same data have been used by Balick and Rasmussen (Ref. 5) for a study on the water budget of an orographic cloud system in this same region.

4.2.2.4 Horizontal and vertical motion fields - Horizontal wind data near the surface at selected locations in the valley were available but not reduced for analysis except on Chalk Mountain. An analysis of 4 meter level winds during three months of the winter showed a definite but small diurnal cycle. Computer computations (Appendix G) of the mean resultant wind direction,

$$\bar{\alpha} = \tan^{-1} \frac{\bar{U}}{\bar{V}} \qquad 4.6$$

mean vectorial wind speed,

$$\vec{V} = \sqrt{(\bar{U})^2 + (\bar{V})^2} \qquad 4.7$$

mean scalar wind speed $(\overline{s})$ and the steadiness

$$S = \frac{\vec{V}}{\overline{s}} \times 100 \qquad 4.8$$

showed that the mean resultant wind direction was more westerly and the steadiness and mean wind speed higher during the afternoon hours (Table 5).

Horizontal velocity profiles with height were obtained from rawinsonde and pilot-balloon flight data that were reduced by computer programs WINDS and PIBAL 1 (Appendix G). The wind profile data were limited to the locations of Minturn and Camp Hale with one exception.

On December 10, 1969 simultaneous pilot-balloon flights were launched at four different locations in the Eagle River Valley area at hourly intervals for six hours during a snow event with strong and gusty winds. Stability conditions were probably near neutral during the early afternoon but was stabilizing by nightfall. Figure 29 shows how the velocity profiles varied throughout the time period. Later, in Chapter V, this particular snow event will be compared with the wind tunnel neutral case.

The velocity profiles obtained at Camp Hale and Minturn were taken under various stability conditions ranging from unstable to stable. A series of these wind profiles are presented in Figs. 30 through 34.

A special type of wind profile was observed within the valley a number of times during northwest flow, e.g., Fig. 30 1115 MST and Fig. 33 2240 MST. The characteristics of the profile may be the result of topographic frictional effects and augmented by stable-stability conditions although the profile did show up during near neutral conditions.

The type of profile observed can be divided into two layers, an inter-valley profile characterized by a layer of small velocities and vertical wind shears which extends to an altitude near the summits of surrounding mountains. An external-valley profile characterized by increased wind velocities and vertical wind shears.

Data on the vertical motion were obtained from flights of constant-volume balloons. A description of this work and the procedures followed are discussed in the next section. Some nine successful flights in different locations within the Eagle River Valley and Climax region were used to compute vertical-motion data. These data were computed from 30 second height changes of each balloon.

The vertical-motion data from all nine flights were grouped together since the weather conditions for all flights were approximately similar. The nonaveraged vertical motion as distributed with height is shown in Fig. 35. The most striking aspect of the distribution was the increase in the variance with height. Averaging the data for all balloons and in 100 meter height intervals plus computations of the variance showed that this was the case (Fig. 36).

Computations of the vertical turbulent intensity σ_w/V with the same data show values ranging from 63.4% to 13.7%. Horizontal velocities from Fig. 32 and those computed from the constant volume balloons were averaged and used to compute σ_w/V.

4.2.3 Transport and dispersion problem

4.2.3.1 Experimental design - The basic features of the Climax weather modification experiment have been discussed by Grant et al. (Ref. 40), Chappell (Ref. 18), Grant and Mielke (Ref. 42) and Grant and colleagues (Ref. 41).

Six silver-iodide ground generators are used in the project. These are Colorado State University modified sky-fire, acetone, needle-type ground generators. The seeding rate of the generators may vary from 2 gm/hr to 200 gm/hr of silver iodide but are usually set at 15 gm/hr which produces about 10^{14} particles per gm silver iodide effective at -12°C and 4 x 10^{15} particles per gm silver iodide effective at -20°C.

The location of two of these generators with respect to the primary target (Chalk Mountain) is shown in Fig. 64. The azimuth and distance of each generator from the primary target is shown in Table 6 .

The decision to turn on the generators was made with a randomization scheme. The generators were turned on 1/2 to 1 hour prior to the beginning of the experimental day, and shut off 1/2 to 1 hour prior to the end of the day depending upon their respective distances from the primary target area. Normally, the sampling period was a 24-hr interval of time but during special field programs some of the generators were turned on only for a 6 to 12-hr period.

Two of the six generators are located in the Eagle River Valley which is oriented in a northwest-southeast direction from the primary target area. Since artificial increases of snowfall in the Climax area were favored by northwest windflow and other favorable atmospheric variables (Ref. 18) only this area was selected for topographic modeling.

The two generators located in the Eagle River Valley were placed near the towns of Minturn and Redcliff. The placement of the generators were based primarily on logistics and convenience due to the difficulty of placing generators in more remote locations. Both generators are deep in the valley but the location of the Minturn generator is upwind from Battle Mountain (Fig. 64).

4.2.3.2 Low-level transport of seeding materials - The two generators located at Minturn and Redcliff can be considered as continuous point sources. Thus, one would expect from simple diffusion concepts that the silver-iodide plume would expand vertically and laterally with distance from the sources with the particles moving away from the point of emission with the speed of the wind. However, this relatively simple pattern is made more complex due to the mountainous terrain and in-transit losses due to various mechanisms.

An estimate on the optimum transport time of the seeding material to the target area has been calculated by Chappell (Ref. 18). The optimum time was computed on the basis of transport time into a cloud system, time for snow crystal growth and time for settling to the target surface.

Grant et al. (Refs. 39, 87) has accumulated quantitative and qualitative data to support the thesis that the seeding materials are being transported to the cloud systems over the target area under some weather conditions. The evidence was based on the following:

a) increase in ice-nuclei concentrations at the target area based on ice-nuclei counters,

b) detection of seeding material above the mountain site based on a kite system,

c) observation of visual changes in cloud character with seeded clouds,

d) observed differences in concentration of ice crystals falling from seeded and non-seeded clouds, and

e) detection of silver in falling snow.

Grant also recognizes that at times various of the above evidences may be negative indicating that the cloud seeding material for some reason is not reaching the cloud systems over the target area.

Fundamentally, the theoretical problem of atmospheric transport and diffusion is to relate the spread of the tracer material, and the consequent fall in the concentration of suspended material, to the speed and turbulence of the wind as well as the atmospheric stability. The practical problem is to find means of estimating the rate of the transport and diffusion from direct measurements of the various variables.

The field approach to this problem was from the practical point of view since from the beginning the Climax weather modification project was not designed as a typical diffusion study.

In order to have input into the field transport and diffusion problem two different methods were used to obtain data pertinent to the problem. These were the constant-volume balloon technique and direct aircraft sampling of the seeding material.

4.2.3.3 Transport and dispersion estimates from constant-volume balloons - Estimates of the trajectory and spreading of particulate material releases to the atmosphere have usually been based upon wind statistics obtained at fixed points (Eulerian statistics). Fundamentally, however, atmospheric transport and dispersion depends on the movement of individual air parcels (Lagrangian statistics). In recognition of this fact, current developments in the field of diffusion meteorology have emphasized ways of passing from the easily obtained Eulerian statistics to the desired Lagrangian statistics. However, an alternative method has been to obtain estimates of the Lagrangian statistics utilizing constant-volume balloons.

The possibility of using three-dimensional constant-volume balloon trajectories as approximations to three-dimensional air parcel trajectories has been under investigation for several years. Pack (Ref. 80), Angell (Ref. 2), Pack and Angell (Ref. 81) and others have demonstrated that the constant-volume balloon technique can obtain fairly accurate three-dimensional air-parcel trajectories over water surfaces, level ground and relatively simple mountain ridges. The method has also been successful in complex mountainous areas as long as the balloons are flown at a height higher than the highest ridges.

Although many problems are encountered in obtaining constant-volume balloon trajectories at lower levels in mountainous terrain, such as, the Eagle River Valley-Leadville area, a limited number of trial runs were attempted in order to obtain information on the vertical motion and some independent dispersion estimates.

The observing system used in tracking the constant-volume balloons, the specifications of the equipment, and flight information and weather during the flights is discussed in Appendix D.

a) Analysis of data

1) Dual flights - The data obtained during the dual constant-volume balloon flights were time, elevation, and azimuth at thirty second intervals from each theodolite. For each pair of balloons the consistency of the data was checked for reading and tabulation errors by plotting the azimuth and elevation angles with respect to time.

To obtain balloon positions at thirty second intervals the checked data were placed on punch cards and processed by computer program SUPERB (Appendix G) for (x) east-west, (y) north-south, and (z) vertical positions. In cases where the balloon passed over the baseline the geometric

relations in the computer program could not give reliable results hence it was necessary for these positions to be estimated by interpolation.

A visual tracking system may involve several possible errors. Care was taken to align, orient and level all theodolites properly. Data was checked for consistency as mentioned above.

A plot of the individual balloon horizontal trajectories using the computed x and y positions were compared with the trajectories plotted from the original azimuth readings from the theodolites. Generally, the trajectories compared quite well and were within 50 meters but on some flights the differences were larger near the termination of the flights. All the balloon trajectories were consistent with the visual observations taken that same day.

The computed vertical positions were more difficult to verify. The computer computations actually gave mean heights based on the azimuth and elevation readings from the paired theodolites. Checking the computations indicated that most vertical positions were within $\pm$ 50 meters but larger errors were possible for positions near the baseline and those located at the longest distances from the theodolites.

2) Single flights - Constant-volume balloon positions for transponder flights 8, 9, and 10 were derived from azimuth, elevation, and range data from the M-33 radar. Analysis was done by hand and desk computer. The principal purpose for using these data were to augment the vertical motion data as discussed in Sec. 4.2.2.4.

b) Discussion

The three-dimensional positions of the dual released constant-volume balloons gave data that can be examined in at least three ways: first, comparing the statistics of each flight to see what

differences were observed; second, using the joint statistics to look at the relative positions and separation rates; third, to determine what information on meteorological parameters can be derived and if there were recognizable patterns.

1) Comparative statistics

Figures 37 and 38 show the computed horizontal trajectories of Flight 3, 4, and 5. The most significant difference in the three flights was the more erratic horizontal movement of Flights 4 and 5. These two flights reached high enough altitudes to be influenced by the higher strong shear-flow. Flights 3 and 5 were influenced more by north-northeasterly winds which developed soon after launch times and consequently moved toward the Tennessee Pass area (Fig. 32). Flight 4 reached the altitudes of the west-northwest winds and one balloon rapidly moved over Chicago Ridge toward Chalk Mountain. The green balloon was influenced by some local eddy and moved over the Eagle River Valley toward Elk Ridge. Evidently this balloon eventually was caught in local terrain eddies near Elk Ridge and moved very slowly until tracking was stopped.

Figures 39, 40, and 41 shows the unsmoothed height profiles for the three dual flights. All three show significant oscillations with Flights 4 and 5 showing rather large vertical motions. There were also phase differences in the timing of major vertical motions.

All three flights exhibit cyclic characteristics with the period of major oscillations between 6 and 12 min, although, longer periods of 20 min appear to be present.

The comparative statistics indicate that the dual flights were not only influenced by terrain effects and the particular mean wind flow of

this day but also by possible local eddies (rotors) generated by the combination of stability, terrain effects and strong upper-level shear flow.

2) Joint statistics

Figures 42, 43, and 44 shows the various separation distances for all three flights versus time. The curves show the total three-dimensional separation R and the individual components of this total ΔX, ΔY, and ΔZ.

The most obvious aspect of the flights was that the balloons once released gradually became farther apart but occasionally decreased in separation distance at times.

It should be noted that this type of experiment was examining "relative dispersion" for which Batchelor (Ref. 7) indicated separation rates in a restricted range proportional to t^3. Later the spreading becomes as t^2 and after a sufficiently long time the rate of dispersion approaches t^1.

Figures 45, 46, and 47 show the squared total separation rates as a function of time after release for each set of balloons. Also, shown for convenience are separation rates proportional to various powers of the time. In the preceding figures, the separation rates over the early portions of most flights approached t^4 and at other times even exceeded t^4. Such high separation rates seem to be a little larger than those observed over relatively flat land (Ref. 81).

Negative separation rates also occurred for all flights and may be the result of topographic influences but such features are also observed over undulating terrain.

This may be the first time that an attempt was made to find out the dispersion rate at three different altitudes in mountainous terrain. The experiment was not totally successful since for Flights 4 and 5 mean altitudes were about the same. However, this small difference in altitude was sufficient on this day to cause a rather marked difference in the effective atmospheric dispersion rates for these two flights. An even more pronounced difference was noted between Flight 3, which was totally within the valley and not influenced by the upper cross-valley flow, and the other two flights that were higher.

Generally, these results show that the dispersion rate increased with height. This characteristic should be expected due to the upper-level directional and speed wind-shear. It would be of interest to obtain similar data for a day when the strong wind shear was absent.

These observations point out what others have mentioned in other constant-volume balloon work and, that is, that a reliable measure of the mean atmospheric dispersion rate can only be arrived at by repetition of such experiments over many trials or an ensemble.

3) Meteorological parameters

A number of meteorological parameters can be derived from the constant-volume balloon data which would be of general interest to the transport-dispersion problem. A partial list of parameters follows:

(a) wind-speed profile data,

(b) turbulent fluctuations,

(c) shearing stress,

(d) eddy energy dissipation,

(e) eddy viscosity or diffusivities,

(f) autocorrelations and

(g) turbulent intensities.

Wooldridge (Ref. 111) has used the position data from all three dual flights and a computer technique similar to Kao's (Ref. 52) to compute u-v, u-w, and v-w cross-spectral analyses, spectral densities or variances, eddy diffusivities and phase relationships. A separate paper by the author and Wooldridge will cover the detail aspects of these results.

The eddy diffusivities are of interest since they relate directly to the effective atmospheric dispersion rates shown in Figs. 45, 46, and 47. The vertical-, zonal-, and meridional-eddy diffusivities as calculated by Wooldridge are shown in Table 7 . The w-component diffusivity displayed a marked increase with height from 3.5×10^4 cm^2 sec^{-1} for the lowest flight to 12.4×10^5 cm^2 sec^{-1} at near ridge level. The range is roughly 1½ orders of magnitude, and indicated a strong vertical eddy flux out of the valley during the strong cross-wind flow at ridge level. A strong indicated increase in the zonal eddy diffusivity was also reasonable under these conditions.

Wooldridge's data on phase relationship between the u- and w-components suggested the presence of a helix circulation in the lee of the western ridge north of the Tennessee Pass area. This type of circulation was suggested in the height profile data for dual Flights 3 and 5, Figs. 39 and 41. The green balloon of Flight 5 was closer to the western ridge and appeared to be in the ascending node of the helix, while the orange balloon was located more centrally over the valley and appeared to be in the descending loop of the helix circulation. Dual Flight 3 had similar characteristics but were not as pronounced as Flight 5.

Some independent calculations of the shearing stress, eddy viscosity, eddy energy dissipation, and stream-wise turbulent intensity were made for the lowest dual constant-volume balloon flight which was not affected by the upper-level shear flow, for the purpose of obtaining quantitative parameters that might be approximately representative of the valley flow.

The method of computation was as follows: the stream-wise velocities along the path of each balloon were computed for every thirty second time interval starting with 10 minutes after launch. The first ten minutes were neglected to make sure that each balloon had reached equilibrium altitude. These stream-wise velocities were then averaged over arbitrary 2½ min periods.

The stream-wise fluctuation velocities were derived by subtracting the instantaneous velocities within the 2½-minute periods from respective 2½-minute averages. The vertical motion fluctuation data were computed in a similar manner. The product of the two fluctuation quantities gave $u_s'w'$.

The $u_s'w'$ values were then averaged according to 100 meter layers generally from 3000 meters to 3600 meters. From these average values one can compute the shearing stress τ by the relation,

$$\tau = -\rho \, \overline{u_s'w'} \qquad 4.9$$

where ρ the air density was derived from radiosonde data taken the same day.

The vertical eddy viscosity or diffusivity was computed next by the relation,

$$K_z = - \frac{\overline{u_s'w'}}{\partial \overline{U}_s / \partial z} \quad . \qquad 4.10$$

In order to compute this quantity the average wind speed shear was required for each layer. Pilot-balloon data taken the same day did not appear accurate enough to derive this information therefore the average wind speed shear was determined from the constant-volume balloon data.

A priori, it is not evident that the vertical oscillating constant-volume balloon will yield exactly the same wind shear as other instruments. A case in point is when the balloon moves into a region of faster moving air it may not immediately adapt to the new wind speed and this would lead to a slight underestimate of the true shear. Alternatively, the balloon might become embedded in a bubble or column of ascending air which did not exactly partake of the environmental air motion.

A comparison between constant-volume balloon derived wind shear in the vertical and shear derived from fixed-point instruments show that on the average, the constant-volume balloon does underestimate the vertical wind shear (Ref. 2).

The constant-volume balloon data is time and space dependent but then so are pilot-balloon data, nevertheless, the constant-volume balloon statistics proved to be better than the single winds-aloft measurements taken the same afternoon.

The average wind speed shear $\partial \overline{U}_s/\partial z$ was computed for each respective 100 meter layer corresponding to a $\overline{u_s'w'}$ value. From these data the vertical component of the eddy viscosity was computed by Eq. 4.5 for each balloon.

Within any region of the atmosphere, there is a balance between the gain of eddy kinetic energy due to Reynolds stresses, buoyancy forces (unstable environment), and flux convergence, and the loss of eddy

kinetic energy due to viscous dissipation, the work done against gravity in a stable environment, and flux divergence (Ref. 3). This energy budget may be simplified by neglecting all terms except those involving the increase of eddy kinetic energy due to Reynolds stresses and the decrease of eddy kinetic energy due to viscous dissipation.

Angell (Ref. 2) suggests that this simplification may not be as bad as one might expect, because the effect of buoyancy tends to be canceled by the effect of flux divergence. It has been suggested by Pack (Ref. 80) that eddy energy dissipation could be estimated from constant-volume balloon data through use of the above simplification.

The eddy-energy dissipation with the above simplification is given by,

$$\varepsilon = \frac{\tau}{\rho} \frac{\partial \overline{U}_s}{\partial z} \quad . \qquad 4.11$$

Since the shearing stress τ and the average wind speed shear $\partial \overline{U}_s / \partial z$ were already available the eddy energy dissipation was evaluated for each 100 meter layer for each balloon.

The vertical and stream-wise turbulent intensity was also determined since the turbulent fluctuations u_s' and w' had been computed previously for the other calculations. The vertical turbulent intensity was computed for all balloon flights and the results were discussed in section 4.2.2.4 and shown in Fig. 36. The stream-wise turbulent intensity was only computed for dual Flight 3. The results for the average wind speed shear, the Reynolds stresses, shearing stress, eddy viscosity, and eddy-energy dissipation for both balloon flights of dual Flight 3 are presented in Table 7.

The average vertical eddy viscosity as computed from Flight 3 was an order of magnitude larger than the eddy diffusivity derived by Wooldridge for the same flight. This difference in magnitude was probably due in part to the choice of velocities used in the derivation of the eddy viscosities.

The eddy-energy dissipation computations were conservative due to the wind shear calculations and neglect of the other terms in the energy budget. Since Eq. 4.6 is strictly valid only for neutral stability conditions and the stability conditions during this afternoon were generally stable (Table 4) one would expect some contribution from the other terms.

The constant-volume balloon derived wind speed shear indicated negative shears through most of the vertical depth of the valley. The pilot-balloon data (Fig. 32) did not show this negative shear layer in very much detail.

These computations of eddy viscosity or diffusivity, eddy energy dissipation, turbulent intensity, and shear stress will be utilized in Chapter V for order of magnitude comparisons with the model data through similarity relations.

4.2.3.4 Aircraft tracking of silver-iodide plume - The purpose of the aircraft sampling of seeding material was twofold, one, to obtain information on the vertical and horizontal extent of the seeding plume and estimates on concentrations; two, field data for comparisons with model data.

The weather conditions selected for aircraft sampling were these:

Sky conditions: Overcast to broken orographic clouds but with cloud bases high enough to permit VFR flying conditions.

Wind conditions: Northwest winds (5-15 mps) extending to at least the 500 mb level.

Ground conditions: Good snow cover.

a) Experimental plan

The initial plan was to have the NCAR flight facility with their Beech Queen Air aircraft and sampling equipment obtain samples of the silver-iodide seeding plume over the Eagle River Valley and Climax-Leadville area. Three to four flights were actually attempted in December, 1969 and February, 1970 but because of poor communications and improper or inclement weather conditions little useable data were obtained. Scheduling difficulties prevented the NCAR flight facility in making any more such flights.

An alternative plan was then drafted and put into action using flight facilities at Colorado State University. Description of the aircraft, sampling equipment, and flight information and weather is discussed in Appendix E.

b) Analysis of data

The useable flight sampling data came in the form of strip charts from the Rustrak recorder. Due to the small number of flights these data were reduced manually. The data was tabulated according to time, number of counts observed (counts/min) and exponent. The ice nuclei chamber and recorder have an inherent delay time which was used to change observed time to an estimated sampling time. The time delay varied according to the counting rate as,

Counting rate	Time delay
10	3 min
10^2	1 min 12 sec
10^3	1 min 12 sec
10^4	1 min 2 sec

Langer (Ref. 57) reports that the NCAR Ice Nucleus Counter gives a low count as compared with other counters and that the error involved is altitude dependent. For the altitudes flown at during this program correction factors from 10 to 16 were suggested by Grant and Langer (personal communication). Upon recommendation from Grant a correction factor of 10 was applied to all the data, however, realizing that the true values still remain in question.

Using the correction factor the average concentration was computed from the simple relation,

$$\overline{C} = \frac{\overline{R}(\text{counts/min})}{q(10 \text{ liter/min})} = \frac{\text{particles (nuclei)}}{10 \text{ liter}} \times 10 = \frac{\text{nuclei}}{\text{liter}} \cdot \qquad 4.12$$

The average sign show that the measurements were not exact point measurements but included some averaging with respect to time and space.

A plot of the aircraft tracks over the area was made with the appropriate times indicated with the tracks. A plot of the average concentration versus estimated observed time was then made for each aircraft track. Such a presentation was not synoptic but if one assumes that the concentration field originating from the seeding generators was quasi-steady the concentration values can be treated as if they were approximately synoptic. Errors in the spatial location of the concentration data were probably on the order of 1 to 1½ Km.

c) Discussion

A cross-sectional view of the seeding material concentration as generated by the ground generators at Minturn and Redcliff within the Eagle River Valley is shown in Figs. 48, 49, and 50. Table 8 shows the starting times when the generators were turned on for each day and the output rates.

Sampling on March 12 was in progress when the output rates of the generators were changed to a higher rate. This effective nullifies the assumption of a quasi-steady concentration field for this day. Aircraft sampling for the other two days began several hours after the generators were in operation.

The main characteristics of the silver-iodide plume for the three days can be summarized in the following way:

(1) Mean characteristics of plume

The aircraft sampling on all three days indicated that the seeding material filled the principal valley downstream from Minturn and Redcliff.

The main axis of the plume was located between Chicago Ridge and the Tennessee Pass region in the lower elevations. The material was transported some 50 km downwind toward Malta but for some unknown reason quickly dissipated or was lost in the Arkansas River Valley. However, since the directional wind-shear was not very large (Fig. 34) at cloud base level its very probable that the seeding material was being transported upward into the clouds.

(2) Convective-orographic cells

Willis (Ref. 108) made the observation in the Park Range studies that the seeding material may appear in the form of three

dimensional pillars inclined along the mean wind direction due to wind shear. Convective activity was given the reason for such a pattern but complicated by the wind shear spreading parts of the pillars more than other portions.

Figures 48, 49, and 50 show random small-scale features in the main plume which resemble the pillars as described by Willis. Many of these features were inclined in the approximate direction of the wind.

These transitory cells appear to be the result of topography and wind shear and also in some cases to convective effects. These convective-orographic cells enhance the vertical dispersion by transporting local concentration maximums of seeding material into the base of the cloud.

(3) Vertical dispersion

As brought out in section 4.2.3.3 on dispersion estimates from constant-volume balloons the vertical dispersion can be significant at times. Vertical motions on the orders of ± 2 m/s are not uncommon.

At least for the three days that aircraft sampling was successful the vertical transport of the seeding material appears adequate for getting the material into the clouds at concentrations greater than 10 nuclei/liter. This may not be the case if the atmospheric conditions were very stable (Ref. 88).

The angle of inclination at which the seeding material leaves the generator sites for the three days show values between 70-80^{o}. However on March 13 and 16 the 10 particle/liter line did not enter the cloud base until 12 to 15 km from the first generator. On March 12 a relatively clear day the rate of dispersion appears to be of larger magnitude.

(4) Horizontal dispersion

As discussed in section 4.2.3.3 on dispersion estimates from constant-volume balloons the spread of the material could be rather rapid and widespread especially above 11,000 ft (~3350 m). The aircraft sampling essentially verifies the balloon work even though the stability conditions were different for these days.

The lateral spread of the seeding material at elevations around 12,000 ft can be estimated by comparing Figs. 48, 49, and 50 with Fig. 51 Figure 51 shows the concentration of seeding material as observed over the East Fork of the Eagle River Valley, Chalk Mountain and the East Fork of the Arkansas River. Chalk Mountain is approximately 10 km from the Tennessee Pass area. The data shows that the plume width was in excess of 10 km approximately 30 km downstream from the first generator. Ice-nuclei counters based on the surface also showed that the seeding material was being funneled up both valleys (Table 9).

March 12 was the only day when data was sufficient to assess the horizontal dispersion at a higher altitude. Figure 52 shows the estimated spread of the seeding material at 13,000 ft. Since the two seeding generator's output were changed during aircraft sampling these data were not typical of quasi-steady state conditions.

(5) Long-range transport

On March 16 sampling was taken on the leeside of the Tenmile-Mosquito Range some 60 km from Minturn to verify the existence or non-existence of silver-iodide nuclei while seeding operations were occurring.

The sampling was taken before and after the flights in the Eagle River Valley and were taken on a line parallel to the mountains over

the Fairplay region. The flights were taken in VFR-conditions a few kilometers from the orographic cap cloud over the Tenmile-Mosquito Range.

The observations, though tentative, indicated concentrations ranging from 15-55 particles/liter at 13,000 ft, 10-50 particles/liter at 12,000 ft and 1-70 particles/liter at 11,000 ft. Many of these concentrations were well above background counts (~1-5 particles/liter) and suggest that the seeding material was transported into the Fairplay region regardless of the various depletion mechanisms.

4.2.4 Summary

On the basis of these limited field data some tentative generalizations can be made regarding the atmospheric conditions which prevail during storm periods selected for cloud seeding and how these atmospheric conditions may effect the dispersal of the seeding material.

Storm events associated with northwest winds exhibited a strong orographic effect in the Eagle River Valley area. Visual observations of the local weather conditions supported these conclusions.

A diurnal variation in static stability was observed during the storm events. Neutral- or unstable-stability conditions existed in the lower 1000 meters during the late morning and afternoon hours. More stable conditions existed during the night-time hours. These observations do not concure with the steady-state assumption proposed by most model techniques. However, there may be storm situations like that of December 10, 1969 that have quasi-steady state stability conditions for 12 hours or more. The field sampling was not frequent enough to make any definite conclusions concerning the duration of specific stability regimes.

The wind direction and speed were typically variable. The ridge-top wind speeds (~13,000 ft msl) varied between 1 to 16 m/s but the most frequent wind speed was between 8 to 12 m/s. The wind speed shear in the vertical was largest near the ridge-top levels, reaching values of 2.3×10^{-2} sec^{-1} on the day that the constant-volume balloons were launched. However, within the valley wind-speed shears in the vertical may be virtually nothing or even negative at times and, sometimes, occurred on the same days with large ridge-top wind shears in the vertical.

Significant cross-valley flow was observed during the latter stages of the 9-13 December, 1969 snow event. This type of flow may occur quite frequently during the winter, but events with little (~30 deg) directional shear were also observed, e.g., December 18, 1968 (Fig. 30).

Vertical motions of the order of $\pm$ 2 m/s may not be uncommon near the ridge-top levels in the Eagle River Valley area. Vertical motions greater than $\pm$ 4 m/s may be prevalent near prominent ridges and during days with marked directional and speed wind-shear.

The dual constant-volume balloon flights showed that the total dispersion rate approached and exceeded t^3 and t^4 for short time periods during the flights. Stream-wise and cross-valley components of the dispersion appeared to dominate the total dispersion rate but the vertical component became important near the ridge-top levels. Total vector separation rates, zonal and vertical eddy diffusivities increased in magnitude with height. Zonal- and vertical-eddy diffusivities at ridge-top levels were 1 to 1½ orders of magnitude higher than those within the valley.

The constant-volume balloon data and aircraft sampling data of the silver-iodide plume showed that the seeding material was dispersed vertically and horizontally at a fairly rapid rate. Near-neutral stability conditions, orographic effects, wind shear and convection were responsible for spreading the seeding material in the vertical, as well as cross-valley. From the three sampling days, the observed vertical dispersion of seeding material was approximately 1000 to 1200 meters/5 kms. This vertical dispersion rate exceeded the natural slope of the terrain which is approximately 140 m/5 kms. The horizontal dispersion as represented by the approximate plume width was in excess of 10 km/30 km downstream from the first generator.

The direction of the total seeding plume from both generators was not determined very precisely because the aircraft sampling was limited by weather conditions. There were indications that a significant portion of the Minturn plume ascends Battle Mountain and moves directly toward the Climax region. A major portion of the plume from Redcliff moves toward the Tennessee Pass region. Further aircraft and ground sampling is needed to verify this behavior.

Chapter V

EVALUATION OF LABORATORY AND FIELD DATA

In Chapter III the basic similitude parameters were derived for each wind tunnel model airflow for geometrical, kinematical, dynamical, and thermal similarity. The purpose of this chapter is to utilize both model and field data in an effort to determine how well the laboratory flow and dispersion simulated the atmospheric counterparts.

5.1 Similitude Verification

5.1.1 Neutral model

a) Geometrical similarity

This type of similarity was achieved principally through use of the undistorted 1:9600 scale topographic model discussed in Appendix A.

Another check on this type of similarity may be obtained from the relation Z/H from Eq. 3.28. This relation may be written as,

$$\frac{\overline{Z}_m}{\overline{H}_m} = \frac{\overline{Z}_p}{\overline{H}_p} \qquad 5.1$$

where Z refers now to only the vertical dimension and the bars represent averages taken over the actual and model topography. In this case, $\overline{Z}$ represents the average height of the topography above the reference height 7800 ft and $\overline{H}$ is the average thickness of the boundary layer above $\overline{Z}$. $\overline{H}_m$ was based on the momentum boundary-layer thickness as shown in Fig. 4 . The actual boundary-layer thickness $\overline{H}_p$ was not exactly known but was estimated between 17,000 and 20,000 ft msl. This estimate was based on the premise that the local wind direction approaches the geostrophic wind direction at the top of the friction layer and also

on aircraft observations of minimal turbulence above the orographic cloud tops. If

$\overline{Z}_m \sim 10.5$ cm $\qquad$ $\overline{Z}_p \sim 1000$ meters

$\overline{H}_m \sim 34.5$ cm $\qquad$ $\overline{H}_p \sim 2720$ meters

then

$$\frac{\overline{Z}_m \overline{H}_p}{\overline{H}_m \overline{Z}_p} \sim 1.2 \qquad 5.2$$

which shows that approximate similarity was achieved.

b) Thermal similarity

One of the principal assumptions of the neutral flow model was that the atmospheric stability was in a neutral state through a large depth of the atmosphere, i.e.,

$$\left.\frac{\partial T}{\partial Z}\right|_m \equiv \left.\frac{\partial \theta}{\partial Z}\right|_p \quad \text{or} \quad \left.\frac{\partial \theta_e}{\partial Z}\right|_p = 0 \ .$$

One day, December 10, 1969, was observed to be the best approximation to the above conditions. Near-neutral stability conditions with respect to the dry and moist lapse-rate were observed through a depth of 2400 meters at Camp Hale (Fig. 53). This depth exceeded the highest mountains in the area and corresponded to a depth of 25 cm model scale.

This event probably typifies the ideal situation since the sky was totally overcast with moderate to light precipitation and the surface winds were strong and gusty throughout the afternoon within the valley and on the ridges (Fig. 29).

c) Kinematic similarity

Kinematic similarity requires that the streamline and trajectory pattern of the moving air should be geometrically similar

for model and field. In addition, the relation $V(z)/V_g$ should be equal for model and field.

The neutral model airflow was characteristically determined to a large extent by separation phenomena which was observed downwind from ridges and other obstacles. It was difficult to ascertain with certainty from the limited field measurements whether such phenomena existed on a large scale in the field. Unfortunately, this problem must be deferred to a later time when special field measurements can provide specific information on the subject.

The second condition may be checked by comparison of model and field velocity profiles the latter taken during periods of near-neutral stability. Figure 54 shows this comparison for Minturn and Camp Hale. In this case, $V(z)$ and V_g were considered scalar quantities since the wind direction for model and field were closely aligned with respect to the valley, i.e., northwest. The reference wind speed V_g was chosen as the average wind speed near the summits of the highest mountains.

The comparison between model and field especially in the low levels was good. In the higher levels the model and field comparison was not as good. The small discrepancy between model and field velocity profiles in the higher levels was probably due to stability differences and the need for better simulation of shear flow over the model.

d) Dynamic similarity

Several possibilities exist for satisfying dynamic similarity. The relations $V_g/(\tau_o/\rho)^{\frac{1}{2}}$ and τ/τ_o from Eq. 3.28 can be examined as well as the relations in Eqs. 3.32, 3.33, 3.34, and 3.36.

The relation τ/τ_o can be written in terms of the model and prototype as,

$$\frac{\tau_p}{\tau_m}\tau_{o_m} = \tau_{o_p} \quad \text{or}$$

in the case of the vertical dimension,

$$\left(\frac{\tau_p}{\tau_m}\right)\frac{1}{2}C_{D_m}\rho_m U^2_{g_m} = \frac{1}{2}C_{D_p}\rho_p U^2_{g_p} \quad . \qquad 5.3$$

If one assumes that for a fully turbulent flow that $C_{D_m} \sim C_{D_p}$ and that the turbulent shear stresses are equal for model and prototype then

$$\tau_{o_m} = \tau_{o_p}$$

or

$$\rho_m U^2_{g_m} = \rho_p U^2_{g_p} \quad . \qquad 5.4$$

This type of relationship implies that the model freestream velocity should be essentially the same as the prototype. Similar criteria was used by Cermak and Peterka (Ref. 16) and others for determining the characteristic flow speeds for other model studies simulating neutral stability. In the present case of neutral flow simulation a freestream velocity of 15 m/s was chosen on the basis of Eq. 5.4.

The above similarity criteria depends on the assumption of $C_{D_m} \sim C_{D_p}$. This equality can also be obtained from the relation,

$$\overline{V}_g/(\tau_o/\rho)^{\frac{1}{2}}$$

as a necessary similarity condition if we write the above relation as,

$$\frac{\rho_m U^2_m}{\tau_{o_m}} = \frac{\rho_p U^2_p}{\tau_{o_p}} \qquad 5.5$$

or $C_{D_m} = C_{D_p}$.

However, for the model the local skin-friction coefficient depends on the Reynolds number. Schlichting (Ref. 92, p. 552) shows that for rough plates the local skin-friction coefficient becomes constant once a critical Reynolds number is reached for a particular roughness. A rough check was made to insure that this was the case for the model. In the following analysis it was necessary to assume that the data of Schlichting would be a fairly reliable guide even though it is difficult to assign equivalent values to such parameters as the "equivalent sand roughness" from the model. It is assumed that geometric heights are sufficient for defining "equivalent sand roughness."

If we let

k_r ~ 1.168 mm to 1.68 mm (roughness)

k_t ~ 5 cm to 10 cm (terrain features)

X ~ 5 meters*

$\frac{X}{k_r}$ ~ 2.7×10^3

$\frac{X}{k_t}$ ~ 91.5

then from Fig. 21.12, p. 552, Schlichting, one can determine the following:

$$\left.\frac{U_\infty X}{\nu}\right|_{\text{critical}} \sim 10^6 \quad \text{for the small roughness}$$

and 5.6

$$\left.\frac{U_\infty X}{\nu}\right|_{\text{critical}} \sim 10^4 \quad \text{for the terrain features.}$$

*The topographic model was located approximately 3 meters from the leading edge of the initial boundary layer. The extra 2 meters allow for the shift in the origin of the boundary layer due to the placing of screens just upwind from the model.

A simple calculation shows that the critical freestream speed as,

$$U_\infty \sim 10 \text{ m/s} \quad \text{(small roughness)}$$
$$U_\infty \sim 1 \text{ m/s} \quad \text{(terrain features)} \qquad 5.7$$

when $\nu = 1.5 \times 10^{-5}$ m^2/sec.

If it is assumed that the larger terrain features govern the characteristics of the airflow then a freestream speed greater than 1 m/s assures constant C_{D_m}. Since the freestream speed was 15 m/s in the experiments the conditions as expressed by Eqs. 5.6 and 5.7 were easily satisfied.

The assumption $C_{D_m} = C_{D_p}$ still needs to be justified for this type of airflow. This problem is considered in detail in Appendix F and from this argument the equality of the skin friction coefficients seem justified as a first approximation.

The turbulence similarity between model and prototype can be examined by considering the criteria,

$$\frac{\overline{u_i' u_i'}}{U^{*2}} \quad \text{and} \quad \frac{L^* U^*}{K_i} \qquad 5.8$$

Model turbulent intensity data were measured for all three components (Figs. 6, 7, and 8) but field data were not available except for limited measurements of the vertical and longitudinal components by constant-volume balloons in the Camp Hale area. These data showed that the mean vertical and longitudinal turbulent intensity was approximately 35% within the valley. The model data showed the following mean values within the valley,

$$\frac{\sigma_v}{\overline{U}} = 19\% \quad \frac{\sigma_u}{\overline{U}} = 23\% \quad \frac{\sigma_w}{\overline{U}} = 14\% \quad .$$

The field measurements were obtained during relatively stable atmospheric conditions (Table 4) and may not be directly comparable to the neutral model data. Nor can one assume that the field or model data were typical for the whole area of interest. As the model data showed, the turbulent intensity may vary considerable over the whole area. This particular problem points out one of the many difficulties in model and prototype verification.

Further estimates on the turbulence similarity can be obtained by examining the turbulent Reynolds number $\frac{L^* U^*}{K_i}$. This similarity was limited to the vertical dimension since measurements of the other components were not obtained for the model. The premise of the following calculations was to obtain an equivalent field eddy-viscosity or diffusivity on the basis of model and field measurements and see whether the results were within reason based on values from literature and measurements.

The eddy viscosity was determined for the model at Minturn and Redcliff and appear in Table 2 . A mean eddy viscosity was derived to represent a layer between the surface and mountain summits. The other data were readily available from model and field data.

If we write the turbulent Reynolds number for model and field as,

$$\left.\frac{L^* U^*}{\overline{K}_z}\right)_m = \left.\frac{L^* U^*}{\overline{K}_z}\right)_p \qquad 5.9$$

and solve for $\overline{K}_{z_p}$ we find,

$$\overline{K}_{z_p} = \frac{L_p^* U_p^* \overline{K}_{z_m}}{L_m^* U_m^*} \quad . \qquad 5.10$$

The following characteristic values were found for Minturn and Redcliff,

Minturn

$\overline{K}_{z_m} = 1.11 \times 10^3$ cm^2/sec $\quad L_p^* = 960$ m

$L_m^* = 10$ cm $\quad U_p^* = 9.78$ m/s

$U_m^* = 4.5$ m/s

Redcliff

$\overline{K}_{z_m} = 0.886 \times 10^2$ cm^2/sec $\quad L_p^* = 960$ m

$L_m^* = 10$ cm $\quad U_p^* = 9.7$ m/s

$U_m^* = 7.2$ m/s.

Substituting these values into Eq. 5.10 one finds the characteristic values for the equivalent field eddy viscosity as,

$$\overline{K}_{z_p} \begin{cases} \text{Minturn} & 2.31 \times 10^7 \text{ cm}^2/\text{sec} \\ \text{Redcliff} & 1.14 \times 10^6 \text{ cm}^2/\text{sec} \end{cases} \qquad 5.11$$

These approximate values for the equivalent field vertical eddy-viscosity indicated that the model airflow was very turbulent. There was no direct verification of these results. The constant-volume balloon measurements (section 4.2.3.3) taken within the Eagle River Valley were obtained under stable atmospheric conditions which gave an average value of $\overline{K}_z \sim 5 \times 10^5$ cm^2/sec. Kao and Wendell (Ref. 53) calculated a field eddy viscosity by constant-volume balloons in the Idaho desert during July of $K_z \sim 10^6$ cm^2/sec. These tentative comparisons suggest

that vertical turbulent conditions were probably exaggerated for the model especially in the area of Minturn.

A similar type of analysis can be performed by considering the eddy-energy dissipation. If it is assumed that Nemoto's criteria, Eq. 3.34 applies to the problem then the approach can be similar to previous one, i.e., obtain an equivalent field eddy energy dissipation on the basis of model and field measurements.

Nemoto's criteria can be written,

$$\bar{\varepsilon}_p = \frac{(\bar{\varepsilon}_m)}{\left(\frac{U_m^*}{U_p^*}\right)^3} \frac{L_m^*}{L_p^*} \quad . \qquad 5.12$$

The eddy energy dissipation was determined for the model at the same two locations and appear in Table 2. A mean eddy energy dissipation $\bar{\varepsilon}_m$ was derived to represent a layer between the surface and mountain summits. The reference velocities U_m^* and U_p^* represent typical velocities observed near the mountain summits, although, an average velocity through the layer could have been used.

The following characteristic values were used for the calculations,

Minturn

$\bar{\varepsilon}_m = 10^5$ cm^2/sec^3 $\qquad L_p^* = 960$ m

$L_m^* = 10$ cm $\qquad U_p^* = 9.78$ m/s

$U_m^* = 4.5$ m/s

Redcliff

$\bar{\varepsilon}_m = 2.7 \times 10^4$ cm^2/sec^3 $\qquad L_p^* = 960$ m

$L_m^* = 10$ cm $\qquad U_p^* = 9.7$ m/s

$U_m^* = 7.2$ m/s .

Substituting these values into Eq. 5.12 the characteristic values for the equivalent eddy energy dissipation are,

$$\begin{matrix}\text{Minturn} \\ \\ \text{Redcliff}\end{matrix} \quad \overline{\varepsilon}_p \quad \begin{cases} 28.9 \text{ cm}^2/\text{sec}^3 \\ \\ 24.4 \text{ cm}^2/\text{sec}^3 \end{cases} . \qquad 5.13$$

Limited field measurements in the Eagle River Valley indicated a mean value of $\overline{\varepsilon}_p \sim 3 \text{ cm}^2 \text{ sec}^{-3}$ as derived from Table 7 . This figure is probably conservative because of the vertical wind shear derivations and stability conditions. Information on average field eddy-energy dissipation in mountainous regions is not known but several measurements have been made by constant-volume balloons over relatively flat terrains. Angell (Ref. 2) and Pack (Ref. 80) report values ranging from negative values to 30 under various stability, wind speed and altitude conditions.

5.1.2 Barostromatic model

a) Geometrical similarity

A comparison between the model and field boundary-layer thickness provides an additional check on this type of similarity. The thermal and momentum boundary-layer thickness for the model was approximately 30 and 27 cm, respectively. These figures correspond to a field boundary-layer thickness of 17,700 to 19,000 ft msl. This height corresponds to the approximate geostrophic wind direction level and the level of the orographic cloud tops so it was assumed that approximate similarity was achieved.

b) Kinematic, dynamic, and thermal similarity

1) Reynolds number similarity

In general, it is not possible to obtain equality of Reynolds numbers in model and prototype for this type of airflow. In the atmosphere a typical value of the Reynolds number is $Re \sim 10^{10}$ while for the model it is $Re \sim 10^{4}$. Two alternatives are possible, (a) assume that the Reynolds number criteria can be matched according to Abe-Cermaks approach, (b) or neglect the Reynolds number similarity and assume that Richardson number similarity prevails for field and model.

A comparison of the field and model Reynolds numbers Re_p and Re_m on the basis of Cermak's criteria requires comparing the ratio of these two Reynolds numbers, Eq. 3.49. This can be estimated by selecting typical values for the following characteristic variables:

	Field	Model
L^*	1152 meters	12 cm
U^*	10 m/s	8 cm/s
$\overline{K}_{z_p}$	$\sim 10^5$ cm^2/sec	$\nu_m^* \sim 0.170$ cm^2/sec .

The characteristic length L^* was chosen as the height approximating the tops of the highest mountains, U^* the average horizontal velocity at this level and $\overline{K}_{z_p}$, an estimated average value based on field measurements discussed in section 4.2.3.3. Computation shows a favorable but not an exact value for the Reynolds number ratio,

$$\frac{(Re_p)_{turb}}{Re_m} \sim 2 \qquad 5.14$$

2) Prandtl number similarity

The ratio of the two Prandtl numbers Eq. 3.50 can be estimated in a similar manner using the following values,

Field	Model
$\frac{K_M}{K_H} \sim 1$	$\bar{\mu} - 1.77 \times 10^{-4}$ gm cm^{-1} s^{-1}
	$\bar{k} - 6.01 \times 10^{-5}$ cal cm^{-1} s^{-1} °C^{-1}
	$\bar{C}_p - 0.240$ cal g^{-1} °K^{-1}

computation shows a favorable value for the Prandtl number ratio,

$$\frac{Pr_p}{Pr_m} \sim 0.7 \qquad 5.15$$

3) Vertical temperature profile and Richardson number Similarity

A typical vertical distribution of temperature for the model airflow is shown in Fig. 55. This model temperature profile was compared with four field potential temperature soundings that were obtained during snow events. The lowest 12 cm (~1200m) of the model vertical temperature profile compared favorably with the field profiles that indicated near neutral stability conditions. In the higher levels, above 1200 meters, the model profile showed a more stable temperature profile than was observed in the field.

To check Richardson number equality for model and field a bulk Richardson number Eq. 3.60 was computed using model and field data at Camp Hale.

In the case of the model the Richardson number was computed for 2 cm layers up to 27 cm using the temperature and density data from Figs. 20 and 21. For the field, the Richardson number was computed

for corresponding 200 meter layers using the potential temperature. The field soundings were selected by comparing them to the model data. Five soundings were found that resembled the model temperature vertical profiles. Velocity profiles could not be used as a guide because the limited velocity profiles for the field did not match the model velocity profile very exactly.

Table 10 and Fig. 56 show the results for these computations. Exact simulation was not expected; however, the gross aspects of the model Richardson numbers fall within the range of field Richardson numbers which showed that the model simulation was fairly good. Model Richardson numbers based on the density of the carbon dioxide-air mixture were slightly more stable than those computed by temperature.

5.1.3 Models and field conditions - In the preceding sections the similitude criteria were evaluated between the two wind-tunnel models and field conditions. The results indicate that at least partial similarity was achieved for both wind-tunnel models. An examination of the transport and dispersion similarity for model and field is considered next, but before this aspect is considered it is convenient at this point to establish, in general, what type of field conditions the two wind-tunnel models may approximate.

The wind-tunnel models are assumed to simulate field situations with the following principal characteristics.

a) Neutral model

Stability - a field event with a deep near-neutral lapse-rate exceeding the height of the highest mountains (14,200 ft msl) and persisting for a duration of 8 to 12 hours.

Winds - An event with little directional wind-shear in the free stream or geostrophic regions. Moderate to strong winds should prevail within the lower boundary layer. Lower boundary layer should be turbulent (gusty).

b) Barostromatic model

Stability - A field event with a near-neutral layer in the lowest layers then gradually becoming more stable with height. The horizontal temperature gradient for the model although not typical quantitatively does resemble a field situation in which a frontal passage is in progress. The model may be quasi-typical of conditions a few hours after frontal passage when the winds have reached a quasi-steady state.

Winds - Little directional wind shear in the free stream region. Winds within the lower boundary layer should increase markedly then decrease near the summit of the mountains and then increase again above the mountains. So far an exact duplication of this type of velocity profile has not been observed in the field but was approximated at times.

5.2 Comparison of Model and Field Concentration Data

5.2.1 Time similarity between model and field concentration data - In many laboratory studies it has been assumed that concentration distributions obtained from the wind tunnel correlate with field mean or peak values. A thorough analysis of this problem has not been made yet.

Hino (Ref. 50) is probably the first to suggest a relation between model and field concentrations involving the sampling times. Hino used the "inverse 1/2 power law" as a means for relating the maximum axial concentration of the model to the field by the following expression,

$$\frac{C_M)_p}{C_M)_m} = \frac{Q_p U_p^{-1} (h)_p^{-2} (p/q)_p}{Q_m U_m^{-1} (h)_m^{-2} (p/q)_m} \left(\frac{(t_s)_p}{(t_s)_m} \right)^{-\frac{1}{2}} . \qquad 5.16$$

The preceding expression has been used in comparing model and field concentrations for a single elevated source. Field experiments suggest that the "inverse 1/2 power law" is valid for sampling times ranging from 10 min to 5 hr but the applicable range of this law depends on stability. The applicable range is greater in an unstable atmosphere than in nearly neutral cases and has not been verified for stable cases.

The simplest relation connecting the time-scale of the model T_m to that of the actual flow T_p is Eq. 3.43,

$$T_m = \frac{L_m}{L_p} \frac{U_p}{U_m} T_p . \qquad 5.17$$

This expression relates the travel time between the model and actual flow. It should be obvious that time events occur much faster on the model as compared to the field. This can be illustrated by computing the corresponding travel times. If one selects the distance between the Minturn generator and Chalk Mountain as a representative distance then the field travel time is,

$$T_p \sim \frac{31000 \text{ meters}}{10 \text{ m/s}} \sim 3100 \text{ sec} \sim 0.86 \text{ hr} \qquad 5.18$$

and the corresponding model travel time for the neutral case is,

$$T_m \sim \frac{3.23 \text{ meters}}{5 \text{ m/s}} \sim 0.645 \text{ sec} \qquad 5.19$$

and for the barostromatic case is,

$$T_m \sim \frac{3.23 \text{ meters}}{10 \text{ cm/sec}} \sim 32.3 \text{ sec.} \qquad 5.20$$

These travel times are approximate since the detailed effects of the terrain have not been considered.

Now if it is assumed that the concentration at a point downstream from a source is a function of the sampling time t_s and travel time T then from dimensional analysis one can obtain the following relation between model and field,

$$\left.\frac{t_s}{T}\right|_m = \left.\frac{t_s}{T}\right|_p \quad . \tag{5.21}$$

In order to evaluate Eq. 5.21 the sampling times must be known. Generally, the exact sampling time is not known but a close approximation to the sampling time, the residence time can be computed from known characteristics of the sampling equipment. The residence time can be defined as the time required for collecting a given volume of sample at a certain sampling rate or

$$t_R = \frac{\text{volume of sample}}{\text{sampling rate}} \quad . \tag{5.22}$$

A determination of the residence times for the two wind tunnel cases shows the following values,

Neutral Case

$$t_R \sim \frac{37 \text{ cc}}{700 \text{ cc/min}} = 0.053 \text{ min} = 3.17 \text{ sec} \tag{5.23}$$

Barostromatic Case

$$t_R \sim \frac{37 \text{ cc}}{200 \text{ cc/min}} = 0.185 \text{ min} = 11.1 \text{ sec} \quad . \tag{5.24}$$

These residence or sampling times are quite small and one might question whether a representative sample can be obtained in such a short

duration. A rough idea on the representativeness of the residence time can be approached by considering the period or frequency of turbulent eddies generated by the model. In the neutral case, an approximate estimate of the period of larger eddies can be found by

$$t_f^* = \frac{L^*}{U^*} \qquad 5.25$$

where L^* is a characteristic height of the model terrain and U^* is a characteristic velocity generating the turbulent eddies. In this case,

$$t_f^* \sim \frac{13 \text{ cm}}{10 \text{ m/sec}} \sim 1.3 \times 10^{-2} \text{ sec.} \qquad 5.26$$

For the barostromatic case,

$$t_f^* \sim \frac{13 \text{ cm}}{10 \text{ cm/sec}} \sim 1.3 \text{ sec.} \qquad 5.27$$

One notes that the period of fluctuation of eddies for both cases are several times smaller than the residence times therefore the samples obtained during these respective residence times should be fairly representative.

The similarity relation expressed by Eq. 5.21 may now be evaluated by use of the model residence (sampling) and travel times and the field travel time, i.e., one finds the equivalent field sampling time in terms of the other time variables, or

$$t_s)_p = \frac{t_s)_m}{T)_m} \; T)_p \; . \qquad 5.28$$

For the model neutral airflow,

$$t_s)_p \sim \frac{3 \text{ sec}}{0.645 \text{ sec}} \; 3100 \text{ sec} \sim 4 \text{ hours} \qquad 5.29$$

and for the barostromatic airflow,

$$t_s)_p \sim \frac{11.1}{32.3} 3100 \text{ sec} \sim 17.7 \text{ min} \sim 18 \text{ min.} \quad 5.30$$

These results, though very approximate, suggest that for the model neutral case the concentration values correspond to a time-mean field plume which has integrated the fluctuations and meandering effects on the time scale of approximately 4 hours. In the case of the barostromatic model a time-mean plume of approximately 18 min.

Figure 57 denotes, schematically, how the boundaries of a tracer plume would appear at any given instant or as it would appear having been averaged over 18 min. or 4 hr (compare with Figs. 11, 15, and 26). The right side of the figure represents the ideal distributions of the concentration for each of the three plume types.

If the time-averaged diagrams of the plume were extended to distances quite far from the source, the boundaries of the time-smoothed plume would themselves meander because the longer length of plume would be under the influence of eddies that are quite large in area. It is important to recognize that fluctuations in the wind that are larger than the plume dimensions tend to transport the plume intact whereas those that are smaller tend to tear it apart. Thus, as the plume reaches greater and greater distances and grows in size, larger and larger turbulent eddy sizes become effective in diffusing the plume, and smaller eddies become increasingly ineffective (Ref. 106) (Fig. 57).

In general, the wind tunnel, in contrast to the field, does not generate the appropriate equivalent large-scale eddies which cause a tracer plume to meander. Part of the reason for this restriction is due to the constricting effect of the wind tunnel walls on the airflow.

However, with the present sampling equipment for the wind tunnel it would be difficult to detect, quantitatively, such phenomena as meandering even if it did occur.

5.2.2 Surface features

a) Direction of tracer plume

Both model airflows show a definite direction of the tracer plume on the surface and with height. In the barostromatic airflow the direction of the plume from both generator locations was generally determined by the major topographic feature, i.e., the Eagle River Valley (see Figs. 22, 24, and 26). At Camp Hale where the Eagle River Valley divides into two forks it was observed that the tracer material divided also but with a major portion choosing the Mitchell Creek-Tennessee Pass Fork.

In the neutral case the direction of the tracer plume was approximately in the direction of the freestream velocity, i.e., ~320 deg. For the Minturn source the maximum concentration moves over Battle Mountain with little material detected in the Eagle River Valley (Figs. 9 and 11). In the case of the Redcliff source the maximum concentration follows the valley then ascends the saddle between Chicago Ridge and Chalk Mountain. Very little material was detected near Tennessee Pass (Figs. 13 and 15).

The aircraft sampling of silver iodide (Figs. 48, 49 and 50), the constant volume balloon flights (Figs. 37 and 38) and the surface sampling (Table 9 and Figs. 57) indicated that during some conditions the direction of a major portion of the seeding plume was toward the Tennessee Pass region as suggested by the barostromatic model results. The only probable confirmation on the neutral model results was the

constant-volume balloon flight #2. On this day the static stability was near neutral and the winds were stronger than on the 12th of December. One balloon moved in the direction of the saddle between Chalk Mountain and Chicago Ridge but was lost before reaching that area (see Fig. 37, Flight #2).

On the whole, the model results suggest that during certain wind and stability conditions a major portion of the concentration tends to move toward the Tennessee Pass region while for the stronger wind and more neutral situations the maximum concentration may tend toward the saddle between Chicago Ridge and Chalk Mountain.

Field data was not sufficient to verify this behavior. Surface data based on ground ice-nuclei counts (Table 9) indicate that significant concentrations of ice nuclei may be found near Chalk Mountain or Tennessee Pass. One site may have more counts on the average than the other site and vice versa suggesting that the model results may be somewhat typical of field conditions.

b) Comparison of surface concentration

1) Decrease of concentration downstream

Since the time-averaged plume from a continuously maintained point source expands both laterally and vertically with downwind distance from the source, the centerline concentration within the plume will decrease continuously with distance. The rate at which the centerline concentration decreases varies with atmospheric stability or, equivalently, with the magnitude and scale of the turbulence.

According to Sutton (Ref. 37) the theoretical expression for the rate of decrease in ground concentration from a point source in neutral

equilibrium is $C_{max} \propto X^{-1}$. This decrease is generally smaller than field observations indicate for similar stability conditions.

Gifford (Ref. 37) compared theoretical calculations based on Lagrangian similarity with Cramer's Prairie Grass data on downwind ground-level concentrations and showed that both results gave the decrease in concentration up to 800 meters as follows,

Very stable stability	$C \propto X^{-1.0 \text{ to } -1.3}$	
Moderately stable stability	$C \propto X^{-1.4 \text{ to } -1.6}$	
Near neutral stability	$C \propto X^{-1.8 \text{ to } -2.0}$	5.31
Moderately unstable stability	$C \propto X^{-2.6 \text{ to } -2.8}$	
Very unstable stability	$C \propto X^{-3.0 \text{ to } -3.3}$.	

The power index values are those by means of which Cramer has characterized the Prairie Grass data on downwind ground-level concentration. These data have been incorporated into an empirical method for forecasting dispersion up to 10 km or more (see section 2.3.3).

Similar type of data were not obtainable in the field because sufficient ground sampling equipment were not available. In fact it is doubtful whether this type of data exists for any complex mountain region.

The maximum concentration data from the wind-tunnel models were plotted on semi-logarithmic paper with respect to distance (scaled to the field) to determine the decrease of concentration with distance. The following approximate results were determined for the two wind-tunnel airflows,

Barostromatic Airflow

Redcliff and Minturn Source	$C_{max} \propto X^{-0.8}$	5.32

Neutral Airflow

Minturn Source	$C_{max} \propto X^{-3.2}$	5.33
Minturn and Redcliff	$C_{max} \propto X^{-2.7}$	
Source	$C_{max} \propto X^{-1.3}$ (~6 km or more)	

The wind-tunnel power index values were within the same order of magnitude as suggested by the empirical-observational method over relatively flat land, although, differences were apparent. Under the wind-tunnel barostromatic conditions the decrease in concentration is smaller than theoretical or empirical data. The quasi-laminar airflow and velocity distribution in the lower levels may be a possible reason for the difference since the thermal stratification should have favored a larger decrease in concentration with distance.

Under the wind-tunnel neutral conditions the power index values appear comparable to unstable field conditions which, as suggested by previous calculations in section 5.1.1.d, was probably the result of slightly exaggerated turbulent conditions in the wind-tunnel. However, the effect of the terrain features may have exerted an influence on the decrease in concentration in both wind-tunnel conditions.

2) Model and field local concentrations

The field measurement of ice nuclei ground concentrations was conducted with a USWB - modified Bigg-Warner and Colorado State University expansion counters (Ref. 87). An environmental air sample is pumped into a sealed chamber, precooled by the refrigerated chamber walls to an arbitrary temperature, and subsequently further cooled to the desired nuclei activation temperature by a rapid expansion. Resultant ice crystals are counted by a supercooled sugar solution technique.

The sampling or residence times can be approximated by the same method as the radioactive sampling equipment since the counters obtain their volume samples on a similar principle. The residence times can be computed by Eq. 5.22 as,

C.S.U. Expansion Counter

$$t_R = \frac{10 \text{ liters}}{13.5 \text{ liters/min}} = 0.74 \text{ min} = 44.4 \text{ sec} \qquad 5.34$$

Bigg-Warner Counter

$$t_R = \frac{12.5 \text{ liters}}{28 \text{ liters/min}} = 0.45 \text{ min} = 26.8 \text{ sec.} \qquad 5.35$$

These residence times indicate that the ice nuclei counts are essentially instantaneous or peak values.

Typical traces of ground-level concentration varying with time is shown in Fig. 58. At times, the concentration is equivalent to background, but may increase abruptly by an order of magnitude or more. Apparently, the large fluctuations of concentration are due in part to the characteristic short-period eddies in the atmosphere as well as meandering. Although, some non-meteorological effects may account for some of the variation.

The accumulative average of ice nuclei concentration with respect to time is also shown in Fig. 58. Generally, the average count after the generators have been on for 4 to 6 hours approaches 200 nuclei/liter but this may vary depending on generator output and duration, meteorological conditions and location.

Field measurements of ice nuclei concentrations at downwind locations from the two sources provides a means for checking whether the model surface concentration data were within an order of magnitude of field data.

For the model, one can summarize the surface concentration data as follows:

Barostromatic Case

Location	Source: Minturn	Source: Redcliff
Tennessee Pass	$\overline{C}$~237* μμ curie/cc	$\overline{C}$~488μμ curie/cc
Chalk Mountain	$\overline{C}$~134μμ curie/cc	$\overline{C}$~36μμ curie/cc

Neutral Case

Location	Source: Redcliff and Minturn
Tennessee Pass	$\overline{C} \sim 0$
Chalk Mountain	$\overline{C} \sim 58$μμ curie/cc

In order to relate the model surface data to the field surface data it is necessary to evaluate the dimensionless concentration parameter, Eq. 3.44 for model and field. Dimensional or similarity analysis requires that

$$\left.\frac{\overline{C}\,\overline{U}\,X^2}{Q}\right|_f = \left.\frac{\overline{C}\,\overline{U}\,X^2}{Q}\right|_m . \qquad 5.36$$

A convenient way of checking Eq. 5.36 was to evaluate $\overline{C}\,\overline{U}\,X^2/Q)_m$ then make a plot of the equivalent field surface concentration for various values of $\overline{U}_f$ and Q_f since X is a fixed reference length, i.e.,

$$\overline{C}_f = \frac{\overline{C}_m \overline{U}_m}{Q_m} \frac{X_m^2}{X_f^2} \frac{Q_f}{\overline{U}_f} . \qquad 5.37$$

*Concentration values may vary approximately 10-15% due to the accuracy of the Geiger-Mueller tubes.

The reference length X was selected as the distance between the first source (Minturn) and the two sampling locations, Tennessee Pass and Chalk Mountain. Therefore,

X_{f_1} - distance from Minturn to Chalk Mountain ~ 31000 meters

X_{m_1} - distance from Minturn to Chalk Mountain ~ 322.9 cm

X_{f_2} - distance from Minturn to Tennessee Pass ~ 28000 meters

X_{m_1} - distance from Minturn to Tennessee Pass ~ 291.6 cm.

In the case of the data from the barostromatic case it is necessary to assume that the concentration values as well as the source strengths are additive, hence,

Tennessee Pass $\overline{C}$ ~ 725μμ curie/cc

Chalk Mountain $\overline{C}$ ~ 170μμ curie/cc

Q_T ~ (7.5 + 7.5)μ curie/sec

~ 15μ curie/sec.

The concentration parameter when evaluated for Tennessee Pass and Chalk Mountain gave the following results when $\overline{U}$ ~ 10 cm/sec,

$$\frac{\overline{C}\,\overline{U}\,X_{m_2}^2}{Q} \sim 41 \quad \text{Tennessee Pass} \qquad 5.38$$

$$\frac{\overline{C}\,\overline{U}\,X_{m_1}^2}{Q} \sim 12 \quad \text{Chalk Mountain.}$$

For the neutral case with $\overline{U}$ ~ 8 m/sec,

$$\frac{\overline{C}\,\overline{U}\,X_{m_1}^2}{Q} \sim 35 \quad \text{Chalk Mountain.} \qquad 5.39$$

The equivalent field concentration can now be determined in terms of Q_f and $\bar{U}_f$ by Eq. 5.37. The source strength Q_f was based on two generators operating at three different output rates similar to what was used in the field during seeding operations. These rates are,

60 gm of silver iodide/hr ≡ 6.67×10^{13} particles/sec (effective at -20°C)

20 gm of silver iodide/hr ≡ 2.2×10^{13} particles/sec

1.5 gm of silver iodide/hr ≡ 1.66×10^{3} particles/sec.

Figure 59 presents the results for Tennessee Pass and Chalk Mountain from Eq. 5.37. The results, with some restrictions, were reasonable based on past field data at these locations. For an example, a plume emitted at the rate of 40 gm/hr (two generators) and effected by a mean field velocity of 8 m/s would give on the average (~18 min) 300 nuclei/liter (effective at -20°C) at the Tennessee Pass location and 200 nuclei/liter at Chalk Mountain. Such values are certainly within the range observed in the field (Fig. 58 and Table 9). A complete family of curves for Fig. 59 would be necessary to explore the full range of concentration, source, and velocity combinations.

5.2.3 Horizontal and vertical dispersion

a) Horizontal dispersion

The aircraft and surface sampling indicated that the seeding plume width was in excess of 10 km at approximately 30 km from the first generator. In the barostromatic model, the width of the plume near the surface at the same distance downstream (scaled to the field) was approximately 12 km or more. In this case the topography assisted in spreading the plume although the plume might have been wider if the velocity in the lower levels had not been so fast.

In the neutral model, the width of the plume was approximately 9 km. Hino (Ref. 49) compared wind-tunnel diffusion results from an elevated source with a three-dimensional computer model and suggested that the wind-tunnel underestimates the lateral diffusion due to the restrictions of the side walls. Evidently, this may have been a contributing cause for the narrower plume in the neutral experiment although the high freestream velocity was probably the principal reason for restricting the development of the plume in the lateral direction. Additional experiments are needed at lower freestream velocities to determine whether this problem is due to the confining influence of the side walls or poor simulation of the velocity and lateral turbulence or both.

b) Vertical dispersion

The angle of inclination at which the tracer material leaves the generator sites with respect to the terrain was found to be between 60 to 65 degrees for the models and 70-75 degrees for the field. A different viewpoint of these results is presented in Fig. 60. For the model data, the vertical rise of the plume was approximated by finding the height above the source where the concentration was 10% of the surface maximum at various distances from the source. For the field data, the 10 nuclei/liter line was taken as the approximate forward edge of the plume. All field plume boundaries were evaluated from the Minturn source.

It is interesting to note that the results from the barostromatic model agreed quite well with the field observations. For the neutral case, the vertical rise of the plume was exaggerated from 2 to 2.5 times that of the field results. At least three reasons can be cited for this

discrepancy. One, exaggerated vertical turbulence, two, errors in concentration data and three, no vertical compressibility or stabilizing influence on the plume in the higher layers which is normally observed in the atmosphere.

An extreme test for the models is to compare the vertical distribution of concentration between model and field through the concentration parameter (Eq. 5.36). This was done for two locations, Camp Hale and Tennessee Pass. For the field, the concentration data from the aircraft sampling for March 13 and 16 (Figs. 49 and 50) were averaged spatially over each ground location for approximately 4 km for each flown altitude. Two generators were operating giving a $Q = 13.34 \times 10^{13}$ nuclei/sec (effective at -20°C). The mean wind speed effecting the plume was $\overline{U} \sim 7$ m/s Camp Hale, $\overline{U} \sim 7.5$ m/s Tennessee Pass and X was 20 km for Camp Hale. The model data was obtained from Figs. 14, 23, and 25 and were adjusted to the new reference length X .

Figure 61 shows the comparison between the model and field dimensionless concentration parameter $\overline{C}\,\overline{U}\,X^2/Q$ as plotted versus height for the two locations. The apparent high field concentration values near 10,500 ft at Camp Hale may be due to lofting of the seeding material as a result of the near neutral stability conditions observed both days. The concentration probably decreases toward the ground but only sporadic ground counts suggested this type of behavior. Too much emphasis should not be placed on these comparisons because of the limited data, although, it appears that the results from the barostromatic model was somewhat better than for the neutral model.

A number of factors such as, differences in sampling times, airflow characteristics differences, accuracy of both model and field data,

depletion mechanisms, etc. can be cited for explaining the differences between model and field.

5.3 Comparison of Model Results With Empirical Methods and Other Field Observations

A number of field diffusion experiments have been made over relatively flat terrain for continuous point sources. Most of these experiments have been summarized in Ref. 106.

The relation between normalized axial surface concentration and travel distance from continuous point sources for approximately 200 individual diffusion experiments selected from Green Glow-30, Prairie Grass, National Reactor Testing Station, Ocean Breeze, and Dry Gulch series are shown in Fig. 62. The normalized concentration data were grouped according to concurrently observed horizontal wind-direction fluctuation (σ_θ) data. The Pasquill type A, D, and F categories were added for comparison (Ref. 82 and 97).

The normalized model surface axial-concentration data for three different sources under the two different airflow regimes and the approximate range of field concentration values for the Climax area (~30 km) have been plotted on Fig. 62 for comparison with the other data.

The model data tends to fall between the neutral and unstable categories and the slopes were different than the Pasquill categories and other data. For the barostromatic model the slope and dilution appears to be quite different from the other data. A partial explanation for this feature may be the result of the stability in the near surface layers. According to Fig. 20 the stability in the surface layer over the model was generally unstable in a very thin layer near

the surface. These conditions could cause lofting of the tracer material from the surface resulting in a slower decrease of concentration with distance. Other reasons for the characteristics of the slope have been mentioned in section 5.2.2.b.

The effects of topography such as, the depletion of the main plume by tributary valleys and the confining influence of the valley walls may also be contributing factors for explaining the differences between the model data and other data.

Turner (Ref. 105) suggests that a modified version of the Gaussian distribution may be used for approximating the surface axial concentration within a valley. The principal assumption is that the horizontal dispersion coefficient σ_y becomes great enough that the concentration can be assumed to be uniform across the width of the valley. In this case, the horizontal dispersion is restricted by the valley sides.

The concentration for this case is calculated according to the following equation where Y is the width of the valley,

$$\frac{\overline{C}\,\overline{U}}{Q} = \frac{2}{\sqrt{2\pi}\,\sigma_z Y} \exp\left[-\frac{1}{2}\left(\frac{h}{\sigma_z}\right)^2\right] \quad . \qquad 5.40$$

The following equation was evaluated by first making a gross approximation for the width of the Eagle River Valley from the Redcliff generator site to the Tennessee Pass region. The valley width varied from 500 m to 2100 m. The vertical dispersion coefficient σ_z was evaluated with respect to distance for four of the Pasquill stability categories A, B, C, and D from Fig. 3-3 in Turner (Ref. 105). The effective height of the source was arbitrarily set at 10 m which is probably a little more realistic than assuming a plume of no

effective rise rate. If the latter was chosen a different equation would be required and the difference between the two methods would be a factor of three.

The quantity $\overline{C}\,\overline{U}/Q$ was determined for every 1 km from the Redcliff source to the Tennessee Pass region. Figure 63 shows these ground concentration estimates along the valley floor as compared to two of the model estimates. The calculations from Eq. 5.40 were very sensitive to the width of the valley. Since the valley varied irregularly in width these variations show in the concentration values. Model or field data were not extensive enough to verify this type of behavior in the concentration distribution.

A multitude of scientific and technical limitations makes the calculated ground-level centerline concentrations only gross estimates and, even for level ground, correct within a factor of three. One can not expect too much from the comparison between model and calculated data under these reliability conditions but nevertheless there seems to be a slight improvement in the correlation between the two sets of data over that of Fig. 62.

Although, these results may be interpreted as encouraging, better model and field data are a necessity in order to obtain a better understanding of the effects of irregular topography on plume ground concentrations.

Chapter VI

SUMMARY AND CONCLUSIONS

6.1 Summary

The first objective of this study was to develop a laboratory airflow model which would be adequate in estimating airflow and transport-dispersion characteristics during winter storms over the Eagle River Valley-Climax topographic complex. Both barostromatic and neutral airflow models were investigated because detail information on the meteorological characteristics associated with the winter storms were not established at the outset. The following findings resulted from investigations using the barostromatic airflow model:

1) Large (~1^{o}C/cm) vertical temperature gradients and low-speed (~10 cm/sec) airflow may be obtained by utilizing dry ice with a wind tunnel.

2) The resultant temperature and airflow conditions were sufficient for satisfying the gross requirements of Richardson number similarity with the atmosphere.

3) The addition of carbon-dioxide to air in the wind tunnel increases the vertical density gradient by approximately 5%; therefore, Richardson number equality was achieved primarily by means of thermal stratification.

4) Low-airflow velocity profiles can be measured reliably by the "smoke-wire" method.

Use of a neutral model greatly facilitated the measurement of turbulence in an effort to determine the effect of topography upon the dispersion. Studies using the neutral model revealed that

separation of flow occurred downwind of many topographic features and produced a turbulence field which was highly nonhomogeneous and with large energy content in scales comparable to dimensions of the topographic features.

The second objective was to compare model and field data for correspondence and to determine how well the laboratory models can simulate actual atmospheric airflow and transport-dispersion. Similarity analysis of the relevant equations governing the models showed that "exact" similarity can be achieved between models and field in only an approximate sense. The results indicate that in spite of the compromise in exact similarity resulting principally from inequality of Reynolds numbers useful results can be obtained from the physical airflow models.

The comparison of model and field results on transport and dispersion over the topographic model showed the following favorable results for both barostromatic and neutral airflows:

1) Concentration plume patterns over the model correspond approximately to field plumes averaged over periods of 18 min to 4 hours.

2) Both model and field data show that the tracer material diffused throughout the principal valley.

3) The directions of the tracer plumes were approximately the same for model and field.

4) Comparison of normalized field ground-level concentrations at approximately 30 km from the first source (Minturn) with normalized model ground-level concentrations showed that model results fall within the observed range of field values.

5) The width of the tracer plume (>12 km) near the surface at field sites approximately 30 km from the first source compared favorably with the width of the plume as generated by the barostromatic model. However, the neutral model underestimated the average field plume width by approximately 25%.

6) The angle-of-inclination of the plume's center of mass immediately downwind from generator sites was approximately equal for prototype and models. Comparison of barostromatic model- and field-plume rise rates compared favorably, however, the neutral model exaggerated the plume-rise rate by a factor of 2 to 2.5. A comparison of the vertical distribution of normalized concentration for model and field was inconclusive because of the limited amount of field data.

7) The comparison of the neutral and barostromatic model results with the field data showed that the barostromatic model simulated the atmospheric conditions corresponding to winter storms with northwest winds better than the neutral model.

8) Comparison of normalized model axial-ground concentrations as a function of distance with empirical methods of Pasquill and a modified Gaussian method showed that model dilution and decrease of concentration with distance were generally different from the other two methods. Differences between model results and the other two methods were the result of topography, partial simulation of the actual airflow and dispersion and the inadequacy of the empirical and Gaussian methods for predicting dispersion in irregular terrain.

The model and field results of this study also provide information on whether ground-based generators is a good mode of seeding orographic clouds. The results suggest that ground-based generator sites

are effective for distributing the seeding agent to orographic cloud systems for the following reasons:

1) The distribution of artificial nuclei with height is proper for optimum seeding, i.e., the largest number of nuclei are found in the lowest levels where the cloud temperatures are warmest and the least number is located where the cloud temperatures are coldest.

2) Ground generators operated over several hours can create a large potential source region (e.g., filling of valleys) where the seeding material can be distributed to a cloud system over a period of time by convection, orographic effects (advection), and turbulent mixing.

3) The ground-based generator is mobile and its location can be varied depending on the desired design conditions. However, the location may not be so critical during good orographic cloud situations when the atmospheric stability may be near neutral through a deep layer. The model and field results show that even valley locations of generators may be sufficient for distributing the seeding material to the cloud system under these atmospheric conditions.

A question does remain on the efficiency of ground generators in seeding operations during very stable or inversion temperature conditions. Perhaps other means of dispersing the seeding material, such as, rockets or airplanes would be more efficient during these atmospheric conditions. The subject remains open for further investigation.

Comparison of the model and field results showed that several improvements should be made in the barostromatic airflow model. Improvements in the simulation of the horizontal temperature gradient,

vertical profile of velocity, and the surface boundary layer are needed to improve model-field correspondence. In the case of the neutral model, the improvements to be considered are better simulation of three-dimensional turbulence fields over the topographic model and upstream, side and upper boundary conditions.

The third objective was to determine the transport-dispersion mechanisms and characteristics over the Eagle River Valley-Climax region during storm periods typical for cloud seeding by use of both the model and field data. The field data was limited but were of practical importance to the problem. The following interesting features were found:

1) Aircraft sampling flights of the silver-iodide seeding material showed that the observed vertical dispersion of seeding material was approximately 1000 to 1200 meters/5kms of horizontal transport. This vertical dispersion rate exceeded the natural slope of the terrain which is approximately 140m/5kms.

2) Dual constant-volume balloon flights showed that the total dispersion rate equaled and exceeded t^3 and t^4 for short periods. Zonal, meridional and vertical eddy diffusivities varied from 10^4 to 10^6 $cm^2 sec^{-1}$. The zonal and vertical eddy diffusivities increase in magnitude with height.

3) Turbulence augmented by near-neutral stability conditions within the valley, orographically induced eddies, directional wind-shear and convection were found to be the various physical mechanisms acting to disperse the seeding material.

The fourth objective was to examine the feasibility of utilizing model studies of transport-dispersion over scaled topographic models for application to weather modification programs.

The best procedure in utilizing the laboratory model technique in weather modification programs is to have a model study proceed for a selected target area before extensive preparations have been completed on the physical location of seeding generators. Some preliminary meteorological data are needed on temperatures, winds and turbulence to guide the modeling program. With data from the model study, field program personnel could then proceed in an objective manner to establish the optimum field configuration for seeding operations.

The results show that laboratory experiments can assist development of field programs by providing the following types of pre-operational data:

1) Definition of the general direction of seeding plumes in mountainous terrain.

2) Approximate estimates on the decrease of concentration with downstream distance.

3) Approximate estimates on vertical and horizontal dispersion and the cloud volume occupied by the seeding material.

4) Relative diffusion characteristics for the evaluation of seeding generator sites.

Several limitations associated with the laboratory modeling technique place some restrictions on the general use of this technique. Anyone planning a model study should be aware of the following:

1) Area limitations - Designated areas to be modeled would have to be less than 3200 sq. mi. in order to not exceed the space requirements of present laboratory facilities. This limitation assures reasonable scaling of length for the model and reasonable confidence that the Coriolis accelerations can be neglected.

2) Scale-ratio limitations - With the area limitations noted above, length-scale ratios between 1:10,000 and 1:5,000 can be utilized in the laboratory studies.

3) Wind direction limitations - In general, only one geostrophic or freestream wind direction can be simulated for a topographic model. However, a little extra effort in constructing extra model sections will help alleviate this problem.

6.2 Conclusions

In the light of these findings the following conclusions are made:

1) Exact similarity between all physical variables in the field and model is not necessary in order to obtain practical operational data from laboratory studies on atmospheric transport and dispersion.

2) The negative speculations by previous writers regarding laboratory simulation (sec. 2.5.2) can be discounted, i.e., laboratory simulation with its inherent limitations is a practical tool for estimating airflow as well as transport-dispersion characteristics over mountainous terrain. The laboratory studies can provide useful pre-operational data for planning proposed field programs on weather modification and other diffusion oriented problems.

3) The model and field results indicate that the atmospheric dispersion during orographic storm events is large enough to transport the seeding material from ground generators to cloud systems. Mechanical

turbulence enhanced by near-neutral stability conditions and orographically induced eddies are principal physical mechanisms for dispersing the seeding material from the source generators.

4) Current limitations of the modeling technique is due primarily to modeling facility limitations and not to fundamental physical restrictions.

5) On the basis of these results the most immediate research problem to be considered at the present time is the continuation of coordinated laboratory, field and numerical studies on atmospheric transport-dispersion in mountainous terrain. The results from these studies should prove beneficial to present and future weather modification and air pollution problems. A list of recommendations for further research is found in Appendix H.

BIBLIOGRAPHY

REFERENCES

1. Abe, M., 1941: Mountain clouds, their forms and connected air currents. Part II Bull. Centr. Met. Obs. of Japan, 7(3), 93-145.

2. Angell, J. K., 1962: Use of tetroons for the estimation of atmospheric dispersion on the mesoscale. Monthly Weather Review, Vol. 90, No. 7, 263-270.

3. Arya, S. P. S., 1968: Structure of stably stratified turbulent boundary layer. Ph.D. dissertation, College of Engineering, Colorado State University.

4. Auer, A. H., D. L. Veal, and J. D. Marwitz, 1968: Plume tracking and mass flow studies within the Elk Mountain water resource observatory and western South Dakota. Natural Resources Research Inst. Info. Circ. No. 54, University of Wyoming.

5. Balick, L. and J. Rasmussen, 1971: Observational study of an orographic cloud. Atmospheric Science Paper (to be published), Colorado State University.

6. Barnes, A. H., 1970: Wind tunnel velocities by photogrammetry. Paper presented at the American Society of Photogrammetry, October 8, 1970, Denver, Colorado.

7. Batchelor, G. K., 1950: The application of the similarity theory of turbulence to atmospheric diffusion. Q. Jour. R. Meteor. S., Vol. 76, 133-146.

8. Batchelor, G. K., 1953: The conditions for dynamical similarity of motions of a frictionless perfect-gas atmosphere. Q. Jour. R. Meteor. S., Vol. 79, 224-235.

9. Beran, D. N., 1967: Large amplitude lee waves and chinook winds. Jour. of Appld. Meteor., Vol. 6, No. 5, 865-877.

10. Booker, R. D. and L. W. Cooper, 1965: Superpressure balloons for weather research. Jour. of Appld. Meteor., Vol. 4, No. 1, 122-129.

11. Braham, R. R., et al., 1952: A technique for tagging and tracing air parcels. Transactions of Amer. Geophys. Union, Vol. 33, No. 6, 825-833.

12. Briggs, J., 1963: Airflow around a model of the Rock of Gibraltar. Scientific Paper No. 18, Meteorological Office, London, England.

13. Buettner, K. J. K., J. Zimmerman, and G. Maykut, 1962-1963: Orographic deformation of wind flow. Report 1, 2, and Final Report, Dept. of Atmos. Sciences, University of Washington.

14. Cermak, J. E., et al., 1966: Simulation of atmospheric motion by wind-tunnel flows. Fluid Dynamics and Diffusion Laboratory Report No. CER66JEC-VAS-ESP-GJB-HC-RNM-SI17, Colorado State University.

15. Cermak, J. E., L. O. Grant, and M. M. Orgill, 1969: Research and development technique for estimating airflow and diffusion parameters in connection with the atmospheric water resources program. Interim Report, CER68-69JEC-LOG-MMO-27, College of Engineering, Colorado State University.

16. Cermak, J. E., and J. Peterka, 1966: Simulation of wind fields over Point Arguello, California, by wind-tunnel flow over a topographic model. Final Report, CER65JEC-JAP64, Colorado State University.

17. Chang, S. C., 1966: Velocity distributions in the separated flow behind a wedge-shaped model hill. Technical Report, CER65SCC66, Colorado State University.

18. Chappell, C. F., 1967: Cloud seeding opportunity recognition, Atmospheric Science Paper No. 118, Colorado State University.

19. Chappell, C. F., L. O. Grant and P. W. Mielke, Jr., 1969: Operational definition for weather modification applications to orographic clouds. Internal Report, Dept. of Atmos. Sci., Colorado State University.

20. Chaudhry, F. H., 1969: Turbulent diffusion in a stably stratified shear layer. Ph.D. dissertation, College of Engineering, Colorado State University.

21. Chopra, K. P., and Hubert, L. F., 1965: Kármán vortex streets in wakes of islands. AIAA Journal, Vol. 3, No. 10, 1941-1943.

22. College of Engineering, 1966: Fluid Mechanics Program. Fluid Dynamics and Diffusion Laboratory, Colorado State University.

23. Corby, G. A., 1954: The airflow over mountains - A review of the state of current knowledge. Q. Jour. R. Meteor. S., Vol. 80, 491-521.

24. Cramer, H. E., 1957: A practical method for estimating the dispersal of atmospheric contaminants. Proceedings of the First National Conference on Applied Meteorology, American Meteorological Society, C-33 - C-55.

25. Cressman, G. P., 1960: Improved terrain effects in barostropic forecasts. Monthly Weather Review, Vol. 88, No. 9-12, 327-342.

26. Crozier, W. D. and B. K. Seely, 1955: Concentration distributions in aerosol plumes three to twenty-two miles from a point source. Transactions of Amer. Geophys. Union, Vol. 36, No. 1, 42-52.

27. Davidson, B., 1963: Some turbulence and wind variability observations in the lee of mountain ridges. Journal of Appld. Meteor., Vol. 2, No. 4, 463-472.

28. De Pena, R. G., 1964: Measures de la diffusion de noyaux glacogenes d'iodure d'argent. Jour. Rech. Atmos., No. 1, 19-27.

29. Disa-S and B Inc., 1970: Disa probe manual. Leaflet No. 2004 Disa electronics, Franklin Lakes, New Jersey.

30. E. Bollay Associates, Inc., 1965: Park range atmospheric water resources program Phase I, Final Report Contract No. 14-06-D-5281, Bureau of Reclamation, Boulder, Colorado.

31. Faires, R. A., and B. H. Parks, 1960: Radioisotope laboratory techniques, George Newnes Ltd., London, p. 129.

32. Field, J. H. and R. Warden, 1929-30: A survey of air currents in the Bay of Gibraltar. Geophysical Memoirs No. 59(Rand M 1563), Her Majesty's Stationery Office.

33. Förchtgott, J., 1949: Wave streaming in the lee of mountain ridges. Bull. Met. Czech., Prague, 3, p. 49.

34. Furman, R. W., 1967: Radar characteristics of wintertime storms in the Colorado Rockies. Atmospheric Science Technical Paper 112, Department of Atmospheric Science, Colorado State University.

35. Garrison, J. A. and J. E. Cermak, 1968: San Bruno mountain wind investigation - A wind-tunnel model study. Fluid Dynamics and Diffusion Laboratory Report CER67-68JEC-JAG58, Colorado State University.

36. Gifford, F. A., 1961: Uses of routine meteorological observations for estimating atmospheric dispersion. Nuclear Safety, 2, 4, 47-51.

37. Gifford, F. A., 1962: Diffusion in the diabatic surface layer Jour. of Geophysical Research, Vol. 67, No. 8, 3207-3212.

38. Grant, L. O., 1963: Indications of residual effects from silver iodide released into the atmosphere. Proceedings of Western Snow Conference, 109-115 and Atmospheric Science Technical Paper No. 49, Colorado State University.

39. Grant, L. O., J. E. Cermak, and M. M. Orgill, 1968: Delivery of nucleating materials to cloud systems from individual ground generators. Proceedings of the Third Sky Water Conference on the Production and Delivery of Cloud Nucleating Materials, 99-134.

40. Grant, L. O., C. F. Chappell, and P. W. Mielke, Jr., 1968: The recognition of cloud seeding opportunity. Proc. of the First National Conference on Weather Modification, 372-385.

41. Grant, L. O., et al., 1969: Weather modification - An operational adaptation program for the Colorado River Basin. Interim Report, Bureau of Reclamation Cont. No. 14-06-D-6467, Dept. of Atmospheric Science, Colorado State University.

42. Grant, L. O., and P. W. Mielke, Jr., 1967: A randomized cloud seeding experiment at Climax, Colorado, 1960-1965. Proc. of the Fifth Berkeley Symposium of Mathematical Statistics and Probability, 5, 115-131.

43. Grant, L. O., and R. A. Schleusener, 1961: Snowfall and snowfall accumulation near Climax, Colorado. Atmospheric Science Technical Paper No. 17, CER61LOG24, Colorado State University.

44. Halitsky, J., J. Tolciss, and E. J. Kaplin, 1962-63: Wind tunnel study of turbulence in the Bear Mountain wake. Quarterly Progress Reports, No. 1 through 4, Dept. of Meteorology and Oceanography, New York University.

45. Halitsky, J., G. A. Magony, and P. Halpern, 1964: Turbulence due to topographical effects. Geophysical Sciences Lab. Report No. TR65-2, New York University.

46. Halitsky, J., G. A. Magony, and P. Halpern, 1965: Turbulence due to topographical effects. Geophysical Sciences Lab. Report No. TR66-5, New York University.

47. Hanna, S. R., 1969: The thickness of the planetary boundary layer. Atmospheric Environment, Vol. 3, 519-536.

48. Henderson, T. J., 1965: Tracking silver iodide nuclei under orographic influence. Paper presented at the 24th National Meeting of the American Meteorological Society on Cloud Physics and Severe Local Storms.

49. Hino, M., 1968: Computer experiment on smoke diffusion over a complicated topography. Atmospheric Environment, Vol. 2, No. 6, 541-558.

50. Hino, M., 1968: Maximum ground-level concentration and sampling time. Atmospheric Environment, Vol. 2, 149-165.

51. Houghton, D. D., and A. Kasahara, 1968: Nonlinear shallow fluid flow over an isolated ridge. Communications on Pure and Applied Mathematics, Vol. 21, 1-23.

52. Kao, S.-K., 1962: Large-scale turbulent diffusion in a rotating fluid with applications to the atmosphere. Jour. of Geophysical Research, Vol. 67, No. 6, 2347-2359.

53. Kao, S.-K., and L. L. Wendell, 1968: Some characteristics of relative particle dispersion in the atmosphere's boundary layer. Atmospheric Environment, Vol. 2, 397-407.

54. Kao, T. W., 1965: The phenomenon of blocking in stratified flows. Jour. of Geophysical Research, Vol. 70, No. 4, 815-822.

55. Kassander, R. A., 1959: A study of the trajectories and diffusion patterns of ground-generated airborne particulates under orographic wind-flow conditions. Jour. of Meteor., Vol. 16, No. 6, 617-625.

56. Krishnamurti, T. N., 1964: Theory of two-dimensional mountain waves. Reviews of Geophysics, Vol. 2, No. 4, 593-624.

57. Langer, G., 1969: Evaluation of NCAR ice and cloud condensation nucleus counters. Proceedings of 7th International Conference on Condensation and Ice Nuclei, Prague and Vienna, Czechoslovakia, 288-292.

58. Langer, G., J. Rosinski, and C. P. Edwards, 1967: A continuous ice nucleus counter and its application to tracking in the troposhpere. Jour. of Appld. Meteor., Vol. 6, No. 1, 114-125.

59. Lawson, A. E. and J. M. Miller, 1966: Thermal conductivity detectors in gas chromatography. Jour. of Gas Chromatography, Vol. 4, No. 8, 273-284.

60. Lawson, T. V., 1968: Methods of producing velocity profiles in wind tunnels. Atmospheric Environment, Vol. 2, 73-76.

61. Lin, J. T., and G. J. Binder, 1967: Simulation of mountain lee waves in a wind tunnel. Technical Report, CER67-68JTL-GJB24, College of Engineering, Colorado State University.

62. Long, R. R., 1954: Some aspects of the flow of stratified fluids II, Experiments with a two-fluid system. Tellus, Vol. 6, 97-115.

63. Long, R. R., 1959: A laboratory model of airflow over the Sierra Nevada mountains. The Atmosphere and the Sea in Motion - The Rossby Memorial Volume, 372-380.

64. Ludlam, F. H., 1955: Artificial snowfall from mountain clouds. Tellus, Vol. 7, 277-290.

65. MacCready, P. B., et al., 1955: Investigations of silver-iodide decay and transport and natural nuclei. Paper prepared for the Advisory Committee on Weather control, Meteorology Research, Inc.

66. McDonald, J. E., 1958: Physics of cloud modification. Advances in Geophysics, Vol. 5, 278-280.

67. McMullen, R. W., and W. A. Perkins, 1963: Particulate diffusion over irregular terrain. Technical Report No. 96, Metronics Associates, Inc.

68. McVehil, G. E., G. R. Ludwig and T. R. Sundaram, 1967: On the feasibility of modeling small scale atmospheric motions. CAL Report No. ZB-2328-P-1. Cornell Aeronautical Laboratory.

69. Meroney, R. N. and J. E. Cermak, 1967: Wind tunnel modeling of flow and diffusion over San Nicolas Island, California. Technical Report CER66-67RNM-JEC44, Colorado State University.

70. Milly, G. H., J. T. Ball, and D. B. Spiegler, 1969: A numerical experiment on the spatial distribution of cloud seeding nuclei. Jour. of Appld. Meteor., Vol. 8, No. 1, 83-91.

71. Monin, A. S., and A. M. Obukhov, 1954: Basic regularity in turbulent mixing in the surface layer of the atmosphere. Trudy Geophys. Inst. ANSSSR, No. 24.

72. Munn, R. E., 1966: Descriptive Micrometeorology. Advances in Geophysics, Supplement 1, Academic Press, London.

73. Myers, V. A., 1962: Airflow on the windward side of a large ridge. Jour. of Geophysical Research, Vol. 67, No. 11, 4267-4291.

74. Natural Resources Research Institute, 1969: Atmospheric water resources research. Final Report, Bureau of Reclamation Cont. No. 14-06-D-6002, College of Engineering, University of Wyoming.

75. Nemoto, S., 1961: Similarity between natural wind in the atmosphere and model wind in a wind tunnel - Modeling criteria for a local wind. Papers in Meteorology and Geophysics, Vol. 12, No. 1, 30-52.

76. Nemoto, S., 1962: Similarity between natural wind in the atmosphere and model wind in a wind tunnel - Modeling criteria for a local wind. Papers in Meteorology and Geophysics, Vol. 13, No. 2, 171-195.

77. Orgill, M. M., 1968: Laboratory simulation of valley-slope wind systems - Feasibility study. Unpublished manuscript, Fluid Dynamics and Diffusion Laboratory, Colorado State University.

78. Orville, H. D., 1967: The numerical modeling of mountain upslope winds and cumulus clouds. Report 67-2, Institute of Atmos. Sci., South Dakota School of Mines and Technology.

79. Overman, R. T., and H. M. Clark, 1960: Radioisotope Techniques, McGraw-Hill Book Co.

80. Pack, D. H., 1962: Air trajectories and turbulence statistics from weather radar using tetroons and radar transponders, Monthly Weather Review, Vol. 90, No. 12, 491-506.

81. Pack, D. H., and J. K. Angell, 1963: Preliminary study of air trajectories in the Los Angeles basin as derived from tetroon flights. Monthly Weather Review, Vol. 91, Nos. 10-12, 583-604.

82. Pasquill, F., 1961: The estimation of the dispersion of windborne material. Meteorol. Mag., Vol. 90, 1063, 33-49.

83. Pasquill, F., 1962: Atmospheric Diffusion. D. Van Nostrand Co. Ltd., London.

84. Plate, E. J., and C. W. Lin, 1965: The velocity field downstream from a two-dimensional model hill. Final Report, Part 1 CER65EJP14 and Part 2 CER65EJP-CWL41, Colorado State University.

85. Plate, E. J. and C. M. Shieh, 1965: Diffusion from a continuous point source into the boundary layer downstream from a model hill. Technical Report, CER65EJP-CMS60, Colorado State University.

86. Queney, P., et al., 1960: The airflow over mountains. Technical Note No. 34, World Meteorological Organization, Geneva.

87. Reinking, R. F., and L. O. Grant, 1968: The advection of artificial ice nuclei to mountain clouds from ground-based generators. Proceedings of the First National Conference on Weather Modification, Albany, New York, 433-445.

88. Rhea, J. O., P. Willis and L. G. Davis, 1969: Park Range atmospheric water resources program. Final Report, Bureau of Recleamtion Cont. No. 14-06-D-5640, E. G. and G. Environmental Services Operation, Boulder, Colorado.

89. Sanders, C. I. and J. F. Thompson, Jr., 1967: An evaluation of the smoke-wire technique for measuring velocities in air. USAAVLABS Technical Report 67-29, Mississippi State University.

90. Sawyer, J. S., 1959: The introduction of the effects of topography into methods of numerical forecasting. Q. Jour. Meteor. S., Vol. 85, No. 363, 31-43.

91. Schaefer, V. J., 1958: The use of silver iodide as an air tracer. Jour. of Meteor., Vol. 15, No. 1, 121-122.

92. Schlichting, H., 1960: Boundary Layer Theory, McGraw-Hill Book Co.

93. Scorer, R. S., 1953: Theory of airflow over mountains: II - The flow over a ridge. Quart. Jour. Royal Meteor. Soc., 79, 70-83.

94. Scorer, R. S., 1955: Theory of airflow over mountains: IV - Separation of flow from the surface. Quart. Jour. Royal Meteor. Soc., Vol. 81, 340-350.

95. Serra, L., 1954: Diffusion dans l'atmosphere des noyaux d'iodure d'argent. Bull. Obs. Puy de Dome.

96. Simmons, L. F. G., 1949: A shielded hot-wire anemometer for low speeds. Jour. of Scientific Instruments, Vol. 26, 407-411.

97. Slade, D. H., 1965: Dispersion estimates from pollutant releases of a few seconds to 8 hours in duration. Technical note 2-ARL-1, Weather Bureau, Washington, D.C.

98. Smith, T. B., 1965: Diffusion study in complex mountainous terrain, Vol. I, MRI 65-FR-236, Meteorology Research Inc.

99. Smith, E. J., and K. J. Heffernan, 1954: Airborne measurements of the concentration of natural and artificial freezing nuclei. Quart. Jour. Royal Meteor. Soc., 80, 182-197.

100. Smith, E. J., and K. J. Heffernan, 1956: The decay of ice-nucleating properties of silver iodide released from a mountain top. Quart. Jour. Royal Meteor. Soc., 82, 301-309.

101. Smith, T. B., and E. K. Kauper, 1963: Meteorological study of North American Aviation - Nevada facility, Vol. I and II, MRI 63 FR-88, Meteorology Research Inc.

102. Smith, T. B., and M. A. Wolf, 1963: Vertical diffusion from an elevated line source over a variety of terrains. Part A, Final Report, MRI63 FR-71, Meteorology Research Inc.

103. Sutton, O. G., 1953: Micrometeorology. McGraw-Hill, New York.

104. Thyer, N. H., 1966: Theoretical explanation of mountain and valley winds by a numerical method. Archiv für Meteorologie - Geophysik and Bioklimatologie. Ser. A, 15 (3/4), 318--38.

105. Turner, D. B., 1967: Workbook of atmospheric dispersion estimates. Public Health Service Publication No. 999-AP-26, U.S. Dept. of Health, Education, and Welfare, Cincinnati, Ohio.

106. U.S. Atomic Energy Commission, 1968: Meteorology and Atomic Energy. USAEC Division of Technical Information, Oak Ridge, Tennessee.

107. U.S. Weather Bureau, 1955: Meteorology and Atomic Energy, USAEC Report AECU-3066.

108. Willis, P. T., 1966: A series of diffusion tests in an orographic environment. E. Bollay Associates Inc., Boulder, Colorado.

109. Willis, P. T., 1968: Diffusion in an orographic environment. Proceedings of the Third Sky Water Conference on the Production and Delivery of and Nucleating Materials, 193-215.

110. Wiskind, H. K., 1962: A uniform gradient turbulent transport experiment. Jour. of Geophysical Research, Vol. 67, No. 8, 3033-3048.

111. Wooldridge, G., 1970: Personal communication.

APPENDICES

APPENDIX A

TOPOGRAPHIC MODEL AND EXPERIMENTAL EQUIPMENT

APPENDIX A

TOPOGRAPHIC MODEL AND EXPERIMENTAL EQUIPMENT

Description of Topographic Area

The area studied by means of the laboratory model is located along the Continental Divide of central Colorado near Climax, Colorado. A weather modification project site of Colorado State University is situated on Chalk Mountain.

The primary terrain features consist of several mountain ranges oriented generally in a north-south direction. Approximately 4 miles to the east of Chalk Mountain is the Tenmile-Mosquito Range which varies in elevation from 12,500 to over 14,000 ft msl. Three miles to the west of Chalk Mountain, Chicago Ridge extends to 12,800 ft and has a north-south dimension of only 8 miles.

Twelve miles west of Chicago Ridge the Sawatch Range, with peaks reaching over 14,000 ft, extends south and north and includes the combination of Mt. Elbert and Mt. Massive. Chalk Mountain is on the southern end of the Gore Range located between Chicago Ridge and Tenmile Range, and has a mean maximum elevation of 12,000 ft msl. Timberline is approximately 11,500 ft and extensive areas of the total region are covered by coniferous forests.

Three major valleys radiate out from the Chalk Mountain area; Eagle River, Arkansas River, and Tenmile Creek. The Eagle River Valley oriented in a northwesterly direction is the major area of interest in this study. Figure 64 shows the major topographic features of the area of study.

Topographic Model

This model simulates the prototype area of the Eagle River Valley and topography surrounding Chalk Mountain. The horizontal and vertical scale of the model is 1:9,600 which was determined by the width of the wind tunnel and the thickness of building material. The construction material was expanded polystyrene beadboard of 1/4 inch and 1/2 inch thickness.

The topographic features of the model were obtained from U.S. Geological Survey maps at a scale of 1:24,000. These maps were enlarged to the correct scale and copied with the aid of slide projection equipment. Only slight modifications of some terrain features were necessary due to fitting together of the maps.

The dimensions of the overall model is approximately 25 ft long and 5 ft 11 inches wide which includes an upstream addition of a ridge line simulating Red and White Mountain. The model is divided into nine major sub-sections which can be fitted together when in the wind tunnel. Roma plasticene was used to fill in the joints between model sections.

The final stages of model construction consisted of sanding and smoothing the model topographic contours and applying several coats of velvet latex paint for protecting and hardening the surface of the model. Forest areas were delineated by forest green latex paint.

An attempt was made to model roughness features such as forests and timberline areas. After a futile search for something more realistic it was decided to model the roughness features by use of fine gravel. A

grain size of 1.168 mm and less was utilized for valley and timberline areas, while a grain size of approximately 1.68 mm was used for simulating the general roughness characteristics of 50 to 100 ft prototype alpine fir and Engelmann spruce.

The model simulates the northwest wind direction (~320°) (Fig. 64). The lowest and reference elevation is 7,800 ft msl (2379 m) which is represented by the plywood base on which the model features are glued too. The maximum elevation is Mt. Lincoln at 14,284 ft msl which represents 8 inches of height for the model.

The principal features of the model are Red and White Mountain, Eagle River Valley, Chicago Ridge and Chalk Mountain, Arkansas River Valley, Continental Divide and the Mosquito Mountain range. The model covers approximately 40 mi. in the northwest-southeast direction and 10 mi. in the northeast-southwest direction.

Figure 65 shows the topographic model during construction and during an experimental period in the wind tunnel.

Wind Tunnel

All the experimental work was accomplished in the Colorado State University low-speed recirculation wind tunnel (Fig. 66). Table 11 details the performance characteristics of this particular tunnel.

The tunnel is equipped with a remotely controlled positioning carriage whose actuators permit placement of test probes within 30 cm of the side walls. Components of the positioning system are two 28 volt D.C. gearhead motors, a precision, low noise, integrated circuit power supply regulator for horizontal and vertical readout and two remote control boxes consisting of two power transistors with manual

speed control potentiometers. Calibration of the vertical and horizontal distances of the positioning carriage was usually accomplished with the assistance of a Moseley Type 135 x-y plotter and HP digital voltmeter.

A slight modification was made to the tunnel in order to utilize radioactive krypton as a passive tracer. An exhaust fan was mounted on the top of the west section of the tunnel where conduit sections extended to an outside window. This arrangement provided the necessary assurance for keeping radioactive background counts in the wind tunnel at very safe working levels during experimental periods.

Instrumentation and Auxilary Equipment

The following is a list of the various transducers and equipment which were used for the wind tunnel measurements. Specifications of the commercial equipment can be found in the various operating manuals. The equipment items are listed according to airflow model and measurement.

A. Neutral airflow model

1) Surface wind direction measurements

Pivoting directional vane - The directional vane was constructed of fine glass tubing approximately 2 cm in length. A piece of nylon thread (1.5 cm) was tied and cemented around the center of the glass tubing. A size 8 sewing needle was inserted into the glass tubing and mounted vertically on the model. Although designed principally for high speed flows the directional vane can detect airflow directional changes for mean winds of about 2 m/s. The vanes are also sensitive to turbulent fluctuations. With proper lighting and camera setting the directional vanes show clearly in motion pictures and slides.

2) Mean velocities and static pressure measurements

Standard pitot-static tubes.

Electronic differential pressure meter (Transonic Equibar Type 120).

X-Y Plotter (Moseley Type 135).

Two fine-mesh screens arrangements approximately 5 ft 10 inches wide. The first, consisting of two screens 5 and 10 cm in height, and the second, consisting of three screens 20 cm in height.

Vortex generator*

Vortex generator consisted of 16 delta wings with each generator a 30 cm semi-span of delta wing with a 45 degree sweep angle. The generators protruded vertically from the floor and were arranged at alternate incidence angles of 10 degrees to the oncoming flow. Mean spacing of the downwind edges was 5 cm.

3) Turbulence measurements

Cross-wire probe. Two platinum-rhodium wires of diameter 7.62×10^{-4} cm.

DISA two channel constant-temperature hot-wire anemometer with rms and auxiliary units.

Sum and difference circuit.

Sum and difference switch box.

Oscilloscope Type 561A.

H.P. Digital voltmeter.

---

*Vortex generator was used only for the preliminary experiments on the development of a turbulent boundary layers.

Standard pitot-static tubes.

Electronic differential pressure meter (Transonic Equibar Type 120).

4) Concentration measurements

Gas tracer - Krypton-85

Source probe (Fig. 69).

Sampling probe (Fig. 69).

Krypton-85 source and detection system (Fig. 68).

B. Barostromatic airflow model

1) Mean temperature measurements

Copper-constantan thermocouple.

Thermocouple cold junction compensator (Omega-CJ). This instrument provides the physical and electrical equivalent of an ice bath reference thermocouple at $0^{o}C$ or $32^{o}F$.

X-Y Plotter (Moseley Type 135).

Standard thermometer.

Ice bath for calibration of thermocouple.

2) Carbon dioxide measurements

Thermal conductivity gas analyzer (Appendix C).

Sampling probe (Fig. 69).

Flasks of dessicant (Magnesium perchorlate).

Multiple sampling valves.

H.P. Digital voltmeter.

3) Mean velocity measurements

Smoke-wire system (Appendix C).

4) Concentration measurements

Radioactive krypton source and detection system (Fig. 68).

APPENDIX B

EXPERIMENTAL PROCEDURES FOR NEUTRAL AIRFLOW MODEL

APPENDIX B

EXPERIMENTAL PROCEDURES FOR NEUTRAL AIRFLOW MODEL

Wind Tunnel Arrangement

The wind tunnel arrangement for the neutral flow case is shown in Fig. 67. Two sets of screens were placed 6 to 8 ft (~207 cm) from the entrance of the tunnel and a few centimeters from the nearest leading edge of the Red and White Mountain ridge which was oriented across the tunnel at approximately 50 deg. No further obstructions or roughness was used except for the topographic model.

Mean Velocity and Static Pressure Measurements

A. Mean longitudinal velocity component

The most common device for measuring velocities in a wind tunnel is the pitot-static tube. A "standard" pitot-static tube contains orifices for reading total head and the static pressure. If the pressures from the two orifices are connected across a manometer or pressure meter, the velocity may be calculated from the pressure differential. The pressure differential and velocity are related by the expression

$$\Delta P = K \tfrac{1}{2} \rho U^2 \qquad \text{B.1}$$

where K is a calibration factor which must be determined experimentally. For incompressible and high Reynolds number flow K has a mean value of 1.000.

To obtain the mean longitudinal velocity component, the following procedure was used:

1) Two pitot-static tubes were used in the wind tunnel - one for free stream and the other for the local velocity over the model. The free stream velocity readings were used to calibrate the Y scale of an X-Y plotter.

2) With the tunnel set at the freestream speed of 15 m/s the local pitot-static tube was traversed vertically so that plots of pressure meter Δp versus height could be obtained by an X-Y plotter. Thirty-one locations on the model were sampled.

3) A mean Δp versus height curve for each location was found by hand analysis. Then an Auto-trol X-Y digitizer was used to digitize the data on punch cards. Computer program Hugger (Appendix G) was used to calculate the velocity by using the expression

$$\overline{U}(m/s) = 0.719 \sqrt{\frac{\Delta p}{\rho}} \qquad B.2$$

where the density of air was determined from tables using barometric pressure and temperature.

A number of inherent errors are present in using a pitot-static tube, these are due to velocity gradients, inclination of pitot-static tube to the airstream, nearness to model, vibration and turbulence. Most errors are within 5% except when the yaw angle becomes greater than 16°. In our experiments the local pitot-tube was placed facing the local near-surface wind direction. In nearly all locations except one or two in separation areas, the angle of yaw of the approaching airflow was less than 16°.

One disadvantage of using the pitot-static tube was that this device only gives the longitudinal component of the velocity vector. However, no attempt was made to measure lateral and vertical components for this flow condition.

B. Near-surface streamlines

A hundred or more pivoting directional vanes were mounted on the topographic model to depict the near surface wind directions. These were mounted so the stiff threads cleared the model surface by 1/8 to 1/4 inches. This height corresponds to approximately 100 to 200 ft in actual field sites.

Observation of the directional vanes was accomplished on top of the wind tunnel looking at the top view of the model. Visual and camera observations provided sufficient data in order to construct not only a mean streamline pattern for the overall model but also qualitative information on the spatial distribution of turbulence regions.

C. Static pressure

The longitudinal static-pressure gradient was measured in the free stream 107 cm above the tunnel floor. These readings were obtained by reading the difference between the local static pressure from a pitot-static tube placed upstream from the model and that from a pitot-static tube moved progressively downstream over the topographic model. Readings were taken from a pressure meter connected by plastic tubings to the static orifices of the pitot-static tubes.

Turbulence Measurements

In order to interpret the experimental data obtained from hot-wire measurements it is necessary to consider some of the principles and concepts involved in hot-wire anemometry. Detailed discussions on the principles and techniques of hot-wire anemometry can be found in textbooks. Only those concepts that are essential to this problem are presented here.

A. Turbulent intensities

The longitudinal, vertical, and lateral components of the velocity fluctuations are measured by operating two well-matched wires mounted on a single probe in the shape of x as in conventional hot-wire anemometry (Fig. 67). In our experiments, the yawed wire was arranged so that it formed angles of ±45° with respect to the direction of the mean velocity. Assuming that the two wires have the same sensitivities, then the basic response equation of the yawed wire (Ref. 3) can be written for $\theta = +45$ as

$$e_1' = S_u(u' + cw')$$

and for $\theta = -45°$ as

$$e_2' = S_u(u' - cw') \quad .$$

If we sum the two fluctuation signals

$$e_1' + e_2' = S_u\, 2\, u'$$

and find the r.m.s. of the sum we find

$$\frac{\sqrt{\overline{(e_1' + e_2')^2}}}{2\, S_u} = \sqrt{\overline{u'^2}} \quad . \qquad \text{B.3}$$

Once S_u has been determined and $\overline{(e_1' + e_2')^2}$ measured, then longitudinal turbulent intensity can be found.

Similarly, when the difference between fluctuation signals are taken, the vertical turbulent intensity can be found, i.e.,; $e_1' - e_2' = S_u\, 2cw'$ and

$$\frac{\sqrt{\overline{(e_1' - e_2')^2}}}{S_u\, 2c} = \sqrt{\overline{w'^2}} \qquad \text{B.4}$$

for $\theta = 45°$ $\quad c = 0.923$, (Ref 3, Appendix A).

For the lateral turbulent intensity $\sqrt{\overline{v'^2}}$, the cross-wire is operated in the x,y plane (rotated 90°) then,

$$e_1' = S_u\ (u' + cv')$$

$$e_2' = S_u(u' - cv')$$

and taking the difference between fluctuation signals $e_1' - e_2' = S_u\ 2cv'$ or

$$\frac{\sqrt{\overline{(e_1' - e_2')^2}}}{S_u\ 2c} = \sqrt{\overline{v'^2}} \quad . \qquad \text{B.5}$$

B. Shear stress

Only the turbulent shear-stress $\overline{u'w'}$ was measured in the turbulence experiments. If we look at the response equation of the yawed wire again under the same assumptions then,

$$e'_{+45°} = S_u[u' + cw']$$

$$e'_{-45°} = S_u[u' - cw']$$

then if we write,

$$\overline{e'^2_{+45}} = (S_u)^2\ [\overline{u'^2} + 2c\ \overline{u'w'} + c^2\ \overline{w'^2}]$$

$$\overline{e'^2_{-45}} = (S_u)^2\ [\overline{u'^2} - 2c\ \overline{u'w'} + c^2\ \overline{w'^2}]$$

the following expression can be found,

$$\overline{u'w'} = \frac{\overline{e'^2_{+45}} - \overline{e'^2_{-45}}}{S_u^2\ 4c} \qquad \text{B.6}$$

Measurements of S_u , $\overline{e'^2_{+45}}$ and $\overline{e'^2_{-45}}$ allows calculation of $\overline{u'w'}$.

C. Calibration and procedure

Figure 67 shows the wind tunnel arrangement and equipment for the turbulence measurements.

The procedure for calibrating the hot wires was to mount them adjacent to the free stream pitot-static tube near the test-section entrance and to take the velocity indicated by the pitot-static tube as being the true velocity. The D.C. voltage output from the two wires were recorded from a digital voltmeter.

For constant temperature operation where the wire resistance and air temperature remains constant, the sensitivity of the wires S_u are normally calculated from King's Law,

$$E^2 = A + B\bar{U}^m \qquad B.7$$

where m depends on the Reynolds number and is close to 0.5 over a velocity range 2 m/s to 15 m/s. The factors A and B are determined experimentally. A check on the E vs $\bar{U}$ calibration curves for each experiment showed that Kings Law could not be applied for finding S_u. An alternative course was to plot E vs $\bar{U}$ for each wire and determine S_u. Then plot S_u vs $\bar{U}$, therefore, S_u could be found for any desired velocity.

Unfortunately, the sensitivity of the two wires were not perfectly matched as required by theory, but were within 5% of each other. In this case an average S_u was determined for the two wires. For two of the experiments calibration of the wires were made before and after each experiment.

Three separate experiments were required to obtain the three turbulent intensities and shear stress. To obtain these quantities the following procedure was used:

1) Check out hot-wire anemometer circuity and place wires in operating condition.

2) Calibrate the cross-wires.

3) Place the cross-wire probe on traversing mechanism of carriage and locate over the model.

4) Start tunnel and establish proper free stream velocity (15 m/s).

5) Commence readings of r.m.s. meter for sum and difference settings of sum and difference circuit. For shear-stress measurements the sum and difference circuit was not utilized, therefore, the readings were taken directly from both r.m.s. meters.

6) Take series of measurements above the model so as to obtain a profile. Move to a different location and repeat measurements.

7) Recalibrate hot-wires after finishing measurements.

In the case of the shear-stress measurements, data were taken for a normal position of the wires and when the wires were rotated 180 degrees.

D. Errors

A proper analysis of the probable errors in the turbulence measurements has not been possible. Many random errors are possible, such as misalignment of the two wires so the same turbulence is not sensed properly, imperfect calibration, and spurious vibration effects. It was not possible to eliminate all the vibration at the selected freestream velocity, so this may have contributed to the imperfect calibration. On the basis of the errors in calibration and current literature on hot-wire anemometry, the turbulence data was probably within 10 to 20% of the true values.

Concentration Measurements

Concentration measurements over the topographic model were obtained by releasing radioactive krypton-85 from sources located in the model and using Geiger-Mueller tubes to determine the relative amount of krypton in samples of the gas-air mixture. The method was developed in detail by Chaudhry (Ref. 20) but only information relevant to this study will be discussed.

Krypton-85 is a radioactive noble gas with a half life of 10.6 years. The gas decays by emission of beta particles with small amounts of gamma rays. The gas has many advantages over the other tracers used in wind-tunnel dispersion studies. It is diluted with air about a million times before use, and as such, has properties very similar to those of air. Its detection procedure is fairly simple and direct.

Figure 68 shows the wind tunnel arrangement for obtaining radioactive concentration measurements. The radioactive method consists of a) release, b) sampling, and c) detection system.

A. Release system

The tracer release system or source is shown schematically in Fig. 68 and Fig. 69. A cylinder of premixed krypton-85 at a concentration of 1.17μ- curie/cc was located outside of the tunnel and provided the tracer gas. The flow rate of krypton-85 mixture was controlled by a pressure regulator at the bottle outlet and monitored by one or two flow meters, depending on the number of sources.

Source probes shown in Fig. 69 were placed on the surface of the model by drilling holes through the model and tunnel floor. Mayon tubing connected the source probes to the cylinder containing krypton-85. The flow rate for the source was approximately 2 m/s (Table 12) and was low enough so as not to excessively disturb the oncoming flow near the source.

B. Sampling and detection system

The samples of gas were drawn from the wind tunnel through a rake of eight sampling tubes 0.2 cm in diameter mounted on a carriage as shown in Figure 68. The eight samples of gas were drawn from the wind tunnel through Mayon tubings at a rate of 3.72 m/s (Table 12) which was low enough to prevent sucking in gas from the sides except in the lowest few centimeters above the model. The samples were then passed through the eight TGC-308 tracerlab Geiger-Mueller sidewall cylindrical counters. A vacuum pump was used to draw the samples and exhaust them back into the wind tunnel. Each sampling line had an electric valve inserted into it in order to avoid intermixing of the samples in different lines. These valves could be opened or closed at the same time by a common switch.

Output from each G.M. tube could be connected to the same scaler and high voltage. Although the count for each G.M. tube had to be recorded one by one, this sampling scheme helped conserve krypton-85 because eight samples were taken for one release of the gas.

C. Experimental procedure

For the neutral case two experiments were performed. One simulating a Minturn source and the other a Minturn and Redcliff source simultaneously. Over 80 different locations on the model were sampled for these two experiments.

A typical experiment for determining concentration data was conducted according to the following procedure:

1) The sampling probe was located at a chosen position on the model by the traversing mechanism of the wind tunnel carriage.

2) The wind tunnel was started and the desired free stream velocity (15 m/s) was established for the experiment.

3) The common valve was opened and the electric valves were switched on to open. The pump was then started and was left running for 1½ minutes to flush the G.M. tubes. The sampling flow rate was set for all the G.M. tubes.

4) The necessary release rate through the source probe was then established by source flowmeters.

5) Samples were drawn for 1½ minutes and then the electric valves were closed and the common valve was also closed. This enclosed krypton-85 gas samples in the jackets. The flow of gas was then stopped.

6) The samples enclosed around the G.M. tube were then counted, one by one, by the scaler from 2 to 4 minutes, depending on the sampling probe distance from the source. The increased counting time improved the accuracy for very dilute samples.

7) The above procedure was then repeated for a new position of the sampling probe.

Since the wind tunnel recirculates a major portion of its air volume, repeated releases of the krypton-85 gas could cause large accumulations to occur within the tunnel. This creates a higher background, lowering the accuracy of measurement and could be hazardous in terms of exposure. As described in Appendix A an exhaust fan was utilized for keeping the background at low levels.

Background readings of concentration were obtained upwind from the sources while the tracer gas was being released through the source probes. This procedure gave higher and more representative background readings than when the readings were obtained after a particular run without the tracer gas being released.

D. Analysis of data

The procedure for analyzing the concentration data was as follows:

1) Counts of the pulses generated in the G.M. tubes and displayed by the ultrascaler counter were recorded for all eight probes at the various locations.

2) These counts were transformed into concentration values by the following steps:

$$\text{Cpm} - \text{Background (Cpm)} = \text{Cpm}^*$$

$$\text{Cpm}^* \times \text{counting yield } (\mu\mu \text{ Curie/cc/Cpm}) = \overline{C}(\mu\mu \text{ Curie/cc})$$

The counting yield varied according to the G.M. tube as shown in Table 12.

3) For counts over 1,000 a dead time correction* had to be applied to the readings, and in this case the correction is,

$$\text{Cpm} - \text{Background} = \text{Cpm}^*$$

$$\frac{\text{Cpm}^*}{1 - 1.77 \times 10^{-6} \times \text{Cpm}^*} = \text{Cpm}^* \qquad \text{B.8}$$

$$\text{Cpm}^* \times \text{Counting yield} = \overline{C}(\mu\mu \text{ Curie/cc}) \ .$$

4) Average concentration values were determined for the known probe heights and then plotted with respect to height. Concentration curves were drawn for each location and then values of the average concentration were interpolated for every 100 meters of prototype scale.

---

* The time taken for the positive space charge to move sufficiently far from the anode for further pulses to occur (Ref. 31).

5) The concentration parameter $\overline{C}\,\overline{U}/Q$ was then computed by desk computer for every 100 meters at all locations. A sample computation is shown below for the Minturn and Redcliff source,

$$q_m = 3550 \text{ cc/min} \qquad q_R = 3550 \text{ cc/min}$$

$$q_m + q_R = 7100 \text{ cc/min} = 118.33 \text{ cc/sec}$$

$$Q_{total} = 1.17 \ \mu \text{ curie/cc} \times 118.33 \text{ cc/sec}$$

$$= 138.45 \ \mu \text{ curie/sec.}$$

Let $\overline{U} = 8$ m/sec = 800 cm/sec and $\overline{C} = 80$ $\mu\mu$ curie/cm^3 then

$$\frac{\overline{C}\,\overline{U}}{Q} = \frac{80 \times 800}{138.45} = \frac{462 \times 10^{-2}}{m^2} \qquad \text{B.9}$$

6) So far the values of the concentration parameter apply to the model and it is desirable to express these values in terms of the field. At the present time there is no set procedure for accomplishing this transformation. The simplest and most straightforward procedure is to make this transformation using the scaling factor of the model. Since

$$1 \text{ meter}]_{model} \equiv 9600 \text{ meters}]_{field}$$

one could write

$$\frac{\overline{C}\,\overline{U}}{Q}\Big]_{model} \quad \frac{1}{(9600)^2} \equiv \frac{\overline{C}\,\overline{U}}{Q}\Big]_{field} \qquad \text{B.10}$$

or in terms of the above example,

$$\frac{462 \times 10^{-2}}{m^2}\Big]_{model} \equiv \frac{\overline{C}\,\overline{U}}{Q} \equiv \frac{50 \times 10^{-9}}{m^2}\Big]_{field} . \qquad \text{B.11}$$

This simple scaling of the concentration parameter from model to field appears to give reasonable results as indicated in Chapter V.

7) Alternatively, the concentration data from model and field could be nondimensionalized by using equation 3.44. Both procedures were used in this work.

E. Errors in concentration measurements

Where data is obtained with a scaler counter, the apparent activity of a radioactive source is found by subtracting the background rate from the observed sample-plus-background rate. The background rate is measured separately and has an uncertainty of its own due to random radioactive sources.

If the background is present, the standard deviation in the net counting rate σ_{R_s} for a sample is

$$\sigma_{R_s} = \left(\frac{R_{s+b}}{t_s} + \frac{R_b}{t_b} \right)^{\frac{1}{2}} \qquad \text{B.12}$$

where R_{s+b} is the observed sample-plus-background rate, R_b is the background rate, t_s and t_b are the measurement time for the sample and background, respectively. The standard deviation in the sample rate depends, then, upon both the time for sample measurement and that for background-rate measurement. When R_{s+b} is large in comparison with R_b, a long background measurement is not needed to make the error contribution from the background rate negligible. On the other hand, when R_{s+b} is comparable to R_b, both t_s and t_b must be very long for small values of σR_s. In the present experiments, an effort was made to keep the probable errors in concentration measurements within 10%. For this reason the simple counting time and background counting time were manipulated with this end in view. More detailed information on errors in radioactivity measurements can be found in Chaudhry (Ref. 20) and Overman and Clark (Ref. 79).

APPENDIX C

EXPERIMENTAL PROCEDURES FOR BAROSTROMATIC AIRFLOW MODEL

APPENDIX C

EXPERIMENTAL PROCEDURES FOR BAROSTROMATIC AIRFLOW MODEL

Wind Tunnel Arrangement

The experimental arrangement in the wind tunnel for the barostromatic airflow model is presented in Figure 70. To produce a stable temperature distribution with height in the wind tunnel 600 lbs of dry ice (-79°C) was placed on the floor of the upstream section of the tunnel. A board 70 x 47 in. blocked the upstream section, forcing the cold air to flow across the topographic model. The resultant airflow due to the dry ice reversed direction with height which was not favorable for simulation of the velocity field.

In order to eliminate the reversed flow of air above the cold air, the wind tunnel was set at a very low-speed setting (~25 cm/sec) in order to move enough warm air against the reversed airflow to cancel its effect. As it turned out, the wind tunnel setting was very critical and only one choice was possible in order to achieve the desired results. Any setting higher than the critical one would produce chaotic airflow and large gravity wave oscillations. However, the critical setting of the tunnel (~25 cm/sec) provided a relatively steady airflow over the cold air which improved the velocity field over the model.

Mean Velocity Measurements

One of the difficult measurement problems was to obtain readings of the low velocities (10-20 cm/sec) in a stable temperature field required to produce such velocity fields. For low velocities the pitot-static tube is unreliable, but the hot-wire anemometer is more reliable once it is calibrated with respect to temperature.

Lin and Binder (Ref. 61) in a wind tunnel study of mountain lee-waves employed a constant temperature hot-wire anemometer to measure the longitudinal velocity component. Accuracies between 3 and 7% were reported. The principal disadvantages of using a hot-wire anemometer are the tedious calibration procedure, possible calibration drift with time, and the necessity of using a traversing mechanism for point by point measurements. A shielded hot-wire anemometer for low speeds which may improve on the regular hot-wire system has been reported by Simmons (Ref. 96). Temperature-compensated probes are also available for low-speed measurements (Ref. 29). A fairly accurate system for measuring low velocities without tedious calibration procedures and point by point measurements appeared in a report by Sanders (Ref. 89).

Sanders and others used a "smoke-wire" method for determining velocity profiles in laminar and turbulent boundary layers with neutral stability. In the "smoke-wire" method, oil is evaporated from a very thin, high-resistance wire by the passage of a large electric current through the wire from a capacitor discharge. This forms a thin line of smoke at the wire. The line of smoke is carried downstream with the local velocity of the air at each point along the line and is thus deformed into the shape of the velocity profile. At the discharge of the capacitor a time-delay circuit is actuated which, after a predetermined time delay, simultaneously fires a strobe light and camera to illuminate and photograph the smoke line. The displacement of the smoke can be measured from the film and by using the known time delay, velocity profiles can be obtained. Velocity measurements obtained by this system were comparable with measurements taken by conventional means.

The smoke-wire system appeared to be a practical and accurate method for determining velocity profiles over the topographic model so a smoke-wire probe and system was constructed for this purpose. Another advantage of this system was the possibility of obtaining two components of the velocity field by utilizing two cameras and analyzing paired pictures by use of a stereocomparator.

The details of the Colorado State University smoke-wire system and how the longitudinal, lateral, and resultant velocity field was estimated by this system is presented next.

A. Colorado State University Smoke-Wire System

The present smoke-wire system consists of the following equipment:

Item	Source
Cameras	One Exakta VX-2A or two Retina IIIC
Trigger circuit	Colorado State University
Strobe delay	General radio 1531P2
Strobe	General radio 1531AB
Electronic counter	Hewlett-Packard 5233L
Smoke-wire probe	Colorado State University

Figure 71 shows details of the smoke-wire probe. A model train smoke fluid (Life-Like or Lionel) is used to coat the wire. This is accomplished by forcing the fluid from the reservoir to the oiler spout by applying pressure to a plastic bulb outside of the wind tunnel. Gravity then pulls an oil drop from the oiler spout over the full length of the wire. Uniform coatings of oil can usually be achieved through practice.

Figure 72 diagrams the control circuit for the smoke-wire system. The trigger and control circuits consist of two power supplies, one high voltage supply adjustable from zero volts to about 750 volts DC and a low voltage supply that is zener diode regulated at 18 volts DC, and two stages of transistor switching and a power relay.

A pair of camera flash contacts are normally used to start the circuit in operation. A test switch on the front panel can also be used when testing or making trial visual observations.

The high voltage power supply charges the two micro-farad capacitor and keeps a charge on it until the start switch or camera contacts close. The closing of the contacts turns on the first transistor which energizes the relay coil. When the relay is energized the high voltage supply is disconnected from the capacitor and the capacitor is connected to the smoke wire. This discharges the capacitor through the smoke-wire causing it to heat up for a very short time. The high temperature vaporizes the oil on the wire causing a line of smoke.

A voltage pulse is taken from the capacitor as it begins to discharge through the smoke-wire and this pulse is used to start the electronic counter. The instant the first transistor turns on to energize the relay coil its current also turns on the second transistor sending a pulse to the delay circuit of the strobe light. At the end of the preset delay time (100-300 m sec), the delay circuit pulses the strobe circuit and fires the lamp. The output pulse from the strobe, which is a portion of the lamp firing pulse, is reduced in amplitude by about a factor of 10 and used to stop the electronic counter. The counter displays the elapsed time between when the smoke-wire is fired and the strobe light flashes. This completes a sequence.

B. Experimental Procedure

The experimental arrangement in the wind tunnel for obtaining velocity profiles by the smoke-wire system is shown in Figs. 73 and 74. Two trial experimental periods were accomplished using a single Exakta VX-2A.

In the third experimental period a pair of Retina IIIC cameras with a 50 mm focal length loaded with Tri-X 135 film and set at f/2 was used for obtaining the photographs. The two cameras were located 15 inches apart (center to center) on an aluminum bar mounted on a tripod. A Polaroid 160 camera with type 47 film was used to check the velocity profiles and lighting before pictures were taken with the paired cameras.

The length of the wire on the probe was 31.7 cm (12.5 in.). This was the maximum length that could be used with the present voltage arrangement.

A grid system (10 x 15 in.) was placed on the far wall of the wind tunnel and was lighted when the camera shutters were open, in order to have the smoke line superimposed on a grid system. This procedure aided in the analysis of pictures.

The smoke-wire probe was located at five different positions on the topographic model. Positioning of the paired cameras and the window supports prevented locating the smoke wire in more than five locations.

Several requirements for setting up the camera equipment were necessary to insure the accuracy of the data; these were:

1. the two cameras must be level with their axes perpendicular to the direction of the flow in the tunnel;

2. the cameras must be set at the same focal length and aperture;

3. the smoke-wire on the topographic model must be vertical;

4. separation distance between cameras and distances from cameras to wire and opposite wall of tunnel are required;

5. grid line on the opposite wall must be visible and easy to identify.

C. Data Analysis

Thirty-two sets of pictures were obtained for the five locations of the smoke-wire probe. The best twenty sets of pictures from the thirty-two were chosen for extracting the required information for computing the two components of velocity and resultant velocity with respect to height. An example of two paired pictures showing the displacement of the smoke plume is shown in Fig. 75.

In order to compute the longitudinal and lateral velocities it is necessary to determine the displacement of the smoke plume from the wire during a measured time interval. This requires determining three unknowns f, the focal length of the cameras, Δy, lateral distance between wire and plume and Δx, the longitudinal distance between wire and plume. Once Δy and Δx are determined for selected increments of height then it is a simple procedure of dividing by the proper time increment Δt for obtaining the velocities with respect to height.

The geometric arrangement necessary to find the appropriate relationships for f, Δy, and Δx is shown in Fig. 76. From the relation between two symmetrical triangles we can write,

$$\frac{B}{H} = \frac{x_1 + x_1'}{f}$$

$$\frac{B}{D} = \frac{x_3 + x_3'}{f} \qquad \text{C.1}$$

or

$$B\left(\frac{1}{H} - \frac{1}{D}\right) = \frac{1}{f}\left[(x_1+x_1') - (x_3+x_3')\right] \quad . \qquad \text{C.2}$$

Rearranging equation C.2, we have

$$f = \frac{px_3}{B\left(\frac{1}{H} - \frac{1}{D}\right)} \qquad \text{C.3}$$

where $px_3 = [(x_1+x_1') - (x_3+x_3')]$ is the parallax of the wire and opposite wall. Since B , H , D are measured quantities and px_3 can be measured from pictures, the focal length can be calculated.

To find Δy we can write,

$$\frac{B}{H} = \frac{x_1 + x_1'}{f} \quad ; \quad \frac{B}{H-\Delta y} = \frac{x_2 + x_2'}{f} \qquad C.4$$

or

$$B\left[\frac{1}{H} - \frac{1}{H- y}\right] = \frac{1}{f}\left[(x_1+x_1') - (x_2+x_2')\right] \qquad C.5$$

Rearranging equation C.5, we have

$$\Delta y = \frac{-1}{\frac{1}{H} - \frac{px_2}{Bf}} + H \qquad C.6$$

where $px_2 = [(x_1+x_1') - (x_2+x_2')]$ is the parallax of the wire and the smoke plume. Since B , H , f are known and px_2 is measured from pictures, Δy can be determined.

The relationship for Δx can be found from Fig. 76 where,

$$\frac{x_2-x_1}{f} = \frac{\Delta x + \frac{x_2 \cdot \Delta y}{f}}{H} \qquad C.7$$

and with rearrangement

$$\Delta x = - x_1 \cdot \frac{H}{f} + x_2 \cdot \frac{H-\Delta y}{f} \qquad C.8$$

In equation C.8 H is known, f and Δy are determined from equations C.3 and C.6 while x_1 and x_2 are measured quantities from the pictures.

The picture measurements were all derived by the use of a Wild STK 2702 stereocomparator and the desired speeds and velocity were calculated and plotted with respect to height from the measured quantities by a CDC 6400 computer. An example of the computer output is shown in Table 13.

The next step in the analysis was to determine average values of lateral velocity component and resultant velocity for the five locations on the topographic model. This was done by tabulating the velocities at selected heights for each computer output available for a specific location and then finding the sum and average for each height.

The distribution of paired pictures with each location was not equal, hence the mean velocities for Pando, Chalk Mountain and Chicago Ridge (based on 4 to 6 pictures each) were more reliable than Bolts Lake and Battle Mountain (based on 2 to 3 pictures each). The unequal distribution of pictures per location was the result of poor pictures due in part to improper lighting and a persistent dense water-vapor cloud formed by the cooling effects of the solid carbon-dioxide near the upstream section of the model.

Two smoke-wire "unsteadiness factors" were determined in a manner similar to computing the root-mean-square of turbulent fluctuation. The mean longitudinal and lateral velocity profile was subtracted from each instantaneous profile, respectively to yield an instantaneous unsteadiness component in the flow direction. The magnitudes of these components were then averaged to obtain a root-mean-square value. These values were then divided by the mean horizontal speed to yield "unsteadiness factors" a quantity similar to turbulent intensities.

The "unsteadiness factors" were computed for four locations which had the best velocity profile data which were Battle Mountain, Pando (Camp Hale), Chicago Ridge and Chalk Mountain. The velocity data were better for the last three stations than the first.

D. Error Analysis

Errors in the velocity measurements with the present smoke-wire system may be due to three factors; 1) inertia and buoyancy of the smoke plume, 2) photographic procedure, and 3) accuracy of the picture measurements.

When the oil vaporizes from the heated wire it is assumed that the resultant oil plume achieves the ambient air movement simultaneously. Since uniform oil coatings were not always possible, thicker sections of the smoke plume would respond slower to the ambient air movement than thinner sections. Quantitative estimates of this error are not available.

Due to the high temperature of the wire and the cold environment, a slight upward displacement of the smoke plume was observed. This displacement was estimated at approximately 1 cm at times, but in most cases was negligible and was neglected in the measurements.

Extreme care was used in setting up the camera equipment at each position. Errors in the measurement of H and D were possible through the calibration of the wind tunnel carriage to which the smoke-wire was attached, and the direct measurement of the distance of the cameras from the wind tunnel windows. The thickness of the windows were known, but distortion of the windows and possible refraction effects of the windows were neglected.

The accuracy of the picture measurements depended principally on determining the focal length of the cameras. Calculations showed that the focal length was 50.8 ± 0.685 mm.

Measurements from two sets of pictures were repeated in order to check the consistency of the stereocomparator operator in obtaining

similar results. A check on the measurements showed differences less than 1%.

No other independent measurements were attempted in order to check the results from the smoke-wire probe. Although this may be a worthwhile endeavor, it was not the purpose of this dissertation to study the problem. On the basis of results taken with a single camera using the smoke-wire probe, measurements taken by hot wires under similar stability conditions (Ref. 61) and detailed error analysis of these photogrammetric measurements by Barnes and Tao (Ref. 6) showed that the errors were within 3 to 10%.

Mean Temperature Measurements

Temperature profiles over the model were obtained using a copper-constantan thermocouple mounted on the vertical and horizontal traversing carriage of the wind tunnel.

Since the thermocouple had a relatively slow response time (~10 sec), a reading was taken at a particular vertical position after the temperature had stabilized. After the reading was observed the thermocouple was repositioned and the procedure repeated. Plots of temperature versus height were obtained with an x-y plotter.

The zero reference for the thermocouple was provided by an Omega-CJ thermocouple cold junction compensator. Calibration of the thermocouple was accomplished using a thermometer, ice bath, and the ambient air.

Vertical temperature profiles were obtained for nine different locations on the topographic model. The accuracy of the temperature measurements may be better than ± 2°C based on the specifications of the Omega-CJ thermocouple cold junction compensator.

Carbon Dioxide and Air Density Measurements

The thermal stratification for the barostromatic airflow model was provided by solid carbon dioxide which by its very nature presents an unwanted constituent, CO_2 vapor. If the proportion of CO_2, which is denser than air, is large, then this may complicate the problem of density similarity between model and prototype. A quantitative measurement of the concentration of CO_2 in the tunnel was accomplished to clarify this problem.

The measurement of the concentration of CO_2 in the wind tunnel while using dry ice was performed with a thermal conductivity analyzer which was constructed at Fluid Dynamics and Diffusion Laboratory at Colorado State University. However, the sensing element was obtained from Gow-Mac Instrument Company. The procedure and data analysis for the carbon-dioxide measurements is discussed next.

A. Thermal Conductivity Analyzer

Thermal conductivity analyzer operates by comparing the difference in the rate of heat loss between sample and reference gases exposed to heated elements.

A thermal conductivity detector consists of heat-sensing elements, each situated in a separate cavity in a metallic block which serves as a heat sink. The heat-sensing elements are either thermistors or resistance wires. In the hot-wire cell, filaments are straight or helical bare wires which are stretched along the axis of a metal cavity. The wire is kept under tension by platinum-iridum springs essential because the length changes with temperature. Filaments are fabricated from some metal or alloy with a high temperature coefficient of resistance, such as platinum or tungsten.

Usually four thermal-conductivity cells, mounted in a cell block, are connected to form the arms of a wheatstone bridge. The electrical circuitry is shown in Fig. 77. Two filaments in opposite arms of the bridge are surrounded by the reference gas, which conducts away heat generated by the current. The temperature of the filaments will rise until the rate of heat flow away from the filament to the metal block matches the heat generated by the current in the hot-wire resistance element. Similarly, the other two filaments are surrounded by the sample gas. The temperature gradient depends upon the thermal conductivity of the gas surrounding the hot wire and the temperature of the wire. As the wire is cooled by the gas stream it assumes a definite resistance: the higher the thermal conductivity of the gas, the lower the resistance of the wire, and vice versa. The greater the difference in thermal conductivities of the reference and sample gas, the greater the unbalance of the Wheatstone bridge. The extent of the unbalance may be measured by a high-impedance recorder.

Details of the theory of thermal-conductivity cells are beyond the scope of this work, however, many detailed reports are available on the subject; such as, Lawson and Miller (Ref. 59).

B. Experimental Procedure

The experimental arrangement for obtaining carbon dioxide concentration measurements is shown in Fig. 78. Five hundred pounds of dry ice located upstream from the model as depicted in Fig. 70 provided the sample gas. The sampling probe (Fig. 69) used in the radioactive dispersion measurements was utilized to sample the gas at several positions in the vertical. A vacuum pump forced the sample gas and reference gas into the thermal conductivity analyzer at the rate of 50 ml/min.

Since only one sample of gas could be monitored at a time, it was necessary to have a valve system to regulate the sample gas from each probe. A drying agent, magnesium perchorlate, prevented water vapor from entering the thermal conductivity cell from the tunnel and the ambient air. The outside ambient air was used as the reference gas.

The unbalance of the bridge from the gas analyzer was recorded by a digital voltmeter. Several voltage readings were taken during a minute for each sample of gas to assure representativeness. Eventually an average voltage reading was obtained for each height where a sample of gas had been taken. Therefore, at this point only the unbalanced bridge voltages versus height were available.

C. Calibration of Thermal-Conductivity Gas Analyzer

The calibration procedure was as follows:

1) The gas analyzer was balanced by forcing ambient air through both sides of the TC cell by the vacuum pump.

2) A large plastic bottle was filled with water and the contents weighed on a scale.

3) An arbitrary amount of water was released and pure CO_2 was forced into the plastic bottle from a separate cylinder.

4) The vacuum pump was started on the gas analyzer and the CO_2 gas was sampled at the rate of 50 ml/min with the reference gas being the ambient air.

5) Unbalanced bridge voltage readings were obtained after waiting 2 to 3 minutes. A digital printer plotted out readings from a digital voltmeter for approximately a minute.

6) More water was released and air was allowed to enter the plastic bottle, diluting the CO_2. A weight measurement was recorded again and

then the vacuum pump was started and another reading was obtained from the voltmeter.

7) The procedure was then repeated until sufficient readings were obtained. The concentration of CO_2 was determined from the following equation

$$\text{Concentration (ppm)} = 10^6 \cdot \frac{\text{Weight of water displaced to admit } CO_2}{\text{Total withdrawal of water for both } CO_2 \text{ and air}}$$

8) A calibration curve of concentration of CO_2 versus voltage could be determined at this point. From this calibration the concentration of CO_2 with height in the tunnel was tabulated and used to calculate the density of the CO_2 and air mixture (see section E).

D. Accuracy of Thermal-Conductivity Method

The general method of thermal conductivity is accurate, simple, and fast. The principle of thermal-conductivity gas analysis has been used by physicists and analytical chemists for several years.

The accuracy and precision in thermal conductivity applications depend on five factors:

1) detector design and construction,

2) cell current regulation,

3) temperature regulation,

4) gas flow system and

5) readout equipment.

The detailed aspects of thermal-conductivity cells is too lengthy to include in this text. Lawson and Miller (Ref. 59) examines some of the problems of thermal conductivity theory.

In calibration and operation Boyle's law must be followed, i.e., both sample and reference gases should pass through the apparatus at

constant pressure and flow rates, as well as at constant temperatures. These conditions were generally satisfied in this laboratory experiment.

In general, the accuracy of the thermal-conductivity method is 1 to 3%. In this experiment a slight drift was noted in the unbalanced bridge voltages during operation and calibration and was large enough to effect the accuracy by an additional 4 to 5%.

E. Carbon Dioxide - Air Density

Table 14 shows the concentration of CO_2 with height for three locations over the topographic model as determined by thermal conductivity analyzer measurements. To find what effect the CO_2 concentration had on the density of the air-CO_2 mixture in the wind tunnel, the air and CO_2 densities were computed for the heights shown in Table 14 by the equation of state and the measured temperatures over the model (Fig. 20). The density of the CO_2-air mixture was then calculated for the selected heights at each location by the following equation,

$$CON \times \rho_{CO_2} + (1 - CON)\ (\rho_{AIR}) = \rho_{CO_2 + AIR}$$

where CON was the carbon dioxide concentration.

Concentration Measurements

The concentration measurements over the topographic model were obtained using the radioactive krypton technique as described in Appendix B. However, there were important differences due to thermal stratification in the wind tunnel. The experimental arrangement in the wind tunnel is shown in Fig. 70.

A. Release System

The tracer release system or source was the same as in the neutral case. However, in order to compensate possible buoyant effects

due to the cold tunnel air, two sets of cooling coils were placed between the gas source and the source opening in the tunnel. Unfortunately, no means were available to check the temperature of the source mixture before it entered the tunnel, therefore, we have no direct quantitative verification on possible buoyancy effects.

The flow rate for the sources was approximately 32.7 cm/sec. This relatively high velocity was necessary to insure releasing enough of the radioactive material so it could be detected at a large distance downstream.

B. Sampling and detection system

Sampling and detection system was essentially the same as for the neutral case. The points of difference are these,

1) the inner diameter of the sampling probes was 0.4 cm,
2) samples were aspirated at approximately 200 cc/min or 26.5 cm/sec and
3) samples were flushed through the counting tubes for at least 5 minutes.

C. Experimental procedure

For the barostromatic case two experiments were performed. One simulating a Minturn source and the other a Redcliff source. Vertical and lateral profiles were made at four different locations downwind from the Minturn source and three different locations downwind from the Redcliff source. The limited number of profiles depended on the duration of the dry ice which was effective for only 6 to 8 hours.

A typical experiment for the barostromatic flow was similar to the steps outlined for the neutral case, but with the above exceptions concerning source and sampling characteristics plus a necessary step of stabilizing the flow before releasing the radioactive krypton mixture. To assure that the airflow was stabilized and that no backflow was

present the smoke-wire probe was placed over the model so it could be test fired intermittently throughout the experiments.

D. Analysis of data

The procedure for analyzing the concentration data was similar to the neutral-flow case as indicated in Appendix B, but values for $\overline{C}$, $\overline{U}$ and Q were representative for this particular experiment, i.e., $Q \sim 7.5\mu$ curie/sec and $\overline{U} \sim 10$ cm/sec.

APPENDIX D

TRANSPORT AND DISPERSION ESTIMATES FROM CONSTANT-VOLUME BALLOONS - EXPERIMENTAL PROCEDURE

APPENDIX D

TRANSPORT AND DISPERSION ESTIMATES FROM CONSTANT-VOLUME BALLOONS - EXPERIMENTAL PROCEDURE

Observing System

The methods and basic equipment used to obtain constant-volume balloon positions were generally similar to those used by other groups. However, for flights made deep in the valley it was necessary to utilize a visual tracking system instead of the more reliable radar-tracking system. The various components of the observing system will be described briefly.

A. Constant-volume balloons - A good description of the constant-volume balloon has been given by Booker (Ref. 10),

> "A superpressure balloon is made of a rigid material so that its volume is essentially constant with superpressure. The balloon will seek a density level where the weight of air displaced by it is exactly equal to the weight of the balloon, helium and all attachments. If the balloon is displaced above or below that density level, it becomes negatively or positively buoyant and seeks to return to its original level. Thus, it is in stable equilibrium on a particular density surface. The only way the balloon will be displaced from the equilibrium density level is by vertical air currents or by a change of mass or volume of the balloon itself. If the balloon is designed so that its mass can not change and if it is free of leaks, it can be expected to remain at its equilibrium density level indefinitely except for temporary displacements due to vertical air movements."

The balloons used in this effort were of two types, a small pillow constant-volume balloon with a skin thickness of 1 mil and a volume of 0.30 cubic meter which were used in the visual tracking and a large pillow balloon with a skin thickness of 2 mil and a volume of 0.65 cubic meter which were used to carry transponders for radar tracking. Both balloons were made of clear mylar plastic.

B. Radar - The radar used was a M-33 type with 3 cm wavelength. The radar was installed on Chalk Mountain at 12,015 ft mean sea level. The radar was automatically directed toward the transponder targets. Numerical values of azimuth (± 2 mills) and elevation angles (± 5 mills) and range (± 50 yds) were read off at 30 sec or 1 min intervals from the appropriate dials.

C. Transponder - The BT-20 transponder made by Weather Science, Inc. was used in these studies. The transponder was 1 in. wide, 1 in. deep, and 8 in. long plus a 6-in. antenna rod. Its weight was approximately 80 gms.

The transponder was powered by batteries and was activated by a 3 cm (x-Band) signal that caused the transmission of a 403-megacycle signal. Most of the transponders functioned satisfactorily.

D. Visual tracking system - When the radar could not be used for automatic tracking, a visual double-theodolite system was substituted for the radar-transponder system. In the case of dual released constant-volume balloons in the Camp Hale region of the Eagle River Valley, four standard meteorological theodolites were used for tracking. Two trackers followed a green balloon while the other two followed an orange balloon. The balloons were painted with a light spray paint to make observation and identification easier. This operation required the services of eight trackers plus two persons for filling, weighing, and launching the balloons. The baseline for the theodolites extended across the valley for approximately 700 meters and was shorter than desired but was limited by the valley walls. The baseline was oriented approximately 67 degrees from north.

Flight Information and Weather

Eleven constant-volume balloon flights were made in the Eagle River Valley and Climax-Leadville area. The primary weather situation of interest was a general northwest flow condition with broken or overcast skies but with cloud ceilings high enough as to not interfere with tracking operations. Unfortunately, none of the flights were released under the above conditions but the dual flights 2, 3, 4, and 5 were flown under weather conditions approaching the ideal situation.

The following gives a brief description of each flight and associated weather. A summary of pertinent launch and flight information is also listed in Table 15.

A. Flight 1 - This initial single flight was released in the Arkansas River Valley on an east-west road connecting Malta and the fish hatchery (Fig. 80). The balloon was visually tracked by a double-theodolite technique. The baseline was approximately 1770 meters. The balloon was released to fly at an equilibrium altitude of about 150 meters above the ground.

The weather consisted of near freezing temperatures with a high broken to overcast sky condition. A pilot balloon taken at 1404 p.m. indicated southeasterly winds in the low levels but changing to southwest around 4500 meters msl.

The track of the balloon followed the Arkansas River into the Tennessee Park area north-northeast of the launch site (Ref. 15).

B. Flight 2 - This initial dual flight was launched near Pando in the northern Camp Hale area. This flight was made in partly cloudy sky following a period of broken to overcast orographic stratocumulus with bases 1200-1500 ft above the Eagle River Valley floor.

Northwest winds prevailed through the period (Fig. 31), while the atmospheric stability was near neutral within the valley (Table 4).

The two balloons were towed to a preset altitude but one balloon apparently ruptured at separation, while the other balloon was tracked sporadically until lost along the eastern ridge line.

C. Flights 3, 4, 5 - These were three successful dual flights launched from the northern end of Camp Hale. One of the purposes of these flights were to obtain trajectory data at three different heights above the ground, 1500 ft, 2000 ft and 2500 ft. The balloons were launched from the ground preset for their equilibrium altitudes.

These flights were made in variable cloudy conditions with rising temperatures. Pilot balloons taken before and after the flights showed general north, northwest, and northeast winds in the valley then turning to the west-northwest after 3400 meters msl (Fig. 32). At the conclusion of the flights the west-northwest winds were found near and above 3700 meters msl. Wind speeds were 1-2 m/s within the valley then increasing rapidly with height. The directional and speed wind shear caused a very turbulent layer near the top of the valley and the balloons once caught in this layer would tumble and gyrate violently. The atmospheric stability was generally more stable than the previous day (Table 4).

D. Flights 6 and 7 - These were single flights launched near the ground and lost before any useful data could be collected. Flight 7 was an initial transponder flight but never achieved sufficient altitude to be tracked continuously by radar. Northwest flow, snow, and slightly stable atmospheric stability existed during flight time (Table 4 and Fig. 33).

E. Flight 8 - This flight was a successful transponder flight launched between Redcliff and Camp Hale. Sky conditions were variable but lowering in the late morning. Winds were generally southerly and light in the valley but changing to westerly winds above the valley.

F. Flights 9 and 10-11 - These three flights launched near the fish hatchery carried transponders and were tracked by radar. Flights 10-11 were two balloons released consecutively (about 15 min apart) but one balloon was tracked only a few minutes and lost.

Weather consisted of cloudy skies with snow occurring on the surrounding mountains. Winds in the valley were southerly changing to west-northwest above the valley.

APPENDIX E

AIRCRAFT TRACKING OF SILVER-IODIDE PLUME - EXPERIMENTAL PROCEDURE

APPENDIX E

AIRCRAFT TRACKING OF SILVER IODIDE PLUME - EXPERIMENTAL PROCEDURE

Observing System

A. Aircraft - The aircraft used for the inflight sampling was the Colorado State University's Aero Commander 500B. The Aero Commander 500B (Fig. 79) is a high wing, two-engine aircraft basically used for research. With a load capacity of approximately 2,000 pounds, the 500B will cruise at 100-170 mph and has a range of 900-1,100 miles. The Aero Commander can be adapted for various kinds of research.

B. Sampling equipment - The principal sampling instrument installed in the aircraft was a NCAR Ice Nucleus Counter (Fig. 79). The nucleus detector was developed by Langer (Ref. 58) and is based on the acoustic particle counter as a detector. The air sample enters a mixing-type cold chamber which humidifies and cools the air sample to form a supercooled cloud. Ice nuclei active at this temperature (usually -20°C) produce ice crystals, which grow to a much larger size than the cloud drops. The crystals are then drawn through the acoustic sensor at 50 - 100 m sec^{-1} giving a loud, audible click if one particle dimension is above 20-30μ. The acoustic sensor only detects particles larger than 20-30μ, and is thus insensitive to the large number of cloud drops present but not to the much larger ice crystals. Further details on the counter can be obtained from Ref. 58.

The NCAR Ice Nucleus Counter was used with a Rustrak recorder for obtaining the signal output. This recorder has three counting ranges (0-10, 0-1000, and 0-10,000) and was set by the observer. For practical

purposes, this limits the count to about 10,000 counts min^{-1} (one count per particle).

A millipore filter system was installed as a secondary sampling system. However, the information received from this instrument was not considered in this study.

The air sample was obtained by a special mounted probe on the top of the aircraft (Fig. 79). For the NCAR Ice Nucleus Counter with 1.5-mm capillary a flow of about 10 liter min^{-1} was obtained at 105 mm Hg suction.

Flight Information and Weather

Five actual flights over the Eagle River Valley and Climax-Leadville area were planned but only four were completed; three of the four were successful data flights. Figure 80 indicates the primary tracks flown over the area. Altitudes at which data were obtained varied with each flight but were generally 10,500 ft to 17,000 ft. All flights were made in VFR or marginal VFR conditions.

The following gives a brief description of each flight and associated weather:

A. Flight 1 (March 12) - This initial flight was conducted over the area of interest during northwest wind conditions but with only scattered clouds. A radiosonde flight (Table 4) taken at 1615 MST revealed near-neutral stability conditions up to 600 mb (14,000 ft) becoming more stable at higher altitudes.

Flight sampling started at 1452 p.m. and ended at 1719 MST. All principal flight tracks (Fig. 80) over the area were flown.

B. Flight 2 (March 13) - The second flight was also conducted under northwest wind conditions but weather conditions were more inclement,

so much so, that it was necessary to enter the area of interest via South Park and the Arkansas River Valley. Weather during sampling consisted of overcast to broken orographic clouds with bases near 12,000 ft msl and tops near 17,000 ft. Snow was occurring along the surrounding mountain peaks but only occasionally in the valley.

A radiosonde flight (Table 4) at 1310 MST showed near-neutral conditions to 650 mb (11,600 msl) with stable conditions at higher altitudes. A second flight at 1650 MST showed the stability approaching a more stable state.

Flight sampling started at 1437 p.m. and ended at 16:18 MST. Weather conditions limited the principal flight tracks to A and B (Fig. 79).

C. Flight 3 (March 16) - Weather conditions for Flight 3 were similar to Flight 2. General northwest winds produced broken orographic clouds over the area with bases near 12,500 ft msl and tops near 17,000 ft. Snow was occurring in the area principally on the major peaks. Although the clouds appeared to be icing out the strong orographic wind component maintained the cloud system throughout the period.

Radiosonde flights (Table 4) at 1415 and 1645 MST showed near-neutral stability conditions to 600 mb (14,000 ft msl) becoming more stable at higher elevations.

Flight sampling started at 1500 MST and ended at 17:47 p.m. Weather conditions limited the principal flight tracks to A and B but a flight was also made along the valley on top of the clouds between 16,900 and 17,000 ft msl.

D. Flight 4 (May 1) - This ill-fated flight was conducted under northwest flow conditions with broken to scattered clouds over the area. Some clouds in the area were convective. Cloud bases varied over the area with intermittent snow showers.

Sampling equipment would not function properly on this day and at a later date it was found that the aircraft had developed a faulty regulator or relay. What little data that was taken this day appeared to be unreliable.

APPENDIX F

SKIN FRICTION COEFFICIENT CALCULATIONS

APPENDIX F

SKIN FRICTION COEFFICIENT CALCULATIONS

To calculate the skin friction coefficient C_D for the model, shear-stress data from Minturn and Redcliff were used in the following equation,

$$\tau_o = \frac{1}{2} C_D \rho U_g^2 \qquad \text{F.1}$$

where τ_o represents the shear stress observed just above the highest ridges of the model. Equation F.1 can be written,

$$C_D = \frac{2\tau_o}{\rho U_g^2} \quad . \qquad \text{F.2}$$

Data for the shear stress at Minturn and Redcliff were obtained from Table 2. The local freestream velocity was $U_g \sim 17$ m/s. Using these values in equation F.2 one finds for the model,

$$\begin{aligned} C_D &= 10.4 \times 10^{-3} \quad \text{Minturn} \\ C_D &= 7.6 \times 10^{-3} \quad \text{Redcliff.} \end{aligned} \qquad \text{F.3}$$

In the field or prototype two different approaches can be used to obtain estimates of the skin friction coefficient. The first approach uses a derivation found in Sutton (Ref. 103, p. 256) and equation F.1 above. If these two equations are set equal to each other then,

$$\tau_o = \frac{f_\rho H U_g^2}{\pi \sqrt{2}} = \frac{1}{2} C_D \rho U_g^2 \quad . \qquad \text{F.4}$$

The first expression for τ_o in equation F.4 was derived assuming that the eddy viscosity is constant. Generally, this assumption is not

acceptable for the total boundary layer but it will be imposed for the following calculations. Let

$$f = 2\Omega \sin \phi = 9.37 \times 10^{-5} s^{-1} \text{ at } \phi = 40°$$

$$H = 2000 \text{ to } 3000 \text{ m (above the mountains)}$$

$$U_g = 20 \text{ m/s.}$$

then the skin friction coefficient is,

$$C_D = \frac{4\Omega \sin\phi \, H}{\pi\sqrt{2} \, U_g} \sim 4.2 \text{ to } 6.3 \times 10^{-3} \quad . \qquad \text{F.5}$$

The second approach considers that the drag coefficient C_D^* is made up of two partial drag coefficients, C_1 and C_2 where C_2 is used to give the form drag of the topographic relief, and C_1 is the drag over flat land (Ref. 25). Sawyer (Ref. 90) made an attempt to evaluate the drag due to a mountain ridge by considering the net downward transport of momentum by gravity waves generated in the flow over the ridge. Cressman takes into account Sawyer's work and other literature on the magnitude of the drag coefficient and estimated C_2 the form drag of very high mountains like the Rocky Mountains as,

$$C_2 = 5 \text{ to } 9 \times 10^{-3}$$

while $C_1 = 1.2 \times 10^{-3}$; this gives

$$C_D^* = 6.2 \text{ to } 10.2 \times 10^{-3} \quad .$$

Since $C_D^* = C_D/2$

$$C_D \sim 12 \text{ to } 20 \times 10^{-3} \quad . \qquad \text{F.6}$$

These latter results are very approximate for our purposes since they were derived for the gross features of large mountain areas.

A comparison of the results F.3, F.5 and F.6 show that the skin friction coefficients for model and prototype are close enough in magnitude that similarity criteria of

$$C_{D_m} \sim C_{D_p}$$

is acceptable, at least, as a first approximation.

APPENDIX G

COMPUTER PROGRAMS

APPENDIX G

COMPUTER PROGRAMS

The number of computer programs that were used in this study were too numerous for detail inclusion in the text. Therefore, the name of the program, what the program does, and where the program is located are listed below for reference purposes.

Computer Program	Results of Programs	Location (Dept.)
MIXRAT	Computation of pressure, temperature, relative humidity, mixing ratio, equivalent potential temperature and potential temperature.	Atmospheric Science
WAV and WIND III	Computation of mean resultant wind direction, mean vectorial wind speed, mean scalar wind speed and steadiness.	Atmospheric Science
WINDS	Computation of height, velocity components, wind direction and resultant velocity	Atmospheric Science
PIBAL I	Computation of height, velocity components, wind direction and resultant velocity	Atmospheric Science and Fluid Mechanics (Civil Engineering)
SUPERPB	Computation of height and horizontal distances for constant-volume balloon flights using double theodolite tracking system.	Atmospheric Science and Fluid Mechanics
HUGGER	Computation of wind tunnel velocity profiles for neutral airflow	Fluid Mechanics
SEAEN	Computation of wind tunnel velocity profiles using the smoke-wire probe.	Fluid Mechanics

APPENDIX H

RECOMMENDATIONS FOR FURTHER RESEARCH

APPENDIX H

RECOMMENDATIONS FOR FURTHER RESEARCH

On the basis of the results from this study the following recommendations for further study are presented to aid future researchers that may have some interest in the various problems.

1) Further laboratory measurements should be made with present facilities in attempt to improve laboratory data. Special attention should be given to modifying the boundary conditions in order to generate a variety of airflow, turbulence and temperature conditions.

2) Various problems should be considered in designing a laboratory facility specifically for studying airflow and dispersion over irregular terrain features. Special attention should be directed toward solving the laboratory simulation problems regarding unsteady-state conditions, Coriolis acceleration effects, directional wind-shear, compressibility and turbulent thermally-stratified airflows.

3) Field data in mountainous terrain are seriously lacking. Vertical profiles of temperature, wind, turbulence, and concentration data taken under different atmospheric stability and wind conditions and in different types of mountainous terrain is needed to fill this information gap. Constant-volume balloon experiments could assist in obtaining information on atmospheric dispersion. Repetition of balloon experiments over many trials would provide data for development of a dispersion climatology.

4) Additional aircraft sampling data on dispersion is needed for mountainous areas. These data are important in relation to evaluating the success of modeling programs and the field operational seeding

programs. Sampling equipment for ice nuclei need further improvement in order to achieve accurate measurements of ice-nuclei concentrations.

5) Depletion variables and mechanisms for cloud-seeding materials need additional study to improve weather-modification program operations.

TABLES

TABLE 1 LABORATORY MODEL STUDIES OF AIRFLOW OVER IRREGULAR TERRAIN

Author	Topographic Site	Problems	Type of Airflow
Garrison and Cermak 1968	San Bruno Mountain, California	Topographic effects on airflow	Neutral and Barostromatic (dry ice)
Hsi, Binder and Cermak 1968	Green River, Utah	Topographic effects on airflow	Neutral
Lin and Binder 1967	Idealized Hill's	Mountain lee waves	Barostromatic
Meroney and Cermak 1967	San Nicolas Island, California	Topographic effects and diffusion	Neutral and Barostromatic
Cermak and Peterka 1966	Point Arguello, California	Topographic effects and diffusion	Barostromatic
Chang 1966	Idealized Hill	Wake effects	Neutral
Plate and Lin 1965	Idealized Hill's	Velocity profiles and wake pattern	Neutral
Halitsky, Magony and Halpern 1964-65	Mountains near Manchester, Vermont	Topographic effects on airflow	Neutral
Briggs 1963	Rock of Gibraltar	Turbulence patterns	Neutral
Halitsky, Tolciss, Kaplin, and Magony 1962-63	Bear Mountain, New York	Turbulence and wake pattern	Neutral
Nemoto 1961	Enoshima and Akashi-channel, Japan	Turbulence and velocity profiles	Neutral
Long 1959	Sierra Nevada Mountains, California	Mountain lee waves	Barostromatic (brine solution)
Suzuki and Yabuki 1956	Idealized Hill's	Mountain lee waves	Barostromatic (brine solution)
Abe 1941	Mt. Fuji, Japan	Mountain clouds and topographic effects	Barostromatic (dry ice)
Field and Warden 1929-30	Rock of Gibraltar	Topographic effects and turbulence	Neutral

TABLE 2 COMPUTATION OF VARIOUS METEOROLOGICAL PARAMETERS FROM SHEAR-STRESS DATA FOR THE NEUTRAL WIND-TUNNEL MODEL AIRFLOW. LOCATION: MINTURN

Elevation		$-\overline{u'w'}$	$\delta\bar{U}/\delta z$	τ	u_*	K_{mz}	ε
meters	cm	m^2/sec^2	sec^{-1}	dynes/cm^2	m/sec	m^2/sec	m^2/sec^2
100	1.1	0.071	50.48	0.62	0.266	.0014	3.58
300	3.2	0.160	14.42	1.40	0.400	.0111	2.31
500	5.3	0.293	06.25	2.60	0.541	.0460	1.83
700	7.3	0.422	00.96	3.70	0.650	.4390	0.41
900	9.4	0.556	09.61	4.90	0.746	.0570	5.34
1100	11.5	0.690	21.63	6.00	0.831	.0316	14.92
1300	13.6	0.880	36.05	7.70	0.938	.0240	31.72
1500	15.7	1.205	52.88	10.5	1.097	.0220	63.72
1700	17.7	1.444	50.48	12.6	1.201	.0280	72.89
1900	19.8	1.488	52.88	13.0	1.220	.0280	78.69
2100	21.9	1.370	57.69	12.0	1.170	.0230	79.04
2300	24.0	1.230	50.48	10.8	1.109	.0240	62.09
2500	26.1	1.120	50.48	9.81	1.058	.0220	56.54
2700	28.1	1.020	43.26	8.93	1.010	.0230	44.13
2900	30.2	0.916	43.26	8.02	0.957	.0210	39.63
3100	32.3	0.795	38.46	6.96	0.892	.0200	30.58
3300	34.4	0.668	28.84	5.85	0.817	.0230	19.27

LOCATION: REDCLIFF

Elevation		$-\overline{u'w'}$	$\delta\bar{U}/\delta z$	τ	u_*	K_{mz}	ε
meters	cm	m^2/sec^2	sec^{-1}	dynes/cm^2	m/sec	m^2/sec	m^2/sec^2
100	1.1	0.03	86.53	0.26	0.173	.0003	2.590
300	3.2	0.33	67.30	2.89	0.574	.0049	22.21
500	5.3	0.33	64.90	2.89	0.574	.0050	21.42
700	7.3	0.49	43.26	4.29	0.700	.0113	21.20
900	9.4	0.66	28.84	5.78	0.812	.0228	19.03
1100	11.5	0.85	38.46	7.45	0.922	.0221	32.69
1300	13.6	0.97	26.44	8.50	0.985	.0366	25.65
1500	15.7	1.06	26.44	9.28	1.029	.0400	28.03
1700	17.5	1.10	28.84	9.68	1.051	.0383	31.87
1900	19.8	1.09	33.65	9.55	1.044	.0323	36.68
2100	21.9	1.06	38.46	9.28	1.032	.0276	40.96
2300	24.0	1.05	28.84	9.20	1.024	.0364	30.28
2500	26.1	1.03	31.25	9.02	1.015	.0329	32.19
2700	28.1	1.00	26.44	8.76	1.000	.0378	26.44
2900	30.2	0.94	33.65	8.23	0.969	.0279	31.63
3100	32.3	0.85	24.03	7.45	0.922	.0353	20.43
3300	34.4	0.70	21.63	6.13	0.837	.0323	15.14

TABLE 3 SPECIAL FIELD PROGRAM DATES FOR THE EAGLE RIVER VALLEY-LEADVILLE AREA

Date	DATA			
	Pilot Balloon	Radio- or Rawinsonde	Constant-Volume Balloon	Ground Ice Nuclei Data
16-20 Dec. 1968	Camp Hale Fish Hatchery	Camp Hale, Fish Hatchery, Chalk Mtn.	Arkansas River Valley near Leadville	Chalk Mountain HAO
8-16 Dec. 1969	Eagle River Valley Chalk Mtn.	Minturn, Camp Hale Fairplay	Camp Hale	Chalk Mountain HAO Tennessee Pass
13-16 Jan. 1970	None	Minturn, Camp Hale, Fairplay	Redcliff, Camp Hale Arkansas River Valley near Leadville	Chalk Mountain HAO Tennessee Pass
*12, 13, & 16 March, 1970	None	Camp Hale	None	Chalk Mountain HAO Tennessee Pass
30 April, *1 May 1970	None	Camp Hale	None	Chalk Mountain HAO Tennessee Pass

*12, 13, & 16 March and 1 May 1970 aircraft sampling days.

TABLE 4 RADIOSONDE DERIVED POTENTIAL TEMPERATURE AND EQUIVALENT POTENTIAL TEMPERATURE LAPSE RATES DURING SPECIAL FIELD TRIALS IN THE EAGLE RIVER VALLEY ($\Delta\theta/\Delta z \times 10^{-3}$ °K/meter)

		Camp Hale				Minturn				
		sfc-4000m		4000m-6000m		sfc-4000m		4000m-6000m		
Date	(MST) Time	$\Delta\theta/\Delta z$	$\Delta\theta_e/\Delta z$	$\Delta\theta/\Delta z$	$\Delta\theta_e/\Delta z$	$\Delta\theta/\Delta z$	$\Delta\theta_e/\Delta z$	$\Delta\theta/\Delta z$	$\Delta\theta_e/\Delta z$	Weather
181268	1826	3.417	3.917	6.000	5.200	---	---	---	---	Ovc Snow
101269	1716	1.017	0.339	2.900	1.444	---	---			Snow & Gusty Winds
111269	0915	---	---	---	---	1.588	0.235	6.150	5.710	Ovc to Brkn
111269	1128	---	---	---	---	0.941	0.176	6.550	5.10	Ovc to Brkn
111269	1210	0	-1.269	7.600	5.750	---	---	---	---	Ovc to Brkn
111269	1445	---	---	---	---	0.422	0	5.400	5.625	Ovc to Brkn
111269	1645	---	---	---	---	2.442	1.395	2.450	8.226	Brkn
111269	1728	5.492	6.393	7.300	6.300	---	---	---	---	Brkn
121269	1100	---	---	---	---	5.872	8.779	2.25	3.194	Brkn - Warming
121269	1130	3.462	2.308	6.350	3.450	---	---	---	---	Brkn - Warming
121269	1645	---	---	---	---	7.176	8.529	---	---	Brkn
121269	1655	5.213	3.511	4.650	2.377	---	---	---	---	Brkn
150170	0528	12.066	9.796	4.500	3.400	---	---	---	---	Cloudy
150170	0752	---	---	---	---	8.269	7.436	3.550	2.25	Cloudy
150170	1350	1.593	-1.167	5.400	3.250	---	---	---	---	Ovc Snow
150170	1352	---	---	---	---	3.671	4.873	4.850	3.000	Ovc Snow
150170	1651	---	---	---	---	3.063	0.438	---	---	Ovc Snow
150170	1657	3.226	0	4.150	1.950	---	---	---	---	Ovc Snow
150170	1850	---	---	---	---	3.540	0.869	3.200	3.500	Ovc Snow
150170	1905	2.320	-0.400	4.85	2.875	---	---	---	---	Ovc Snow
150170	2101	---	---	---	---	2.609	1.366	6.75	4.10	Brkn Snow
150170	2150	1.746	-0.794	7.050	9.20	---	---	---	---	Brkn Snow
150170	2240	---	---	---	---	5.370	4.198	6.400	---	Cloudy
150170	2300	9.200	4.08	9.1	---	---	---	---	---	Cloudy
120370	1615	0.500	-0.417	4.150	3.20	---	---	---	---	Sctd
130370	1310	0.240	-0.480	3.950	2.850	---	---	---	---	Brkn Sctd Snow
130370	1650	2.80	0.640	2.250	0.250	---	---	---	---	Brkn Sctd Snow
160370	1415	0.508	-0.508	3.465	1.930	---	---	---	---	Brkn Sctd Snow
160370	1645	0.763	-0.424	3.500	1.500	---	---	---	---	Brkn Sctd Snow

TABLE 5 DIURNAL VARIATION OF 4 METER LEVEL WINDS AT SUMMIT OF CHALK MOUNTAIN. MEANS BASED UPON THREE WINTER MONTHS JANUARY THROUGH MARCH

Hour of Day (MST)	Mean Resultant Wind Direction (deg)	Mean Scalar Wind Speed (mph)	Steadiness (%)
01	246	7.6	44.0
02	256	7.44	48.2
03	252	7.30	46.5
04	250	7.31	48.0
05	247	6.35	45.5
06	252	6.48	39.3
07	250	6.40	35.8
08	244	6.60	40.4
09	243	7.44	37.9
10	253	7.90	40.2
11	250	8.91	36.1
12	259	9.96	47.0
13	263	11.27	49.0
14	264	11.90	49.6
15	273	11.32	44.8
16	274	10.15	55.8
17	271	9.50	50.6
18	266	9.14	55.8
19	264	8.88	46.9
20	267	8.74	48.8
21	251	8.13	47.4
22	263	7.97	50.4
23	247	7.70	47.0
24	248	7.77	44.1

TABLE 6 LOCATION OF SEEDING GENERATORS WITH RESPECT TO THE PRIMARY TARGET, CHALK MOUNTAIN (after Chappell 1967)

Location	Azimuth and Distance from Target (degrees/nautical miles)
Minturn, Colorado	320/16
Redcliff, Colorado	316/11
South of Tennessee Pass	250/7
West of Leadville, Colorado	218/11
Aspen, Colorado	249/31
Reudi, Colorado	267/20

TABLE 7 COMPUTATION OF VARIOUS METEOROLOGICAL PARAMETERS FROM CONSTANT-VOLUME BALLOONS FLIGHTS 3, 4 AND 5

Vertical Variation of Eddy Diffusivities (after Wooldridge 1970)

Constant-Volume Dual Balloon Run	Mean Elevation (m)	K_u cm^2 sec^{-1}	K_v cm^2 sec^{-1}	K_w cm^2 sec^{-1}
#3	3293	2.4×10^5	2.6×10^5	3.5×10^4
#5	3542	4.5×10^6	4.2×10^5	3.0×10^5
#4	3562	8.5×10^6	4.0×10^5	1.24×10^6

Flight 3

Orange Balloon

Elevation (meters)	$\overline{u'w'}$ cm^2/sec^2	$\delta\bar{U}/\delta z$ $s^{-1} \times 10^{-4}$ sec	τ dynes/cm^2	K_{mz} $\times 10^4 cm^2/sec$	ε cm^2/sec^3	$\frac{\sigma_u}{\bar{U}}$	N
3000-3100	-888	52	0.789	17.10	4.62	0.65	4
3101-3200	-1028	34	0.904	34.30	3.53	0.25	16
3201-3300	3	-42	-0.003	.07	.01	0.13	22
3301-3400	603	-5	-0.518	120.60	.30	0.43	18
3401-3500	59	-10	-0.050	5.90	.06	0.35	34
3501-3600	-945	76	0.798	12.40	7.20	0.38	13
Average	-366	17.5	0.320	31.7	2.62	0.365	

Green Balloon

Elevation (meters)	$\overline{u'w'}$ cm^2/sec^2	$\delta\bar{U}/\delta z$ $s^{-1} \times 10^{-4}$ sec	τ dynes/cm^2	K_{mz} $\times 10^4 cm^2/sec$	ε cm^2/sec^3	$\frac{\sigma_u}{\bar{U}}$	N
3000-3100	---	--	---	---	---	---	0
3101-3200	268	-57	-.235	4.7	1.53	0.16	34
3201-3300	523	-49	-.455	10.7	2.56	0.34	16
3301-3400	450	-34	-.387	13.2	1.53	0.33	21
3401-3500	-66	-26	.056	---	---	0.18	8
3501-3600	2684	-12	-2.268	223	3.22	0.70	5
Average	771.8	-35.6	-0.658	62.9	2.21	0.342	

TABLE 8 STARTING AND ENDING TIMES OF SILVER-IODIDE GENERATORS AND STRENGTH OF SOURCES FOR SELECTED FIELD SAMPLING DAYS

Date	Year	Seeded Day	West-Northwest Winds	Silver-Iodide Generator Redcliff		(gm/hr)	Silver-Iodide Generator Minturn		(gm/hr)
				on	off	Q	on	off	Q
17 Dec.	1968	Yes	Yes	1600	2400	15	1400	2400	15
18 Dec.	1968	Yes	Yes	0000	0830	15	0000	0830	15
9 Dec.	1969	Yes	Yes	0830	2400	15	1230	2400	15
10 Dec.	1969	Yes	Yes	0000	2400	15	0000	0830	15
11 Dec.	1969	Yes	Yes	0000	0830	15	----	----	--
12 Dec.	1969	Yes	Yes	0830	2400	15	----	----	--
14 Jan.	1970	No	Marginal	----	----	--	----	----	--
15 Jan.	1970	No	Yes	----	----	--	----	----	--
16 Jan.	1970	Yes	Yes	0630	1000	15	0600	1030	15
17 Jan.	1970	No	Yes	----	----	--	----	----	--
18 Jan.	1970	Yes	Yes	0830	2400	15	0830	2400	15
19 Jan.	1970	Yes	Yes	0000	0830	15	0000	0830	15
20 Jan.	1970	No	Yes	----	----	--	----	----	--
21 Jan.	1970	Yes	Yes	0830	2400	15	0830	2400	15
22 Jan.	1970	Yes	Marginal	0000	0830	15	0000 1600	0830 2400	15
27 Jan.	1970	Yes	Yes	0830	2400	15	1600	2400	15
12 Mar.	1970	Yes	Yes	0830 1600	1600 1930	15 60	0830 1530	1530 1930	15 60
13 Mar.	1970	Yes	Yes	0000 0900	0830 1800	1.5 60	0000 0900	0830 1800	1.5 60
16 Mar.	1970	Yes	Yes	1300	1800	60	1230	1830	60
30 Apr.	1970	Yes	Yes	1100	2400	1.5	1100 1900	1900 2400	60 1.5
1 May	1970	Yes	Yes	0000	0800	1.5	0000 0930	0930 1900	1.5 60
2 May	1970	No	Yes	----	----	--	----	----	--
7 May	1970	Yes	No	1730	2400	1.5	----	----	--
8 May	1970	Yes	No	0000	0930	1.5	----	----	--
9 May	1970	Yes	Yes	0930	1200	1.5	----	----	--

TABLE 9 VARIATION AND AVERAGE OF NEAR SURFACE ICE-NUCLEI COUNTS (NUCLEI/LITER, EFFECTIVE - 20° C) DURING SELECTED SEEDING EVENTS IN THE EAGLE RIVER VALLEY-CLIMAX AREA

	Chalk Mountain			High Altitude Observatory			Tennessee Pass		
Date	Average	Variation	Time Duration	Average	Variation	Time Duration	Average	Variation	Time Duration
12/17/68	12.4	0.2- 48.0	1712- 2400	36.9	0.9- 270	1704- 2400	--	--	--
12/18/68	36.2	0- 150	0000- 1200	76.8	0.6- 280	0000- 1200	--	--	--
12/9/69	--	--	--	53.6	2.5- 142.5	1813- 2025	--	--	--
12/10/69	--	--	--	75.6	20- 140	0919- 1547	--	--	--
12/12/69	--	--	--	1.10	0.2- 2.8	0907- 2025	5.5	0- 13.2	1155- 1334
1/15/70	5.3	0.9- 9.4	1055- 1755	--	--	--	--	--	--
1/16/70	26.9	1.8- 160	0743- 1524	0.40	0- 2.3	0550- 1946	0.63	0- 0.63	0615- 1914
1/22/70	24.5	0.5- 136	0802- 1657	14.3	0- 116	0807- 1655	3.1	0- 37	0802- 1814
1/27/70	--	--	--	139	8.2- 244	1815- 2046	--	--	--
3/12/70	5.8	1.2- 23	1404- 1650	20.6	0- 82.5	1400- 1855	--	--	--
3/13/70	37.4	0.2- 192	1229- 1906	156	0- 800	0910- 2035	185	0- 380	1045- 1853
3/16/70	23.6	0.2- 160	1420- 1840	107	0- 484	1400- 2107	--	--	--
4/30/70	178	0.20- 492	1600- 1755	46	0- 240	1550- 2103	40	0.2- 132	1300- 1656
5/1/70	11	0- 155	1045- 1655	5	0- 49	0912- 1920	74	0- 339	0905- 2030
5/7/70	--	--	--	3	0- 12	1841- 2050	4.6	0- 17.0	1704- 1834
5/8/70	--	--	--	9	5- 16	1740- 2023	3.6	0- 13	1619- 1747
5/9/70	--	--	--	3.4	1.7- 5.4	1817- 1831	32	0.7- 75	1717- 1906

TABLE 10 BULK RICHARDSON NUMBER FOR MODEL AND FIELD
LOCATION: CAMP HALE

	Model		Field Ri_θ					
Δz(meters)	Ri_T	Ri_ρ	1	2	3	4	5	Ave.
100-300	-0.04	-0.04	-1.55	0.31	-0.11	0.80	0.15	-.808
300-500	0.69	0.65	1.09	8.16	-2.68	-16.4	0.09	-1.95
500-700	431	643	0.78	3.20	-0.29	3.63	7.63	+2.99
700-900	7.98	6.97	0.45	1.13	29.2	4.03	4.46	+7.85
900-1100	1.09	1.65	2.02	0.23	6.14	0.45	2.22	+2.21
1100-1300	1.68	2.78	4.87	4.10	261	0.66	1.40	+54.4
1300-1500	6.60	10.6	2.01	5.24	4.08	3.91	16.5	+6.35
1500-1700	66.1	86.1	8.08	1.62	211	3.62	4.98	+45.9
1700-1900	6.73	8.30	5.87	7.27	15.2	2.28	0.64	+6.25
1900-2100	1.51	2.02	455	10.4	17.1	1.07	16.6	+100
2100-2300	2.93	5.10	5.19	0.31	1.60	0.74	1455	292
2300-2500	18.6	39.5	1.26	0.26	0.36	5.56	0.41	1.57
2500-2700	55.1	167	1.61	0.80	8.00	2.66	0.17	2.65

Ri_T - Richardson number based on temperature

Ri_ρ - Richardson number based on density

Ri_θ - Richardson number based on potential temperature

1 1310 MST March 13, 1970 Camp Hale

2 1650 MST March 13, 1970 Camp Hale

3 1415 MST March 16, 1970 Camp Hale

4 1645 MST March 16, 1970 Camp Hale

5 1826 MST December 18, 1968 Camp Hale

TABLE 11 PERFORMANCE CHARACTERISTICS OF COLORADO STATE UNIVERSITY LOW-SPEED RECIRCULATION WIND TUNNEL

Characteristic	Low-Speed Wind Tunnel
1. Dimensions	
Test-section length	30 ft
Test-section area	36 ft^2
Contraction ratio	9:1
Length of temperature controlled boundary	10 ft
2. Wind-tunnel drive	
Total power	75 hp
Type of drive	16-blade axial fan
Speed control: coarse	single-speed induction motor
Speed control: fine	pitch control
3. Temperatures	
Ambient air temperature	not controlled
Temp. of controlled boundary	ambient to 200° F
4. Velocities	
Mean velocities	approx. 3 fps to 90 fps
Boundary layers	up to 8 inches
Turbulence level	low (about 0.5 percent)
5. Pressures	not controlled
6. Humidity	not controlled

TABLE 12 SOURCE AND SAMPLING CHARACTERISTICS FOR WIND-TUNNEL MODELS

	Source	q_s	Q_s	w_s	t	q_{SA}	V_{SA}
Neutral	Minturn	2340 cc/min	45.6 μCi/sec	1.99 m/s	1.5 min	~700 cc/min	3.72 m/s
Airflow	Minturn and Redcliff	7100 cc/min	138.45 μCi/sec	1.99 m/s	1.5 min	~700 cc/min	3.72 m/s
Barostromatic	Minturn	385 cc/min	7.5 μCi/sec	32.7 cm/sec	5 min	~200 cc/min	26.5 cm/sec
Airflow	Redcliff	385 cc/min	7.5 μCi/sec	32.7 cm/sec	5 min	~200 cc/min	26.5 cm/sec

COUNTING YIELD OF THE EIGHT GEIGER-MUELLER TUBES

G.M. Tube	1	2	3	4	5	6	7	8	
Counting Yield	1.16	1.43	1.16	1.16	1.22	1.25	1.2	1.2	(μμ Ci/cc/Cpm)

Table 13 Example of Computer Output
From Smoke-Wire Computer Program

Run No. 23
Left Picture No. 24 A--25 Right Picture No. 26
Time Delay 287.13 Millisecs
Location: Pando

Origin at Upper End of the Wire
CGS System

z (cm)	DY (cm)	V_y (cm/sec)	DX (cm)	V_x (cm/sec)	V (cm/sec)	*TH (degrees)	St. Div. of DY	St. Div. of DX
0.	-.5136	-1.7889	3.3891	11.8035	11.9383	-8.6178	.0089	.2056
-1.0508	-.6667	-2.3218	3.5669	12.4224	12.6375	-10.5866	.0089	.2032
-1.9633	-.7712	-2.6858	3.6373	12.6678	12.9493	-11.9705	.0107	.2024
-4.7991	-.7913	-2.7558	4.1703	14.5242	14.7833	-10.7433	.0303	.1951
-5.5641	-.8033	-2.7977	4.2346	14.7480	15.0111	-10.7414	.0157	.1942
-6.5934	-.7792	-2.7138	4.2393	14.7645	15.0119	-10.4149	.0225	.1941
-7.4813	-.7390	-2.5739	4.2295	14.7304	14.9536	-9.9112	.0521	.1944
-8.4184	-.7149	-2.4899	4.1811	14.5619	14.7732	-9.7029	.0096	.1949
-9.2295	-.5459	-1.9011	4.0277	14.0273	14.1555	-7.7184	.0350	.1970
-10.1512	-.4128	-1.4377	3.6413	12.6816	12.7628	-6.4678	.0517	.2024
-10.8917	-.2350	-.8184	3.0486	10.6174	10.6489	-4.4079	.0203	.2102
-11.9701	.1137	.3960	2.0344	7.0852	7.0963	3.1991	.0144	.2238
-12.8549	.0203	.0707	1.4602	5.0855	5.0860	.7962	.0115	.2316
-13.5984	-.0365	-.1272	1.2128	4.2239	4.2258	-1.7244	.0172	.2349
-17.5158	.1178	.4102	1.2104	4.2155	4.2354	5.5573	.0834	.2351
-18.4651	-.1257	-.4378	1.7110	5.9591	5.9752	-4.2014	.0230	.2282
-19.4483	-.3078	-1.0719	2.2709	7.9091	7.9814	-7.7184	.0716	.2208
-20.3547	-.5378	-1.8731	2.6568	9.2531	9.4408	-11.4435	.0294	.2155
-21.2641	-.4693	-1.6344	2.8073	9.7772	9.9129	-9.4900	.0085	.2135
-22.2073	-.7591	-2.6438	3.2974	11.4838	11.7842	-12.9648	.0106	.2068
-23.1874	-.9638	-3.3565	3.9245	13.6679	14.0740	-13.7975	.0192	.1984
-23.9248	-.9878	-3.4403	4.3601	15.1851	15.5699	-12.7651	.0338	.1925
-27.9404	-.6425	-2.2377	4.0579	14.1328	14.3088	-8.9972	.0121	.1968
-28.6839	-1.3515	-4.7068	3.5935	12.5151	13.3710	-20.6107	.0181	.2028

*TH - Angular measurement from the X-axis to a point on the smoke plume. With back to wind, positive values indicate that plume is to the left of X-axis of the smoke-wire probe.

TABLE 14 PERCENTAGE OF CARBON-DIOXIDE OVER MODEL LOCATIONS MINTURN, CAMP HALE, AND CHALK LAKE

Height (cm)	Minturn	Camp Hale	Chalk Lake	
0	23.7	22.6	21.1	Minturn
3	23.8	22.5	21.0	Elevation: 8000 ft msl
6	23.8	22.4	20.0	Camp Hale
9	24.0	22.5	17.3	Elevation: 9200 ft msl
12	23.5	21.8	15.1	Chalk Lake
16	23.2	19.8	12.3	Elevation: 11375 ft msl
20	20.8	17.8	10.1	
25	16.2	12.2	7.0	
28	12.3	8.8	6.5	
31	10.2	8.2	6.3	
34	9.2	7.2	6.2	
37	8.2	7.1	6.3	
41	8.0	6.7	6.0	
45	7.2	6.4	5.7	
50	7.2	6.6	5.9	
53	---	---	---	
56	---	---	---	
59	6.6	6.6	---	
62	---	---	---	
66	---	---	---	
70	---	---	---	
75	7.3	6.4	---	

TABLE 15 CONSTANT-VOLUME BALLOON FLIGHT INFORMATION AND ASSOCIATED WEATHER CONDITIONS

Flight	Released			Mean Flight Level (m)	Mean Speed m/s	Synoptic Situation	Comments
	Date	Local Time (MST)	Location				
1	12-19-68	16:21	Near Malta	3080	8	Southerly Flow-Low levels Westerly at High levels Cloudy	Single tracked by theodolites
2	12-11-69	15:15	Pando	Unknown	Unknown	Northwest Flow Cloudy	Dual, one balloon lost tracked by theodolites
3	12-12-69	11:00	North section of Camp Hale	Green 3259 Orange 3327	1.7 1.5	Northly flow in valley cloudy WNW flow above 13,000 ft	Dual tracked by theodolites
4	12-12-69	13:00	Same as above	Green 3635 Orange 3490	3.2 4.6	Same as above	Dual tracked by theodolites
5	12-12-69	14:44	Same as above	Green 3571 Orange 3546	2.6 2.7	Same as above	Dual tracked by theodolites
6	1-15-70	11:45	Fish Hatchery	Unknown	Unknown	SW flow shifting to NW flow	Single flight tracked by theodolites
7	1-15-70	16:45	Camp Hale	Unknown	Unknown	NW flow light snow	Single flight Radar tracked
8	1-16-70	08:48	Between Redcliff and Camp Hale	4293	22	Westerly flow at high levels	Single flight Radar tracked
9	1-16-70	11:20	Near Fish Hatchery	4312	17	Southerly flow in valley shifting to westerly above mountains Snowing on mountains	Single flight Tracked by radar
10-11	1-16-70	1330 1345	Same as above	4701	18	Same as above	Two balloons released consecutively tracked by radar One lost

FIGURES

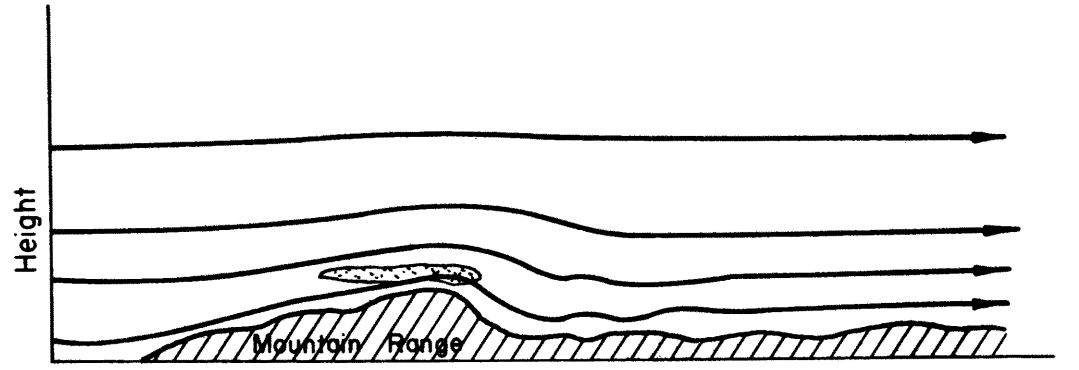

a. Quasi-Laminar Flow

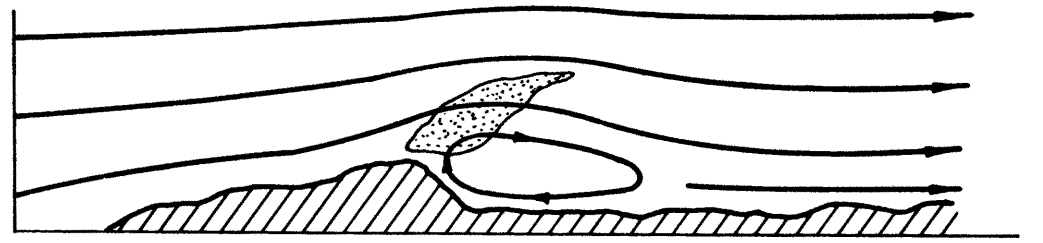

b. Separation Flow

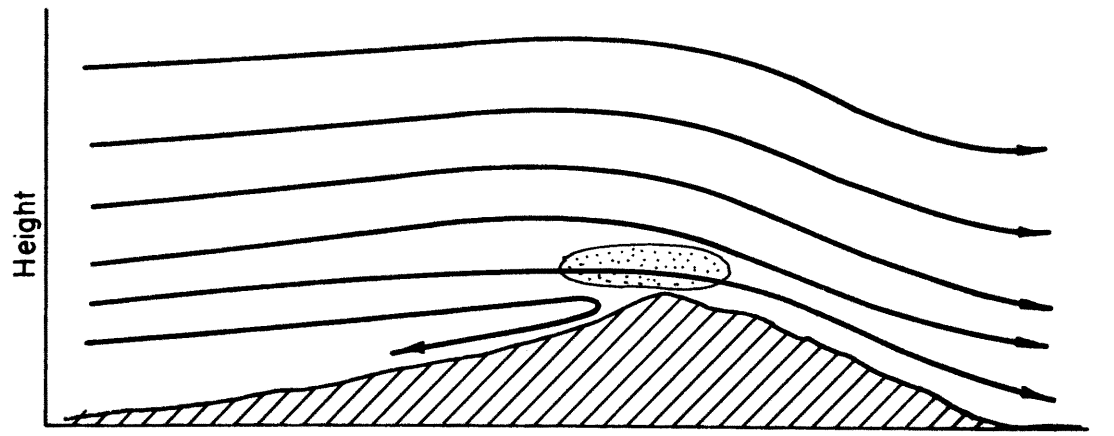

c. Blocking and Stagnation

Fig. 1. Classification of types of airflow over mountainous terrain.

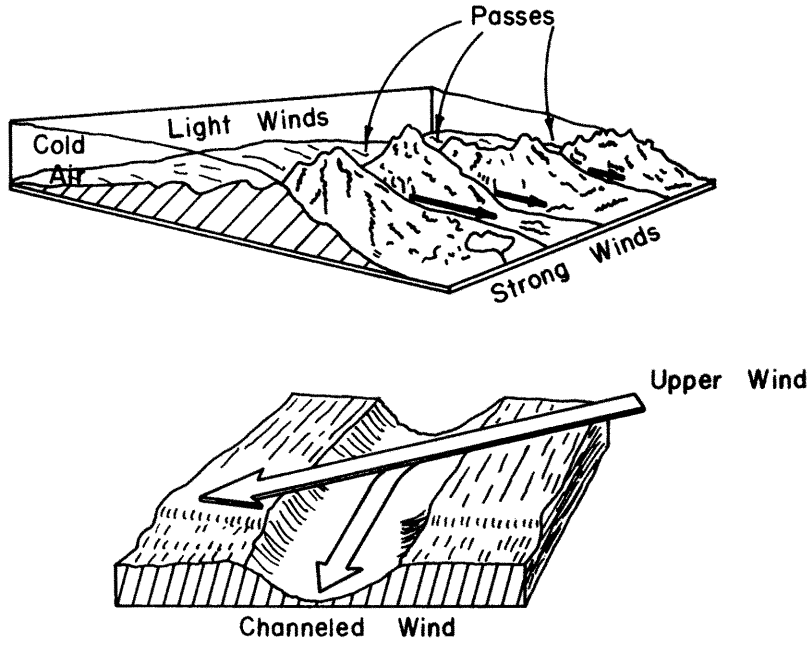

d. Channel and Gap Winds

e. Horizontal Eddying

Fig. 1. Classification of types of airflow over mountainous terrain-(Continued).

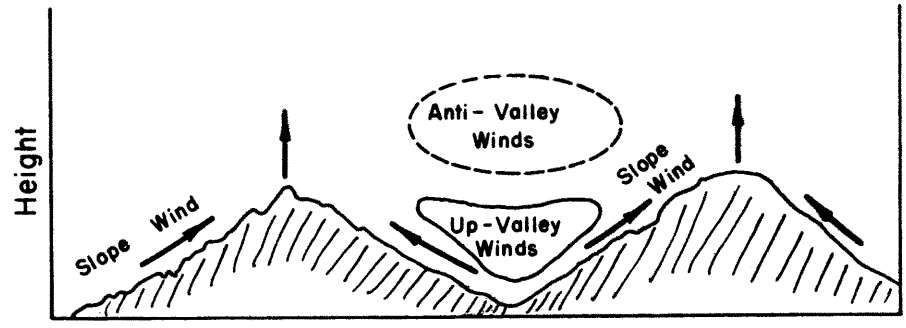

f. Slope and valley winds during daytime (reversed flow for night time)

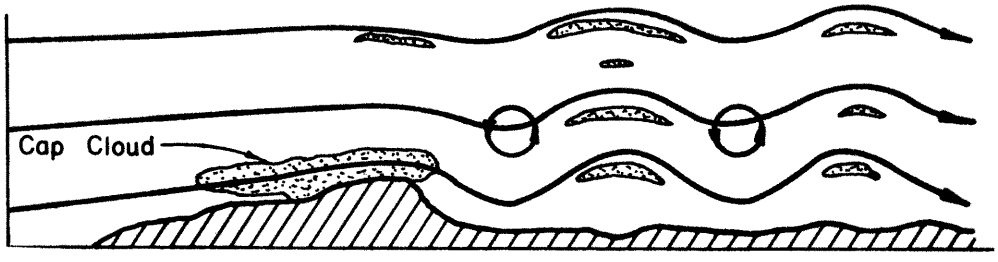

g. Lee Waves

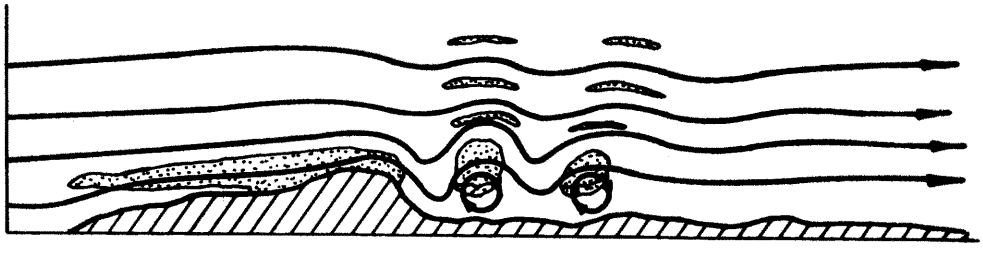

h. Rotors

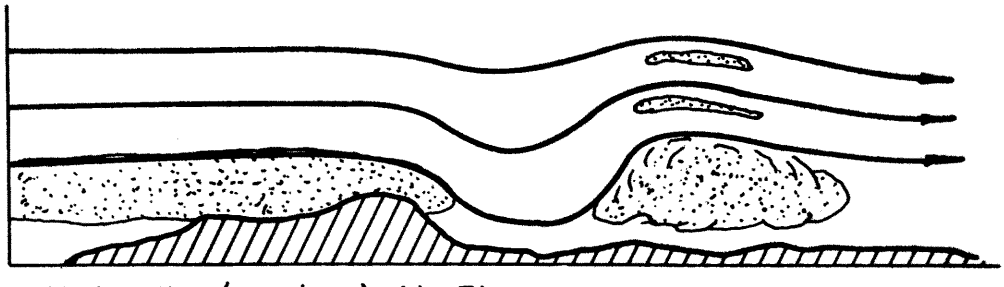

i. Hydraulic (analog) Air Flow

Fig. 1. Classification of types of airflow over mountainous terrain - (Continued).

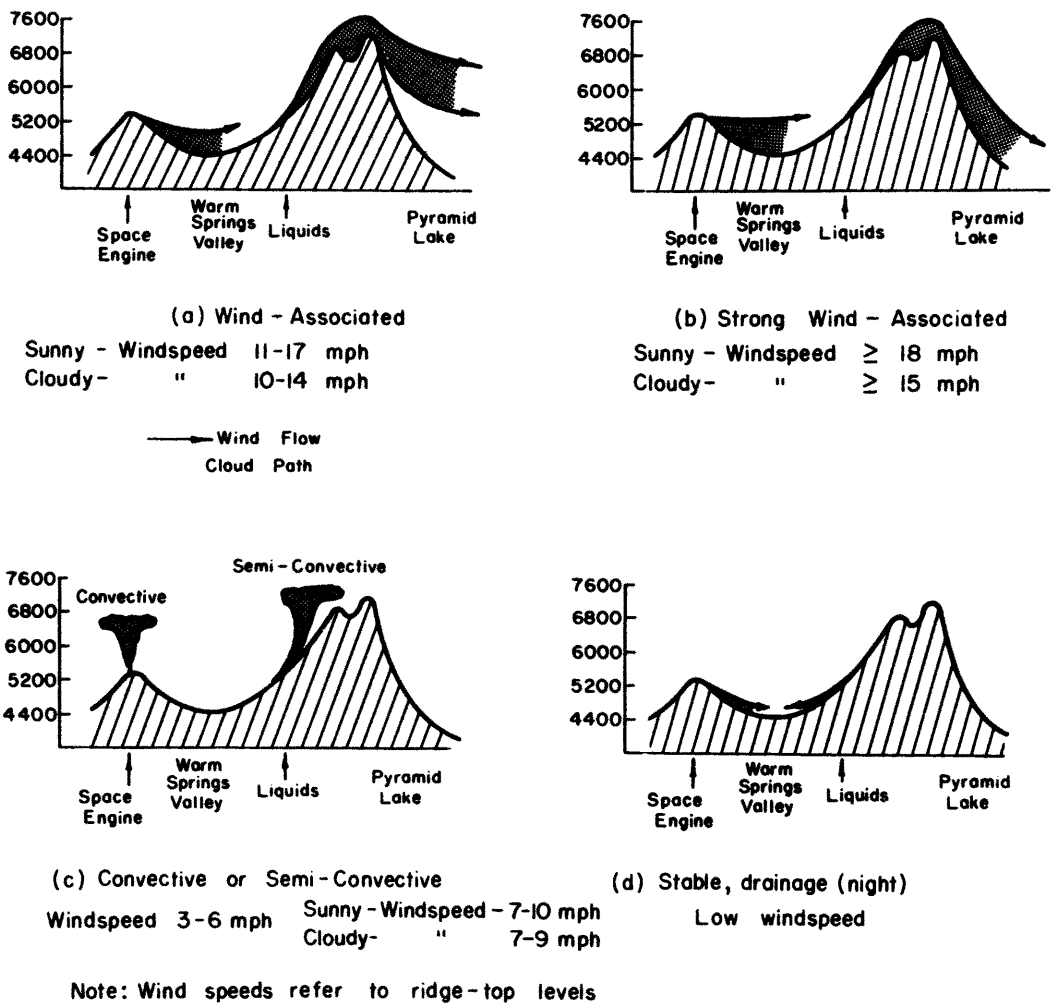

Fig. 2. Schematic patterns of diffusion over mountainous terrain (after Ref. 101).

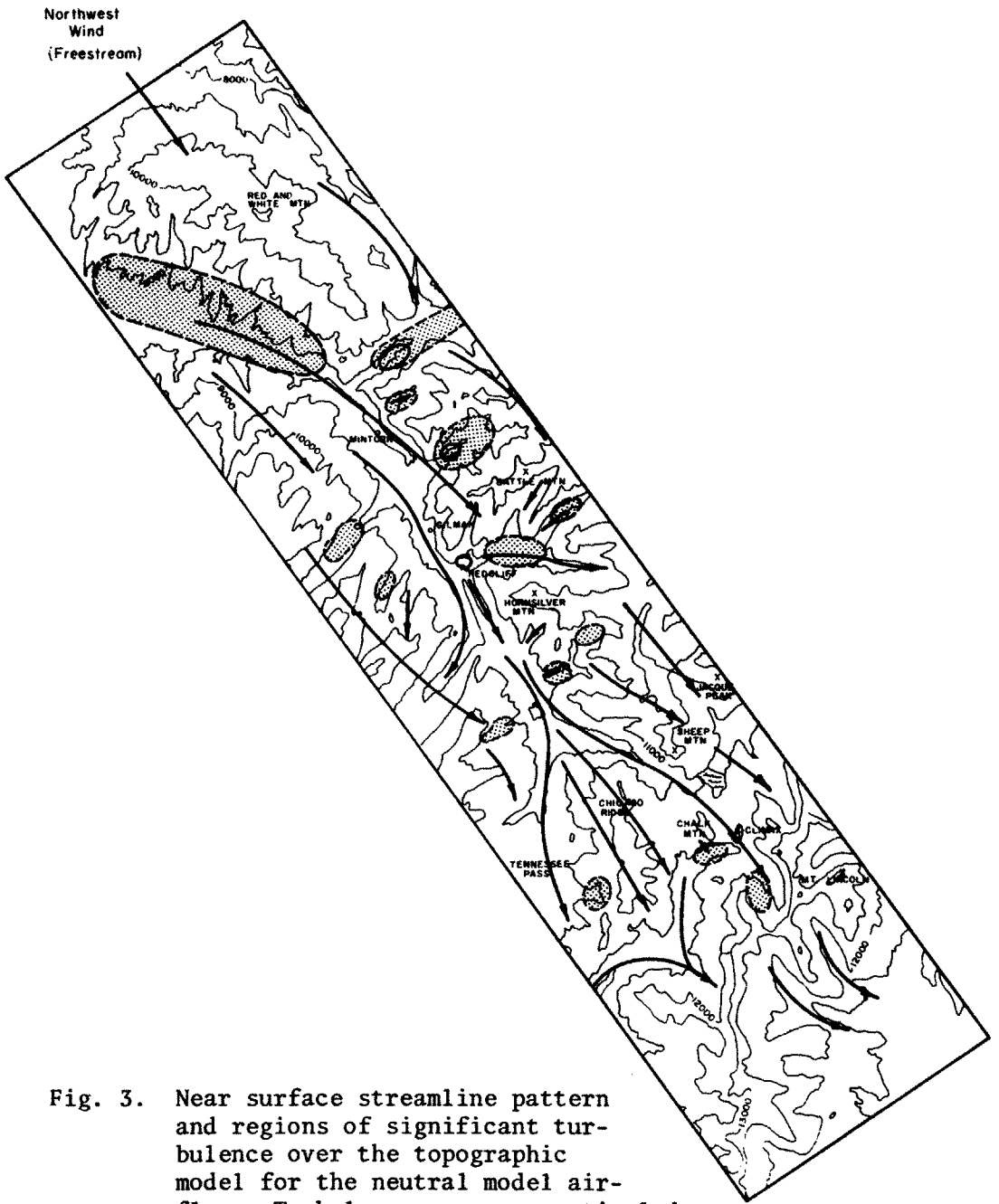

Fig. 3. Near surface streamline pattern and regions of significant turbulence over the topographic model for the neutral model airflow. Turbulence areas are stippled.

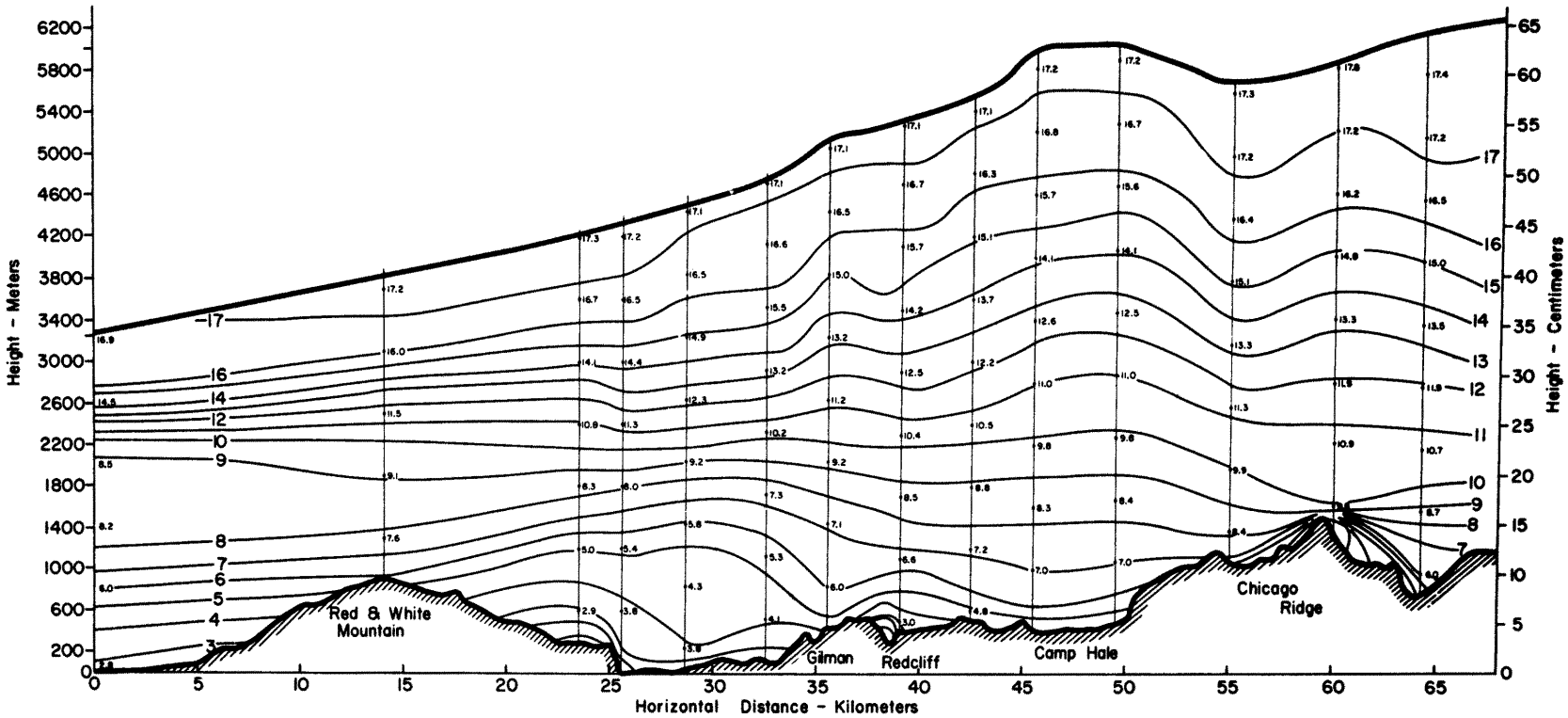

Fig. 4. Development of the momentum boundary-layer thickness and the longitudinal speed field over the model for the neutral model airflow. Thick line represents boundary layer; Velocity (m/s); Distances scaled to prototype 1 cm = 96 meters.

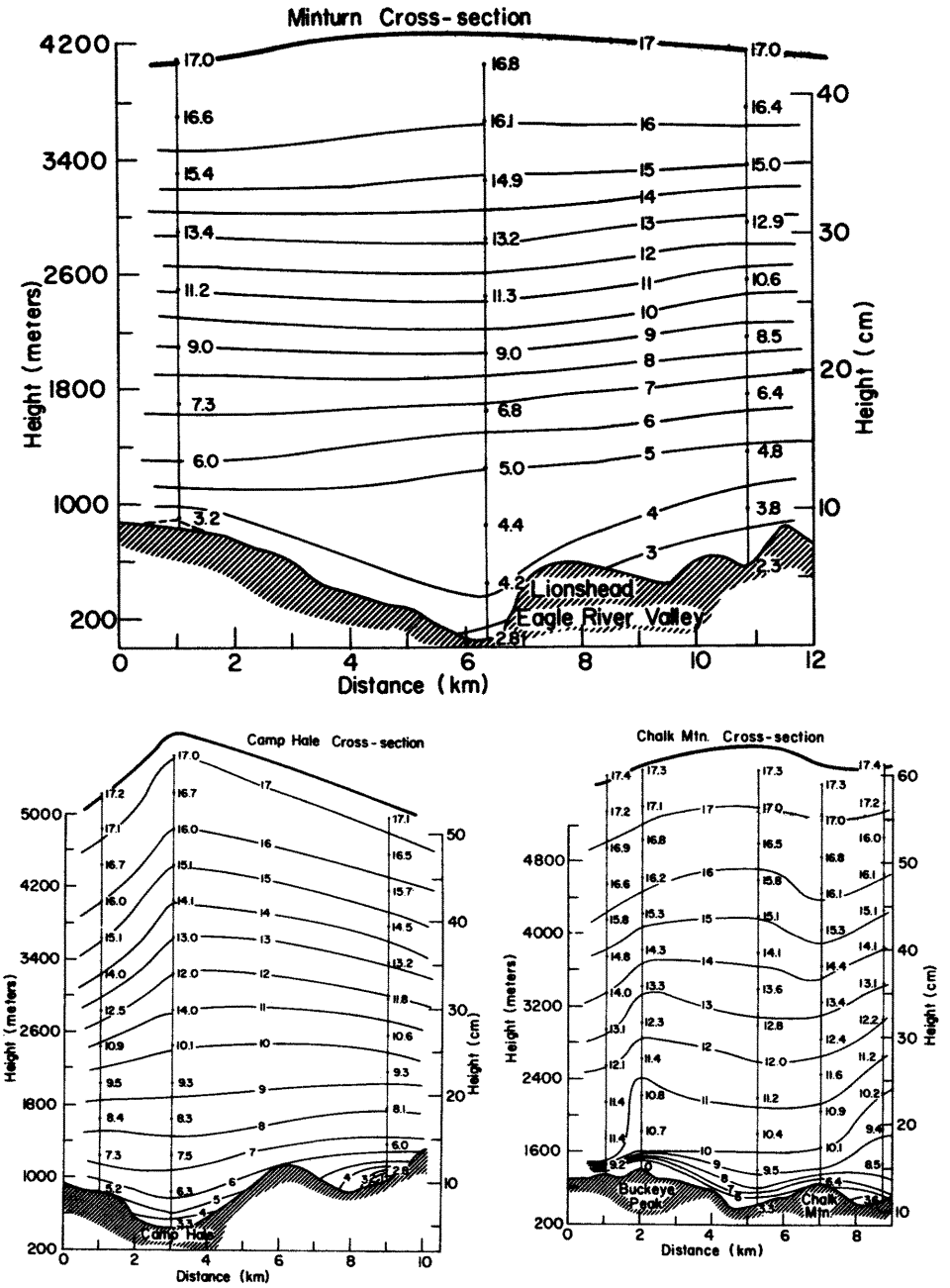

Fig. 5. Selected lateral cross-sections of the vertical distribution of longitudinal velocity over the model for neutral airflow. Thick line represents boundary layer; Velocity (m/s); Distances scaled to prototype 1 cm = 96 meters. Thin vertical lines are measurement locations.

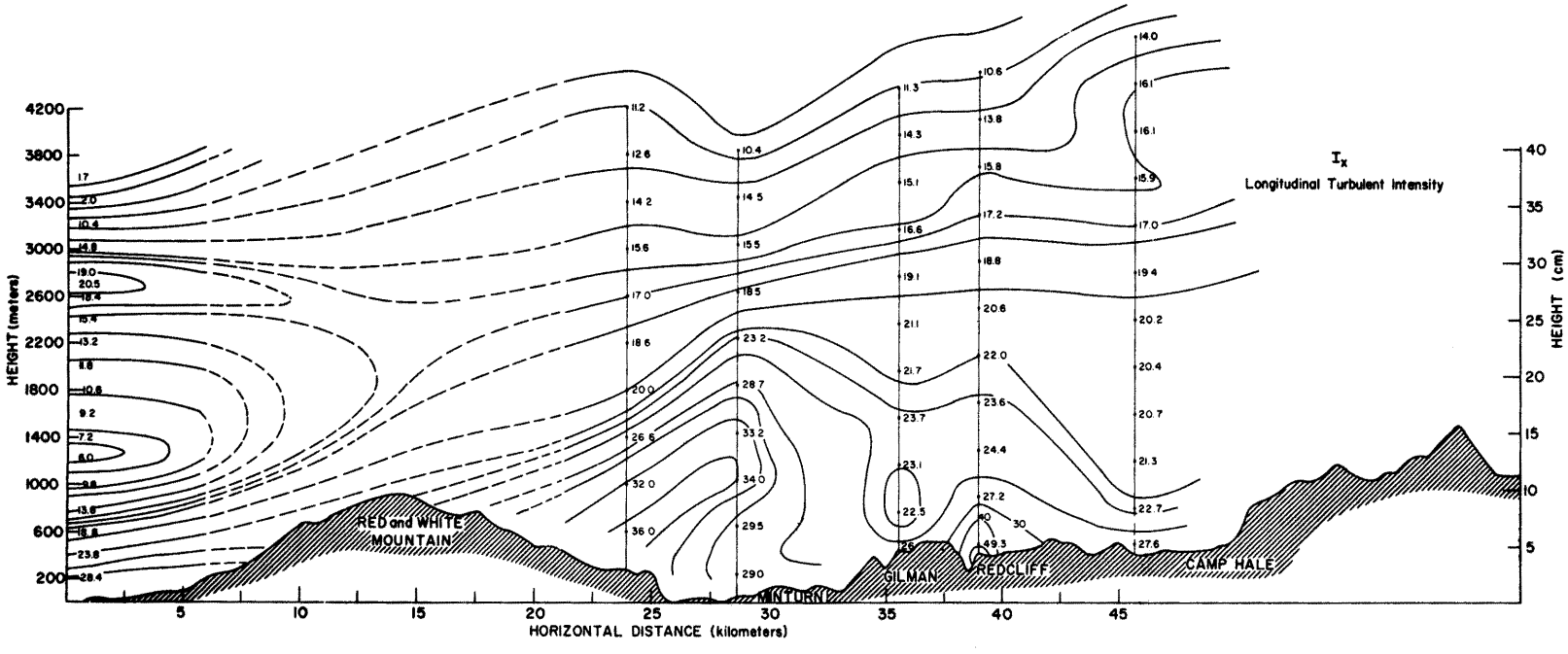

Fig. 6. Vertical distribution of the longitudinal turbulent intensity (%) over the model for neutral airflow. Distances scaled to prototype. Dash lines indicate where analysis may be uncertain.

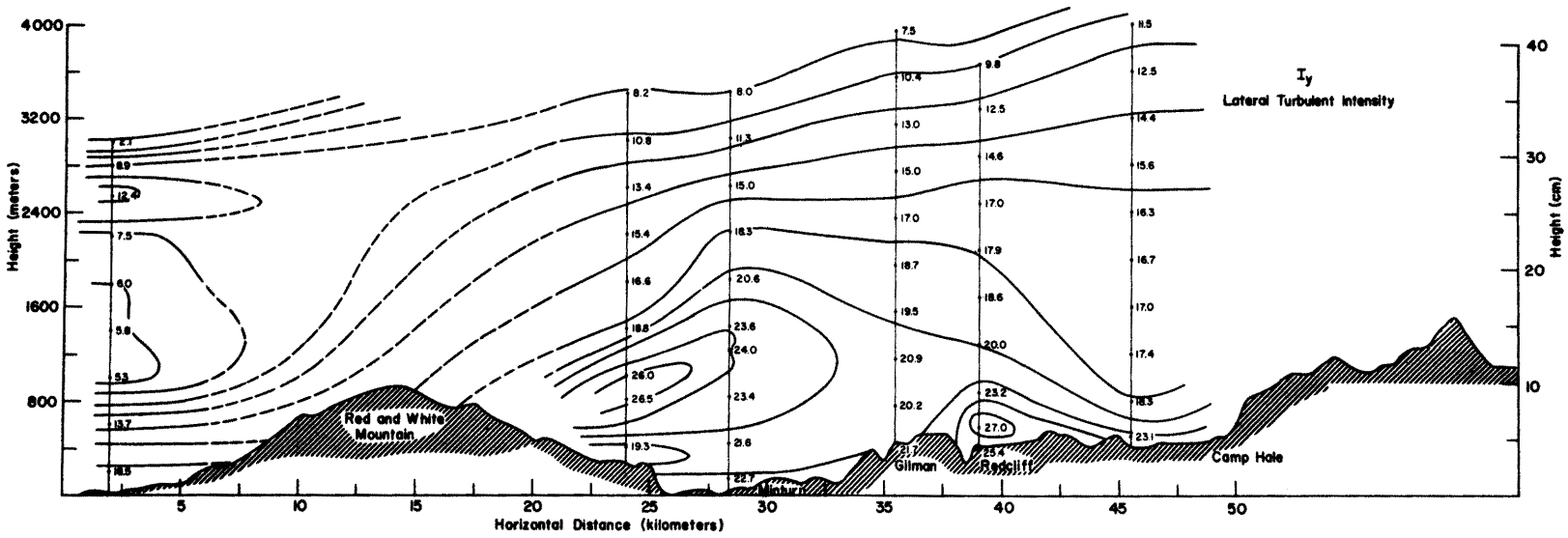

Fig. 7. Vertical distribution of the lateral turbulent intensity (%) over the model for neutral airflow.

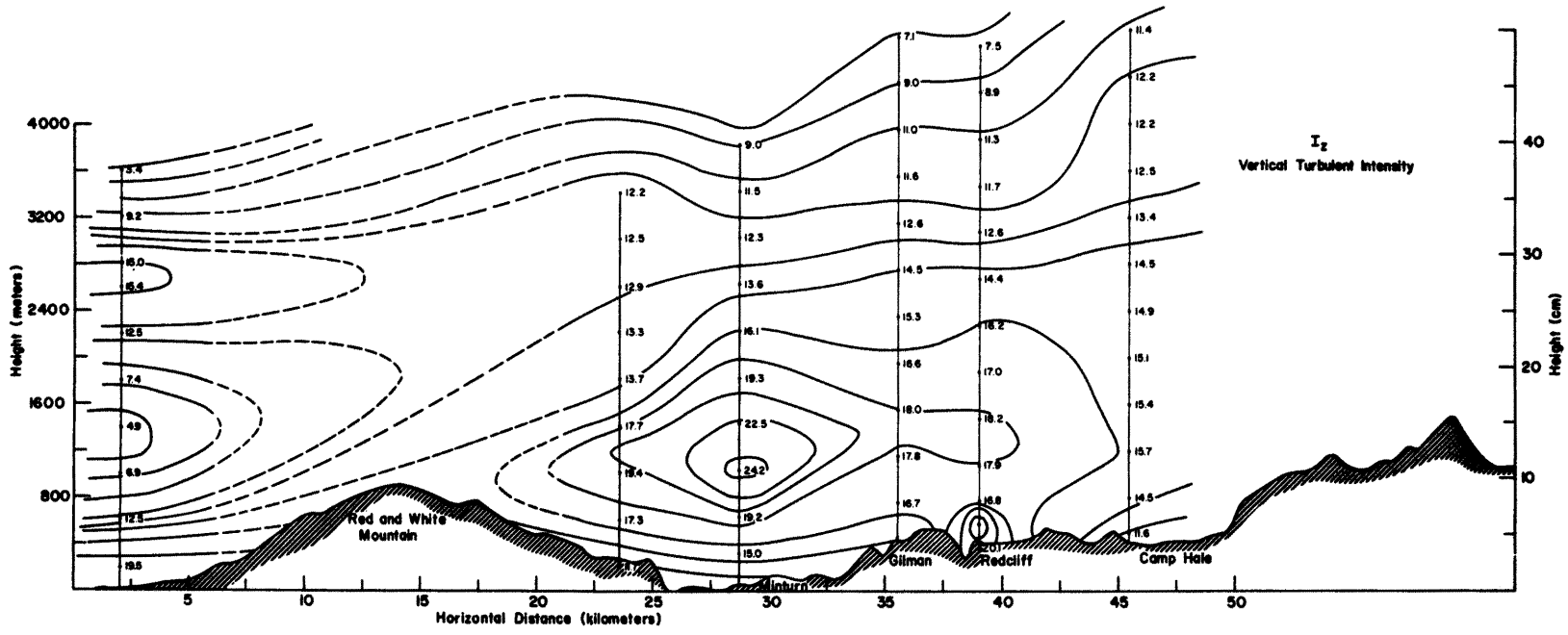

Fig. 8. Vertical distribution of the vertical turbulent intensity (%) over the model for neutral airflow.

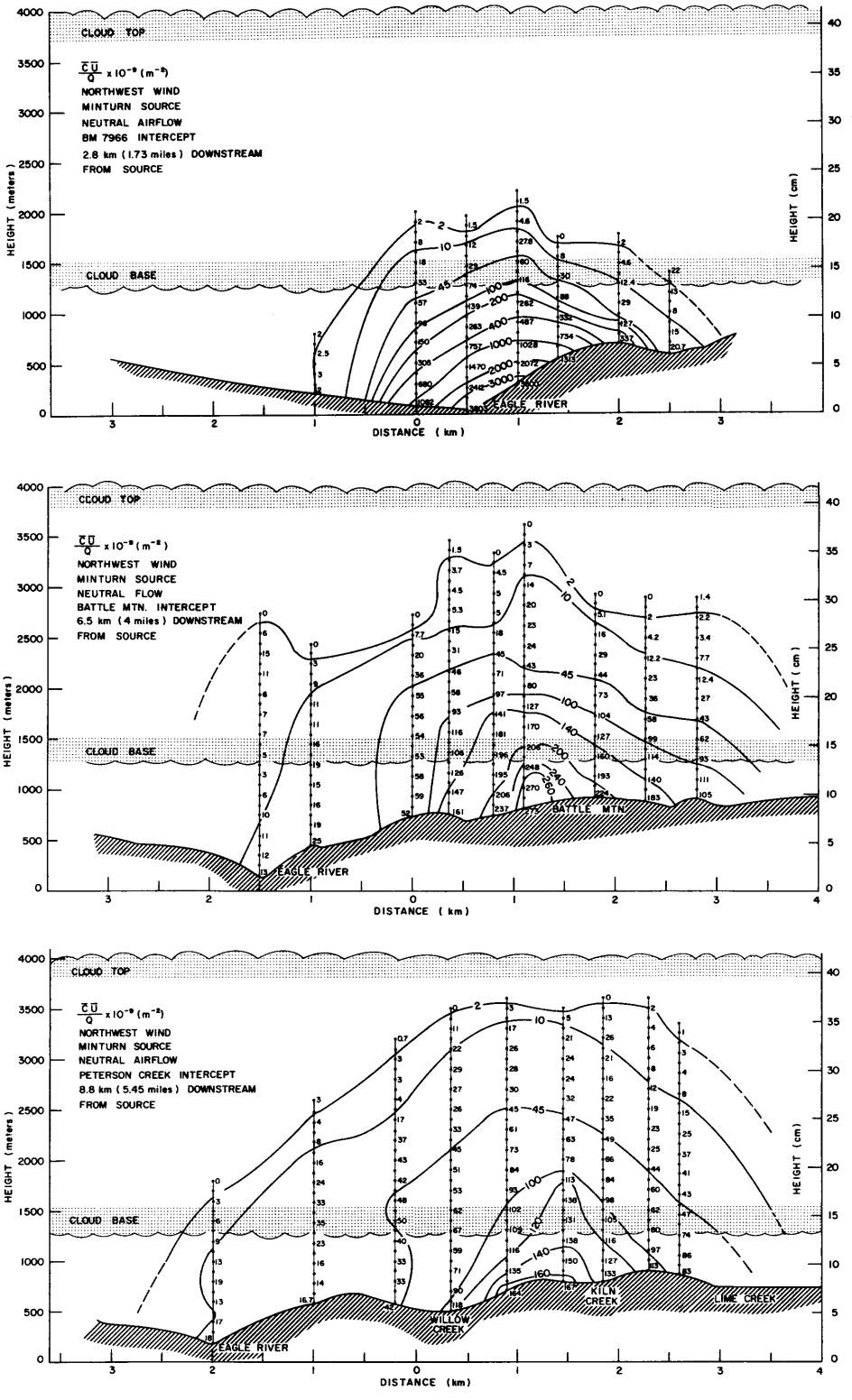

Fig. 9. Lateral cross-sections of the concentration parameter $\overline{C}\,\overline{U}/Qx10^{-9}m^{-2}$ downwind from the Minturn source. Neutral model airflow. Thin vertical lines are measurement locations.

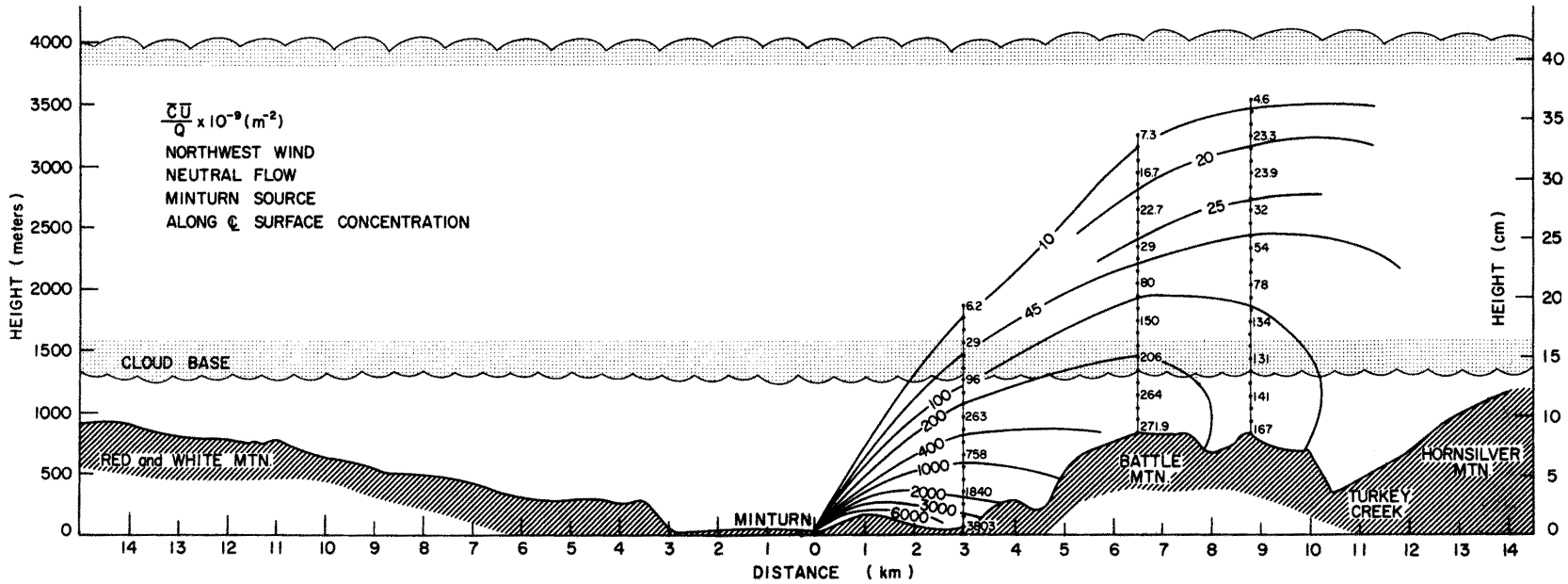

Fig. 10. Vertical cross-section of the concentration parameter $C\ U/Qx10^{-9}m^{-2}$ downwind from the Minturn source. Neutral airflow. Thin vertical lines are measurement locations. Cloud simulates average cloud conditions over the Eagle River Valley.

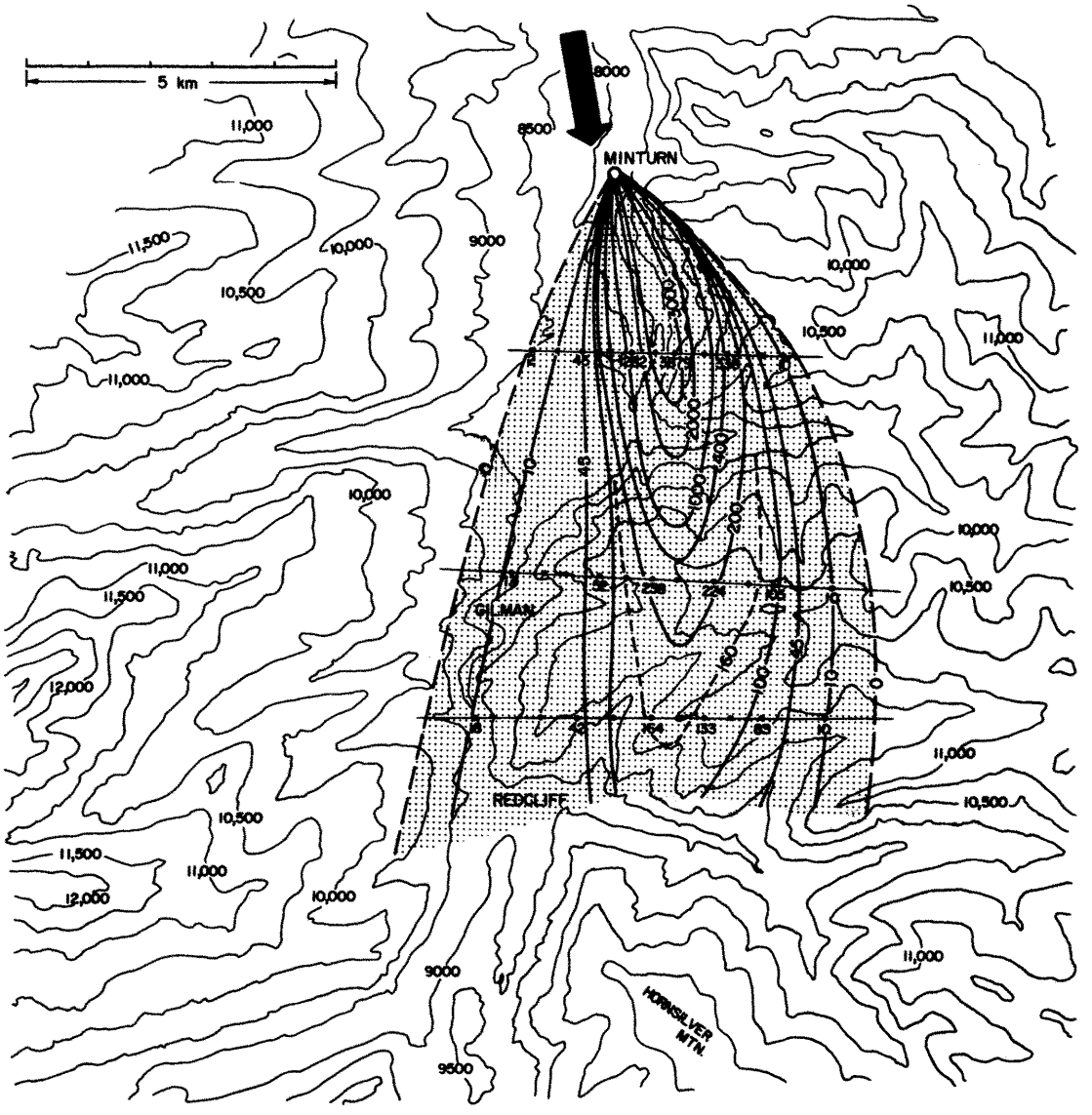

Fig. 11. Surface concentration $\overline{C}\,\overline{U}/Qx10^{-9}m^{-2}$ downwind from the Minturn source. Neutral airflow. Thin lines are mesurement locations.

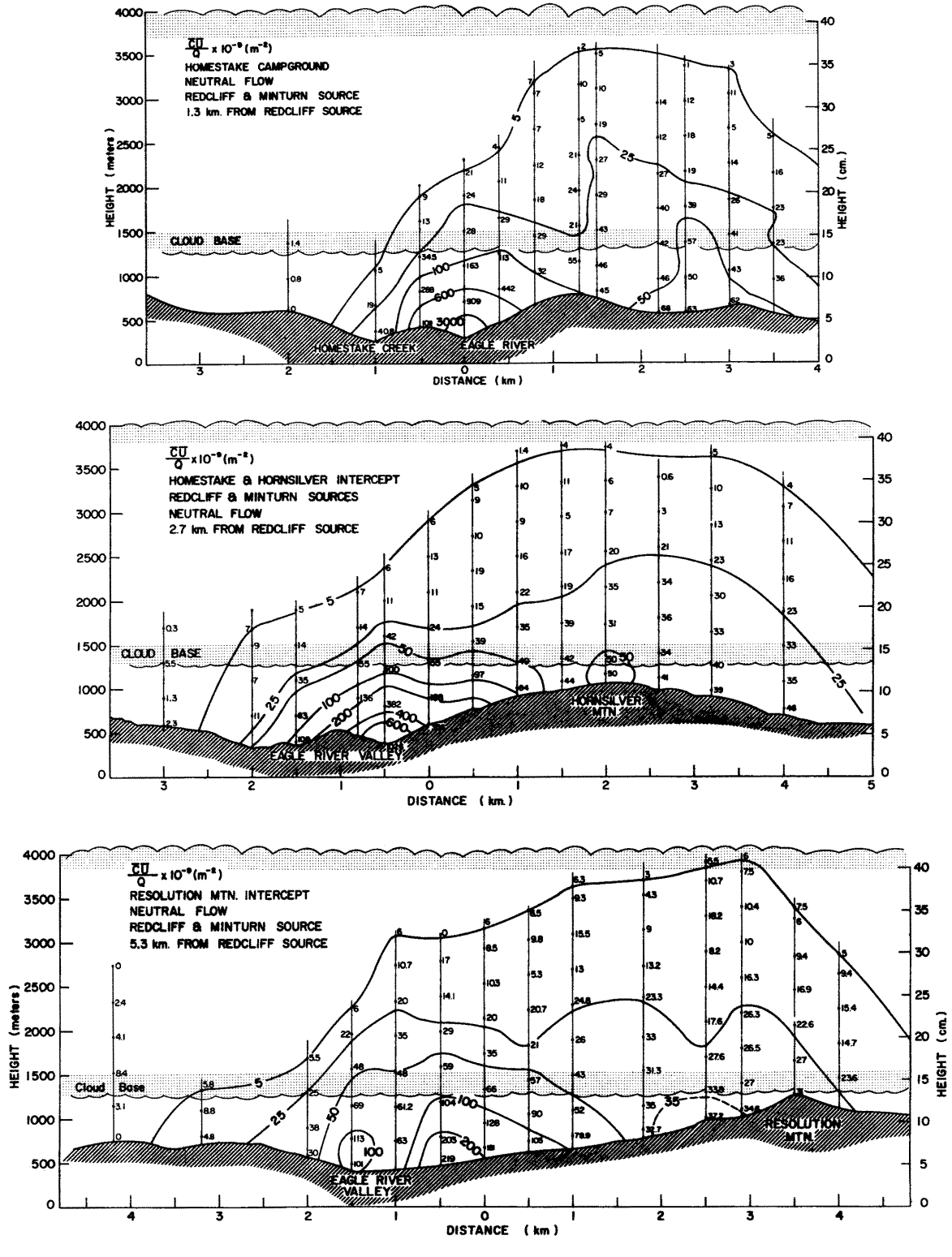

Fig. 12. Lateral cross-section of concentration parameter $\overline{C}\,\overline{U}/Qx10^{-9}m^{-2}$ downwind from Minturn and Redcliff sources. Neutral airflow. Thin vertical lines are measurement locations.

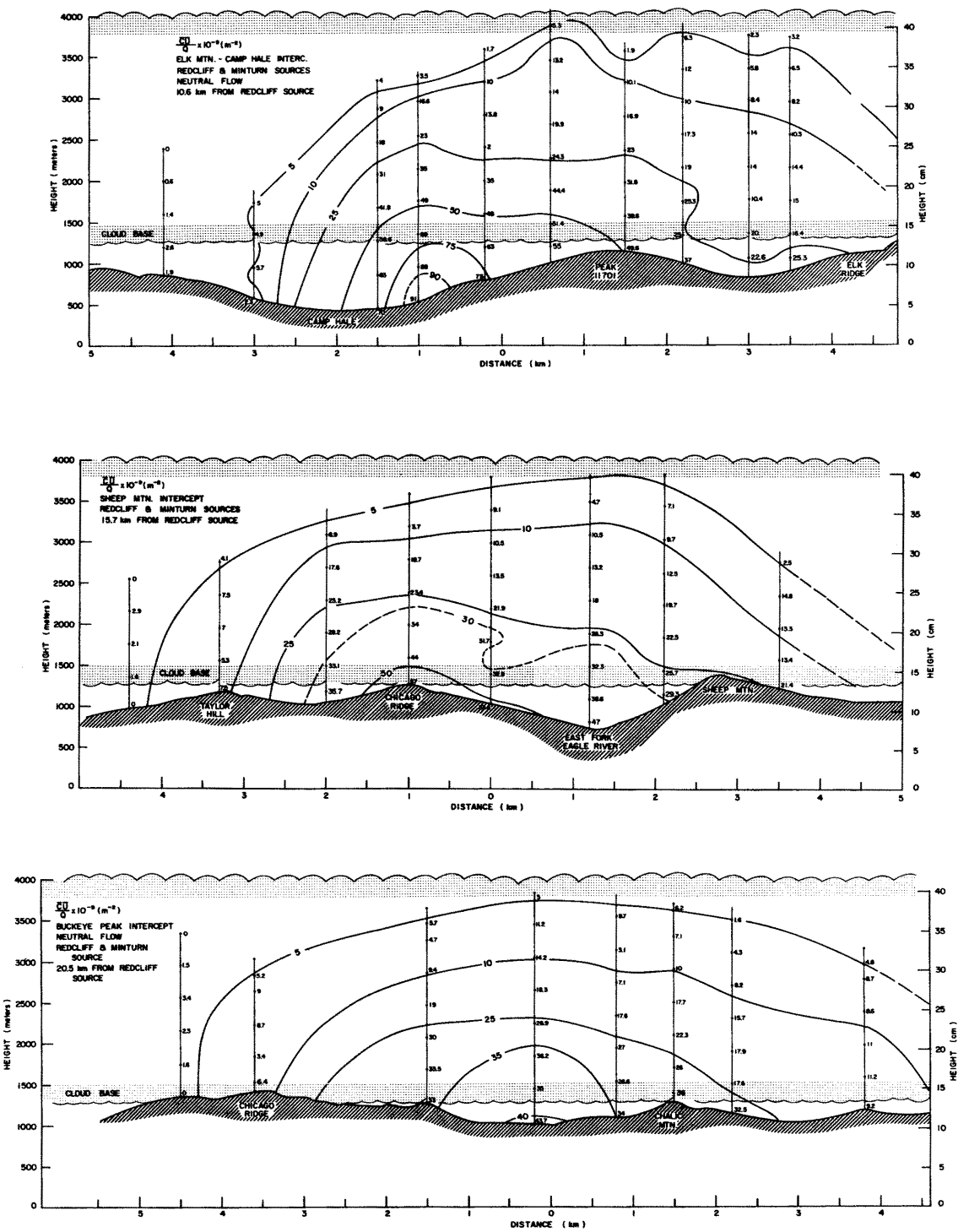

Fig. 13. Same as Figure 12 but further downstream.

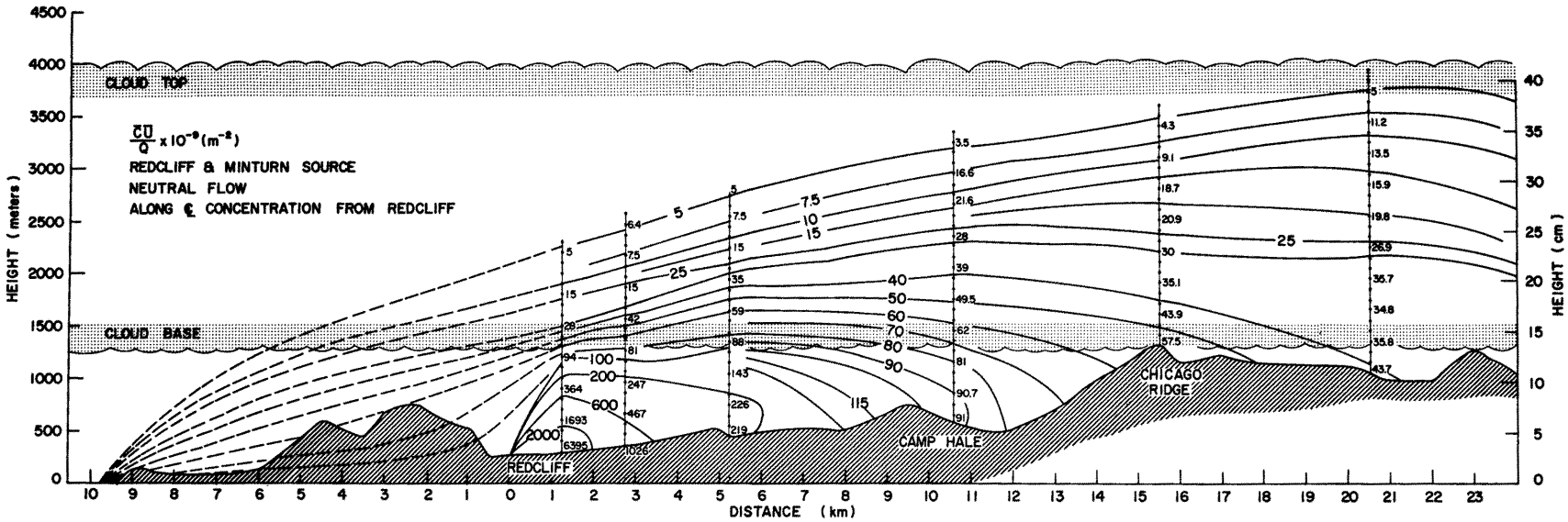

Fig. 14. Vertical cross-section of concentration parameter $\bar{C}\,\bar{U}/Qx10^{-9}m^{-2}$ downwind from Minturn and Redcliff sources. Neutral airflow. Thin lines are measurement locations. Cloud simulates average cloud conditions over the Eagle River Valley.

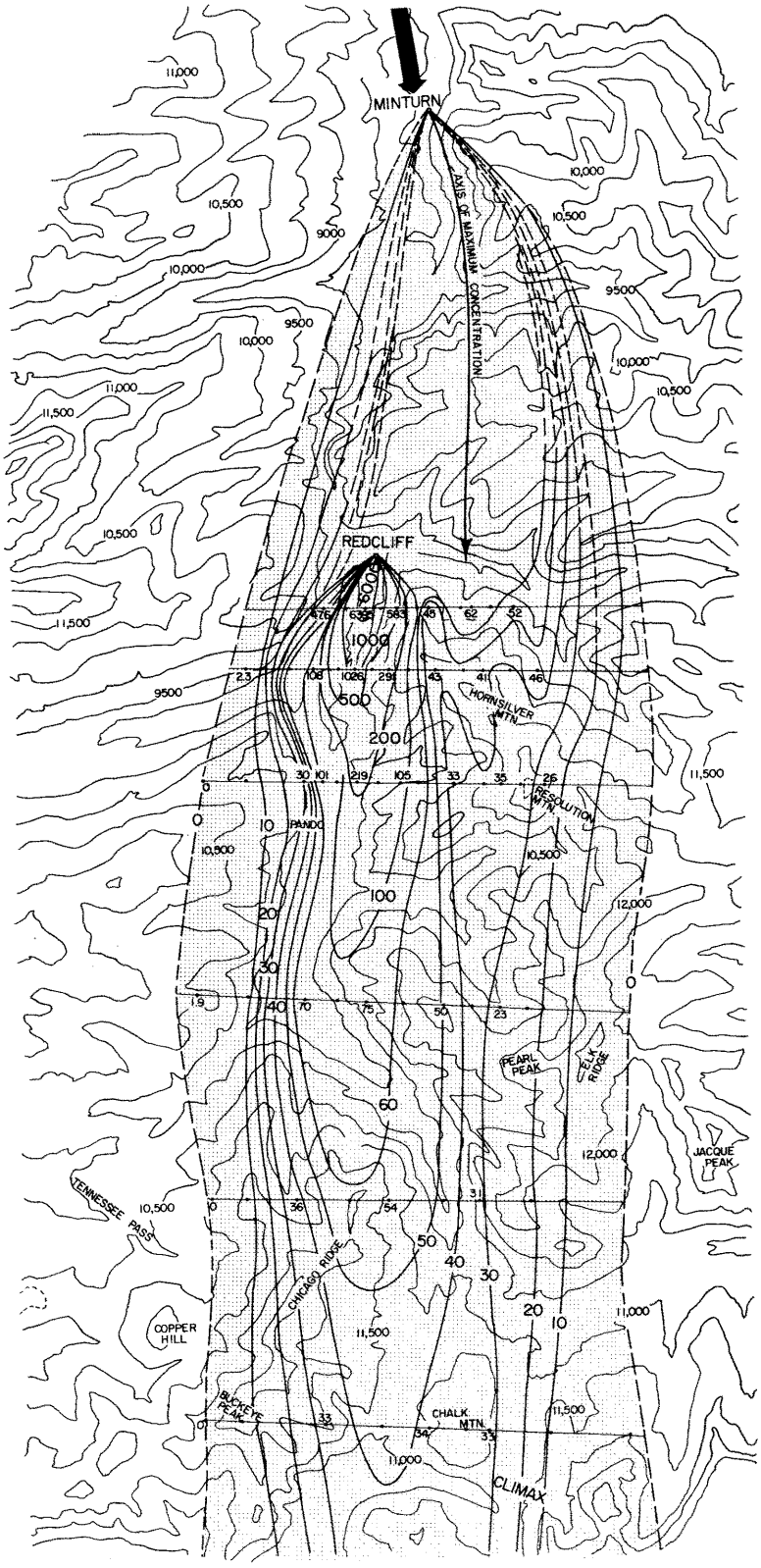

Fig. 15. Surface concentration $\overline{C}\,\overline{U}/Qx10^{-9}m^{-2}$ downwind from Minturn and Redcliff sources. Neutral airflow. Thin lines are measurement locations.

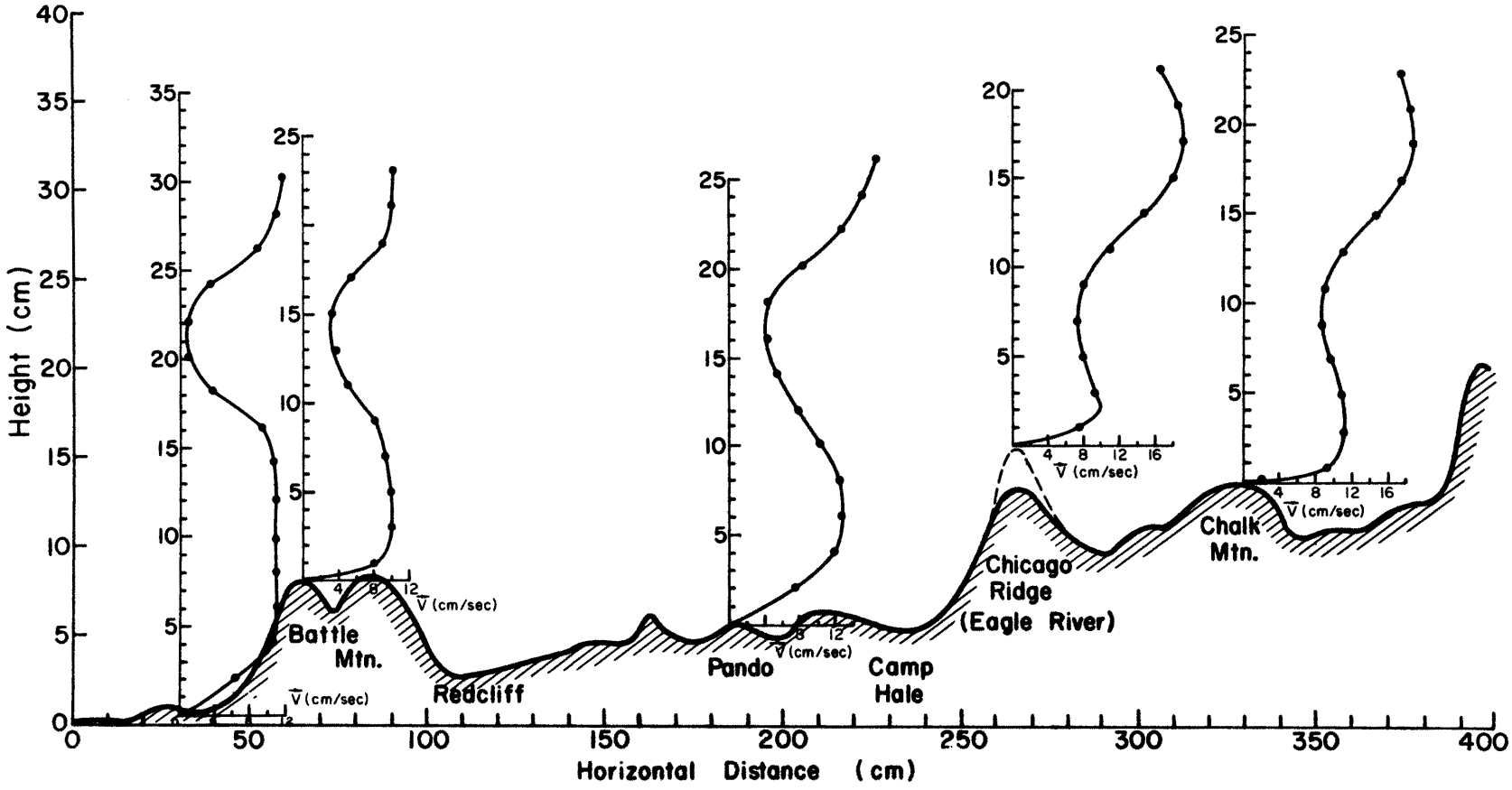

Fig. 16. Vertical distribution of the average resultant airflow velocity (cm/sec) over the model for the barostromatic airflow. Determined by the "smoke-wire" method. Scale ratio: 1 cm = 96 meters.

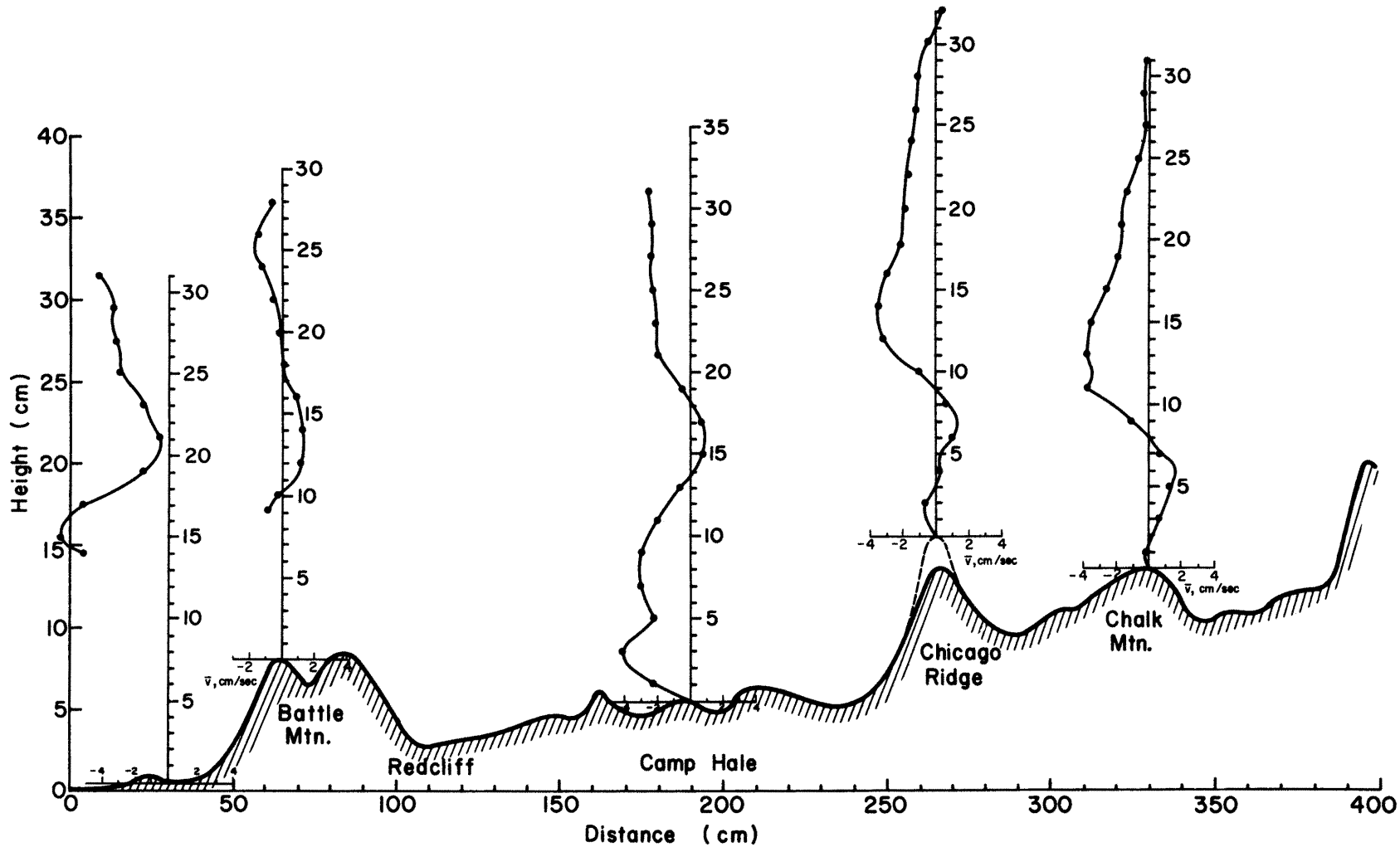

Fig. 17. Vertical distribution of the average lateral airflow velocity (cm/sec) over the model for the barostromatic airflow. Negative values represent north to northeast components; positive, west to southwest components in respect to the field. Scale ratio: 1 cm = 96 meters.

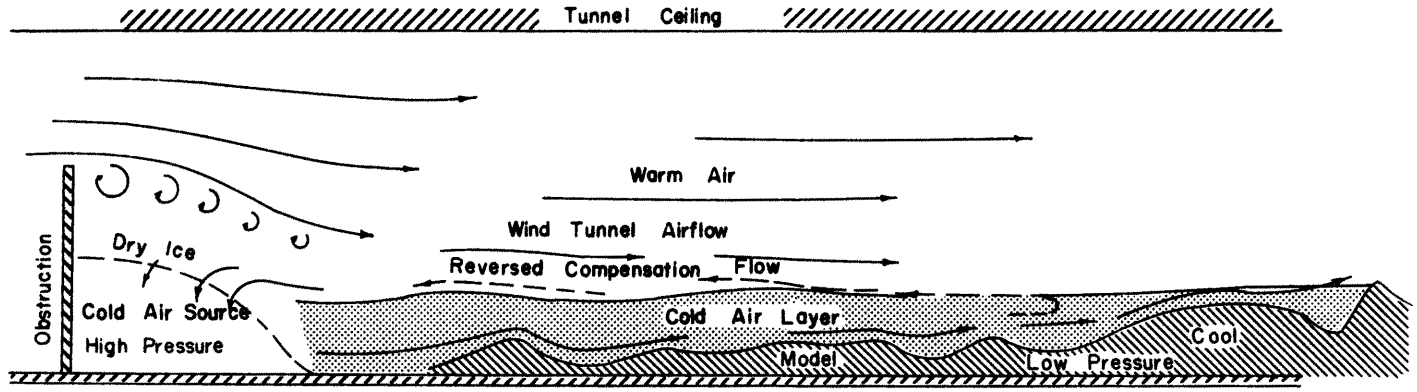

The Reversed Compensation Flow is Counteracted by the Wind Tunnel Air Flow When Wind Tunnel is Operating

Fig. 18. Schematic representation of the wind-tunnel airflow as derived from the combination of wind tunnel and dry ice. Barostromatic airflow.

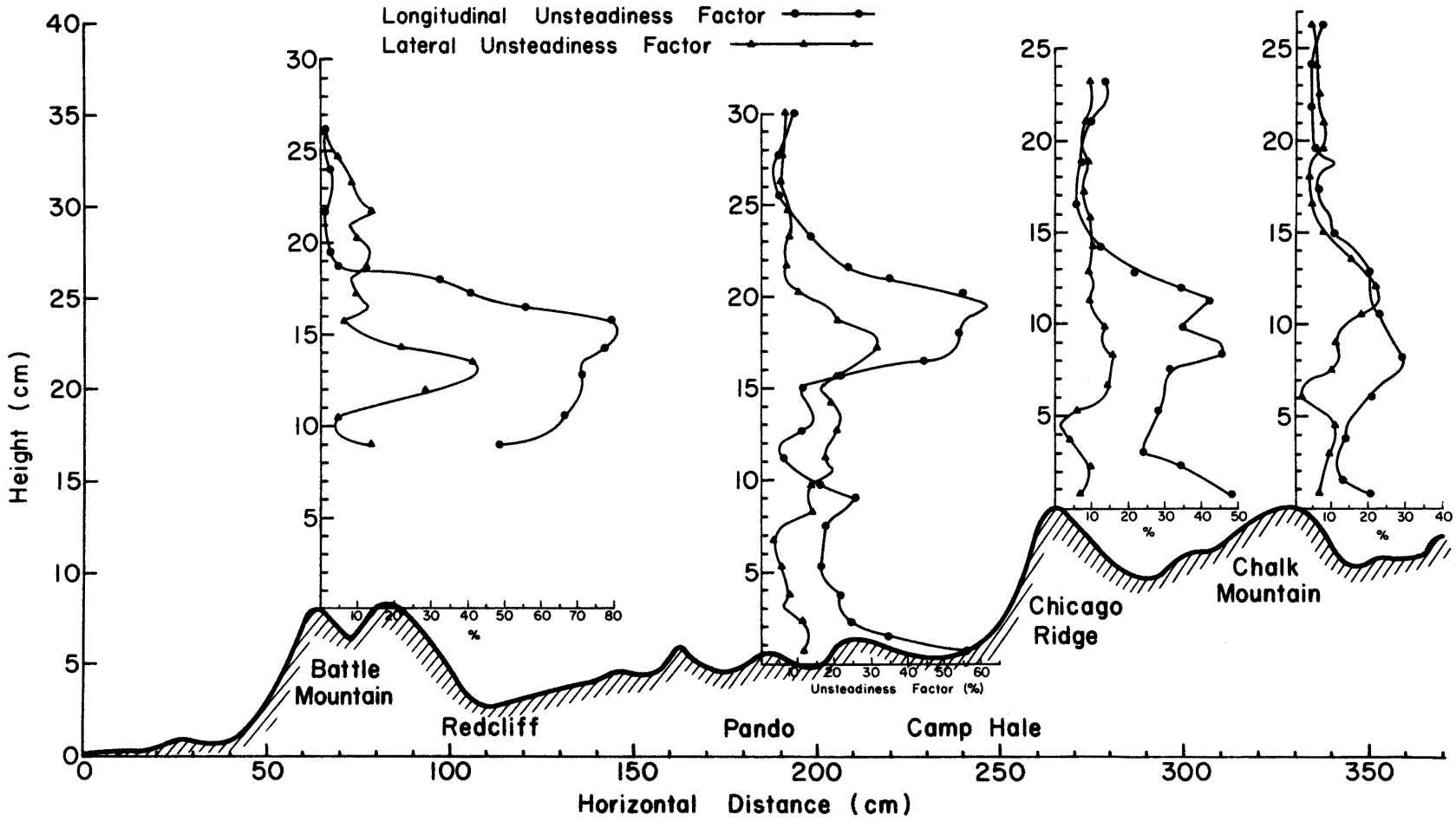

Fig. 19. Vertical distribution of longitudinal and lateral unsteadiness factors (%) for barostromatic airflow. Computed from "smoke-wire" velocity data. Scale ratio: 1 cm = 96 meters.

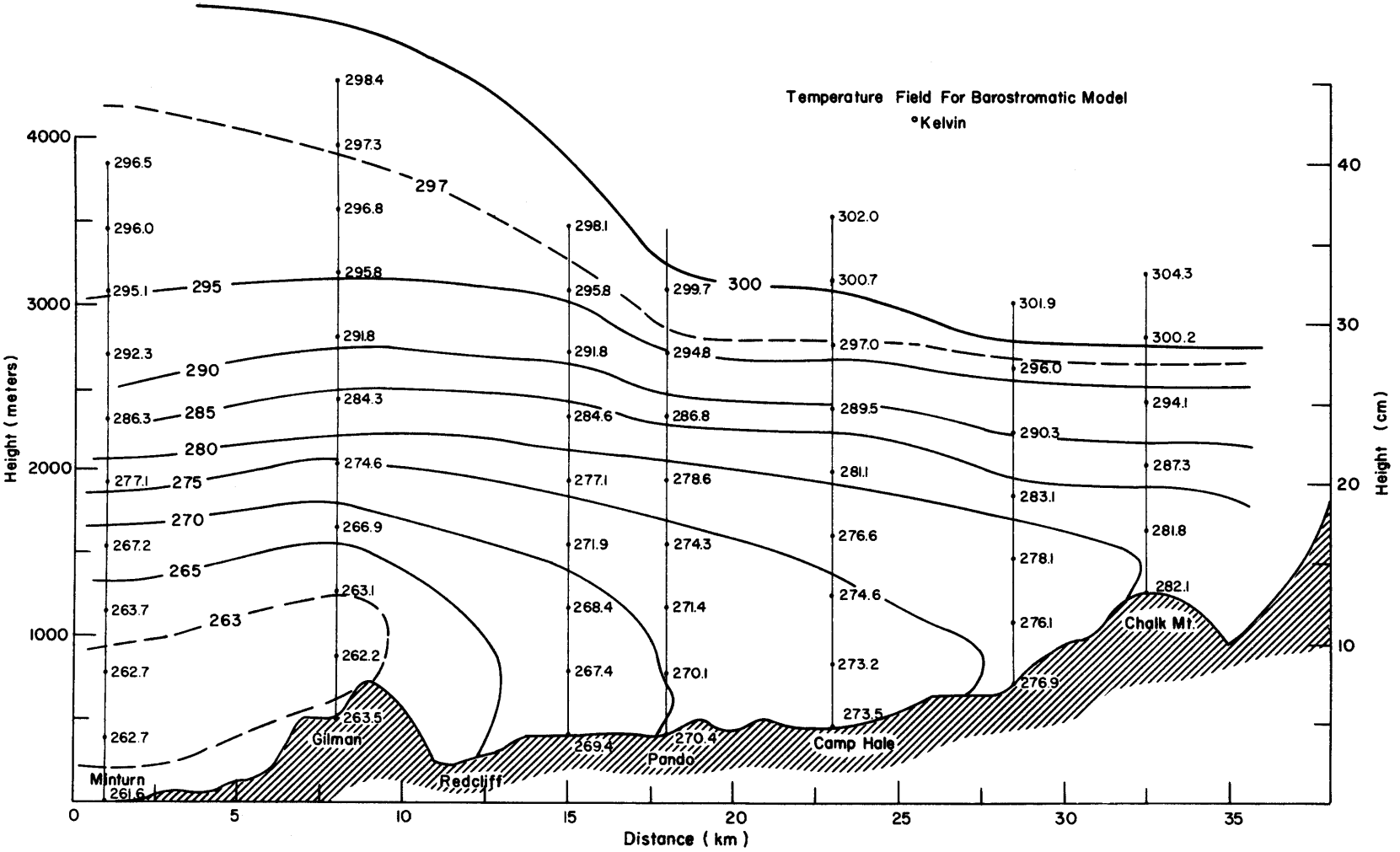

Fig. 20. Vertical distribution of the temperature over the model as produced by the dry ice airflow. Scale length ratio 1 cm = 96 meters.

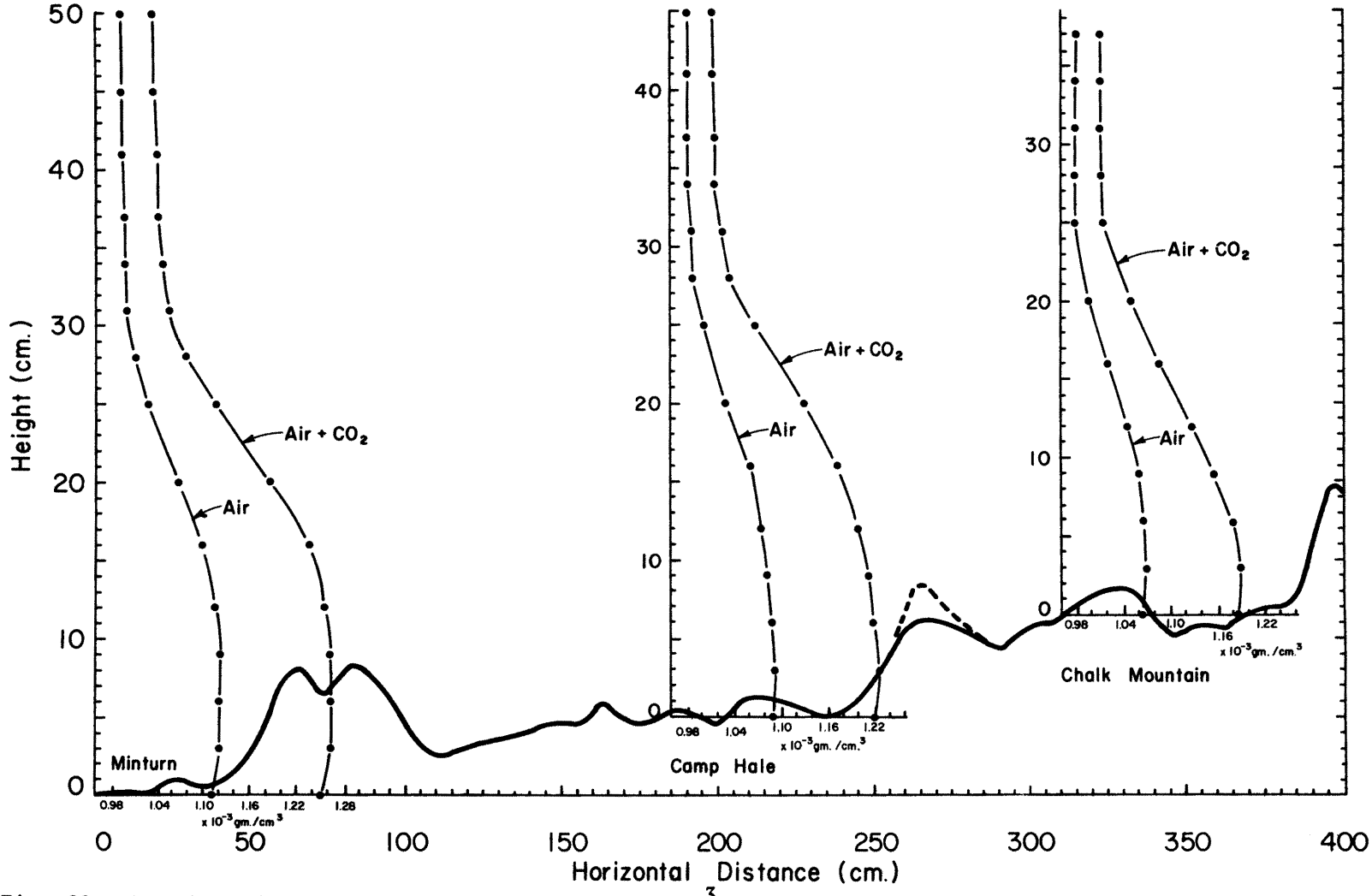

Fig. 21. Vertical distribution of the density (gm/cm^3) for air and air + carbon dioxide over the model for the barostromatic airflow. Scale ratio: 1 cm = 96 meters.

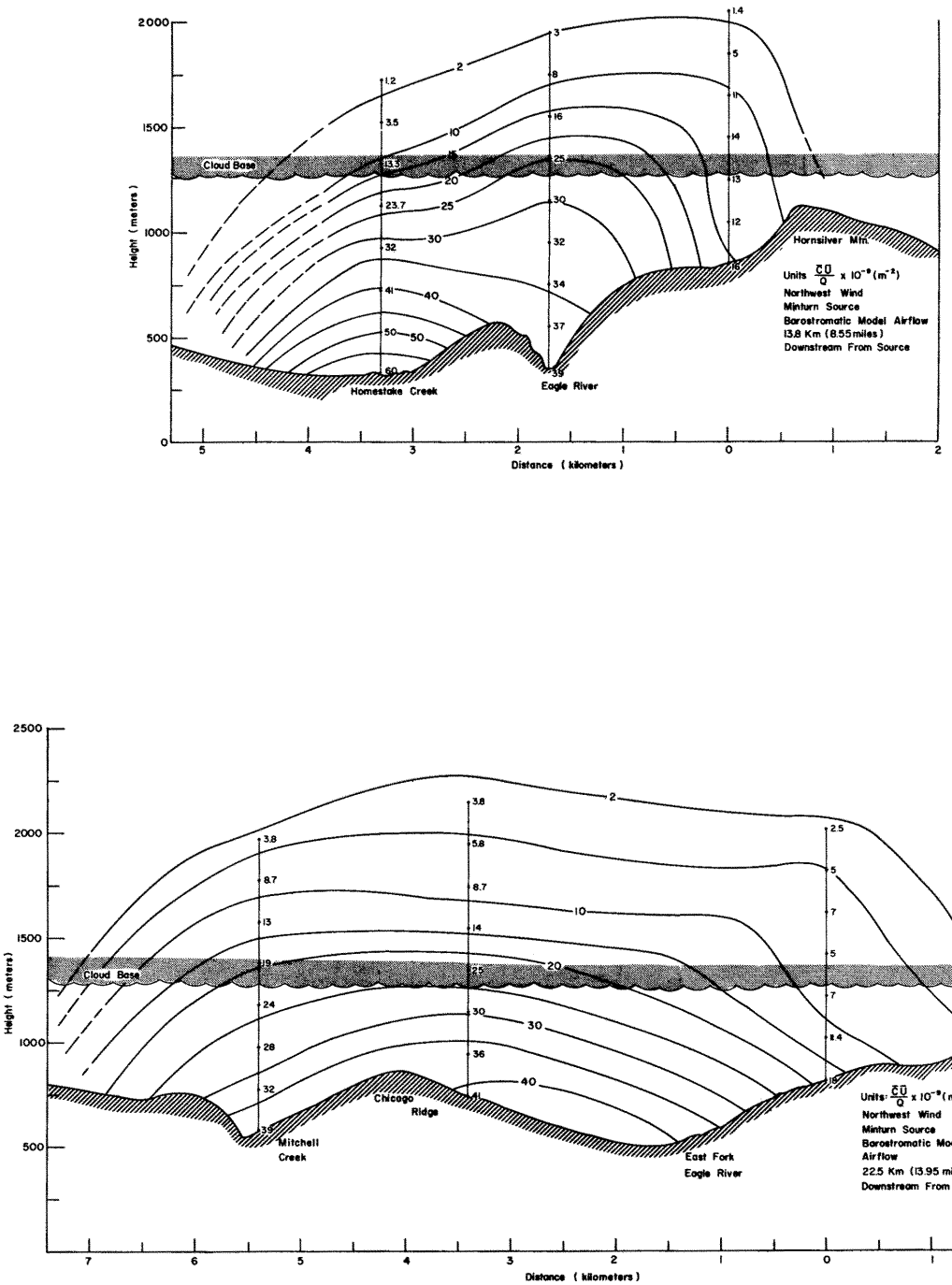

Fig. 22. Lateral cross-sections of the concentration parameter $\overline{C}\,\overline{U}/Qx10^{-9}m^{-2}$ downwind from the Minturn source. Barostromatic model airflow. Thin vertical lines are measurement locations.

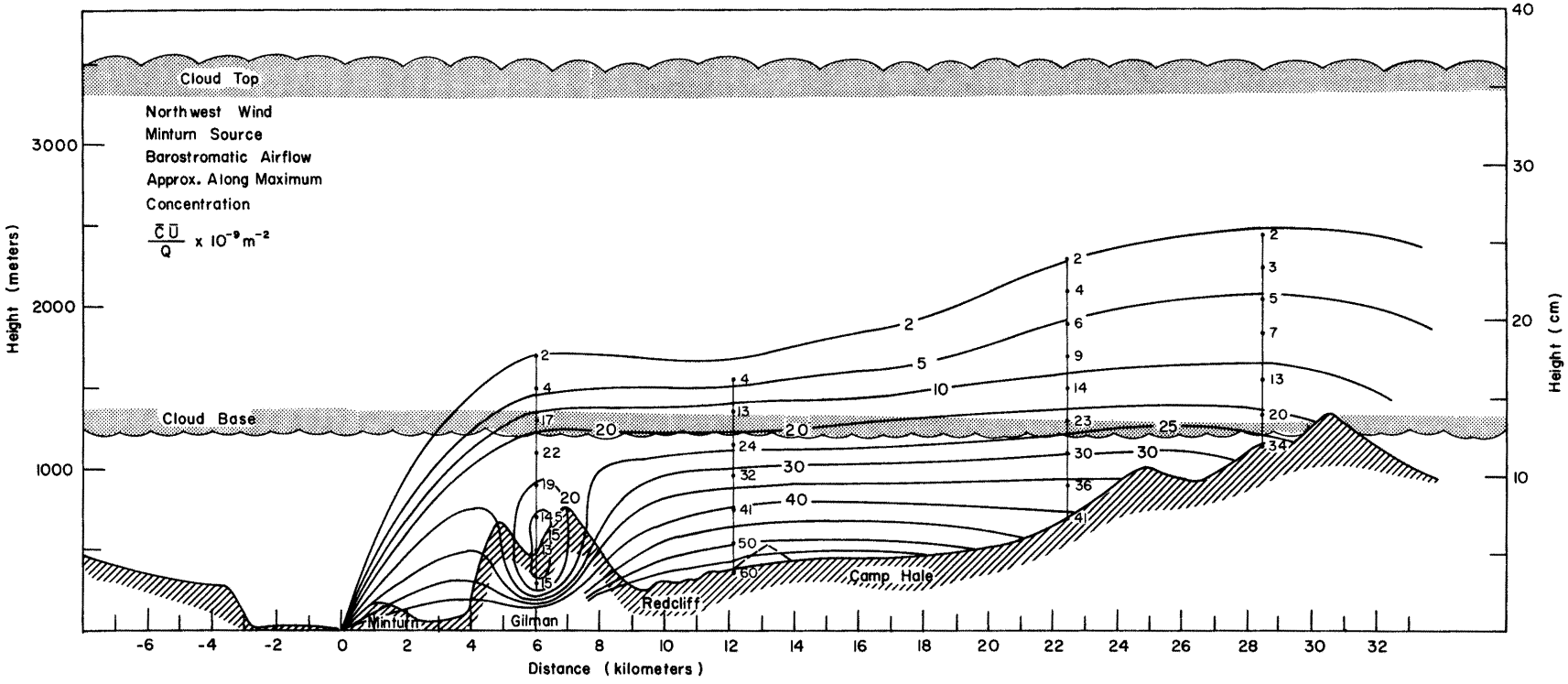

Fig. 23. Vertical cross-section of concentration parameter $\bar{C}\,\bar{U}/Qx10^{-9}m^{-2}$ downwind from the Minturn source. Barostromatic airflow. Thin vertical lines are measurement locations. Cloud simulates average cloud conditions over the Eagle River Valley.

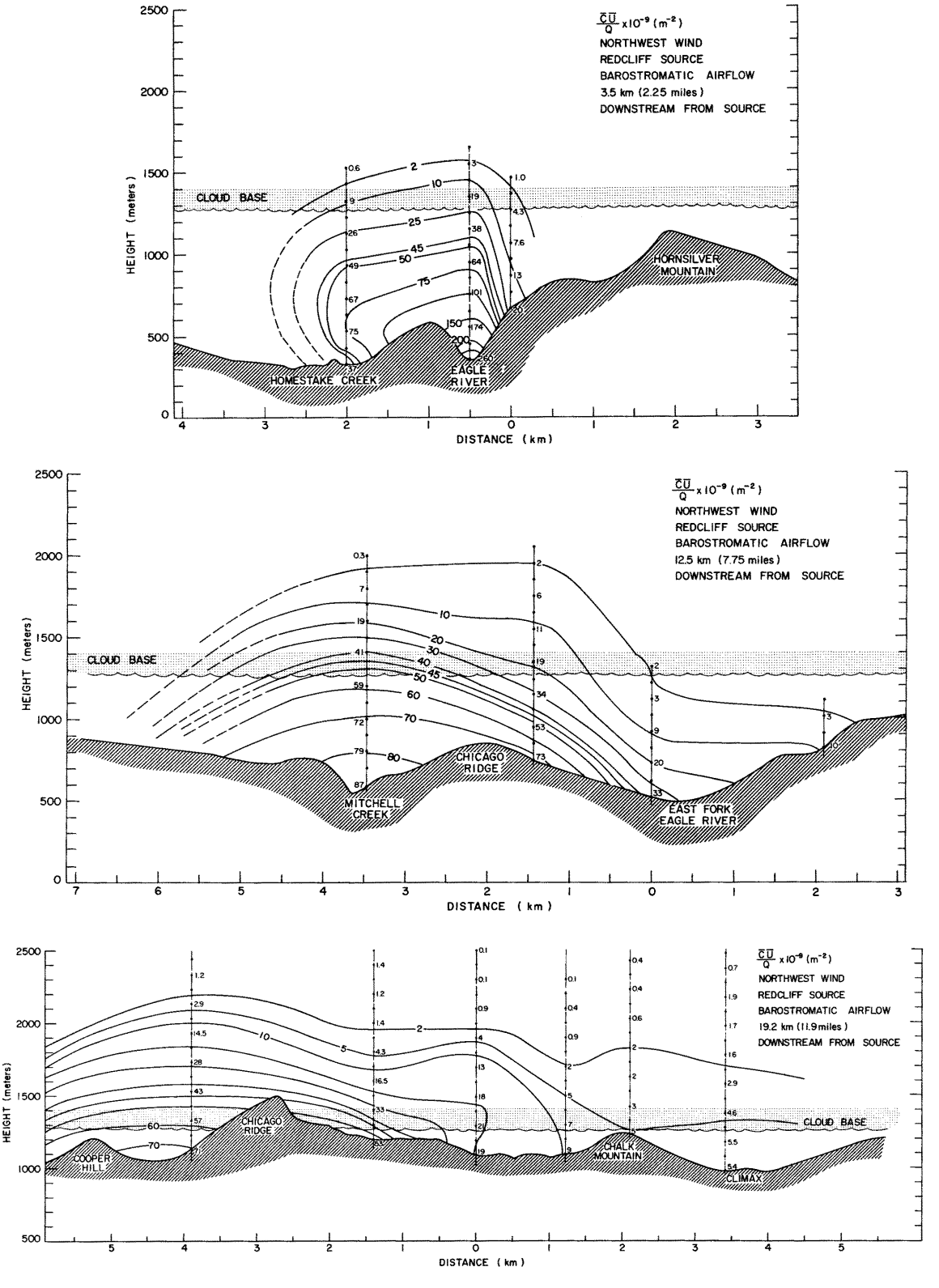

Fig. 24. Lateral cross-section of concentration parameter $\bar{C}\,\bar{U}/Qx10^{-9}m^{-2}$ downwind from Redcliff source. Barostromatic airflow. Thin vertical lines are measurement locations.

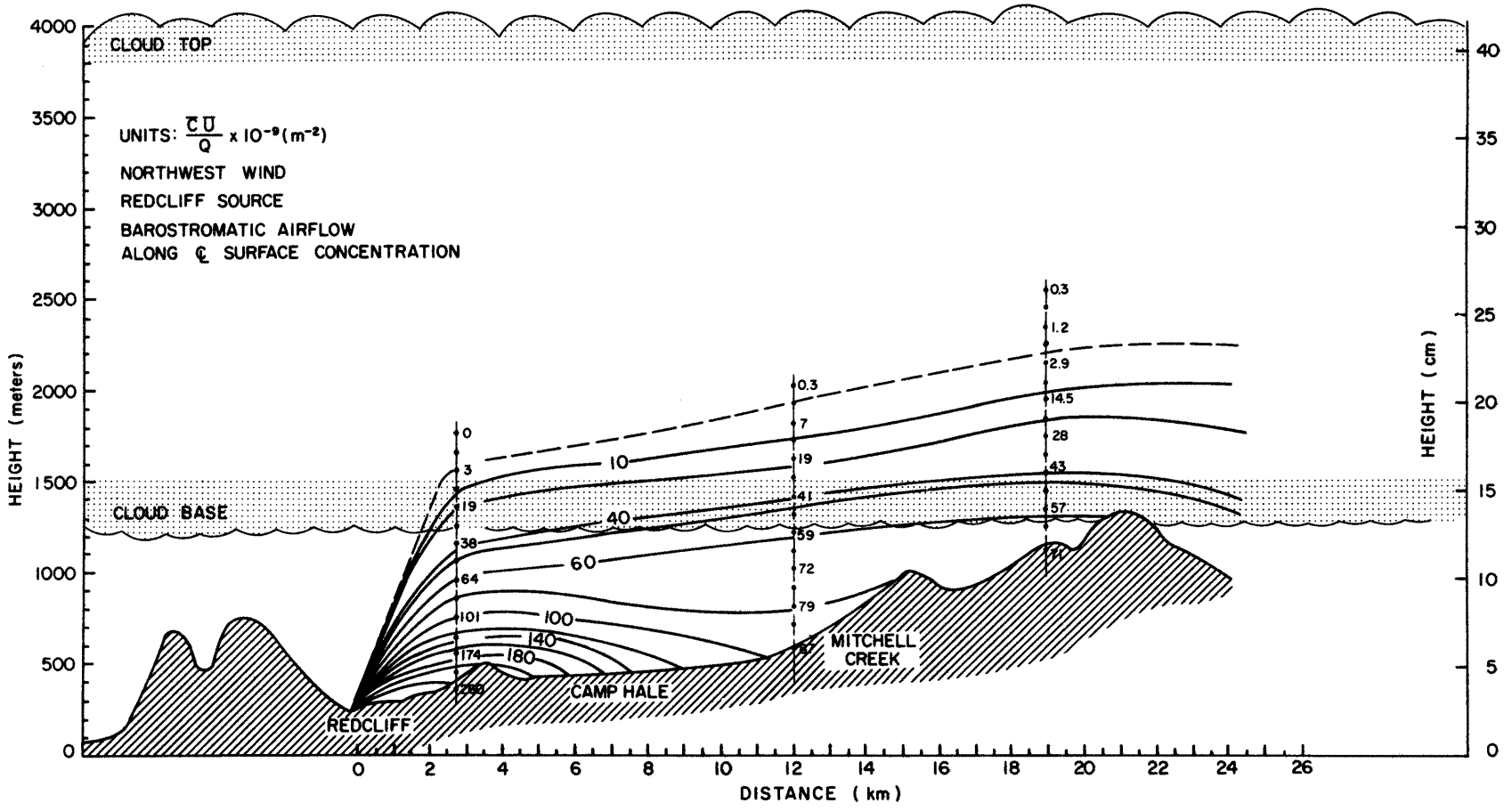

Fig. 25. Vertical cross-section of concentration parameter $\overline{C}\,\overline{U}/Qx10^{-9}m^{-2}$ downwind from Redcliff source. Barostromatic airflow. Thin vertical lines are measurement locations. Cloud simulates average cloud conditions.

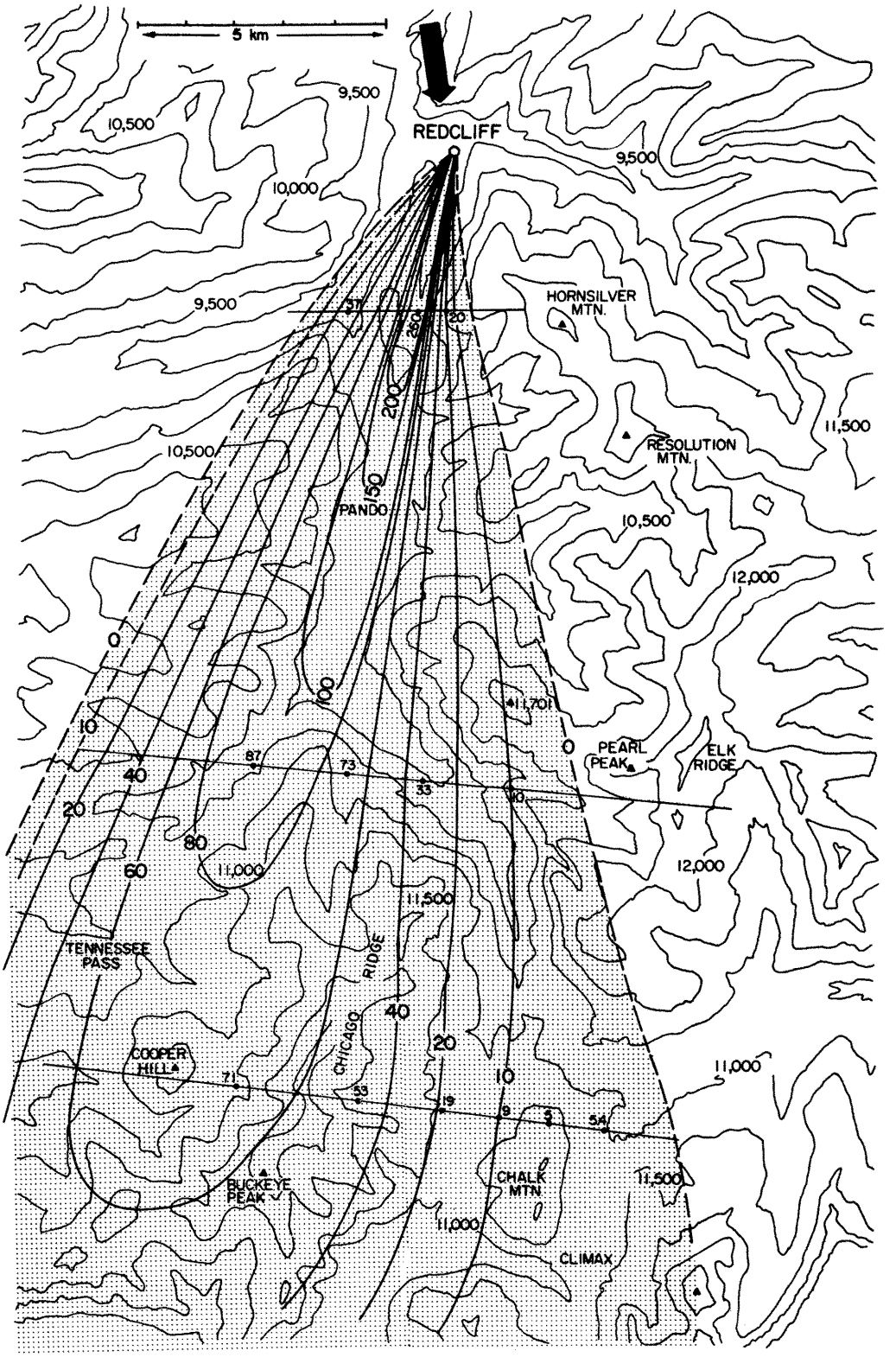

Fig. 26 Surface concentration $\overline{C}\,\overline{U}/Qx10^{-9}m^{-2}$ downwind from Redcliff source. Barostromatic airflow. Thin lines are measurement locations.

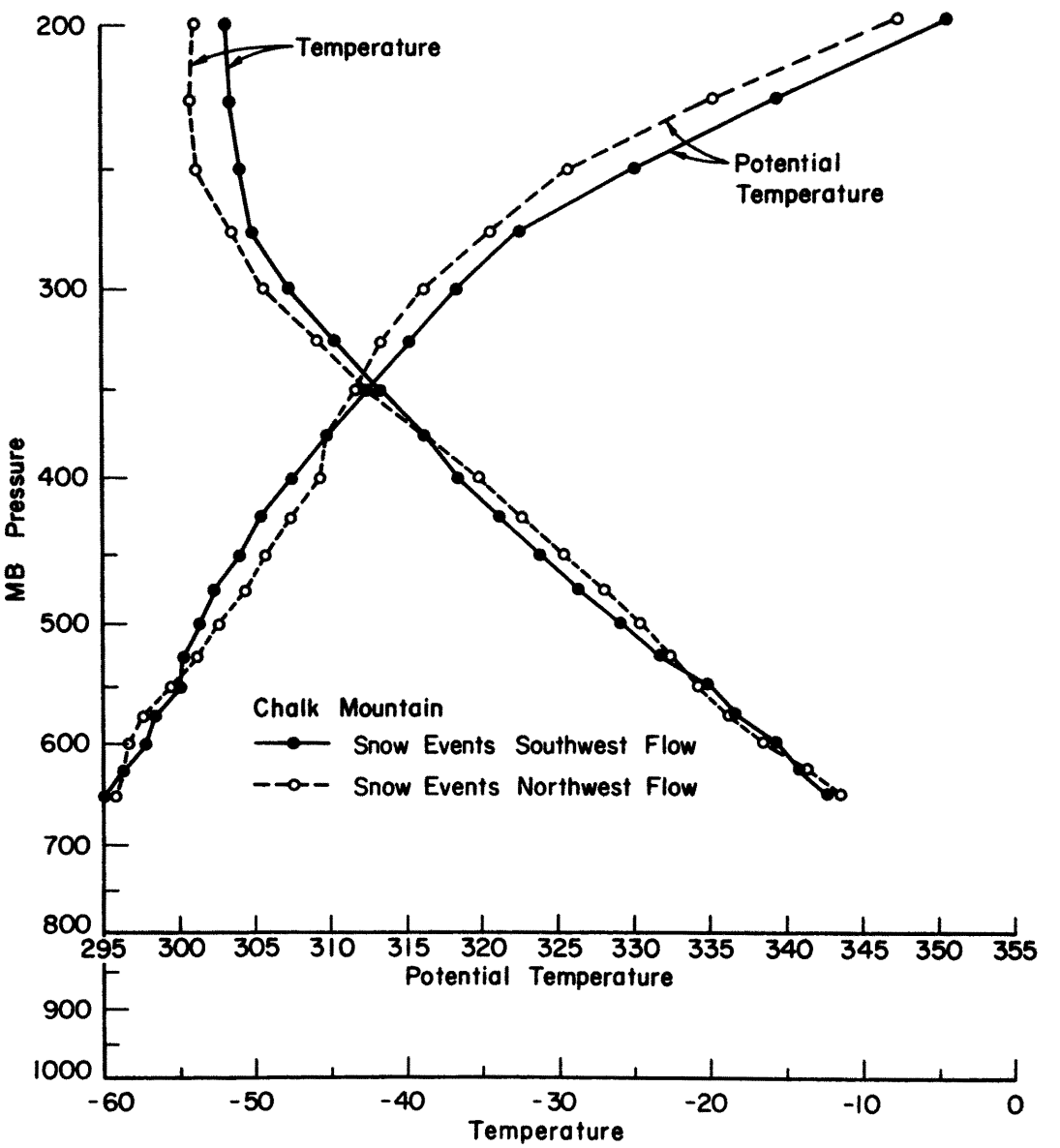

Fig. 27. Vertical distribution of mean temperature (C^{o}) and potential temperature (K^{o}) at Chalk Mountain during snow events with northwest and southwest airflow.

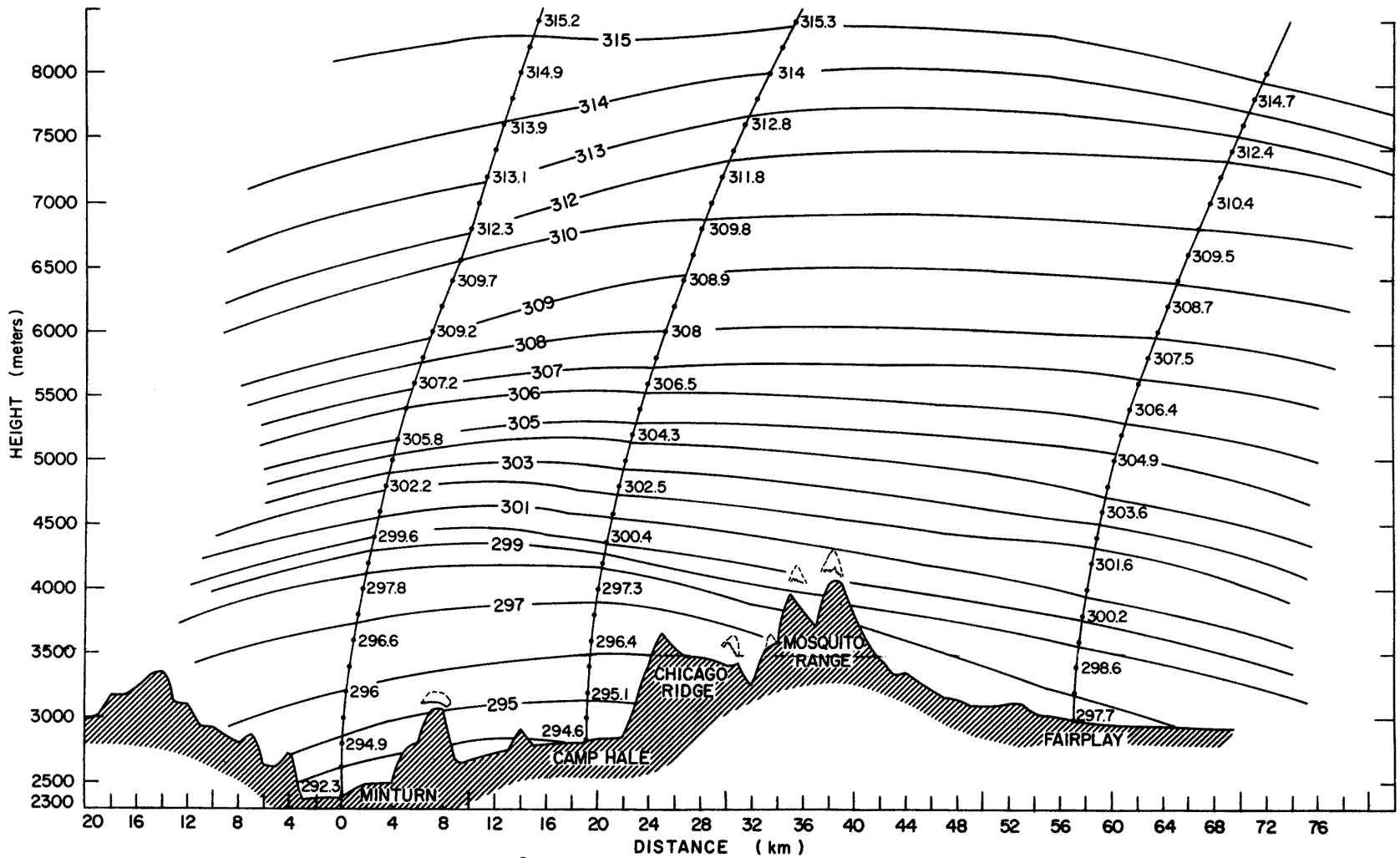

Fig. 28. Mean potential temperature (^{o}K) cross-section based on four soundings from Minturn, Camp Hale, and Fairplay. Time interval approximately 1400 to 2000 MST, 15 January, 1970, Weather: Northwest winds, cloudy and snowing.

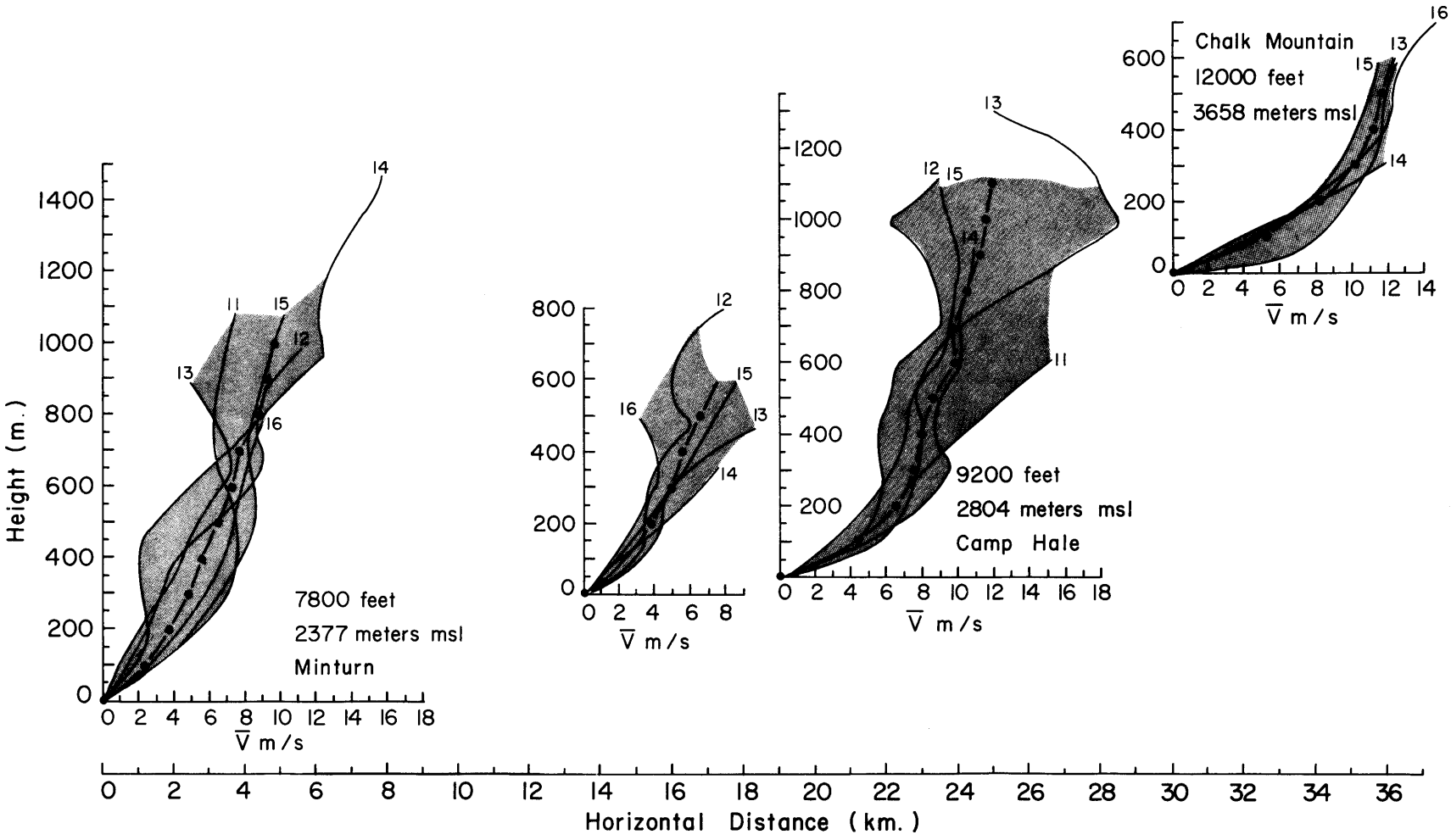

Fig. 29. Variation of the average (dash-dot) and instantaneous (thin line) wind speed with height in the Eagle River Valley during a deep, near-neutral stability snowstorm. Wind direction: Northwest. Numbers are local time. Wind speeds derived from pilot balloons. Weather: Light snow and gusty winds. December 10, 1969.

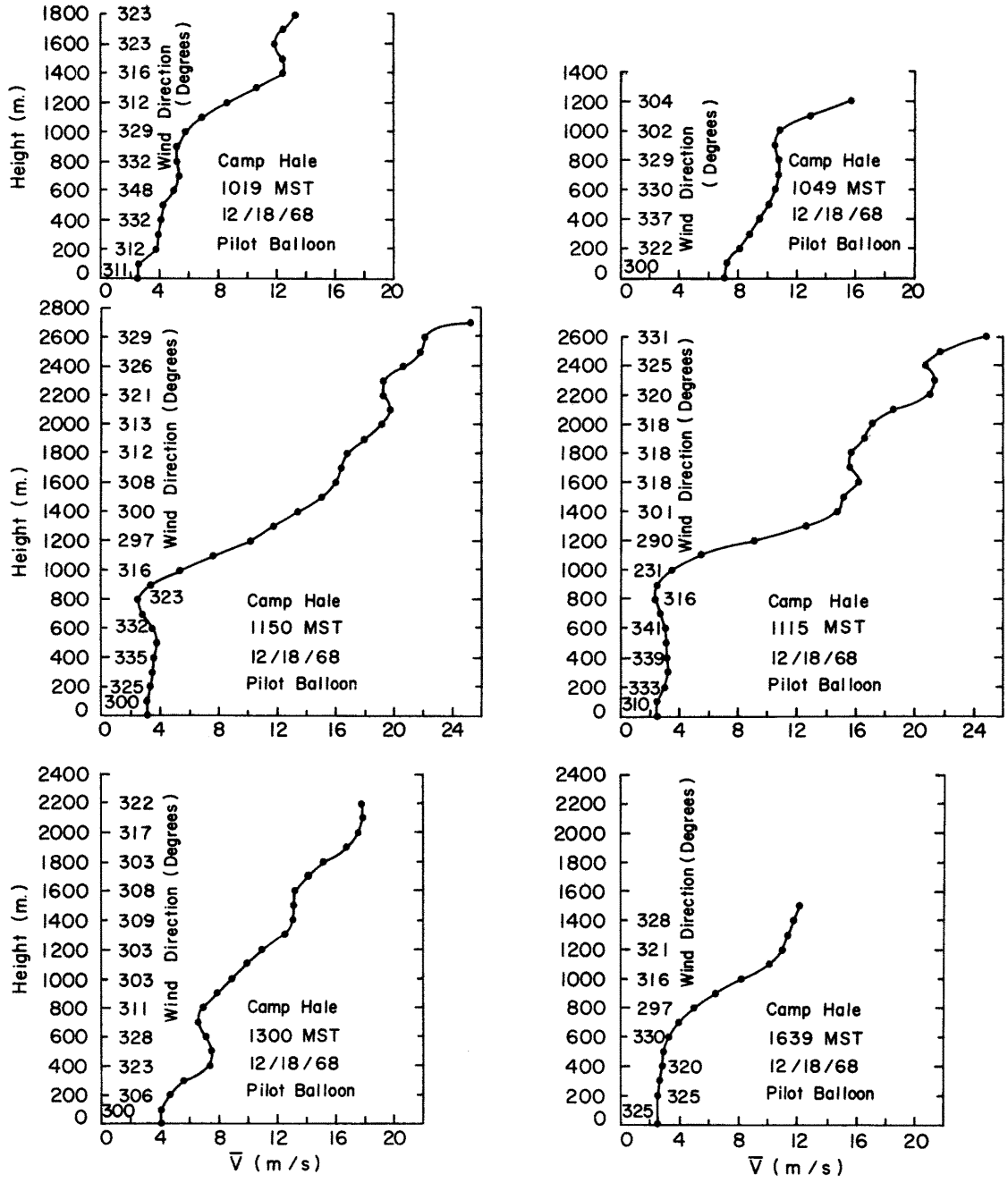

Fig. 30. Vertical distribution of windspeeds (m/s) and directions (degrees) at Camp Hale as determined by pilot balloons. December 18, 1968.

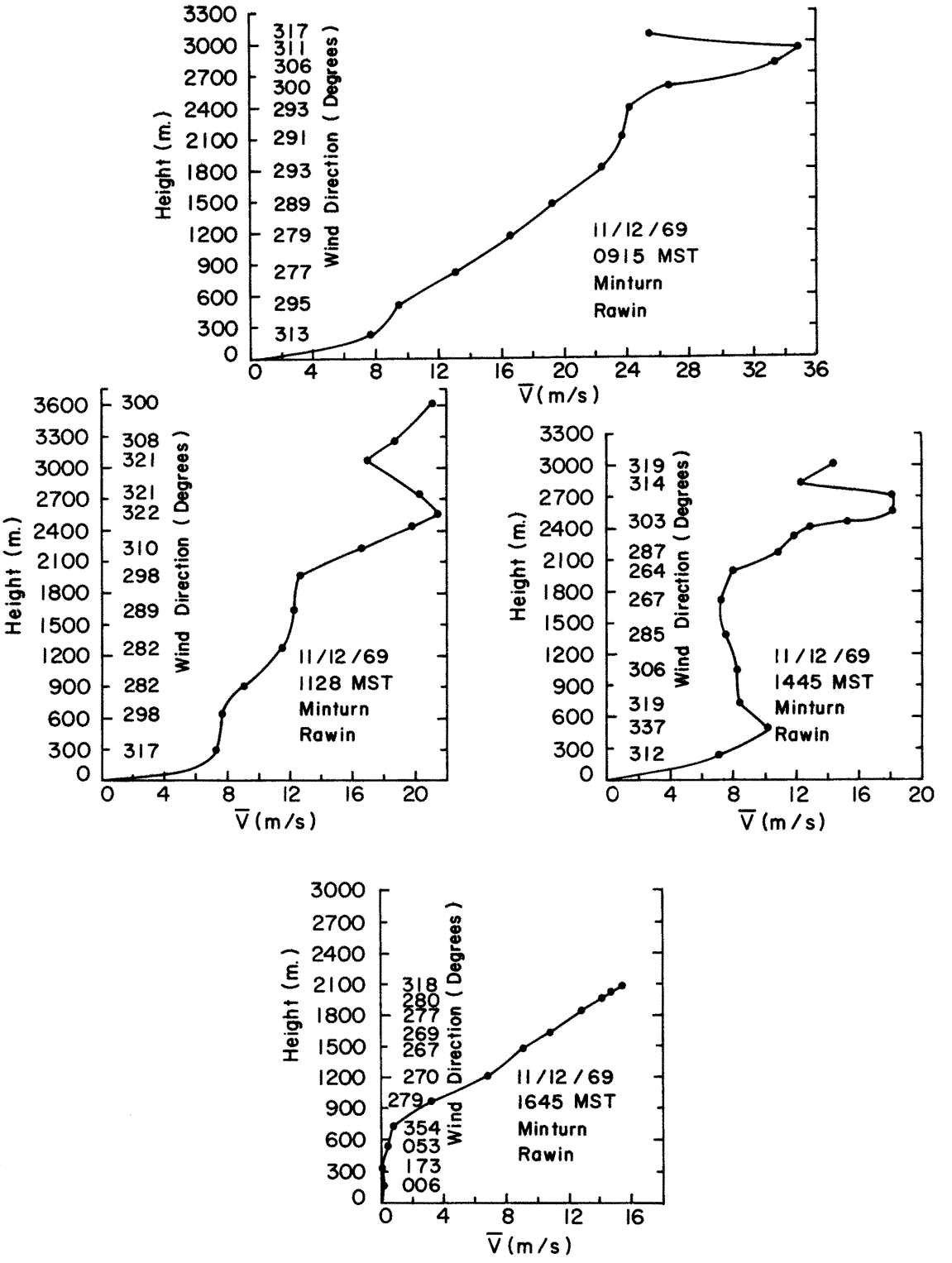

Fig. 31. Vertical distribution of windspeeds (m/s) and directions (degrees) at Minturn as determined by rawinsondes. December 11, 1969.

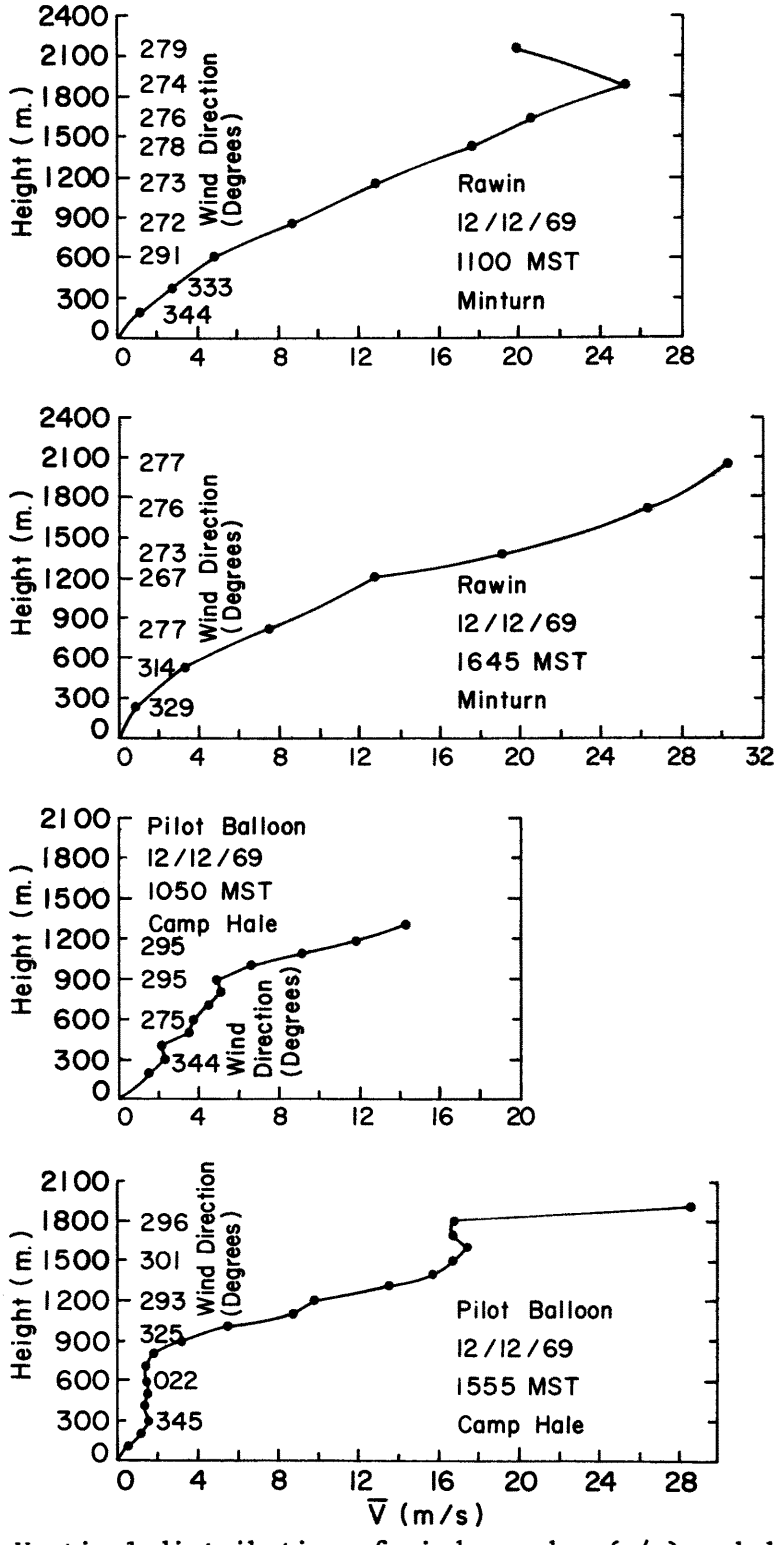

Fig. 32. Vertical distribution of wind speeds (m/s) and directions (degrees) at Minturn and Camp Hale as determined by pilot balloons and rawinsondes. December 12, 1969. Day of launching dual constant-volume balloons.

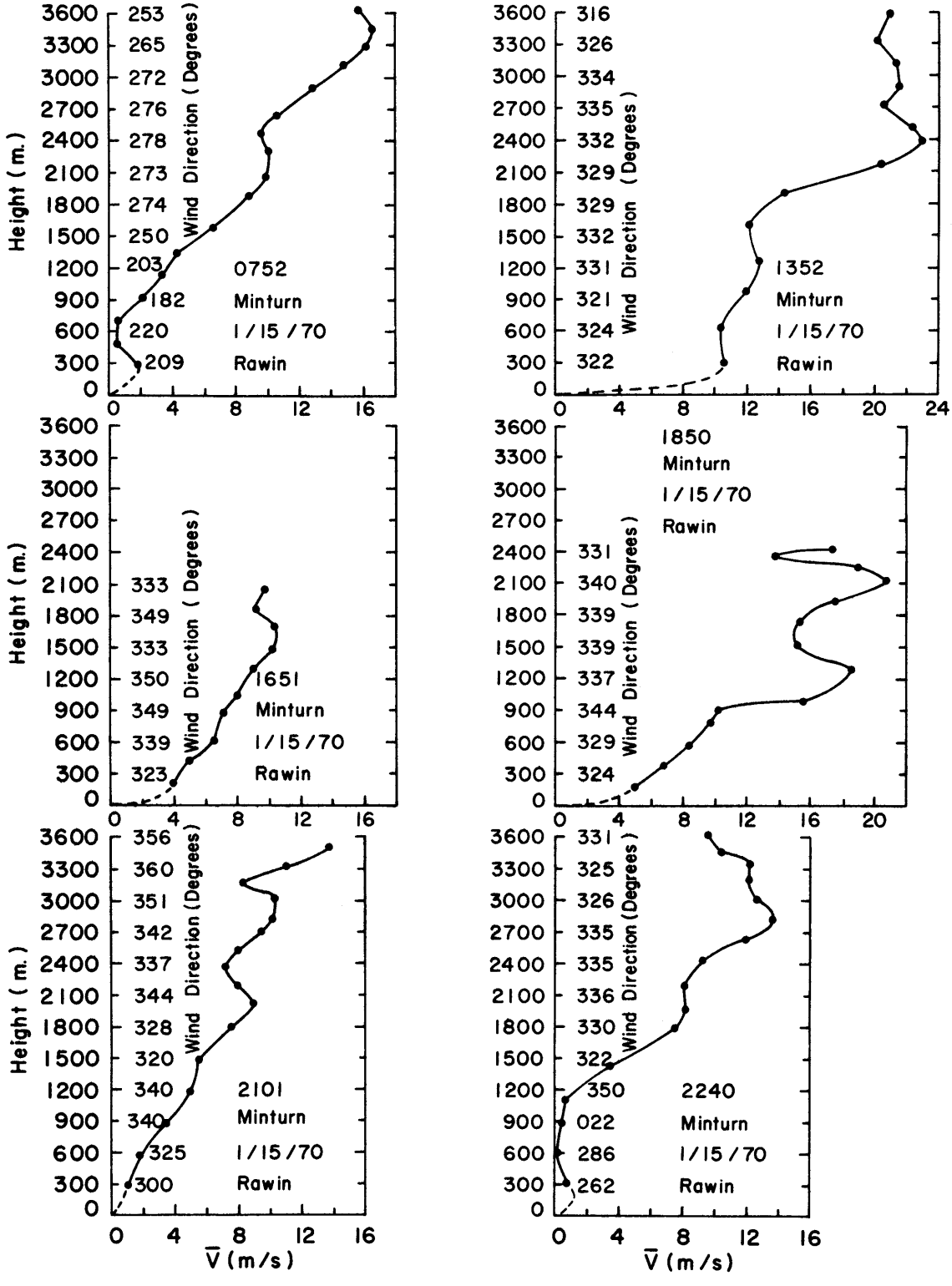

Fig. 33. Vertical distribution of wind speeds (m/s) and directions (degrees) at Minturn as determined by rawinsondes. January 15, 1970.

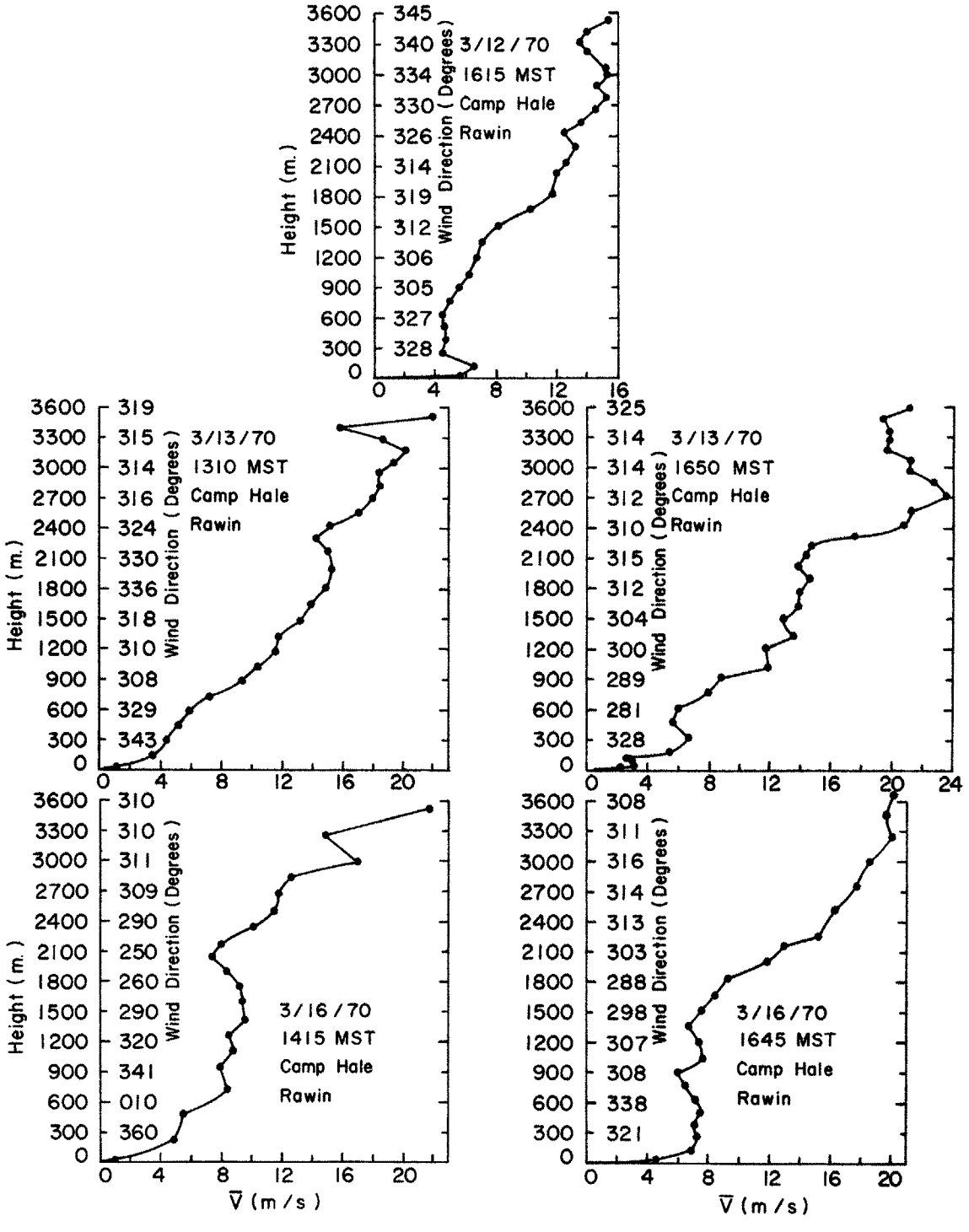

Fig. 34. Vertical distribution of wind speeds (m/s) and directions (degrees) at Camp Hale as determined by rawinsondes. March 12, 13, and 16, 1970. Aircraft sampling days.

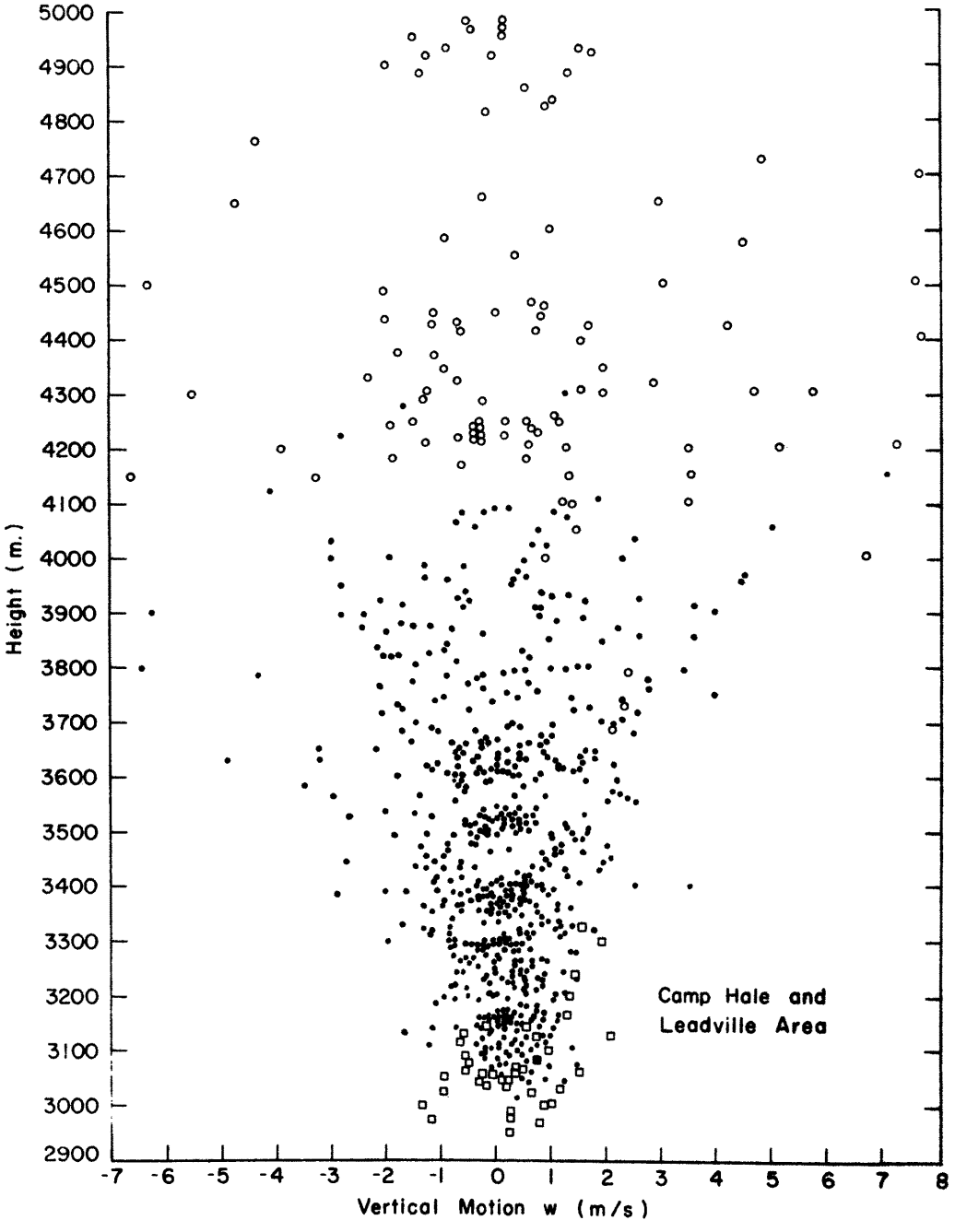

Fig. 35. Vertical distribution of vertical motion (m/s) with height over the Camp Hale and Leadville area for field days in December and January. Squares and open circles were single balloon data taken near Leadville. Closed circles were dual balloon data taken near Camp Hale. Computed from 30 sec height changes of constant-volume balloons.

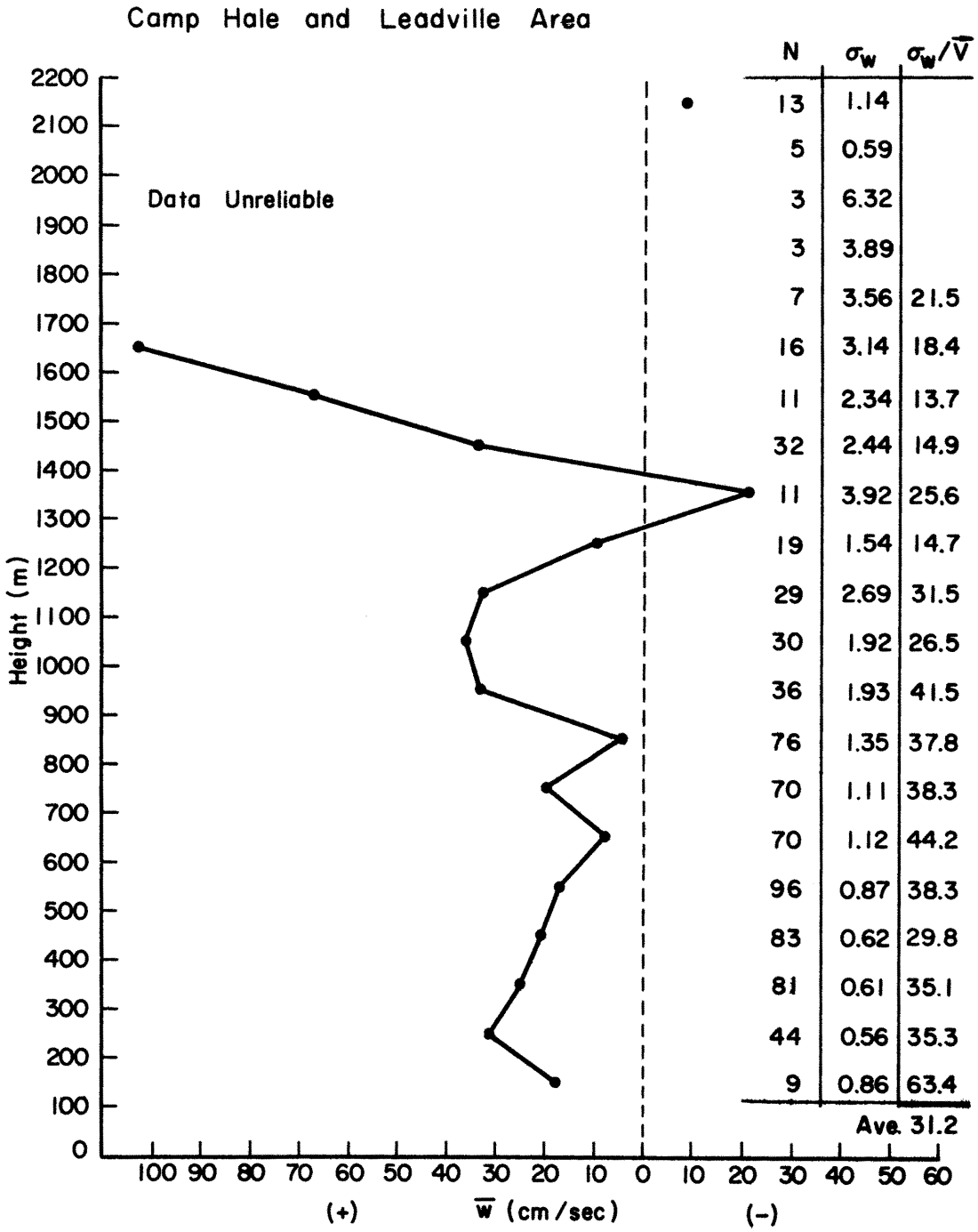

Fig. 36. Vertical distribution of the mean vertical velocity (cm/sec) variance, and vertical turbulent intensity (%) as computed from all constant-volume balloon flights in the Camp Hale and Leadville area.

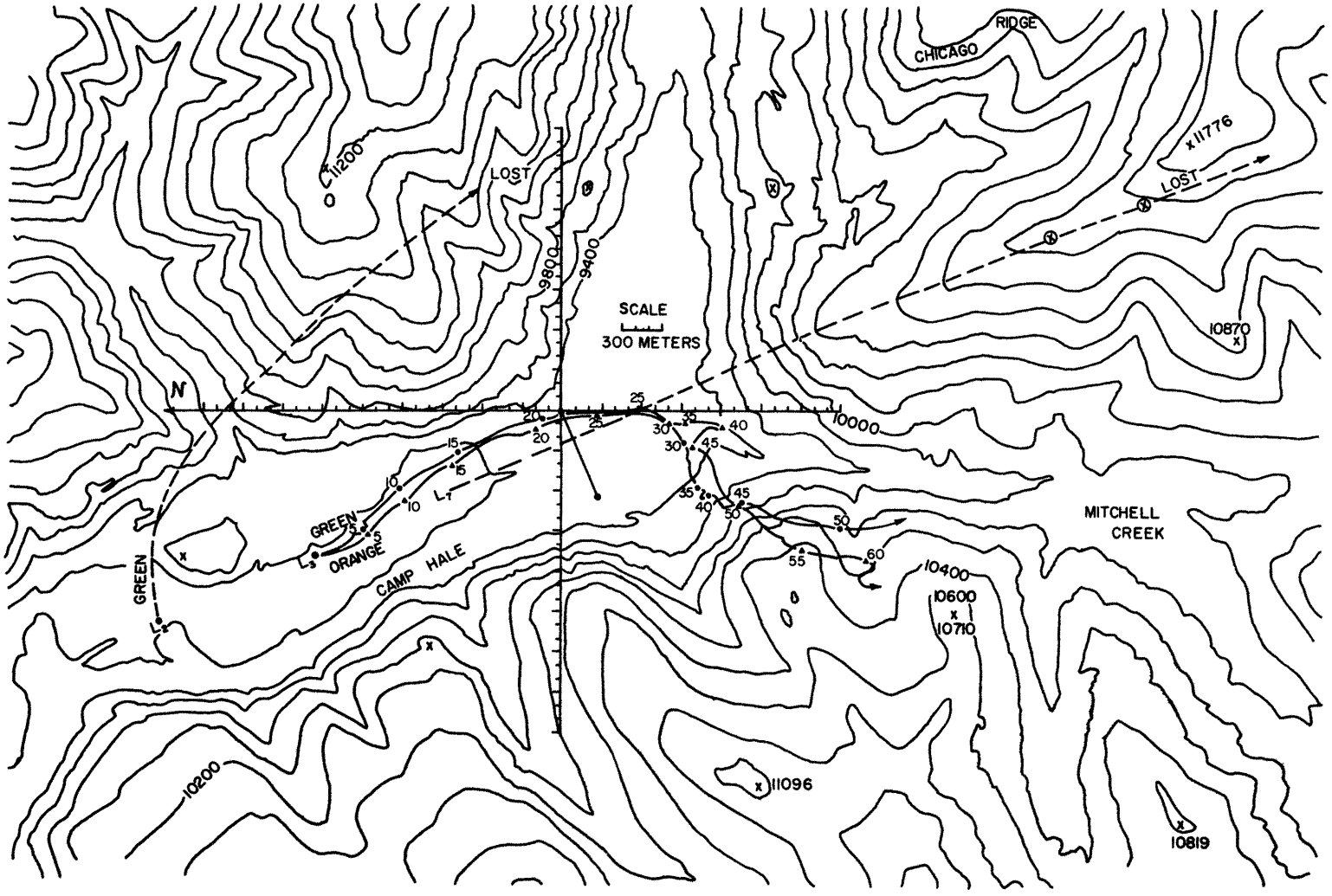

Fig. 37. Constant-volume balloon trajectories for flights 2, 3, and 7 in the Camp Hale area. Flight 3 was a dual balloon flight on December 12, 1969. Numbers represent time in minutes from release.

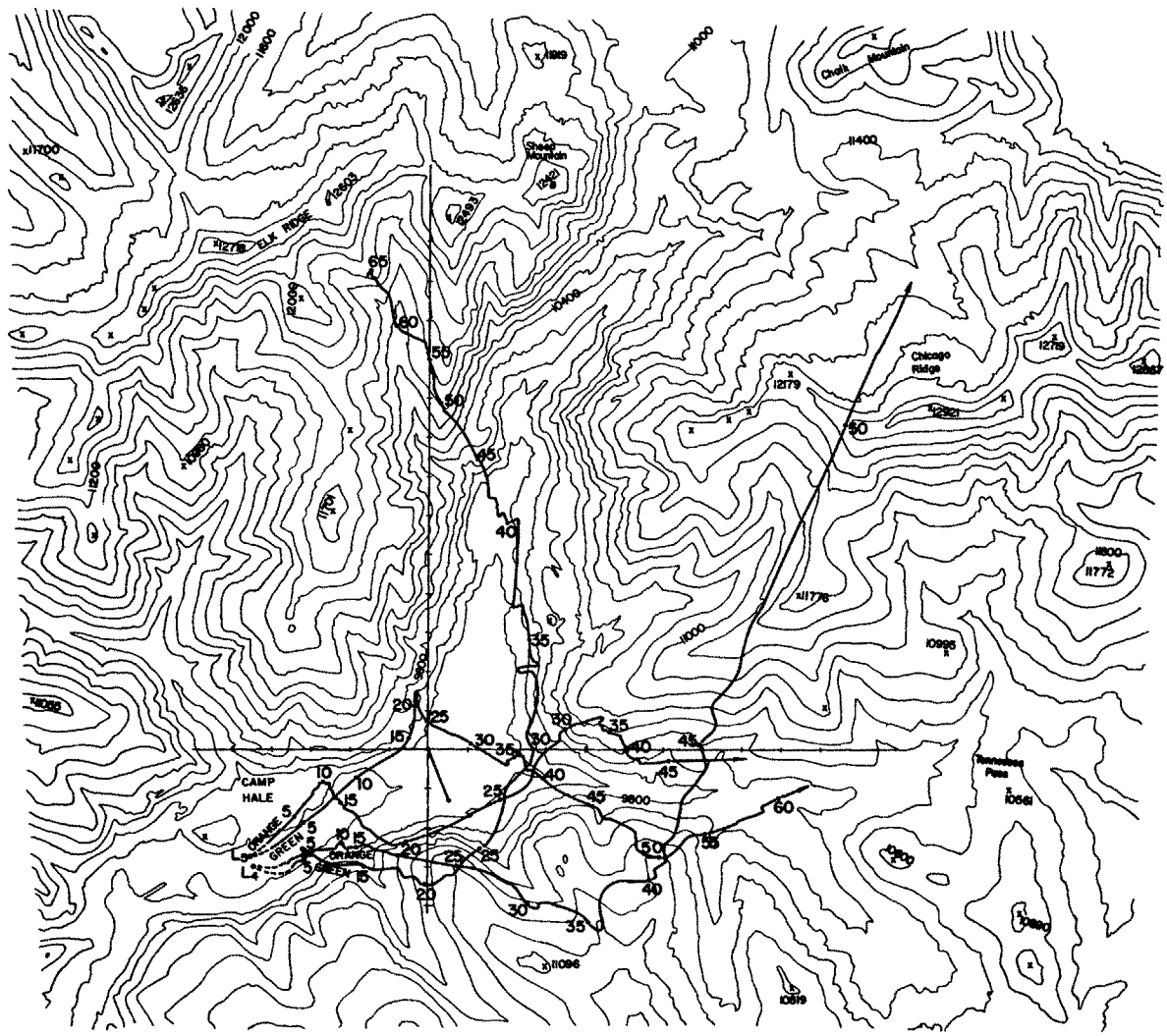

Fig. 38. Constant-volume balloon trajectories for dual flights 4 and 5. December 12, 1969. Numbers represent time after launch in minutes.

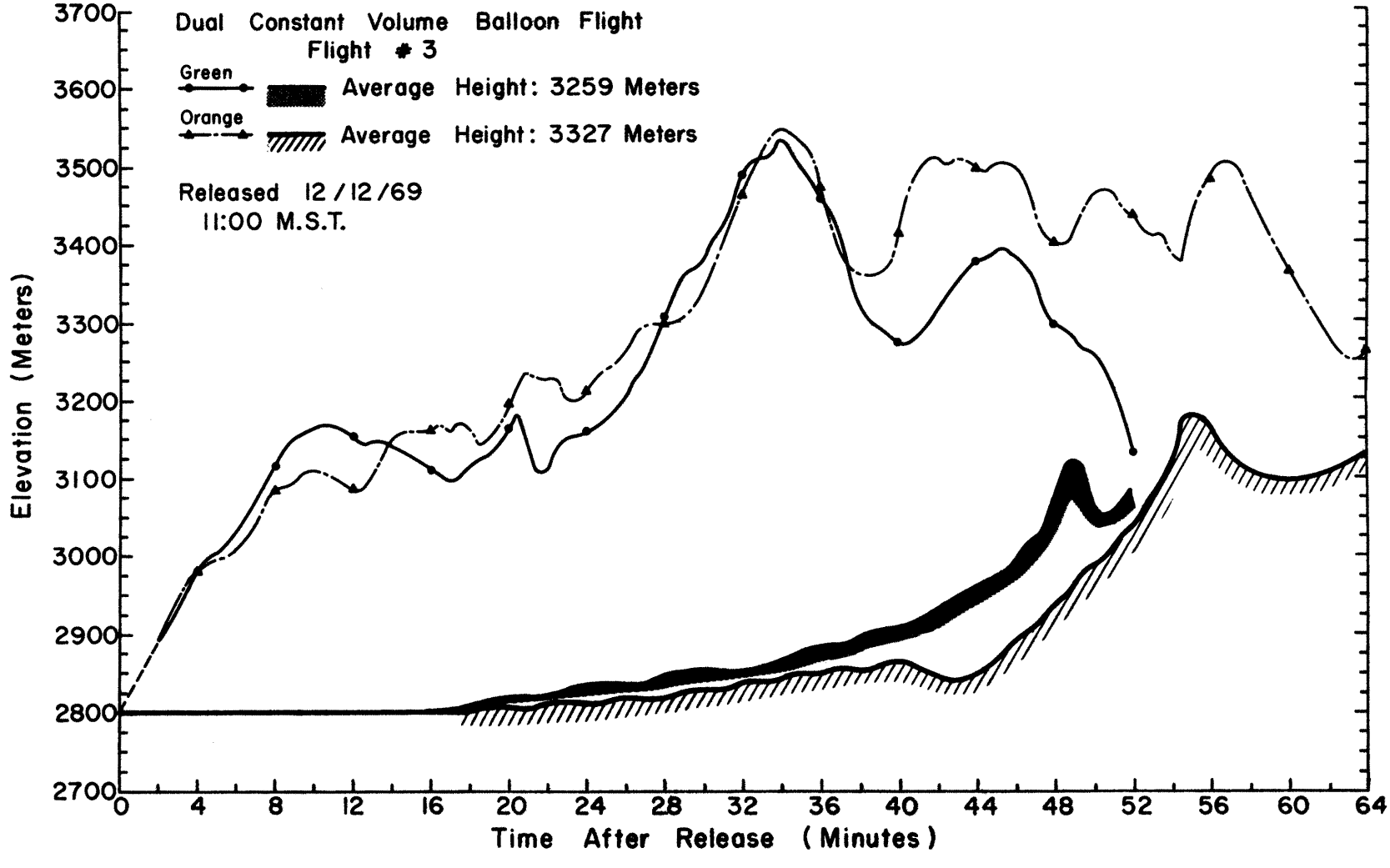

Fig. 39. Dual constant-volume balloon height profiles as a function of time after release. Flight #3. Height of terrain represented by shading and cross-hatching.

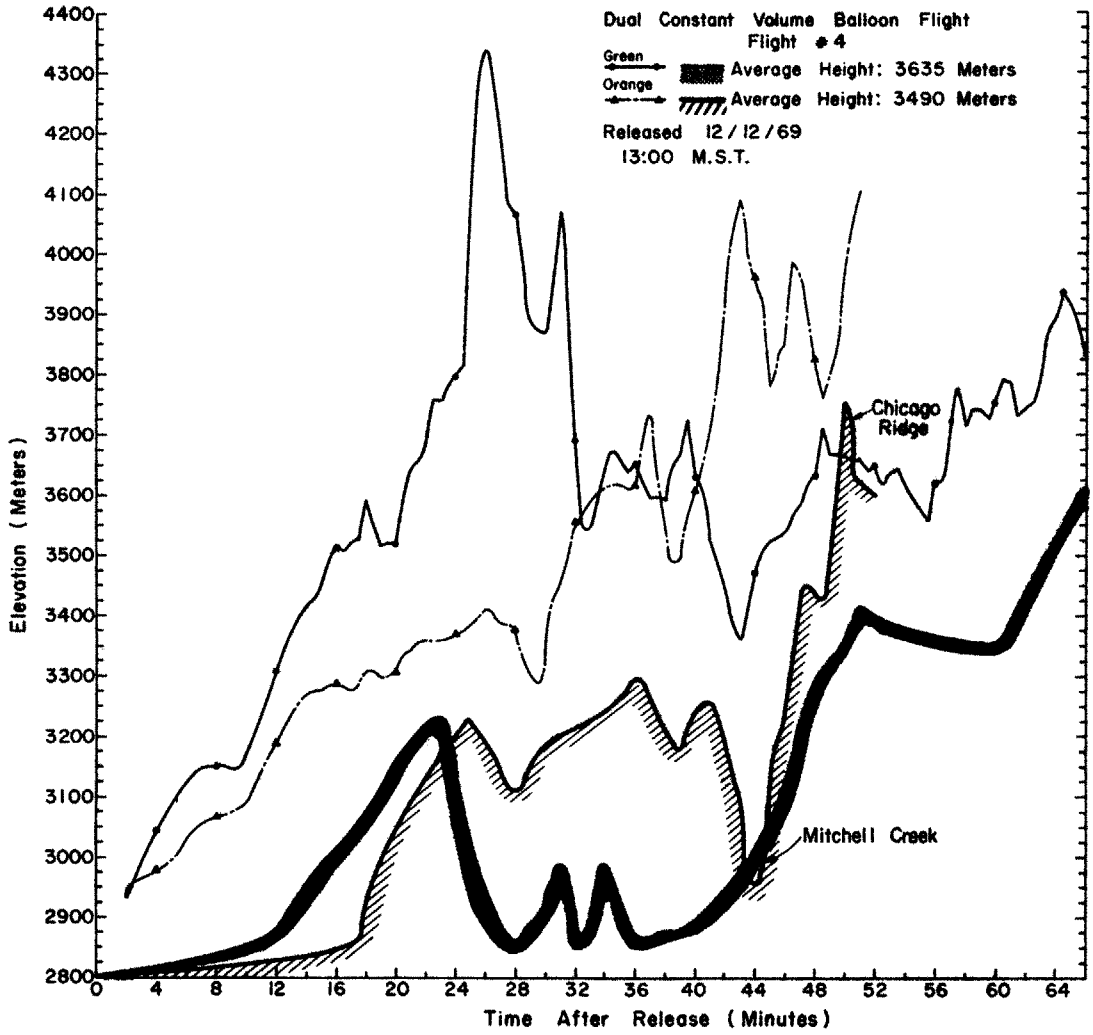

Fig. 40. Dual constant-volume balloon height profiles as a function of time after release. Flight #4. Height of terrain represented by shading and cross-hatching.

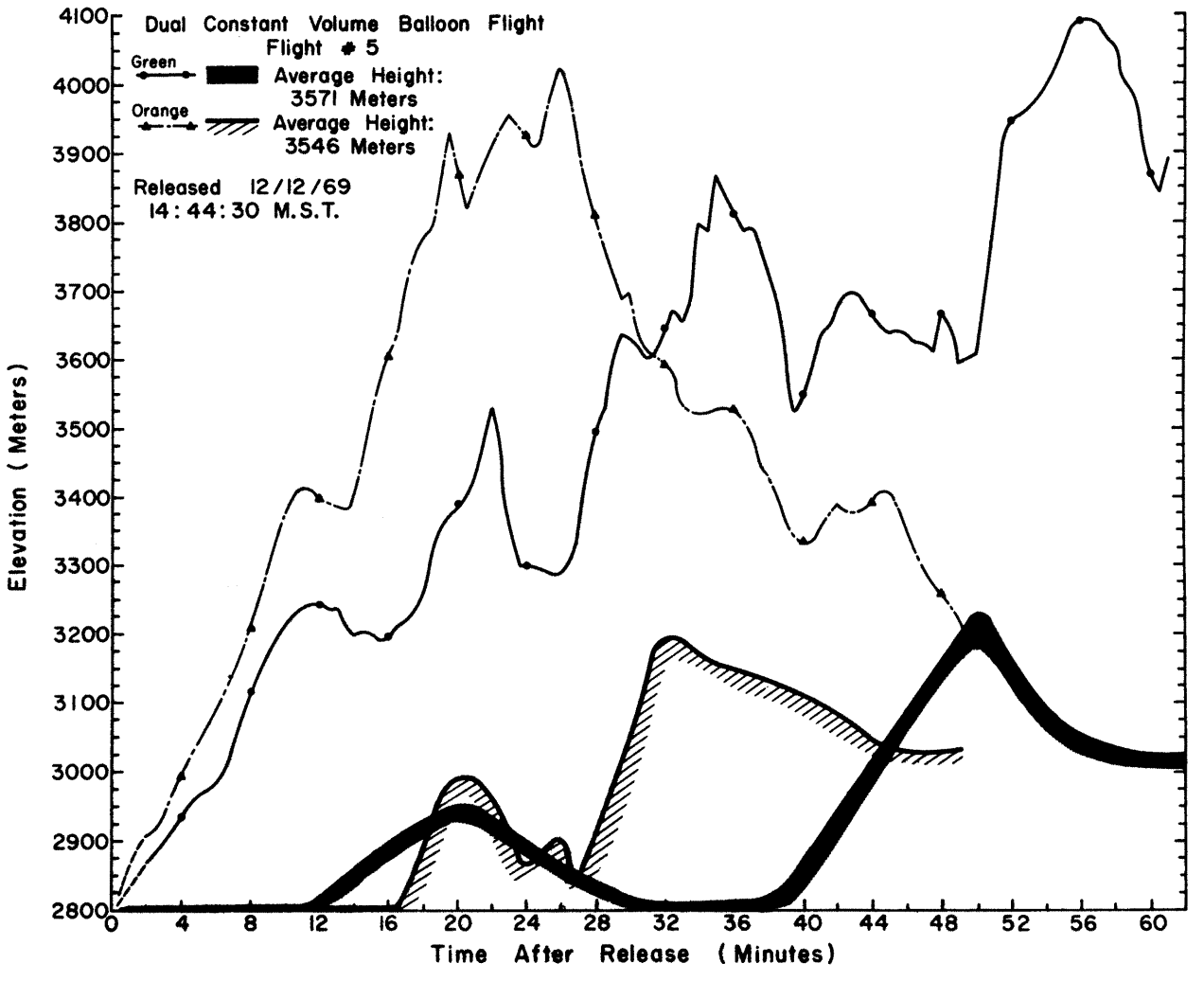

Fig. 41. Dual constant-volume balloon height profiles as a function of time after release. Flight #5.

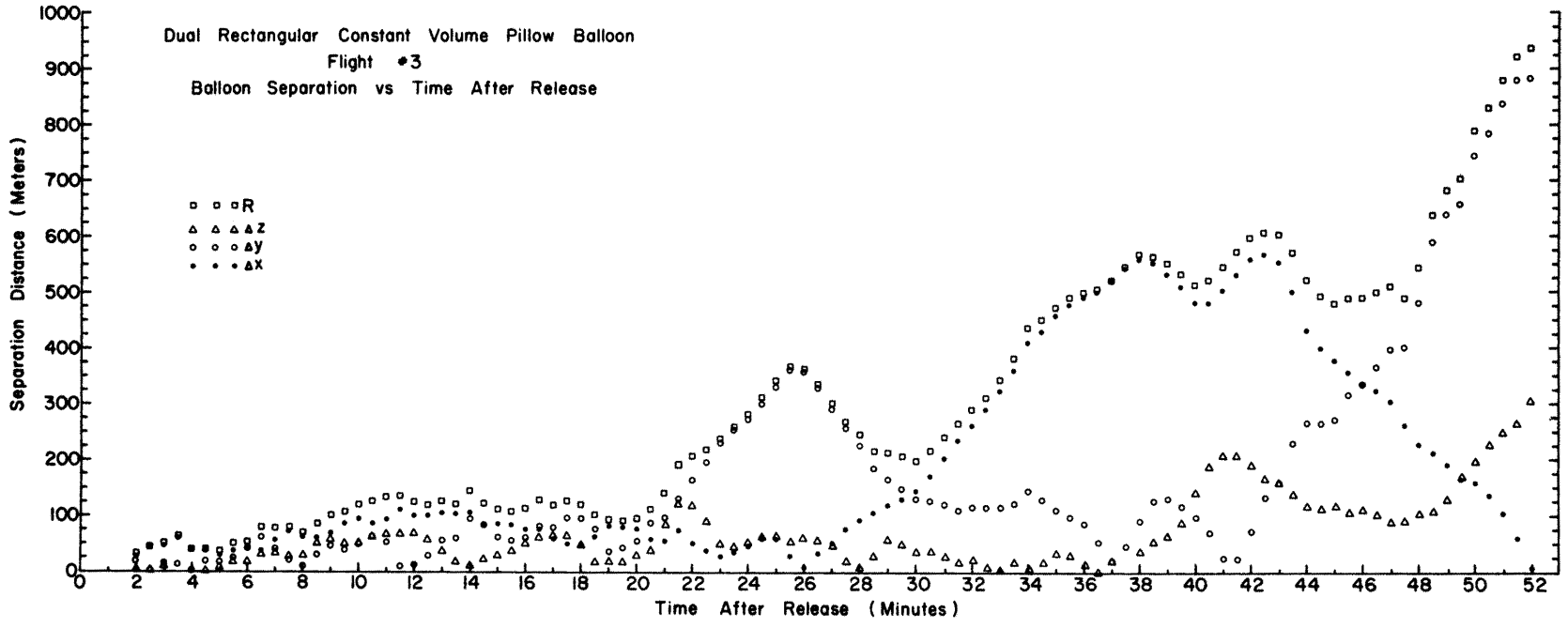

Fig. 42. Dual constant-volume balloon separation versus time after release. Flight #3.
$R = \{(\Delta x)^2 + (\Delta y)^2 + (\Delta z)^2\}^{\frac{1}{2}}$

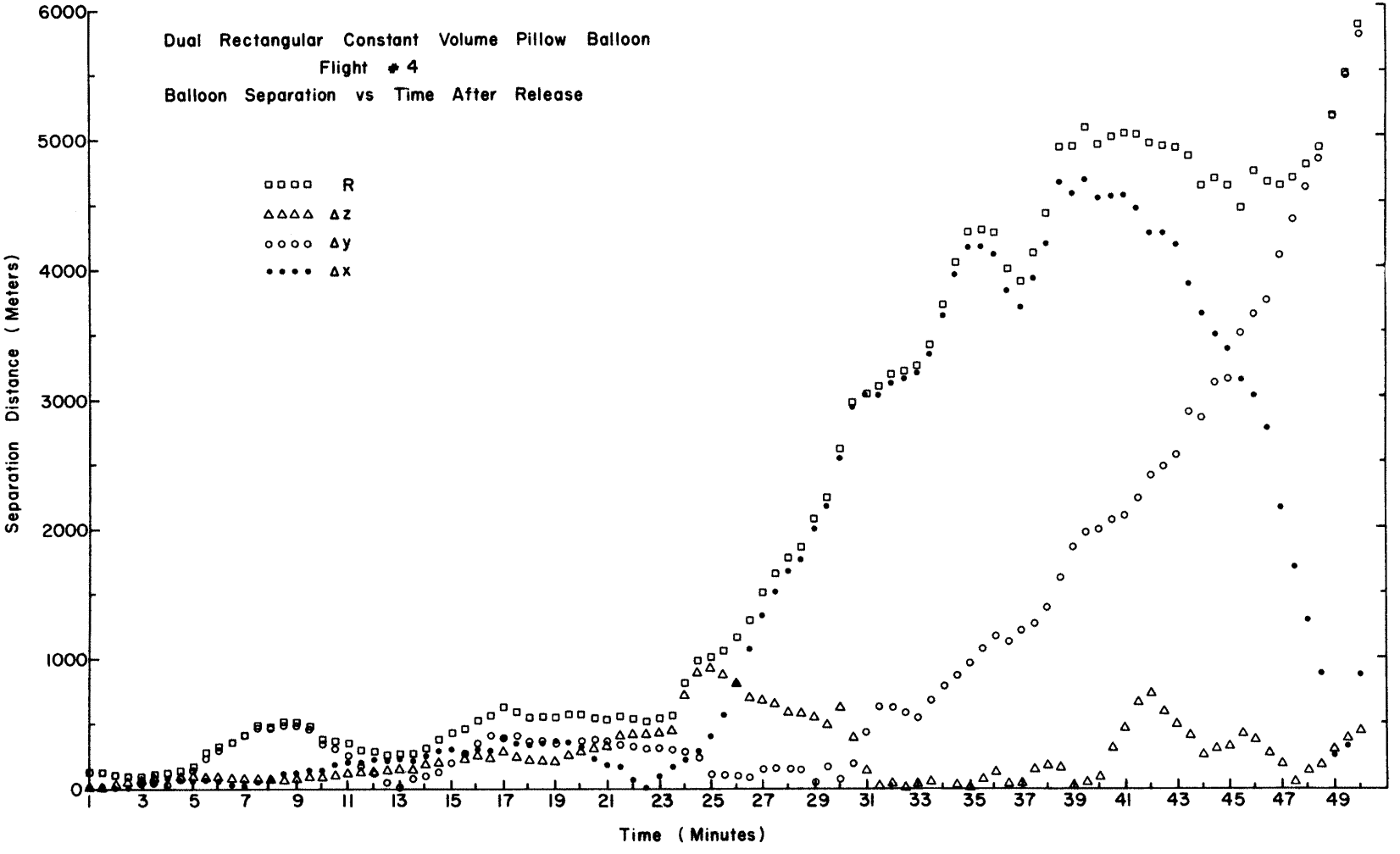

Fig. 43. Dual constant-volume balloon separation versus time after release. Flight #4.

$$R = \{(\Delta x)^2 + (\Delta y)^2 + (\Delta z)^2\}^{\frac{1}{2}}$$

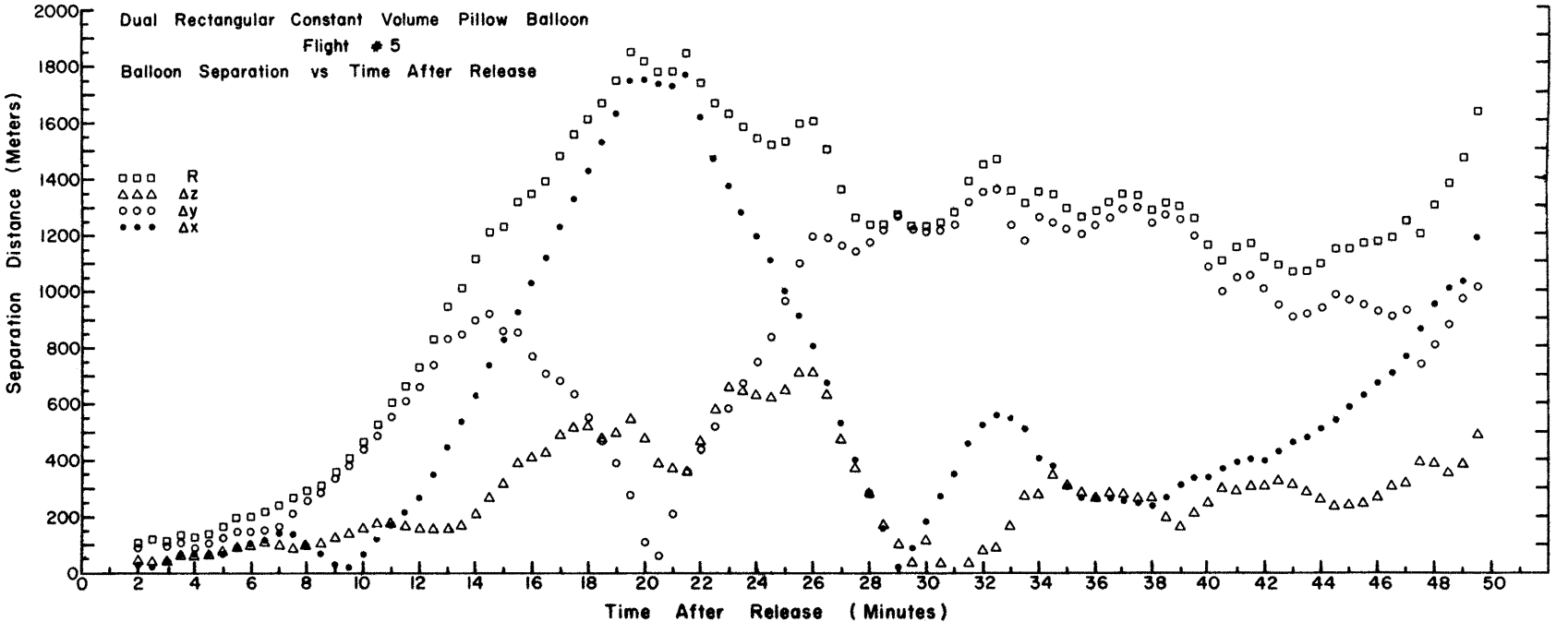

Fig. 44. Dual constant-volume balloon separation versus time after release. Flight #5.

$$R = \{(\Delta x)^2 + (\Delta y)^2 + (\Delta z)^2\}^{\frac{1}{2}}$$

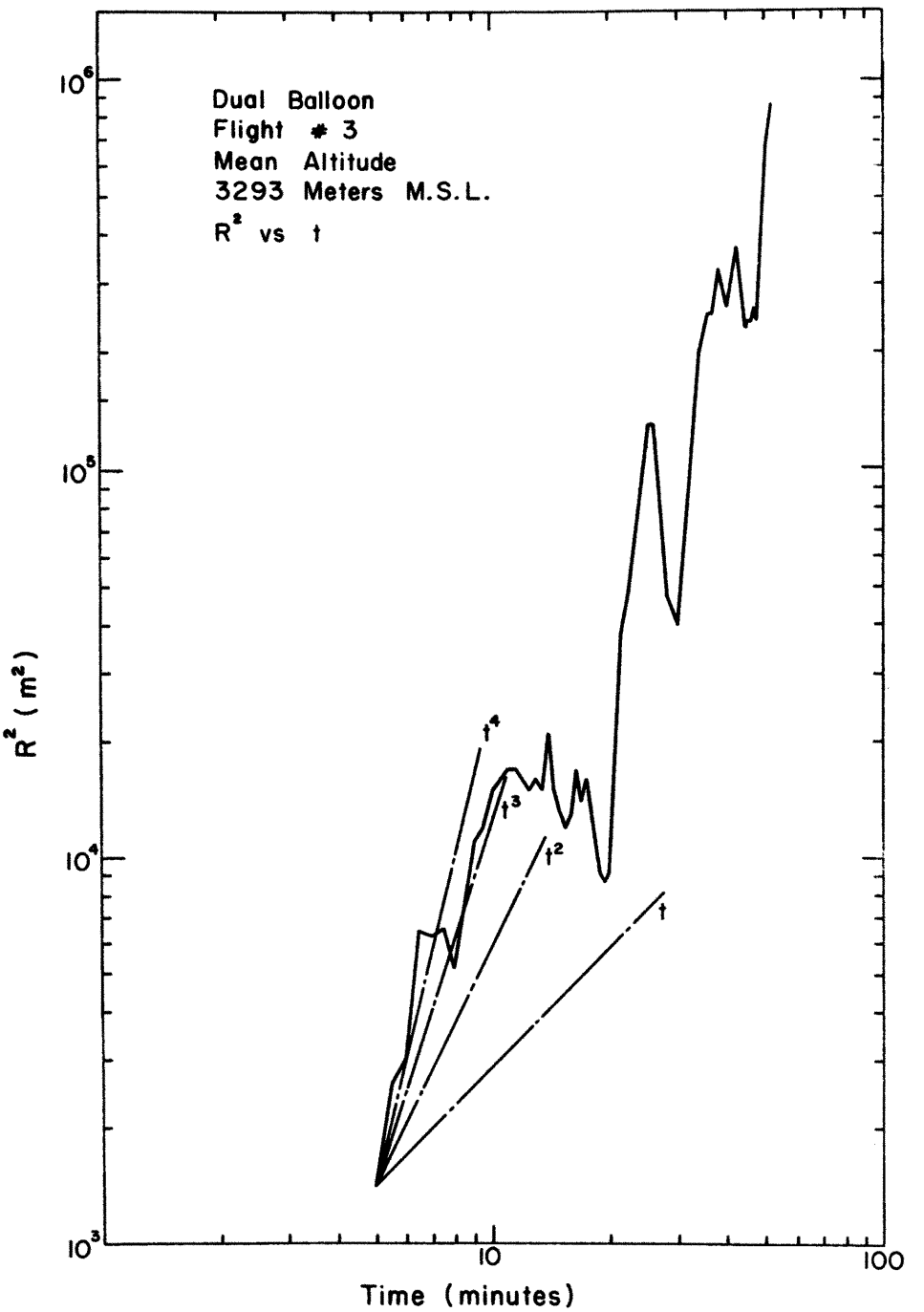

Fig. 45. Square of the total vector separation R^2 versus time. Dual flight #3. Shown for comparison are separation rates $\propto t, t^2, t^3, t^4$.

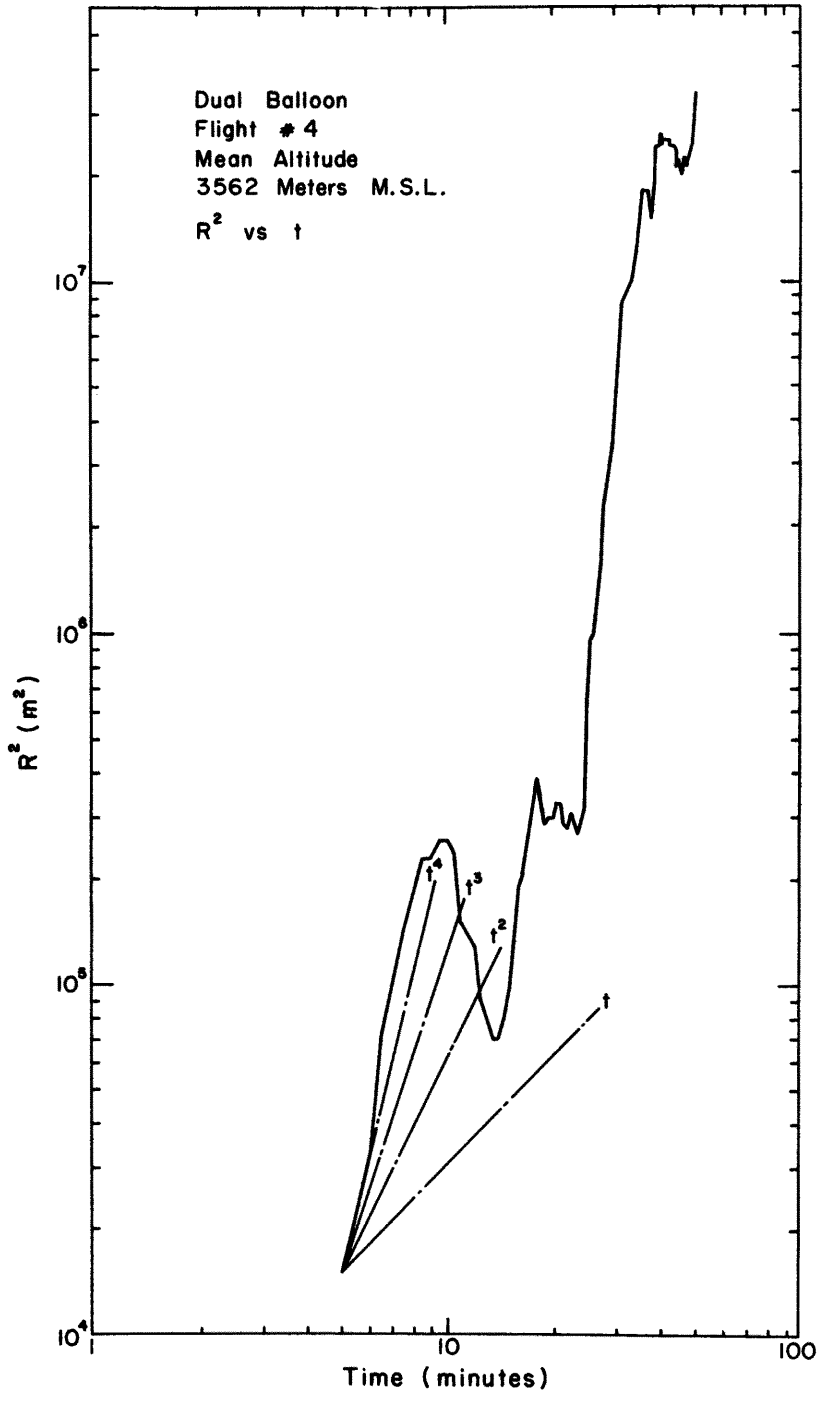

Fig. 46. Square of the total vector separation R^2 versus time. Dual flight #4. Shown for comparison are separation rates $\propto t$, t^2, t^3, t^4.

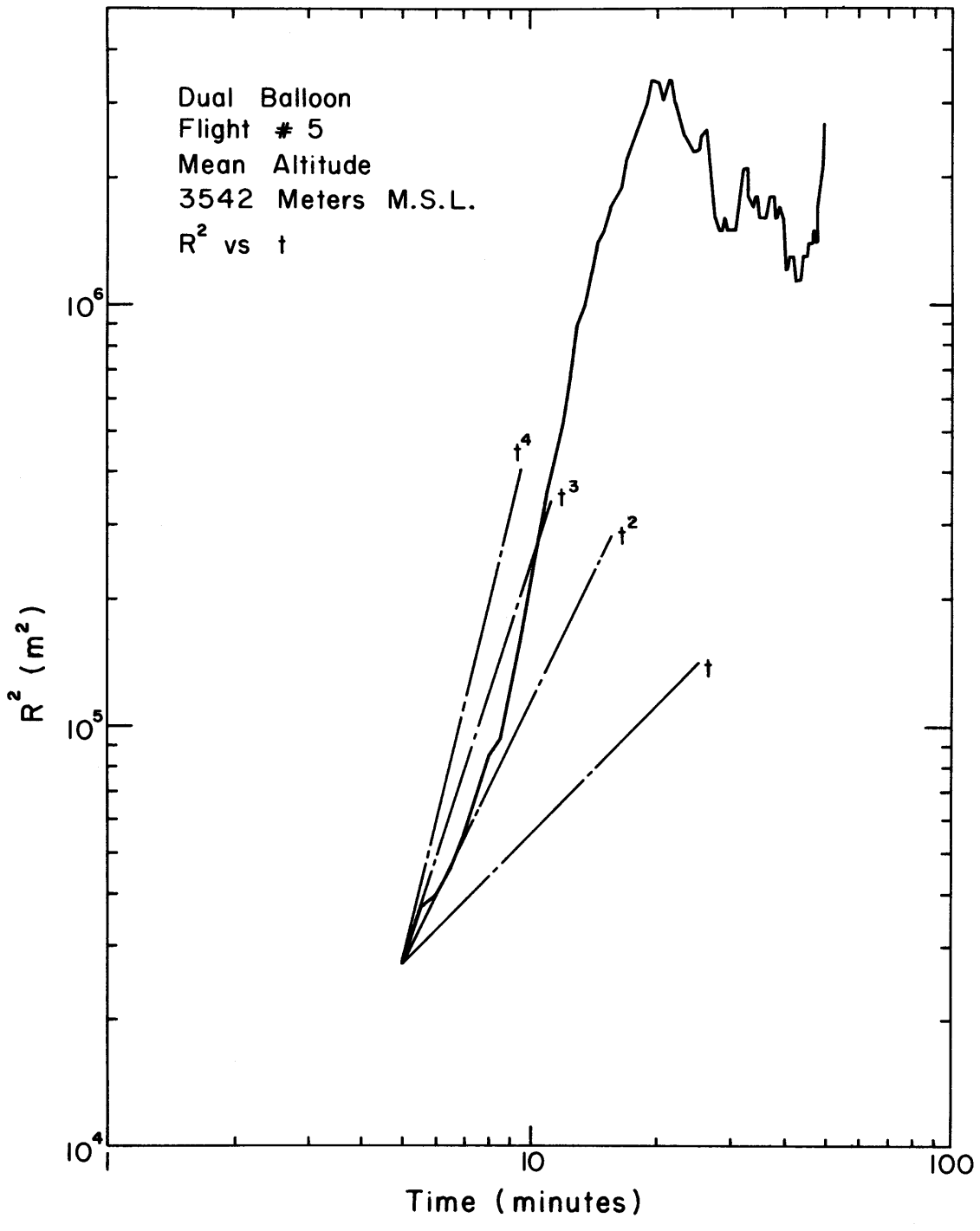

Fig. 47. Square of the total vector separation R^2 versus time. Dual flight #5. Shown for comparison are separation rates $\propto t$, t^2, t^3, t^4.

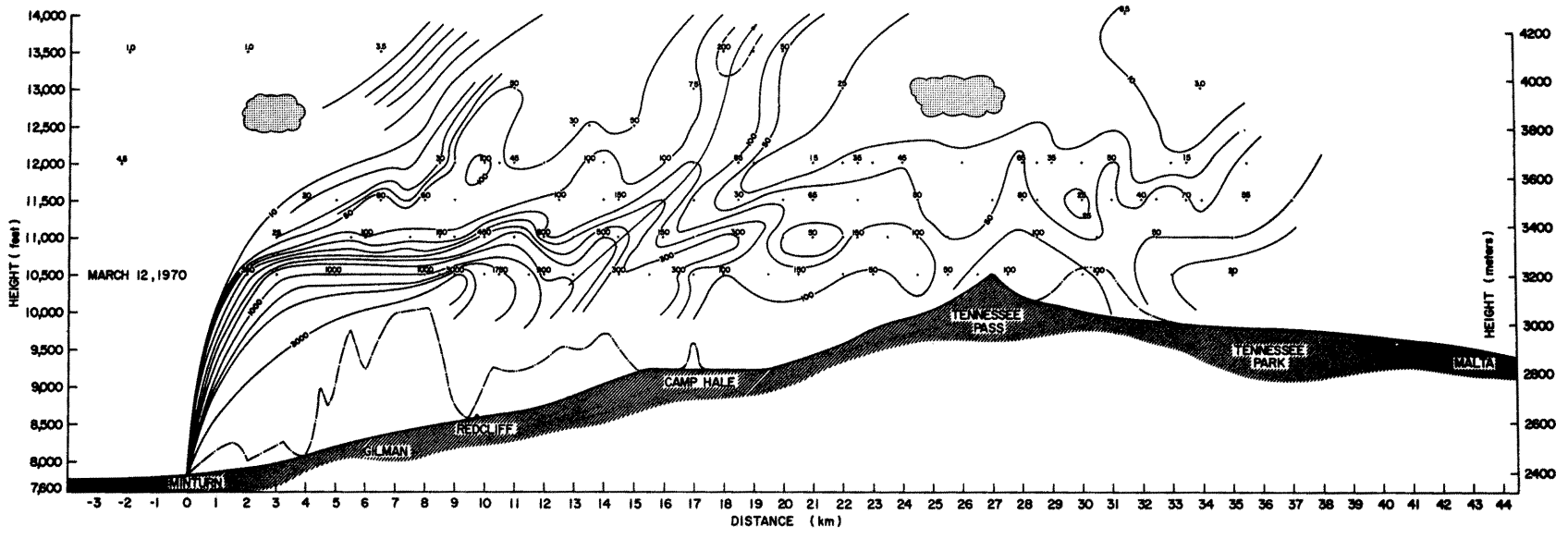

Fig. 48. Vertical distribution of seeding material concentration (nuclei/liter, effective at -20°C) along the Eagle River Valley as generated by silver-iodide generators at Minturn and Redcliff during northwest winds. March 12, 1970. Weather: scattered clouds.

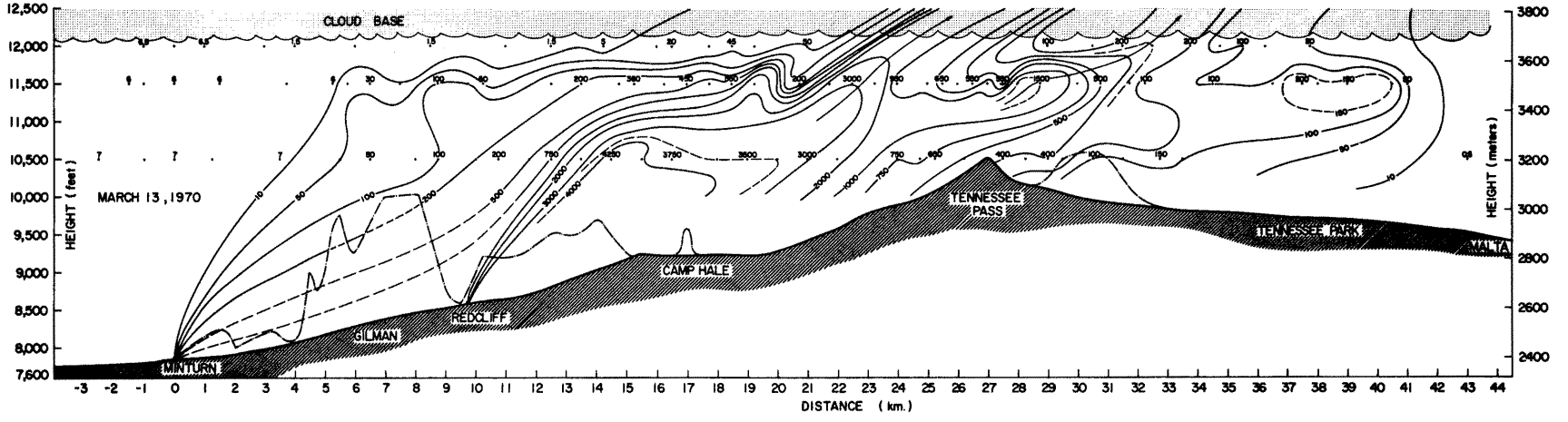

Fig. 49. Vertical distribution of seeding material concentration (nuclei/liter, effective at -20°C) along the Eagle River Valley as generated by silver-iodide generators at Minturn and Redcliff during northwest winds. March 13, 1970. Weather: scattered snow showers.

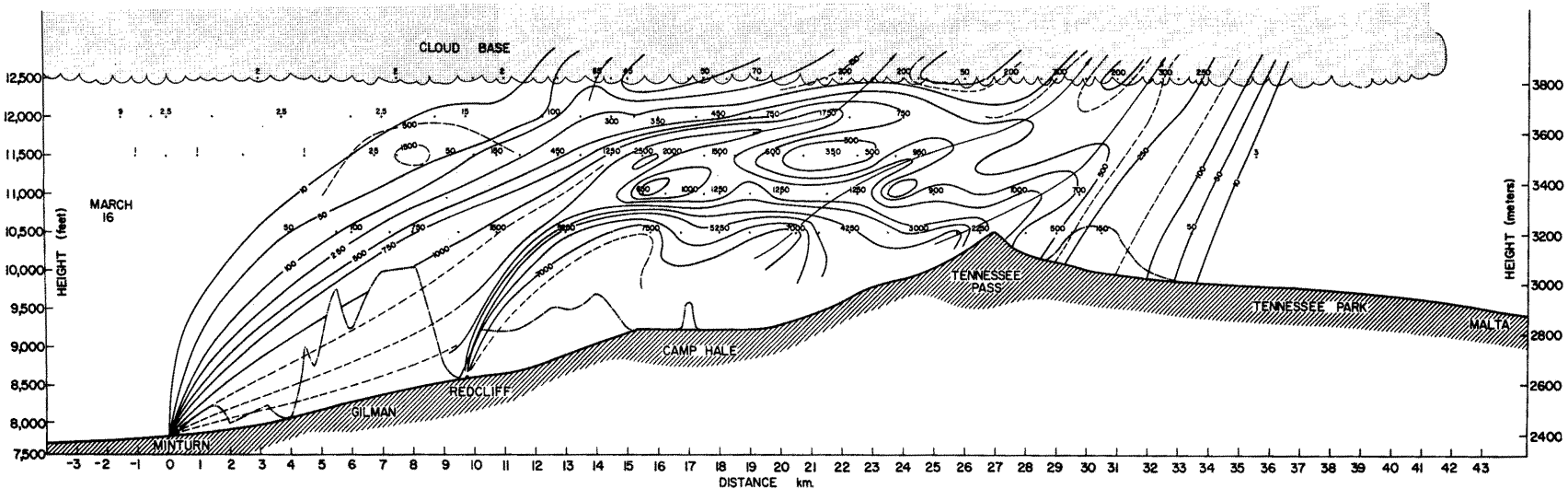

Fig. 50. Vertical distribution of seeding material concentration (nuclei/liter, effective at -20°C) along the Eagle River Valley as generated by silver-iodide generators at Minturn and Redcliff during northwest winds. March 16, 1970. Weather: scattered snow showers.

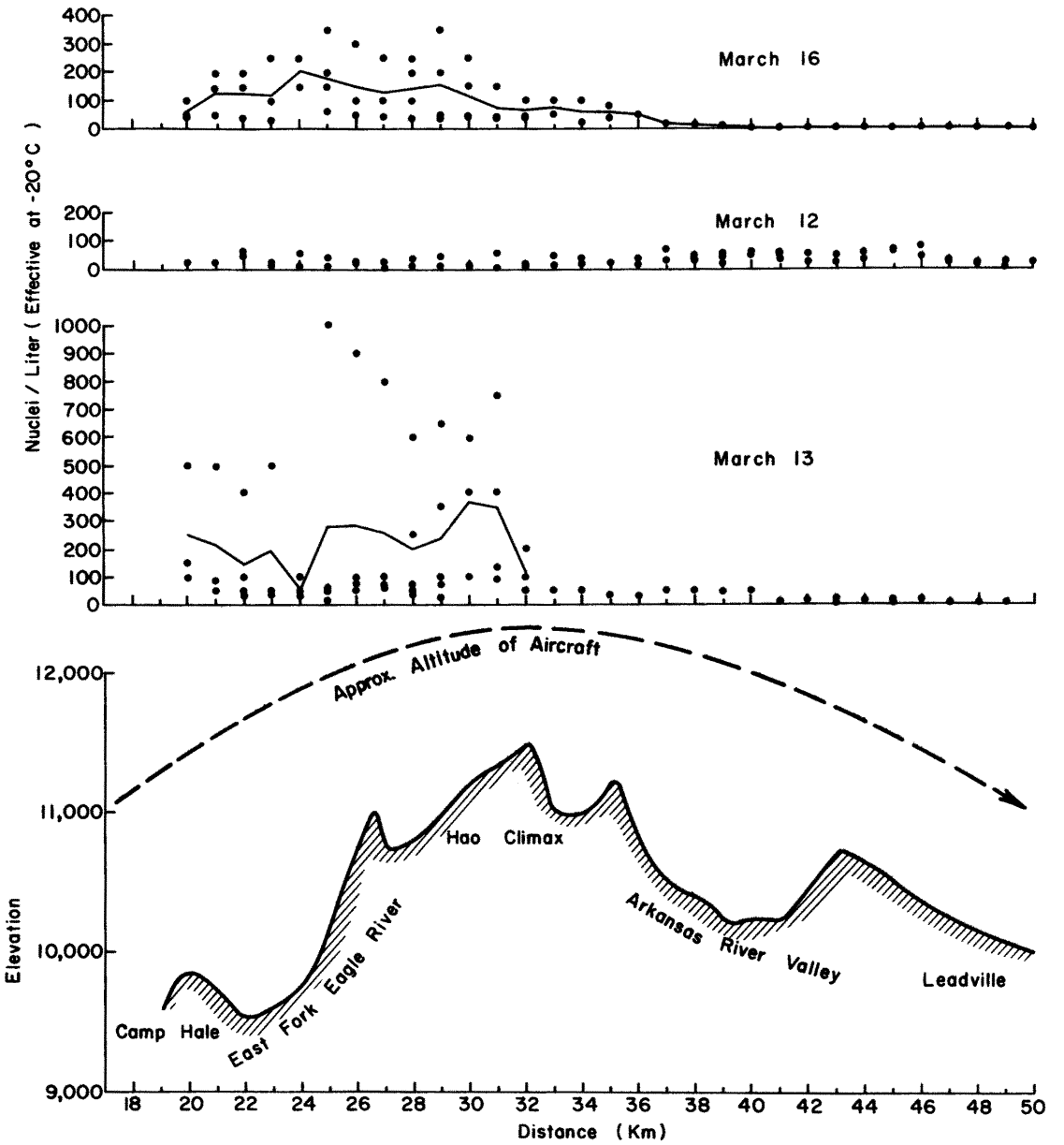

Fig. 51. Variation of seeding material concentration (nuclei/liter, effective at -20°C) as detected by aircraft sampling between 11,500 ft and 12,500 ft msl along flight track B. March 12, 13, and 16, 1970. Solid line represents average.

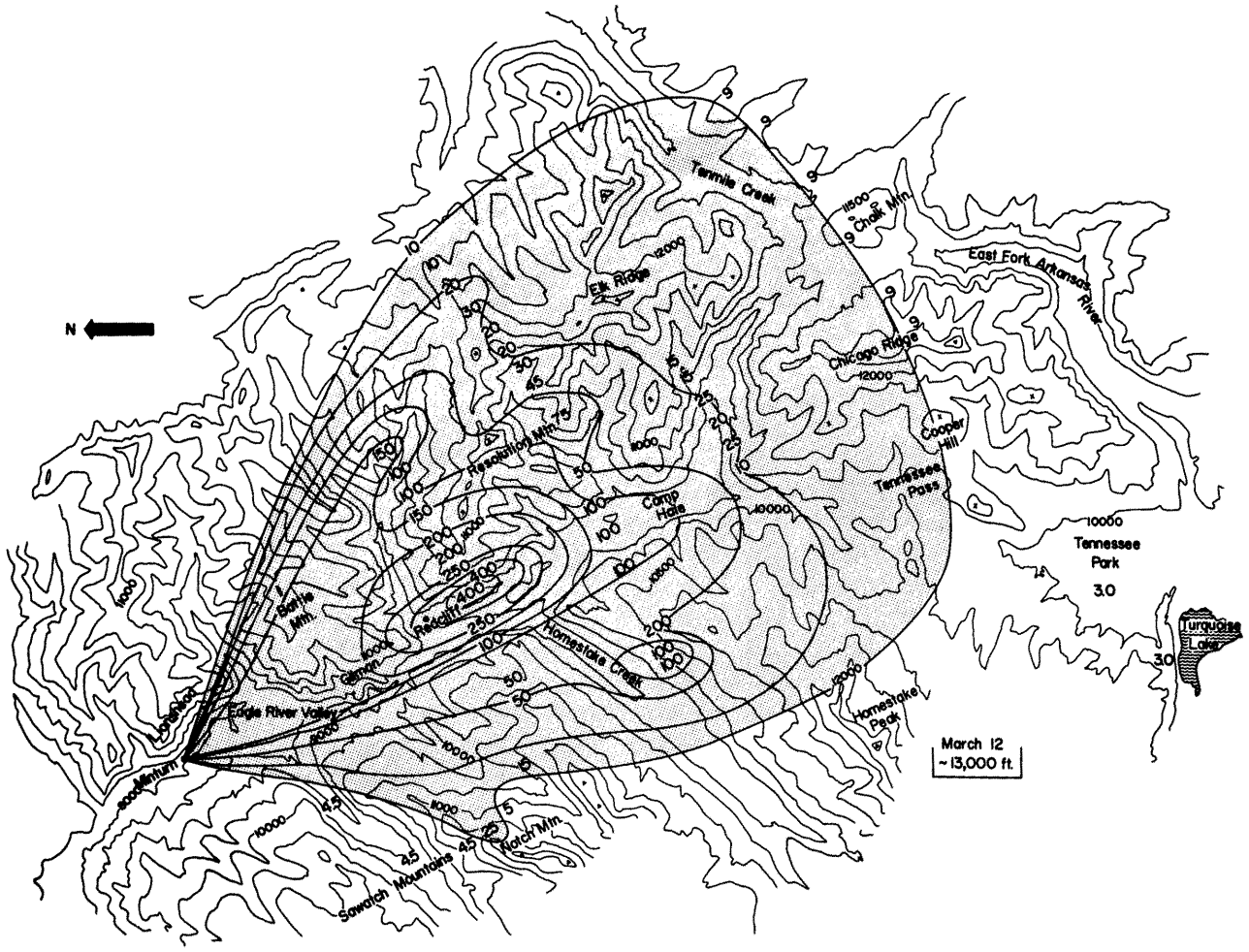

Fig. 52. The estimated horizontal dispersion of silver-iodide seeding material (nuclei/liter, effective at -20°C) at 13,000 ft msl, as released from Minturn and Redcliff sources. March 12, 1970.

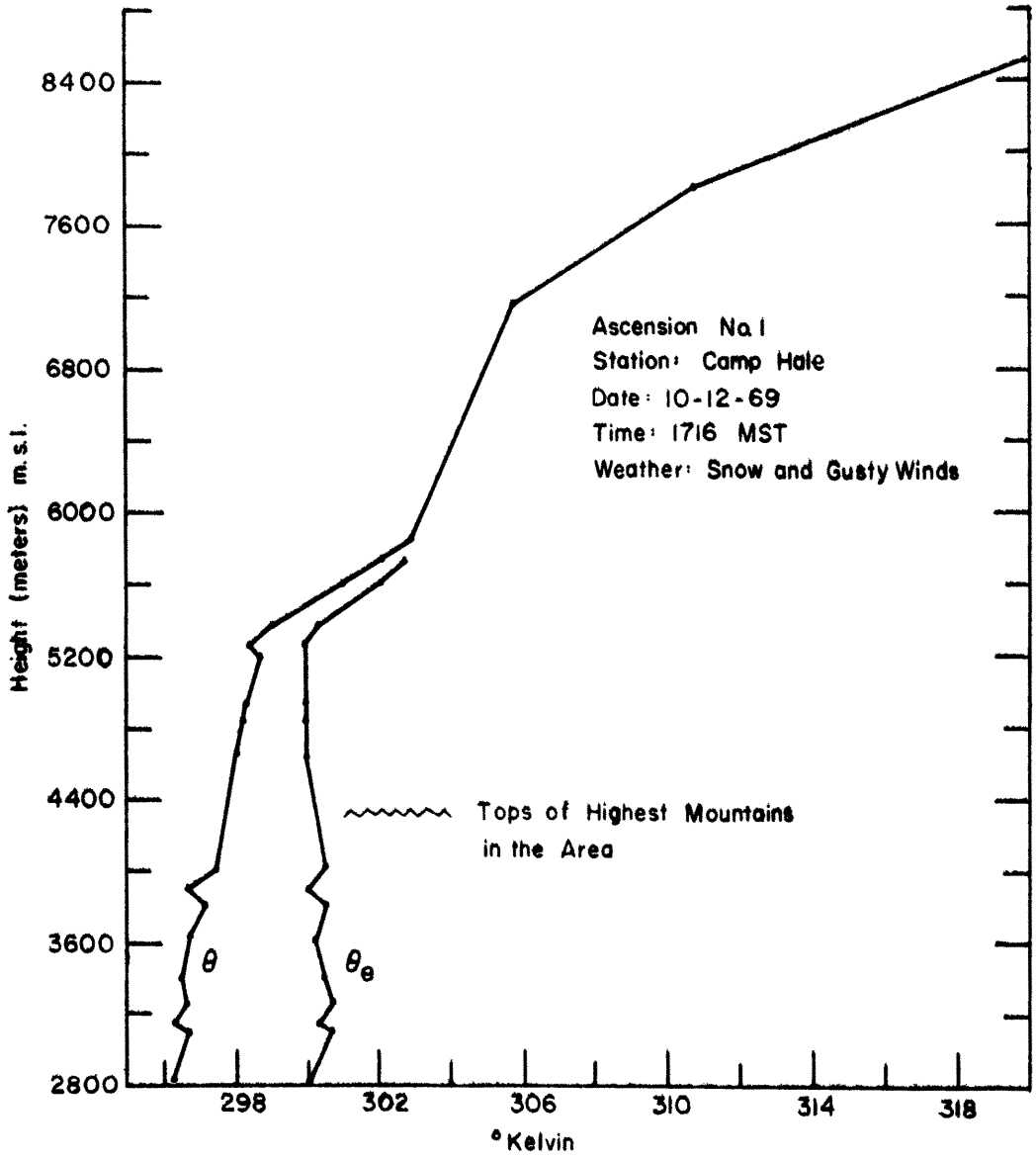

Fig. 53. Vertical distribution of the potential and equivalent potential temperature (^{o}K) during a deep, near-neutral stability snowstorm. December 10, 1969.

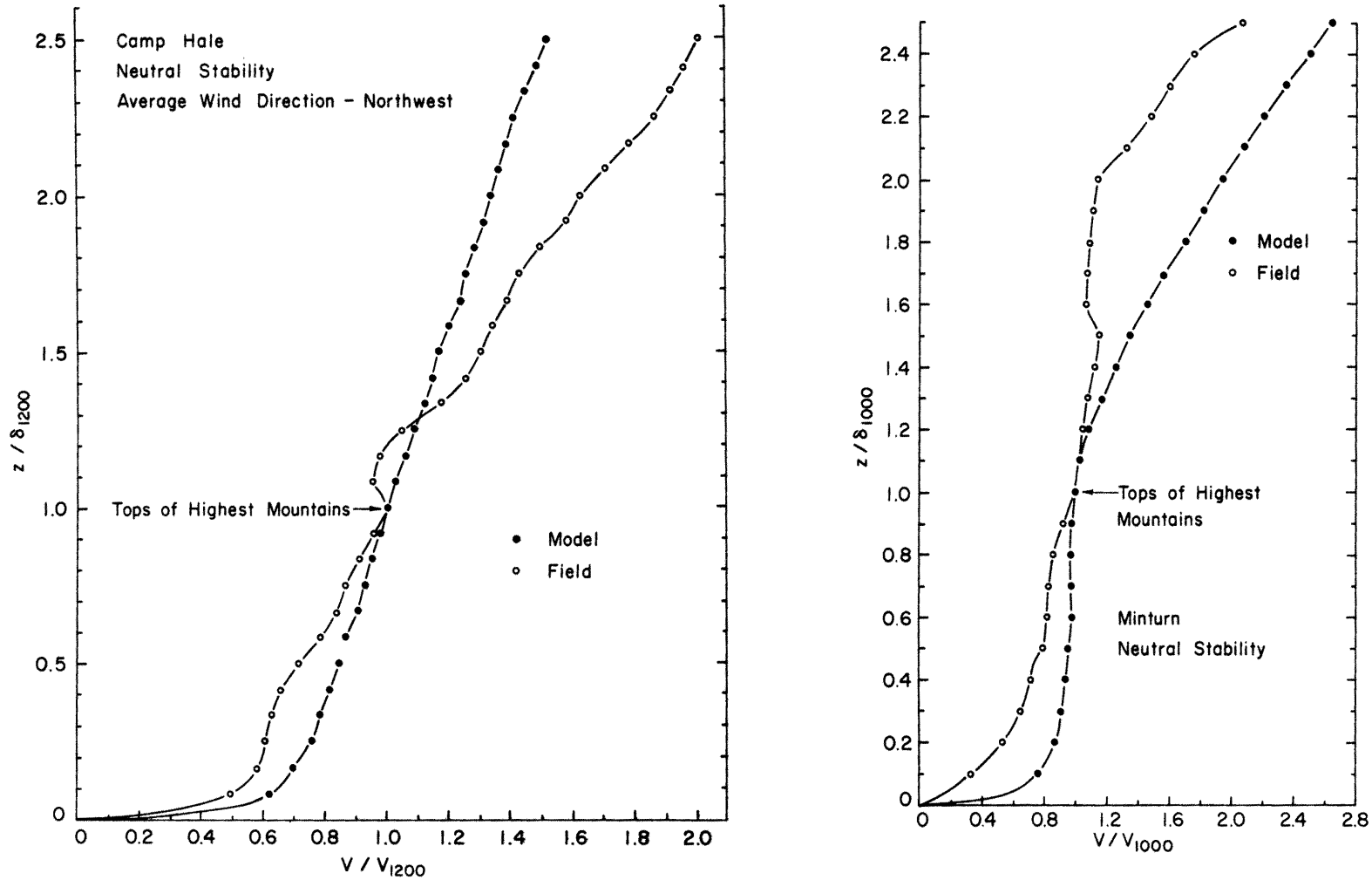

Fig. 54. Comparison of field and model velocity profiles for near-neutral stability conditions. Locations: Minturn and Camp Hale. Average wind direction - northwest.

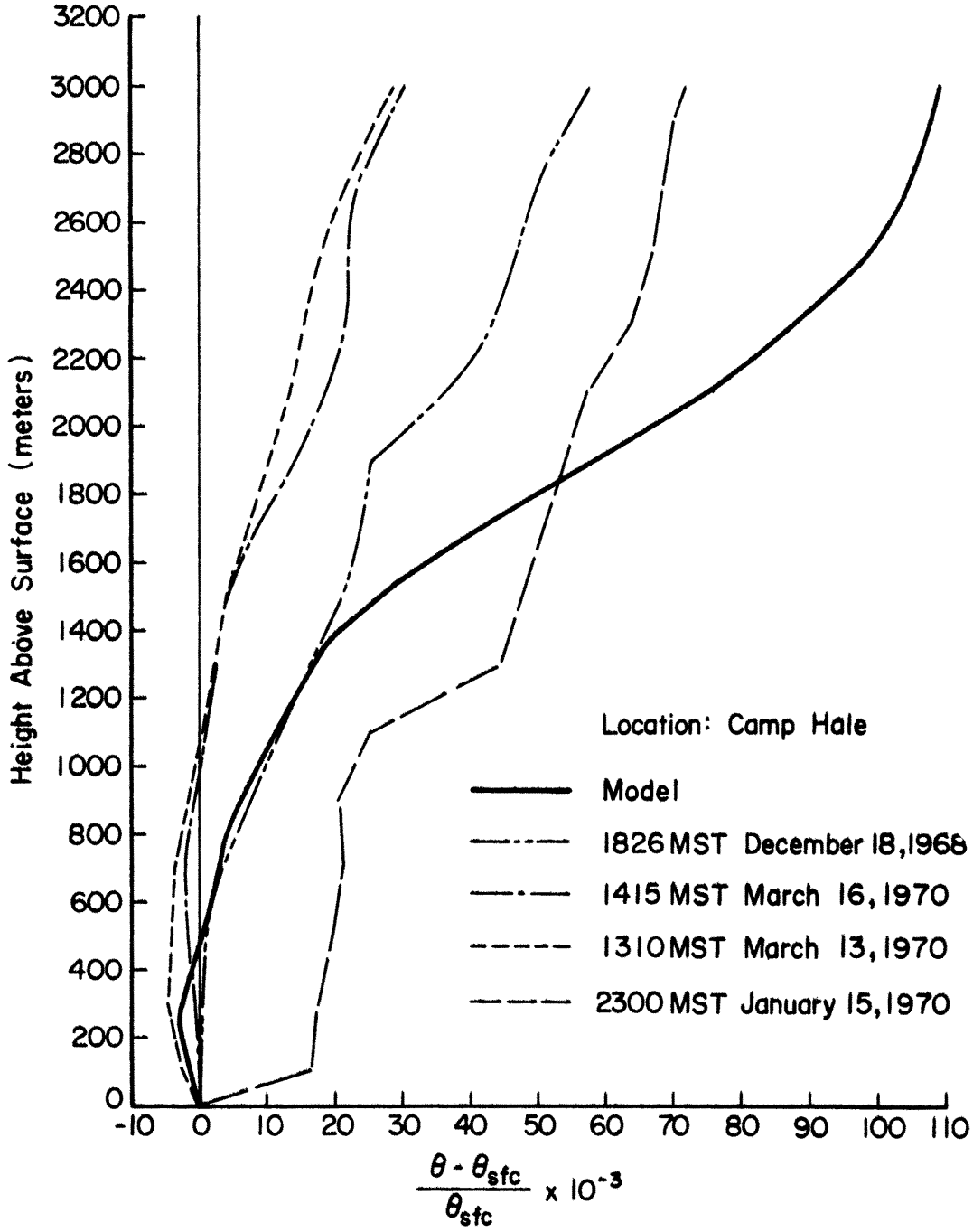

Fig. 55. Comparison of selected field potential temperature vertical profiles with a barostromatic model temperature profile. Heights scaled to prototype.

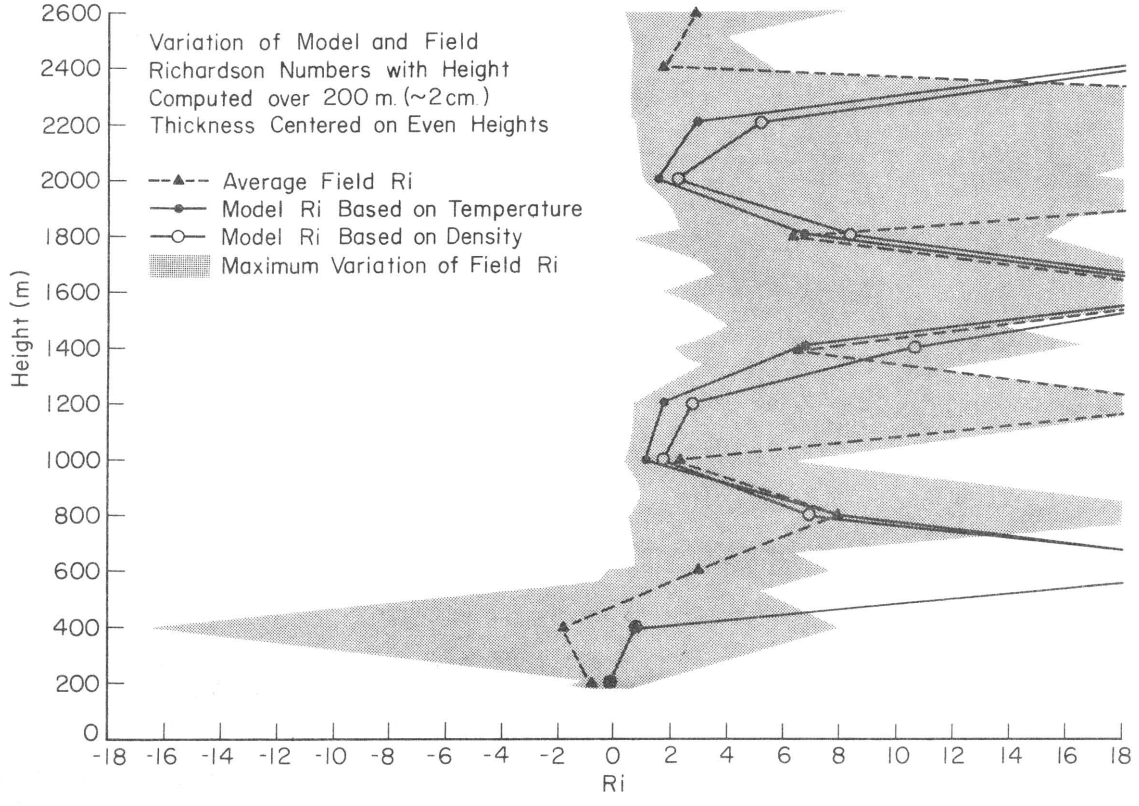

Fig. 56. Comparison of field and model bulk Richardson numbers at the Camp Hale location.

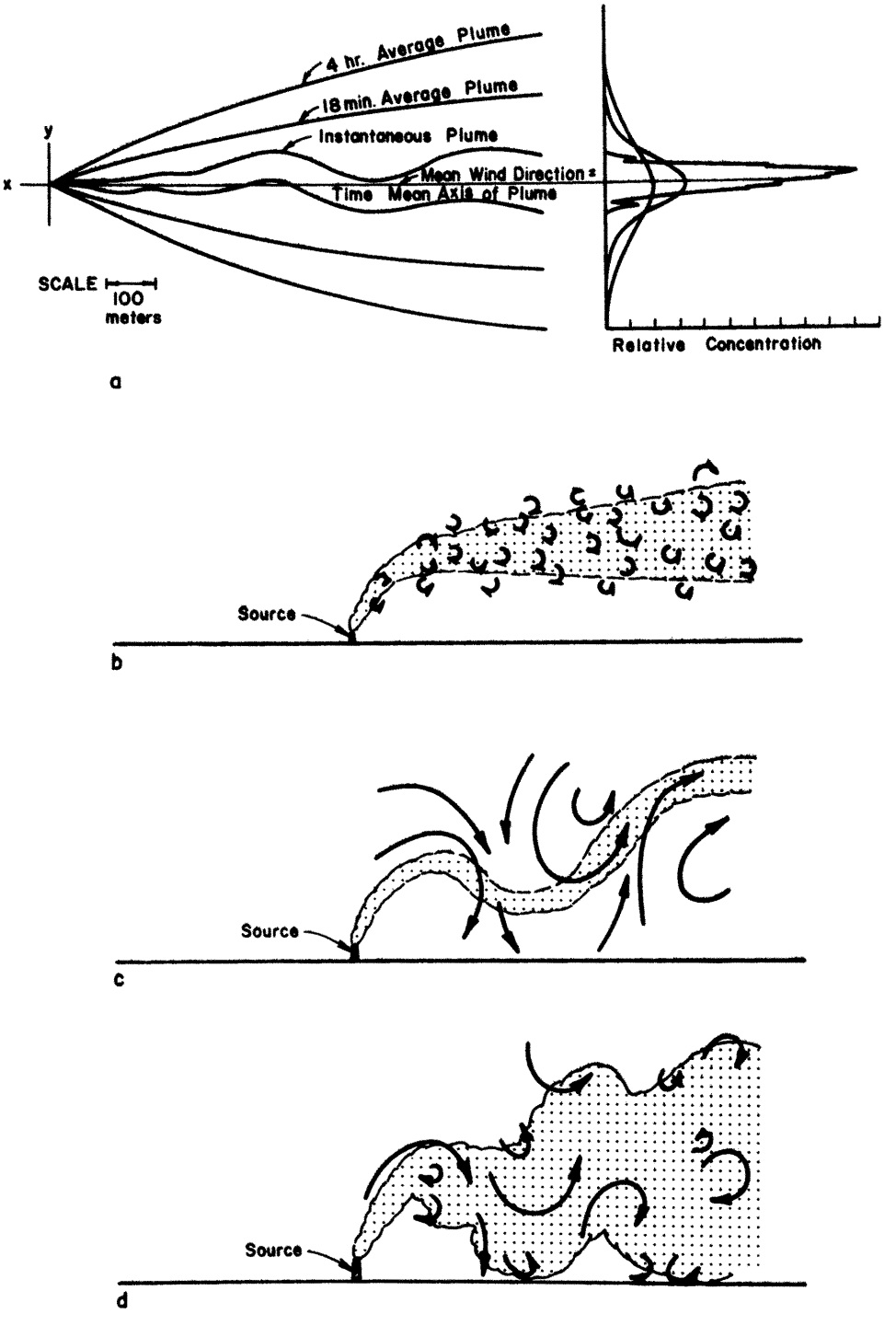

Fig. 57. a. Approximate outlines of a tracer plume observed instantaneously and of plumes averaged over 18 min and 4 hrs. Idealized dispersion patterns. b. A large plume in a field of uniform small eddies. c. A plume in a field of uniform large eddies. d. A plume in a field of varied eddies (see Ref. 106).

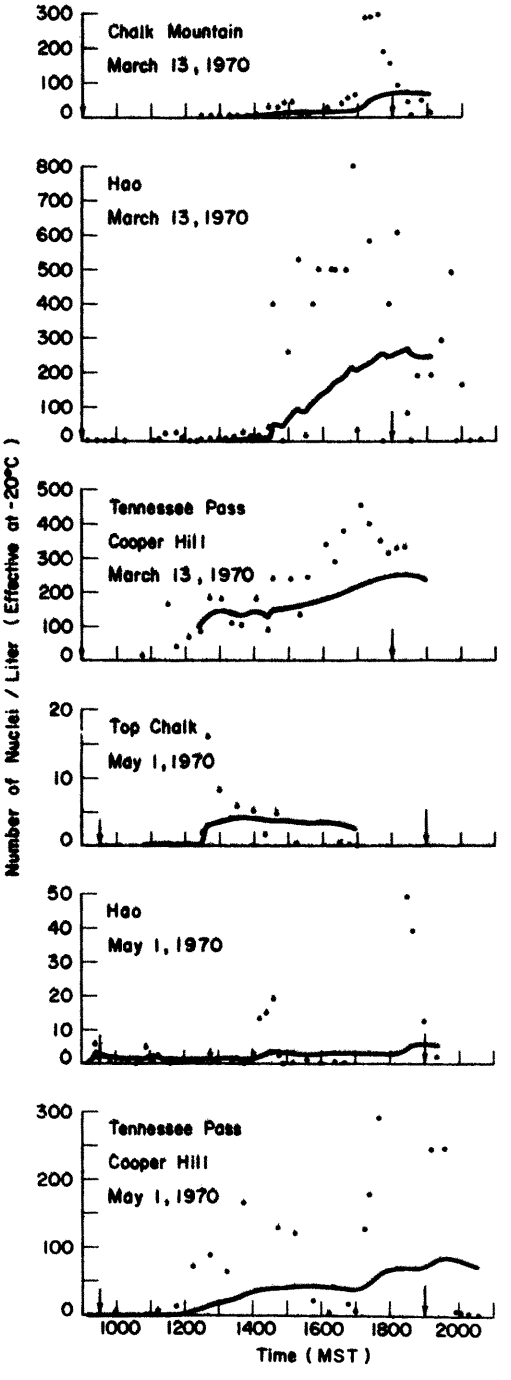

Fig. 58. Variation of seeding material concentration near the ground at three different locations in the Eagle River Valley area during seeding operations. Arrows represent silver iodide generator starting and off times. Thick line represents an accumulative average with respect to time.

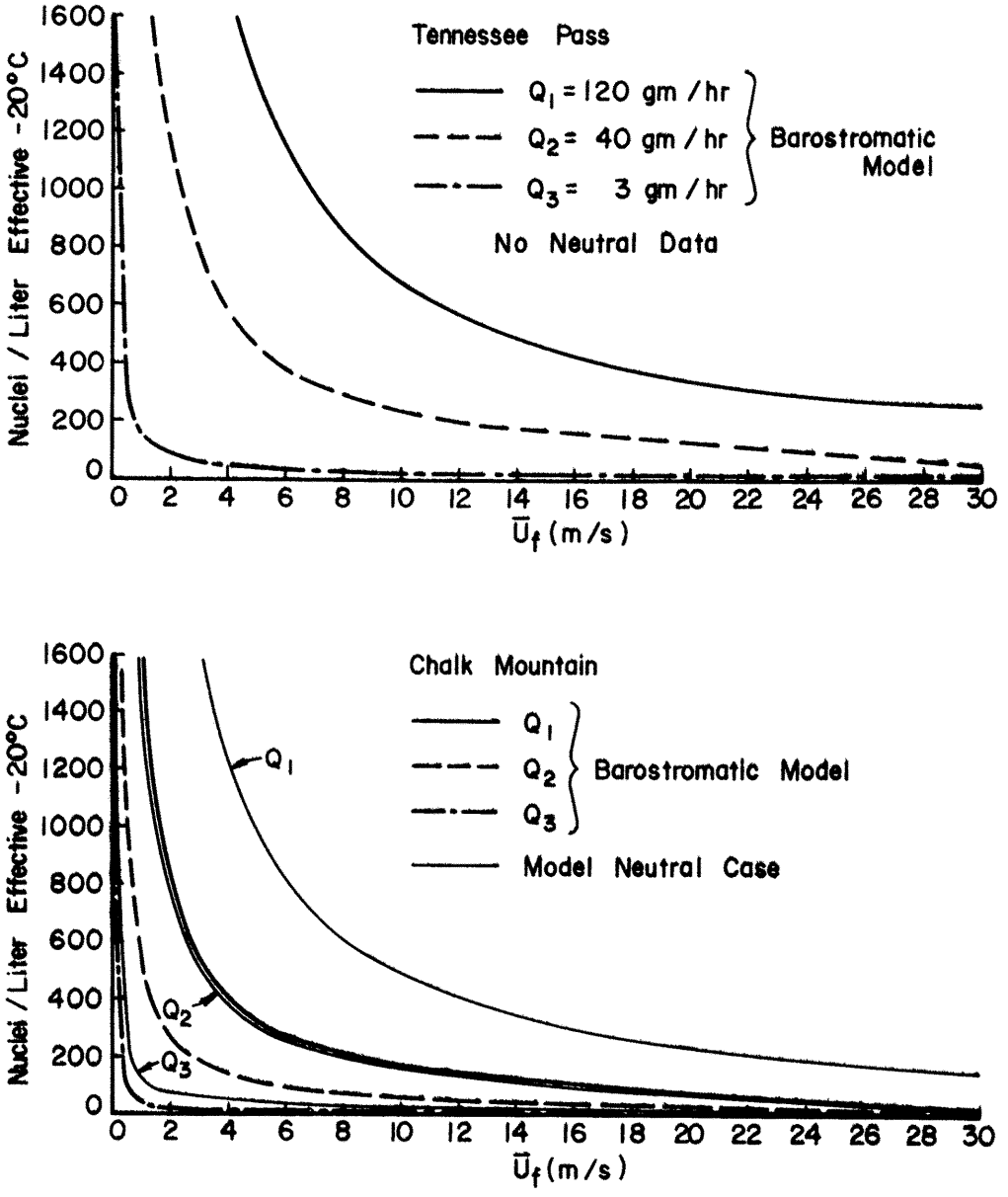

Fig. 59. Equivalent surface field-concentration values for Tennessee Pass and Chalk Mountain based on model velocity and concentration data.

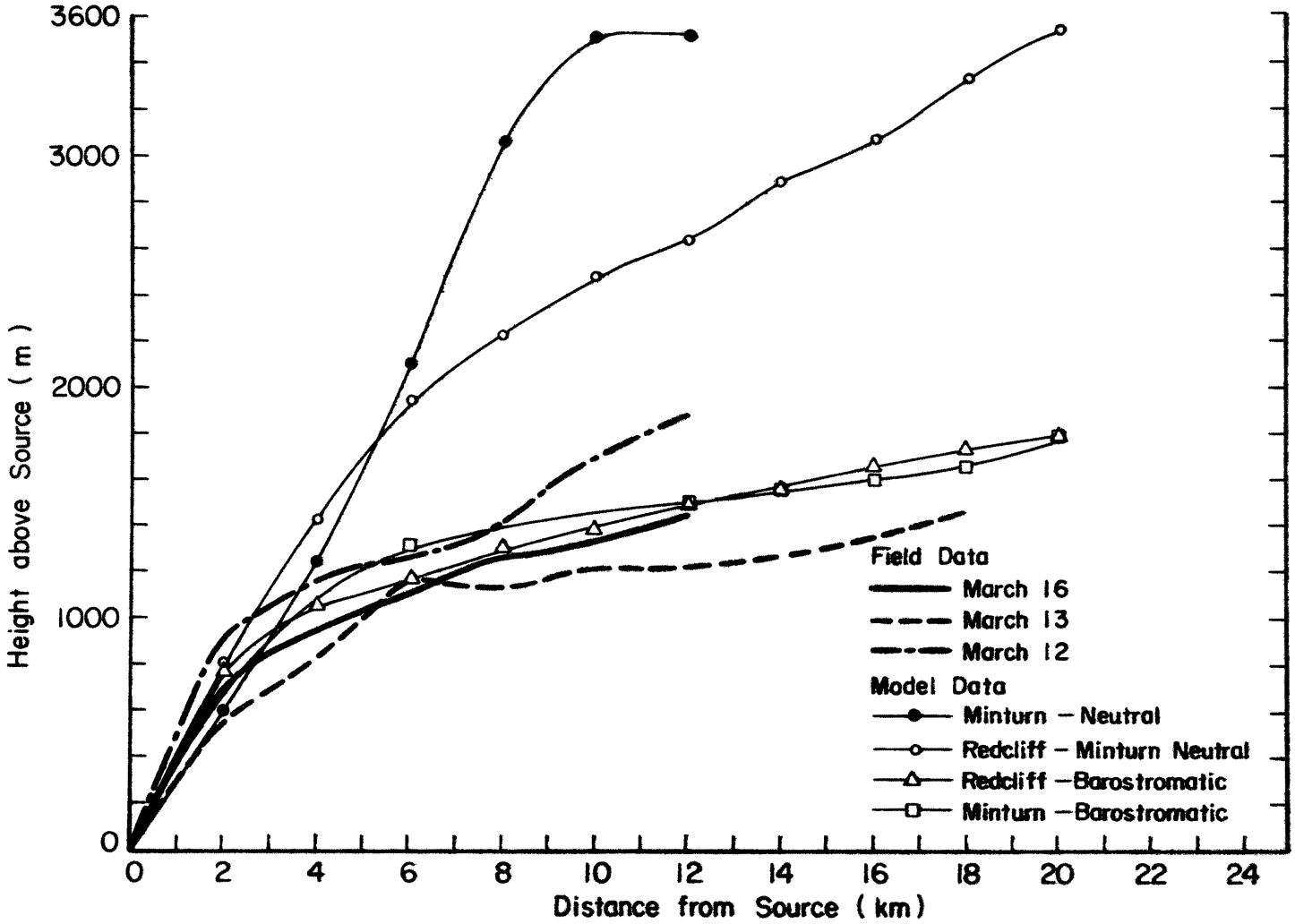

Fig. 60. Comparison between the vertical rise of model and field tracer plumes.

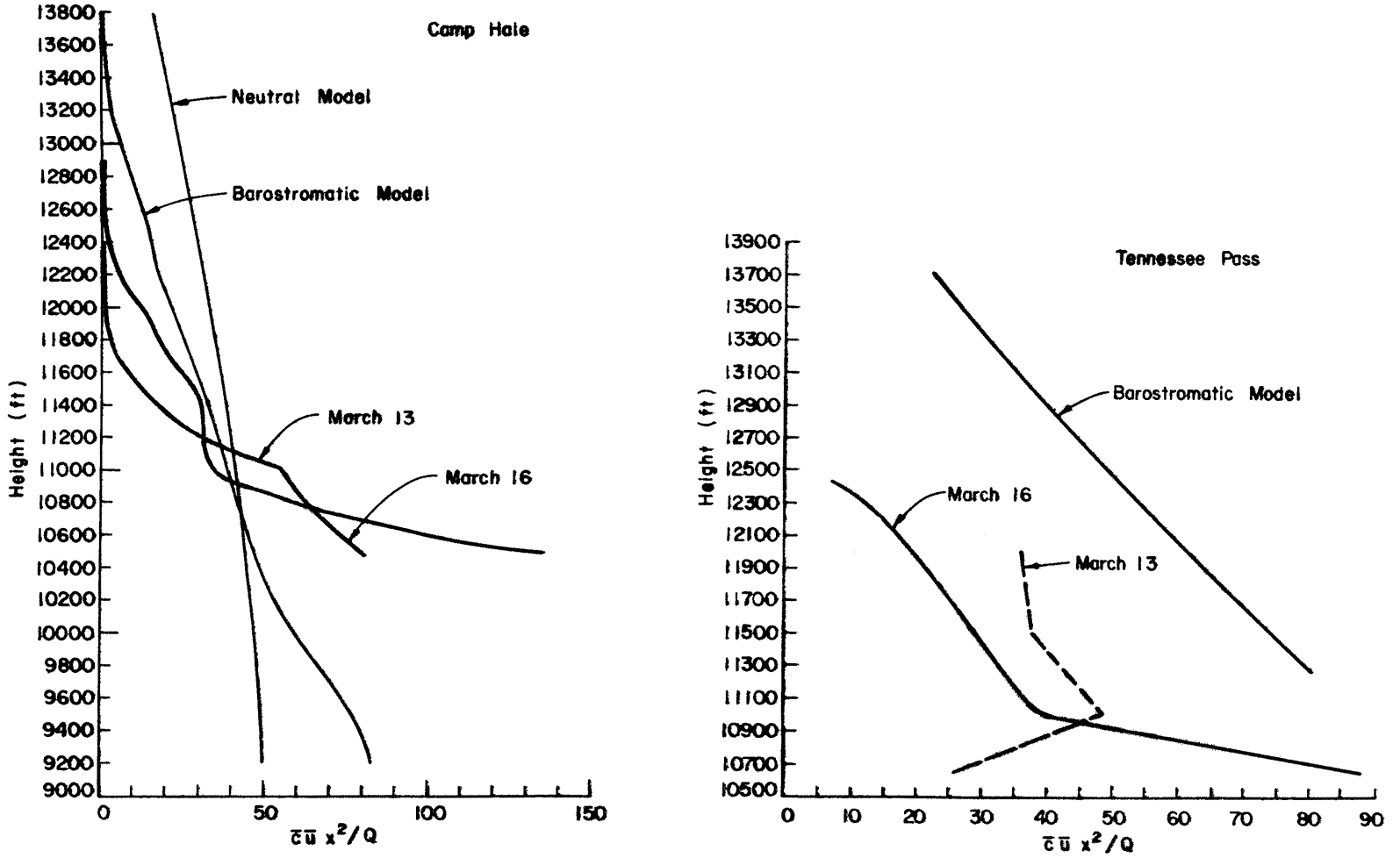

Fig. 61. Comparison between model and field values of $\overline{C}\,\overline{U}\,X^2/Q$ versus height.

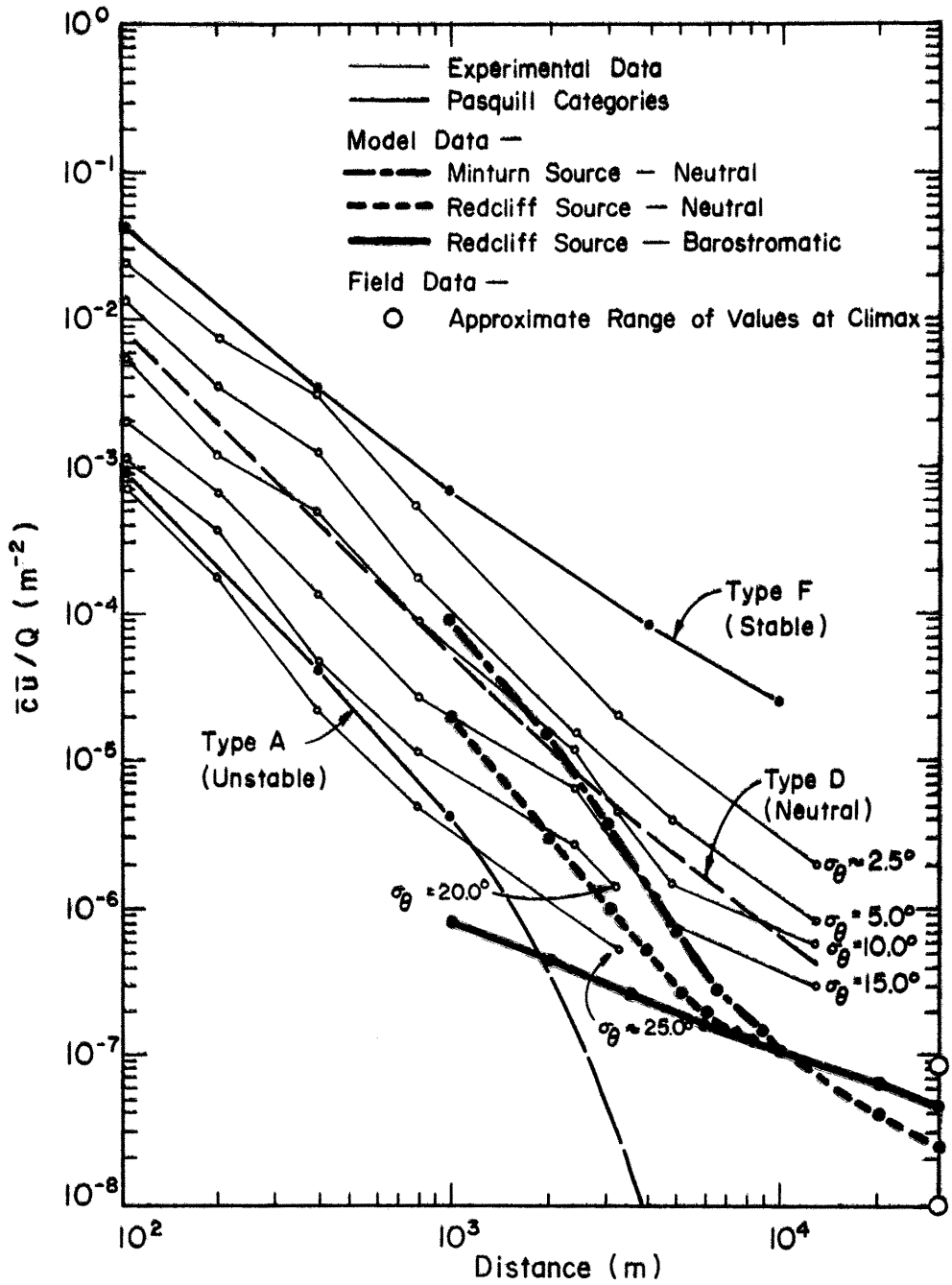

Fig. 62. Comparison of normalized surface-release axial-concentration measurements for models, Pasquill categories, and non-mountainous experimental data. Pasquill categories and experimental data obtained from Ref. 106, p. 153.

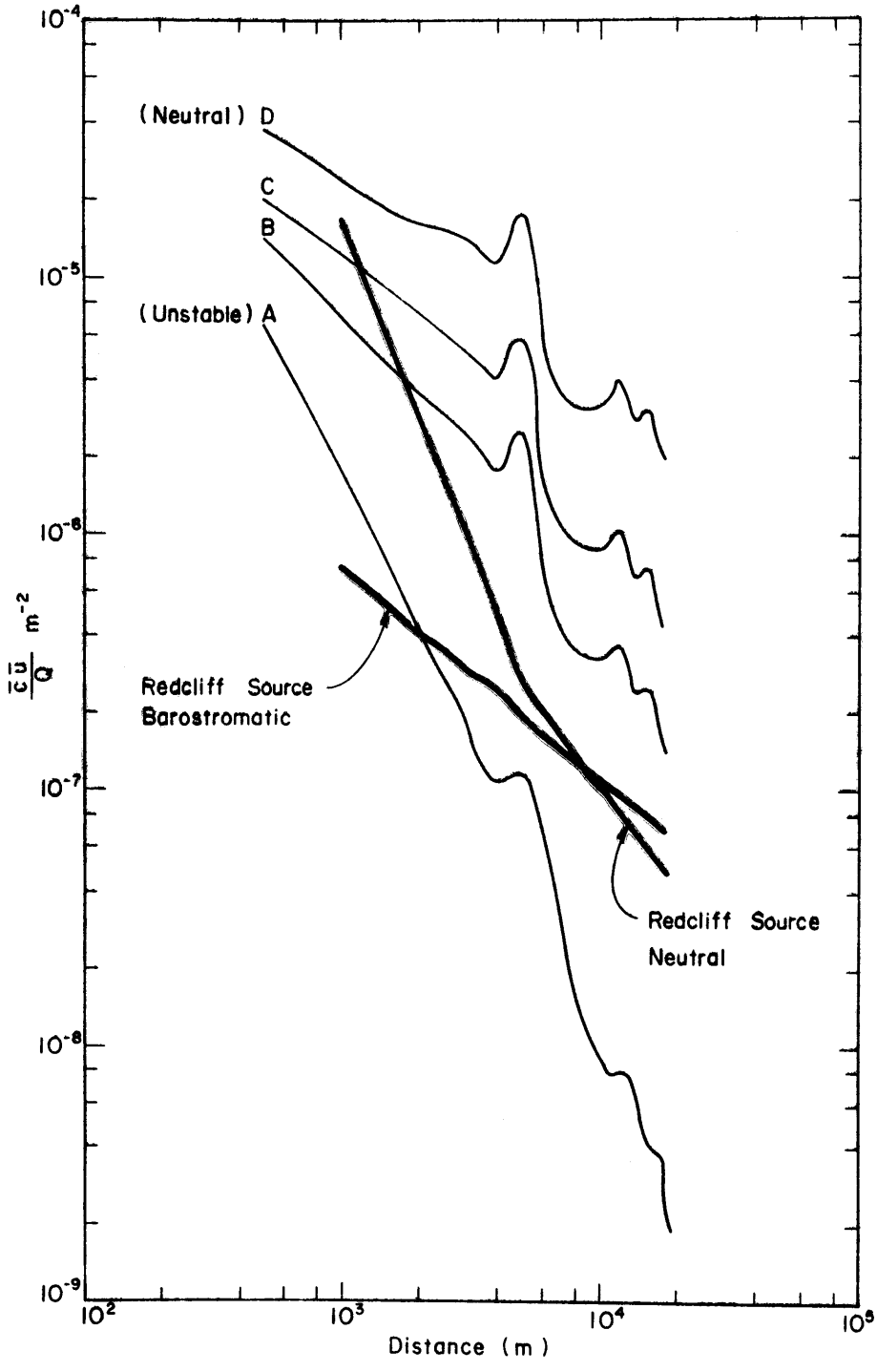

Fig. 63. Normalized ground concentration estimates for model and modified Gaussian distribution where $\sigma_y = Y$. Y is the width of the Eagle River Valley from the Redcliff source (see Ref. 105).

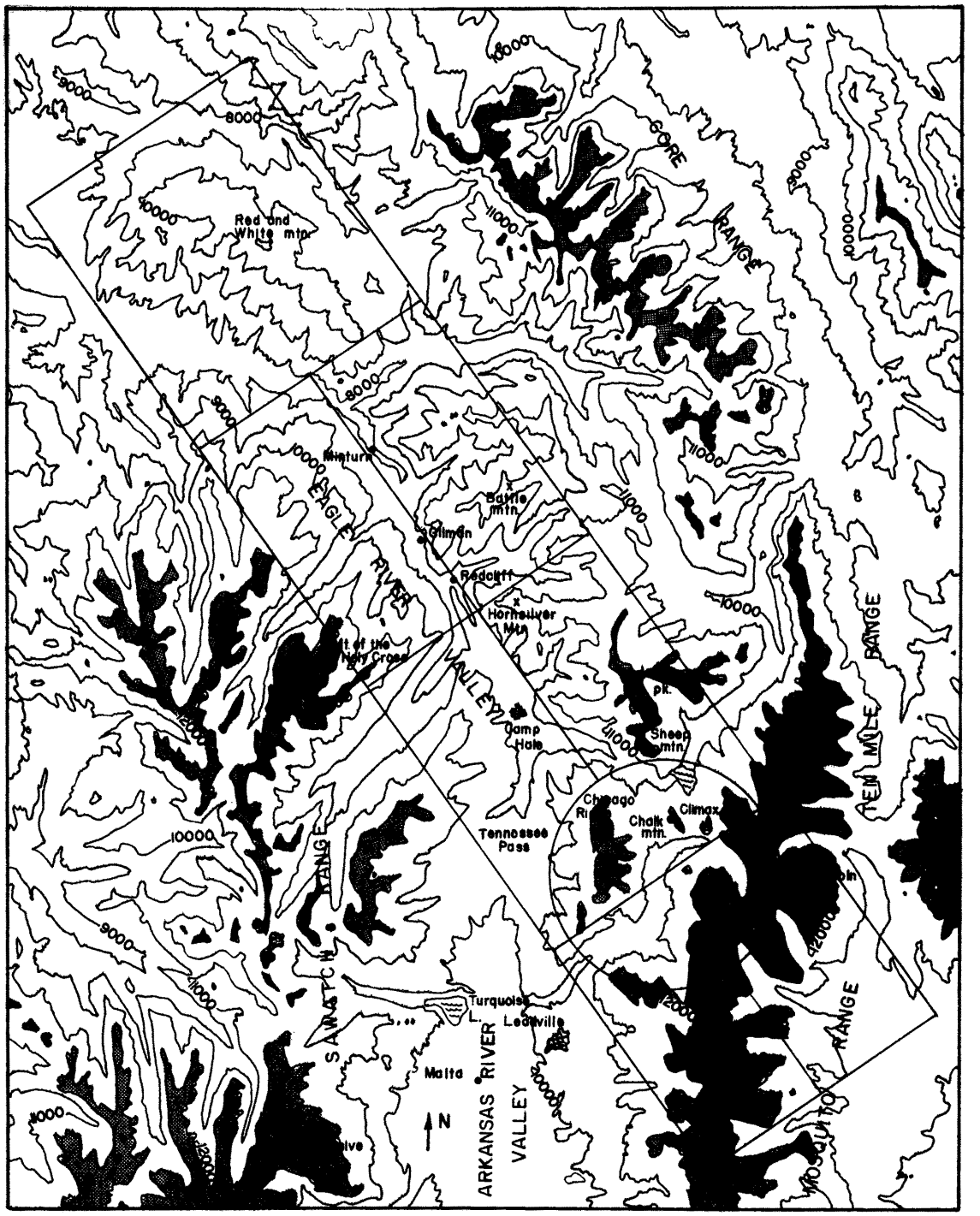

Fig. 64. Eagle River Valley and Climax topography. Rectangular area oriented northwest-southeast was modeled for the wind tunnel. Shaded areas: Over 12,000 ft. msl.

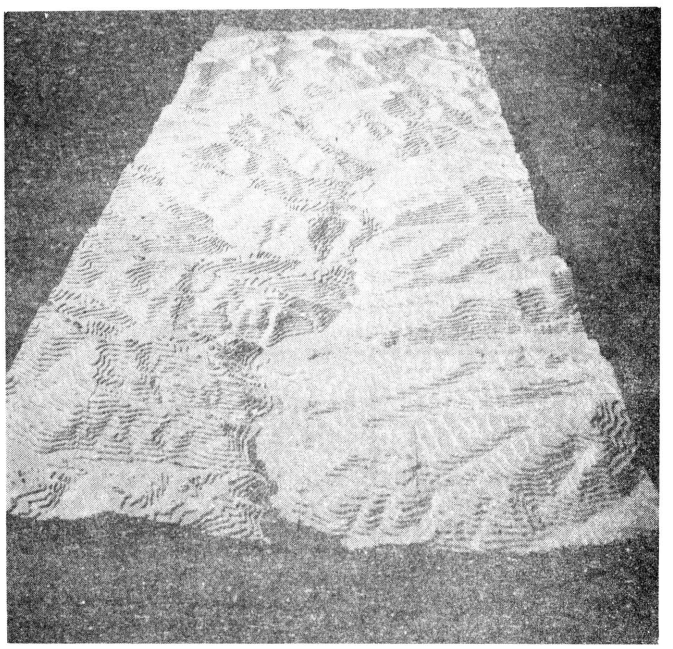

Looking downstream

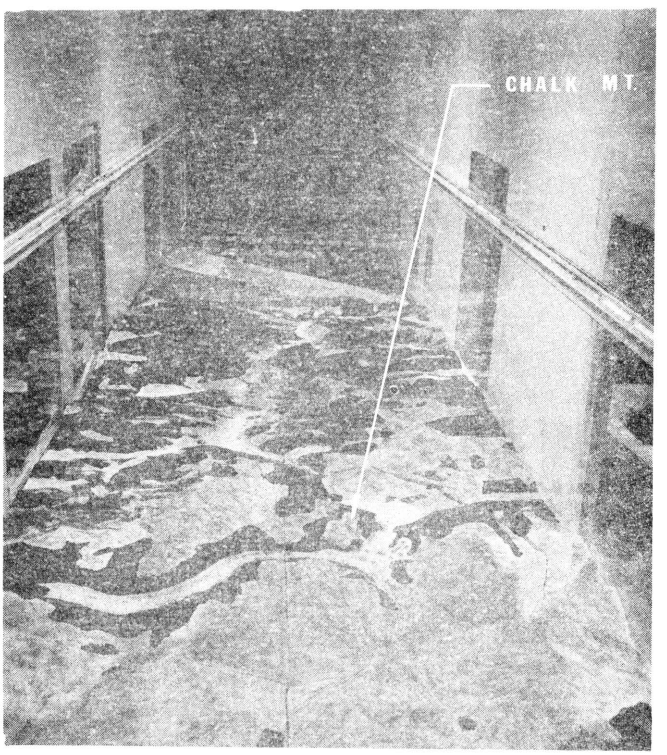

Looking upstream

Fig. 65. Eagle River Valley topographic model during construction and in wind tunnel.

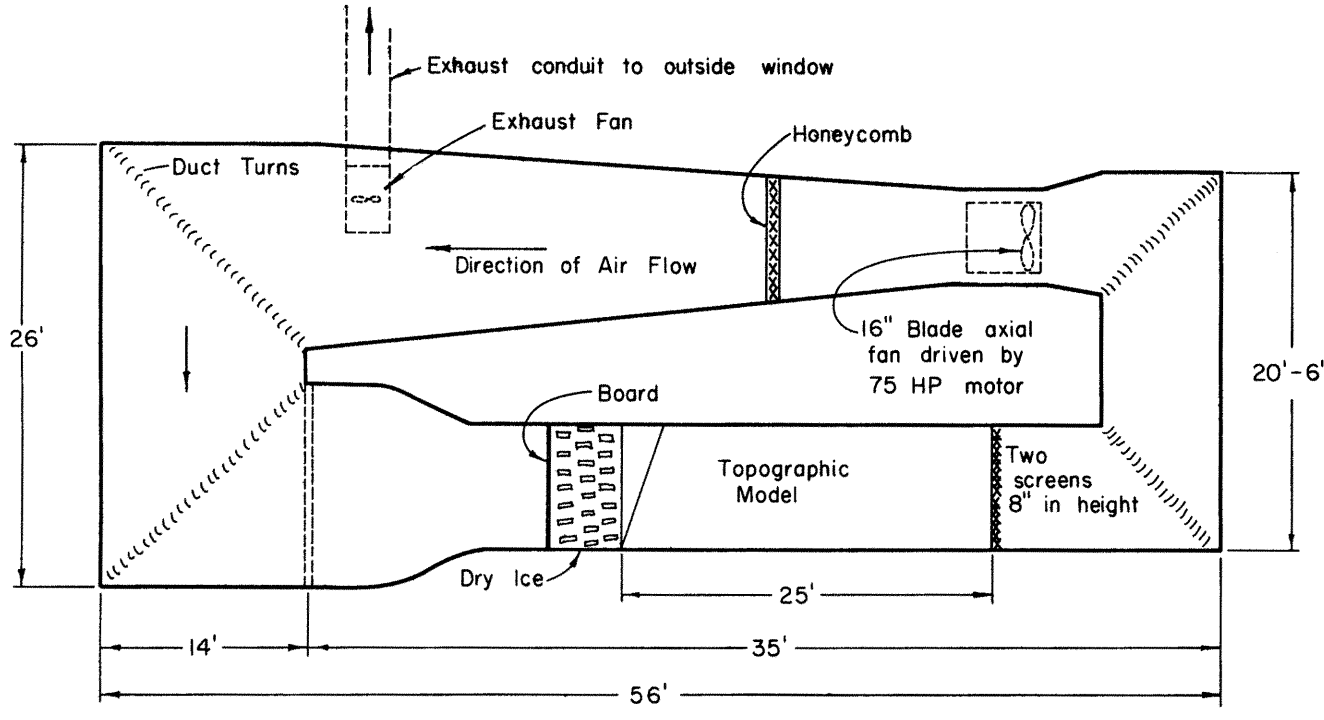

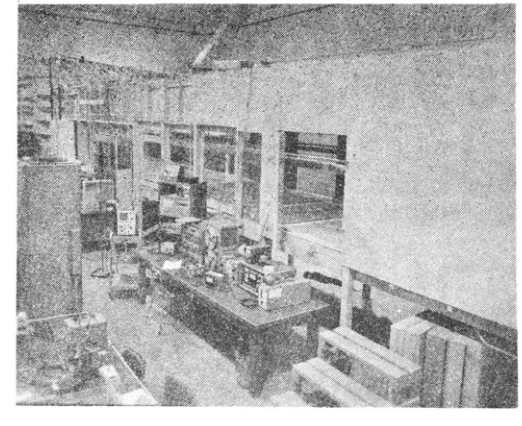

Fig. 66. Colorado State University low-speed recirculation wind tunnel.

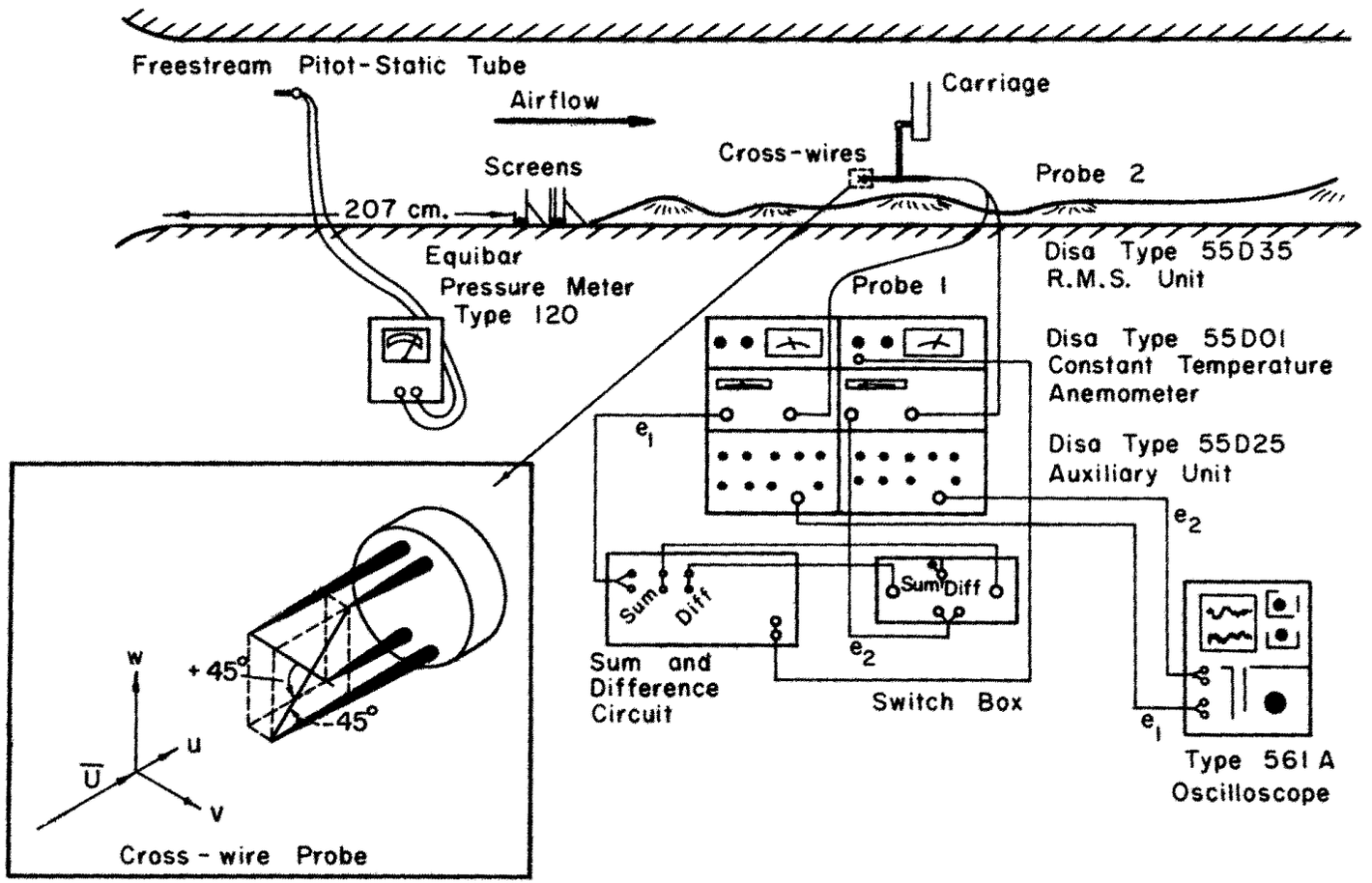

Fig. 67. Laboratory experimental arrangement for the neutral airflow model and for obtaining turbulent intensities and shear stresses.

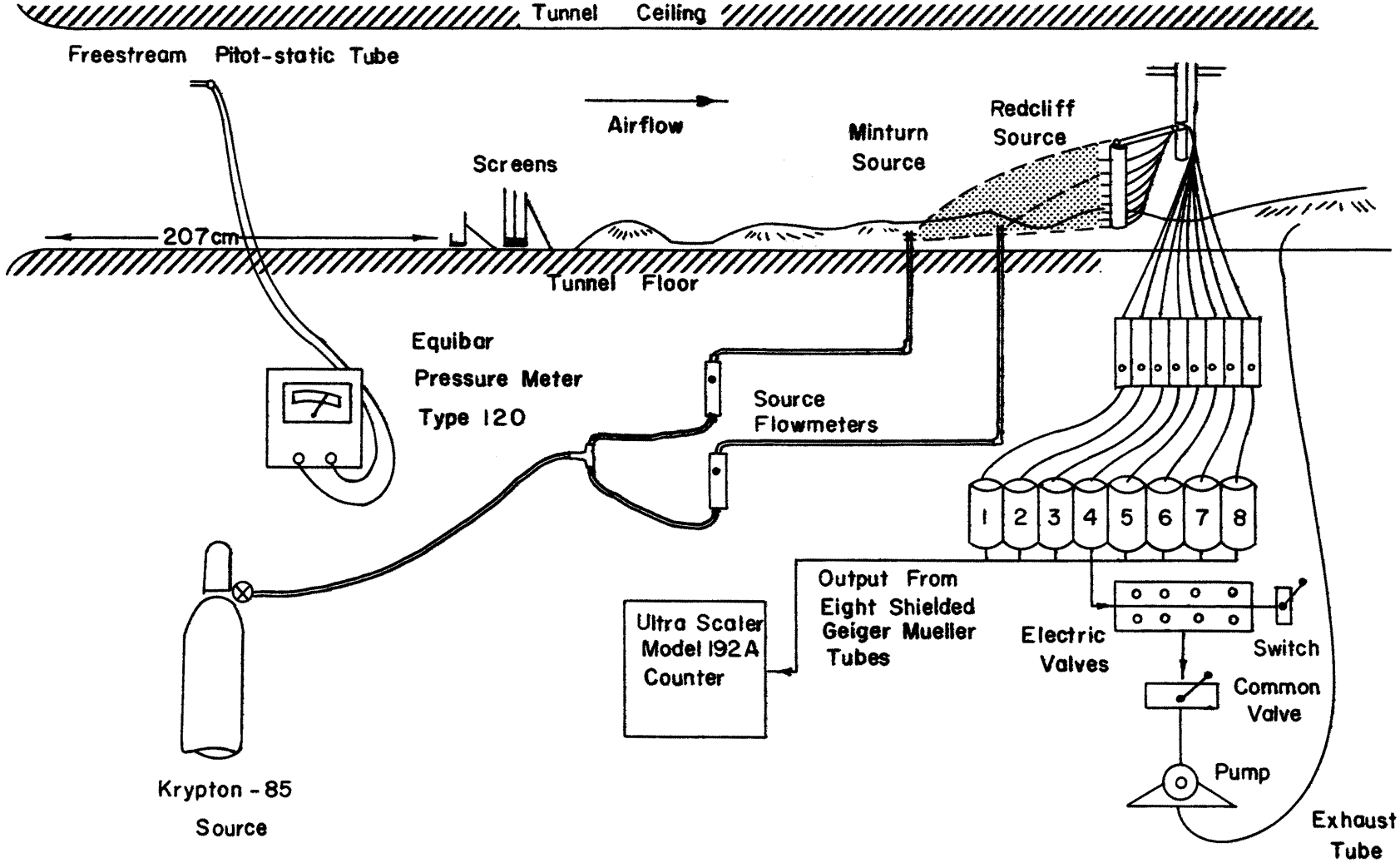

Fig. 68. Laboratory experimental arrangement for measuring radioactive Krypton-85 concentration for the neutral airflow model.

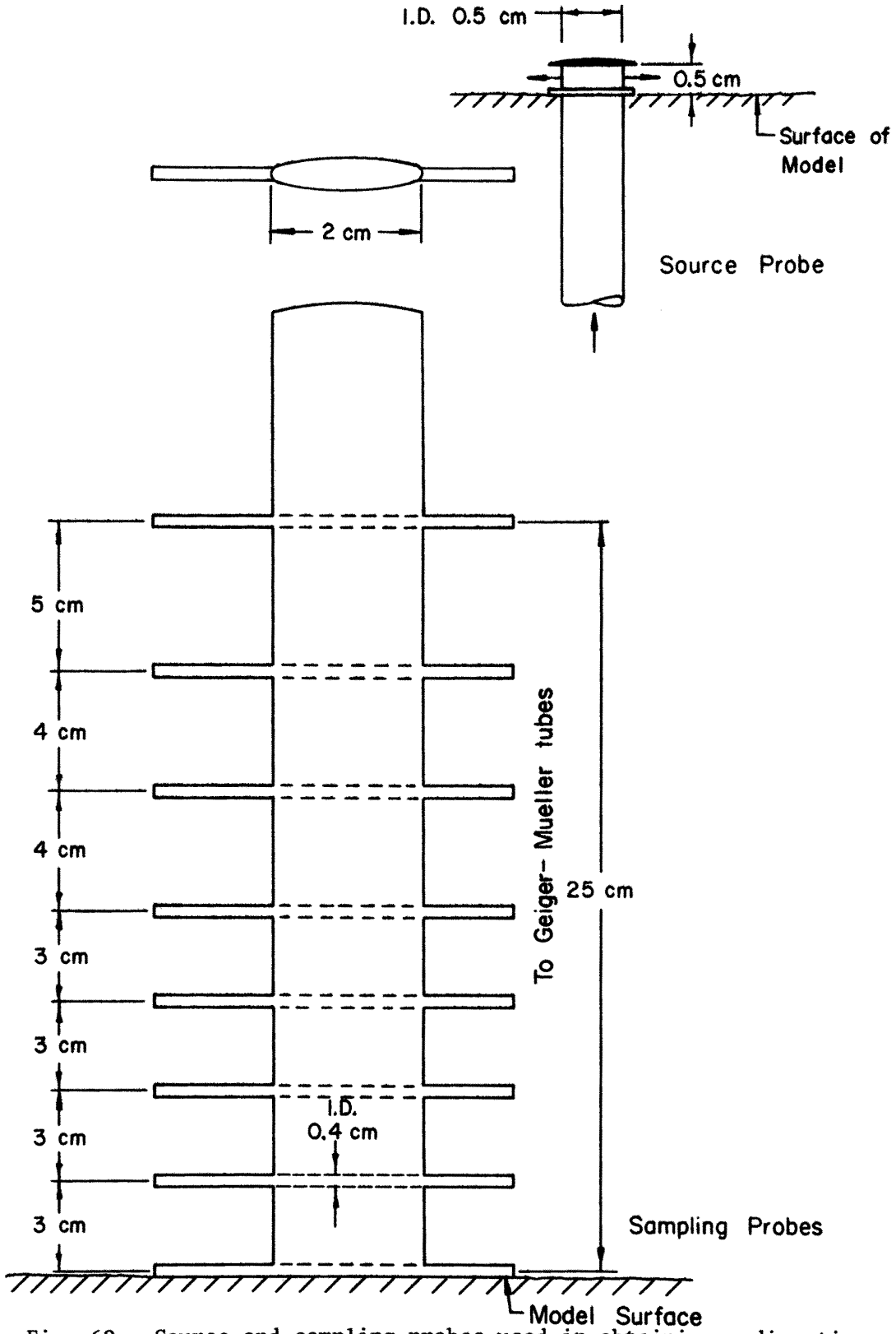

Fig. 69. Source and sampling probes used in obtaining radioactive Krypton-85 concentration measurements.

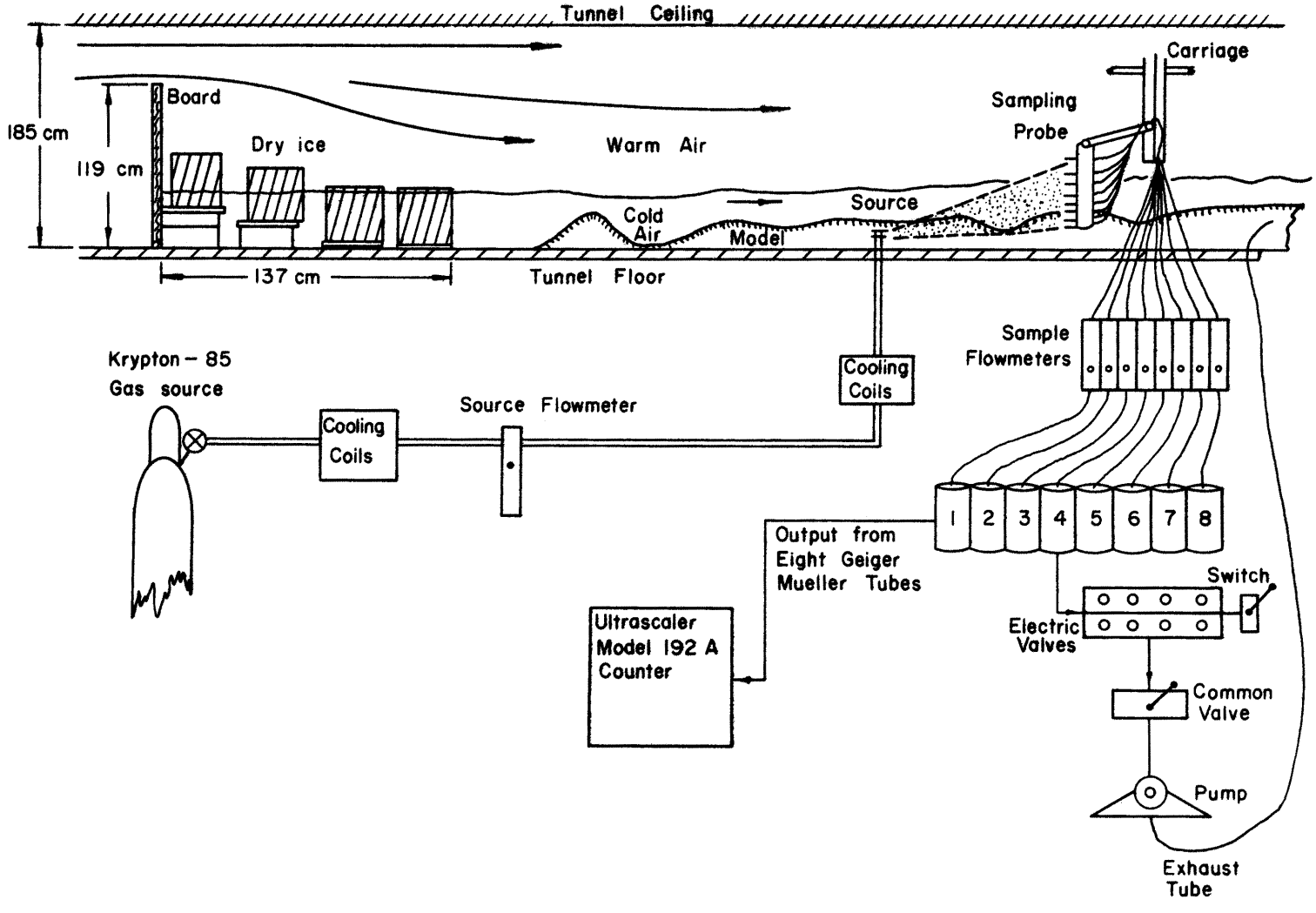

Fig. 70. Laboratory experimental arrangement for obtaining measurements of the radioactive Krypton-85 concentration over the model for the barostromatic model airflow.

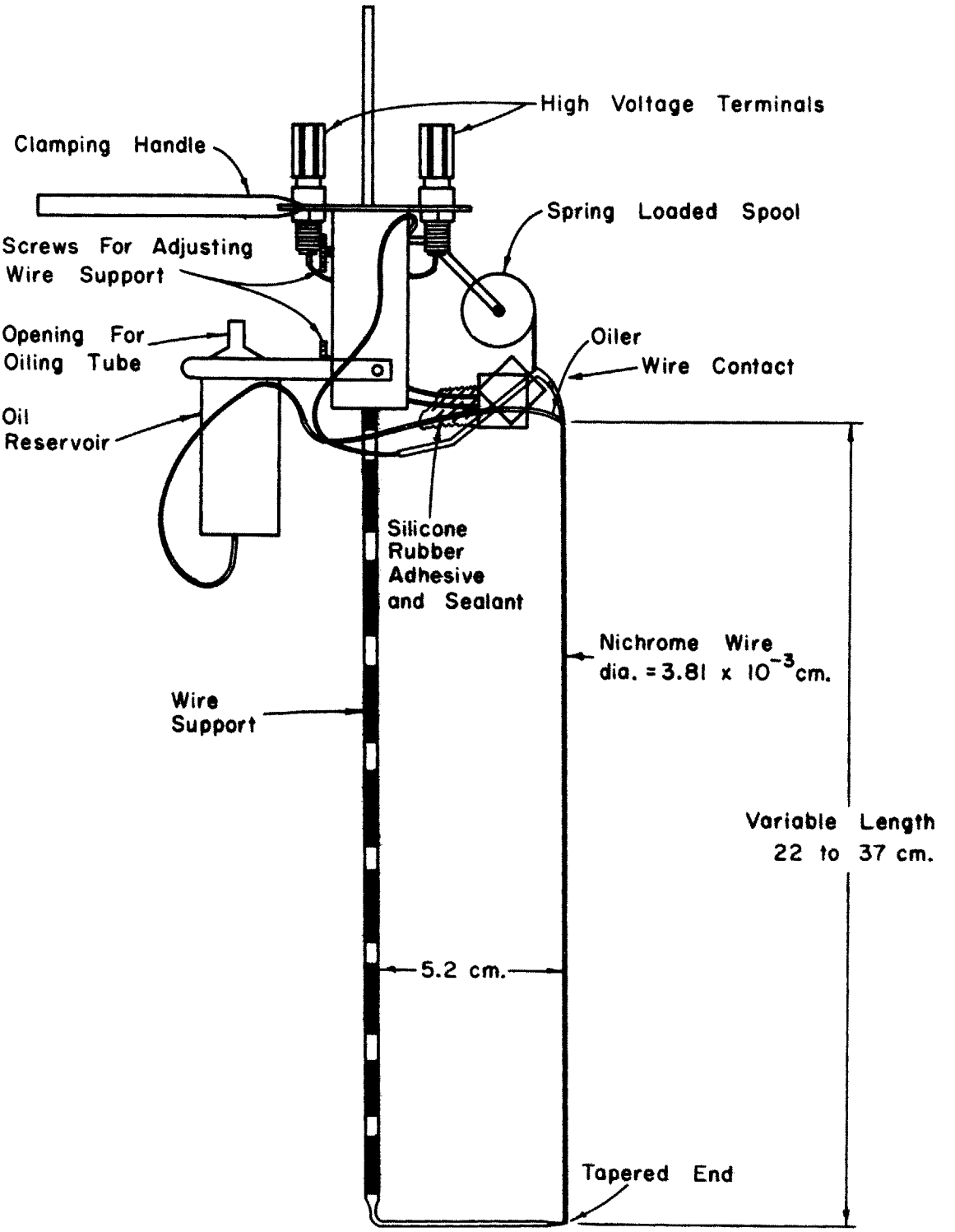

Fig. 71. Details of the smoke-wire probe used in obtaining airflow velocities for the barostromatic model airflow.

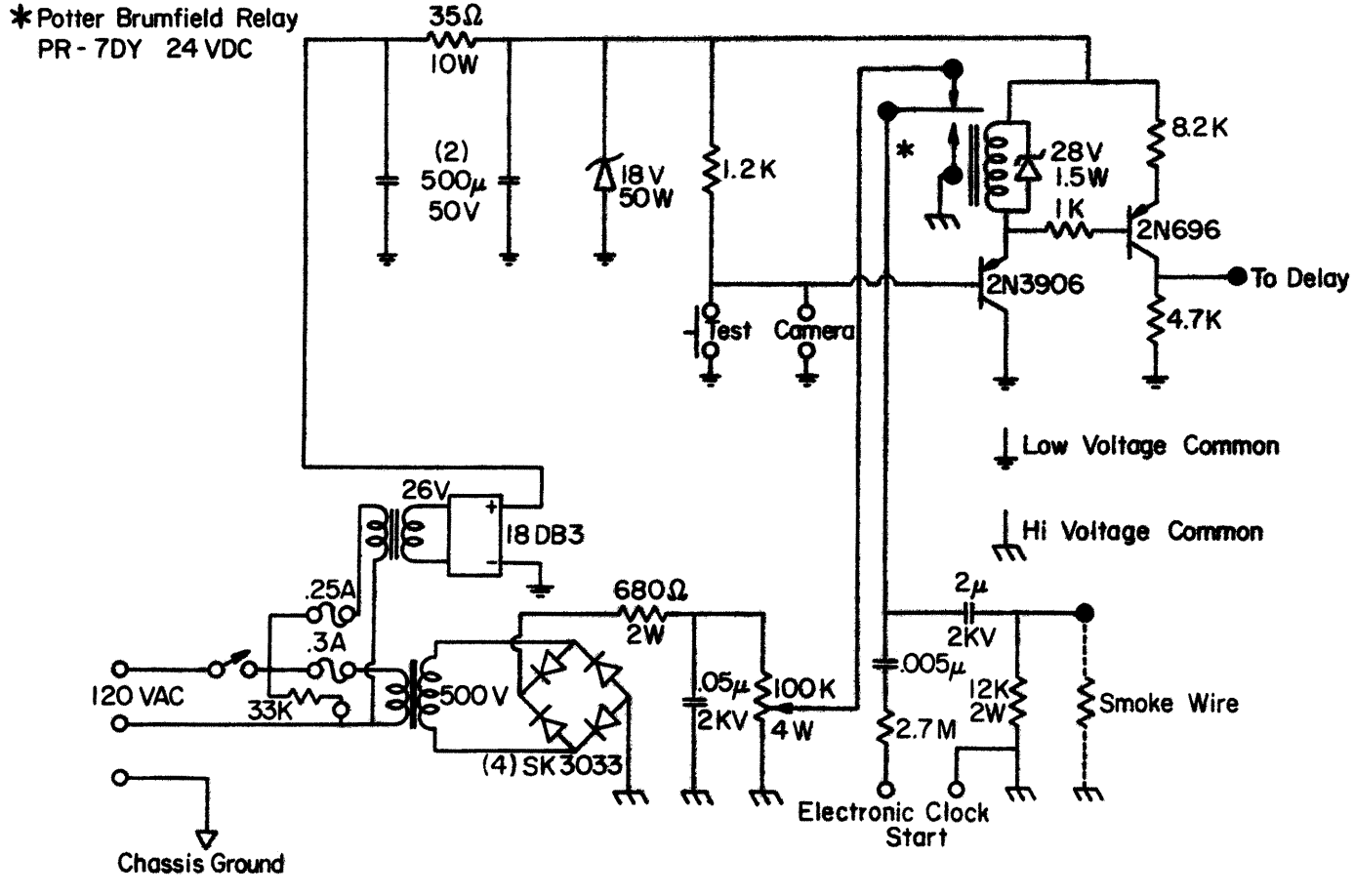

Fig. 72. Electrical circuitry of the "smoke-wire" apparatus for obtaining airflow velocities in a wind tunnel.

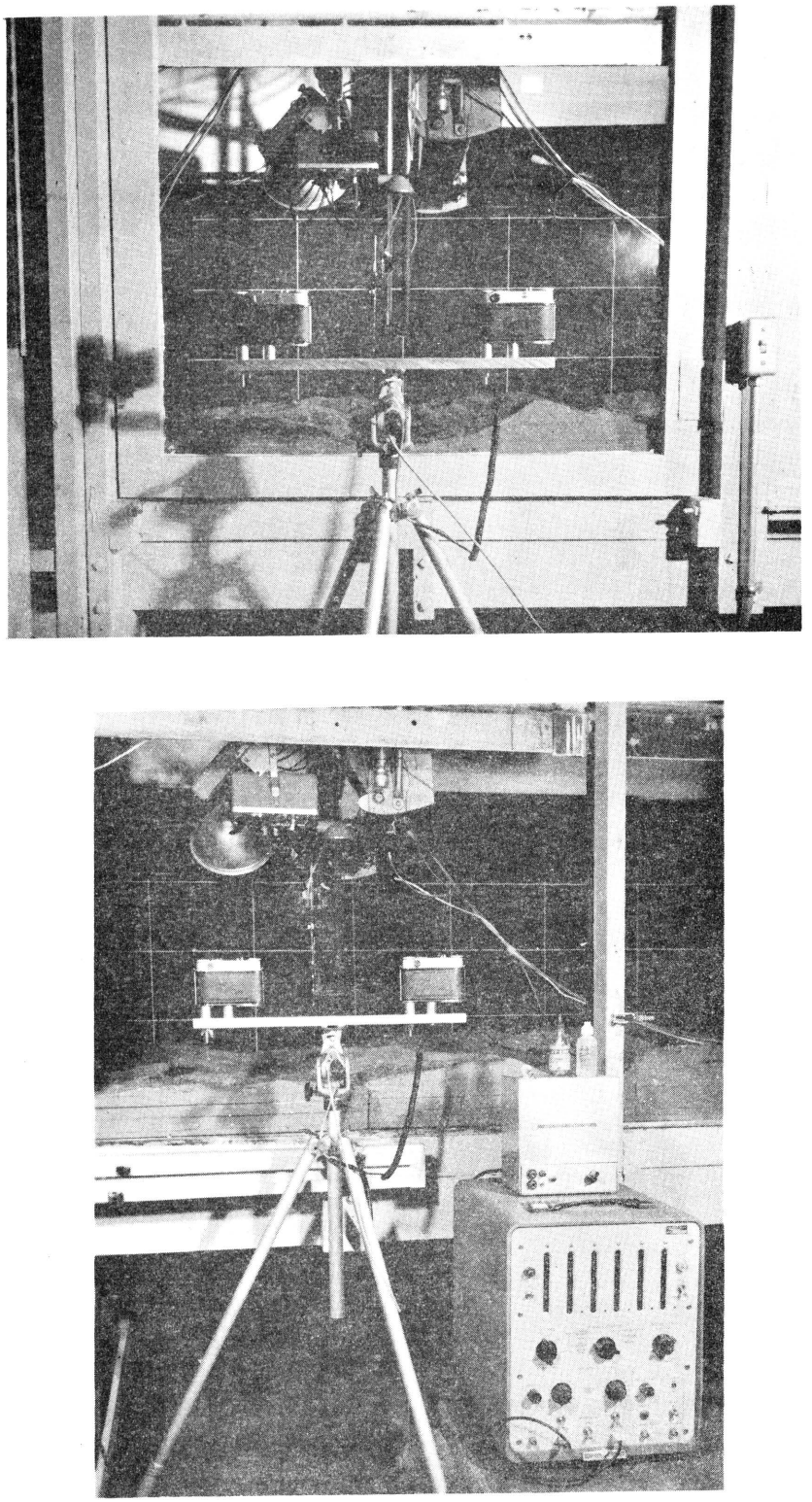

Fig. 73. Laboratory experimental arrangement for obtaining airflow velocity measurements by the two camera "smoke-wire" method.

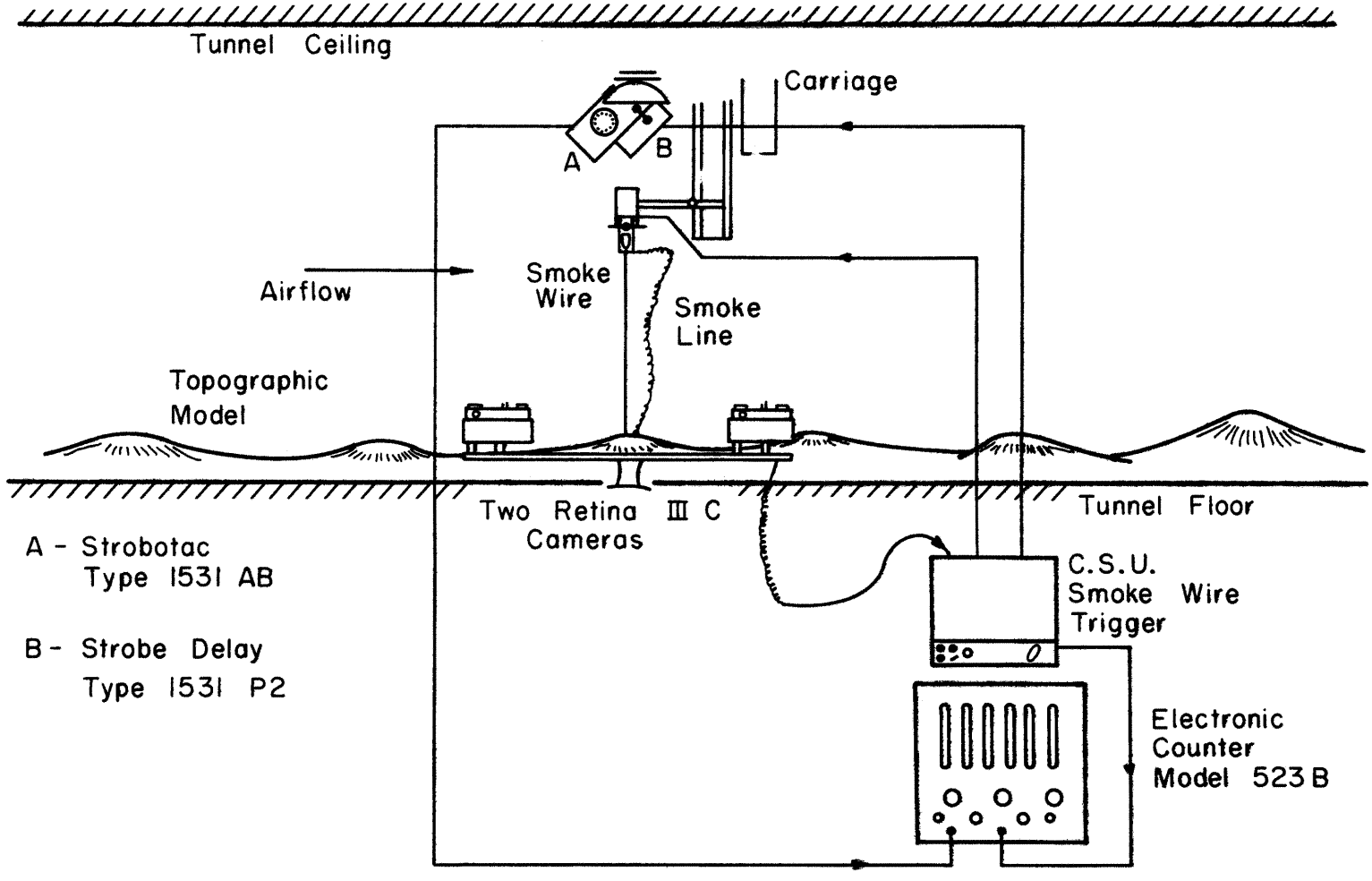

Fig. 74. Schematic diagram of the laboratory experimental arrangement for obtaining airflow velocity measurements by the two-camera "smoke-wire" method.

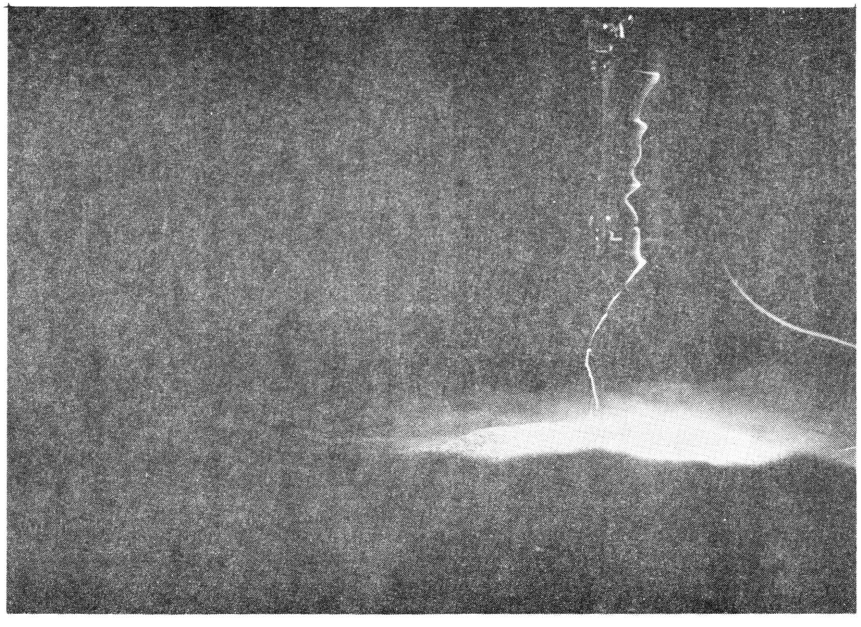

Left Picture

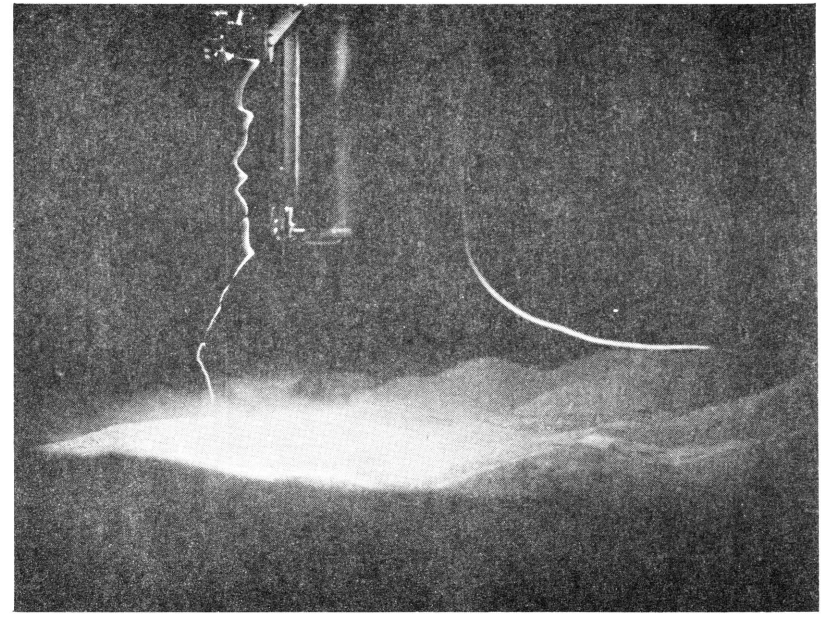

Right Picture

Fig. 75. An example of paired photographs of the smoke-wire probe and displaced smoke plume.

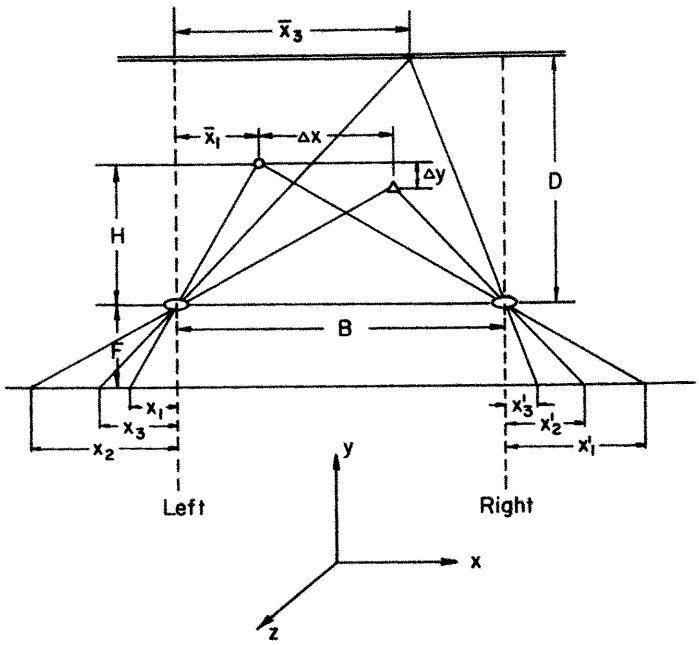

- • Mark on Wind Tunnel Wall
- o Wire
- △ Smoke Filament
- ⬭ Camera
- B Distance Between Two Cameras (15")
- H Distance Between Camera and Wire (y - Direction)
- D Distance Between Camera and Opposite Wall (y - Direction)
- F Focal Length of Cameras
- Δy Distance Between Wire and Smoke Filament (y - Direction)
- Δx Distance Between Wire and Smoke Filament (x - Direction)

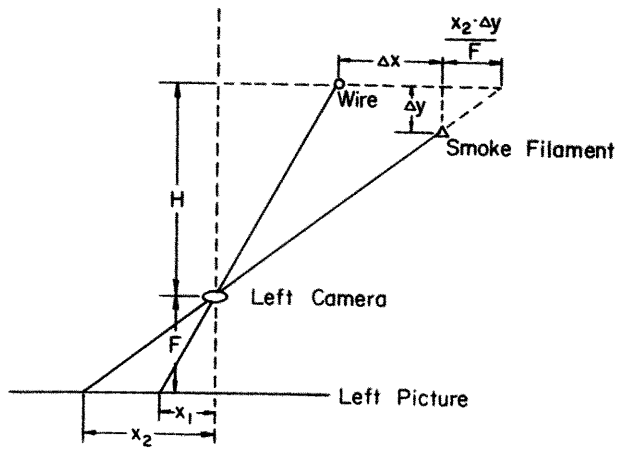

Fig. 76. Geometry for determining the longitudinal and lateral velocity components with the two camera "smoke-wire" method. Top view.

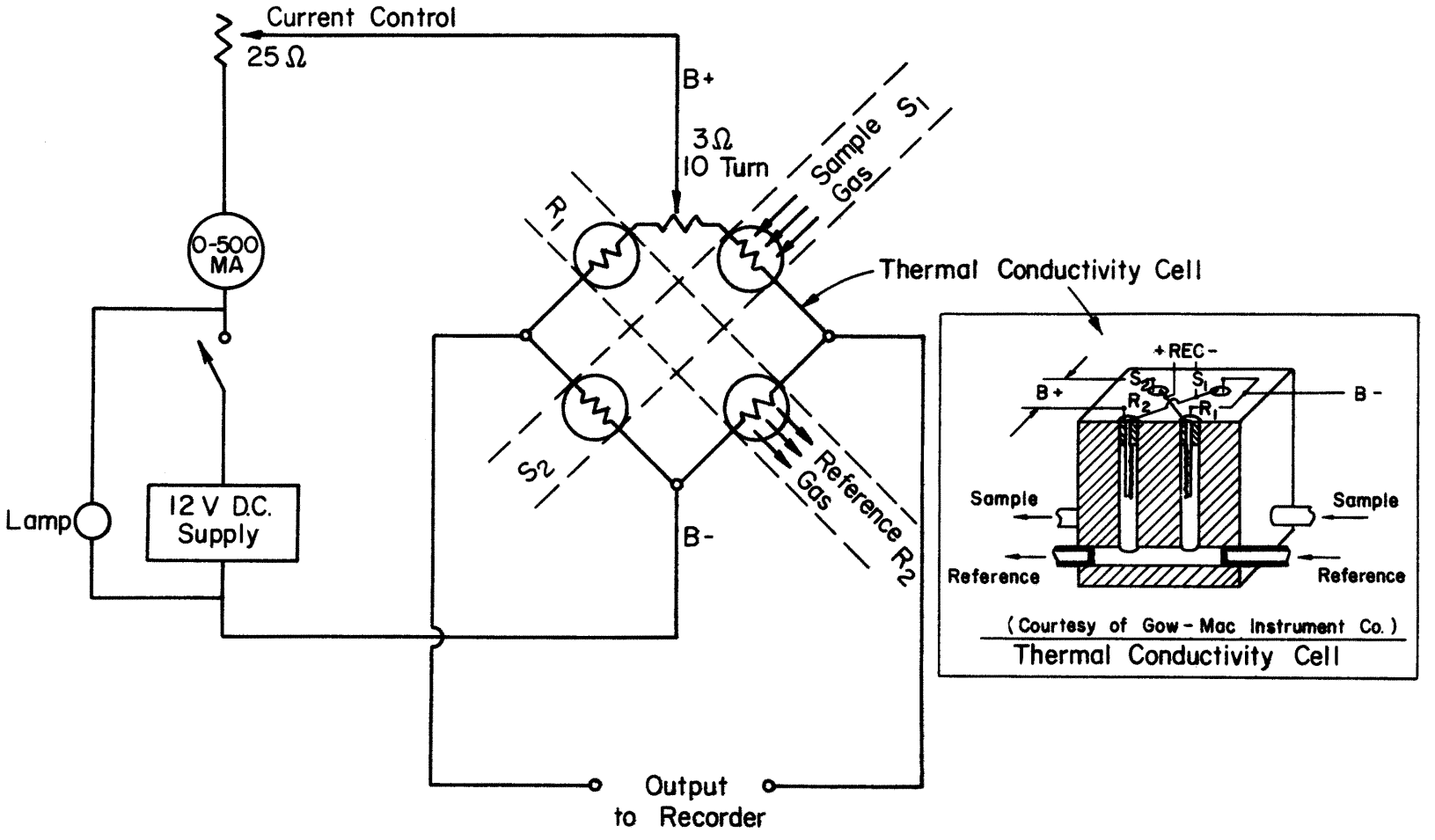

Fig. 77. Electrical circuitry of the thermal conductivity cell used in obtaining carbon dioxide concentrations.

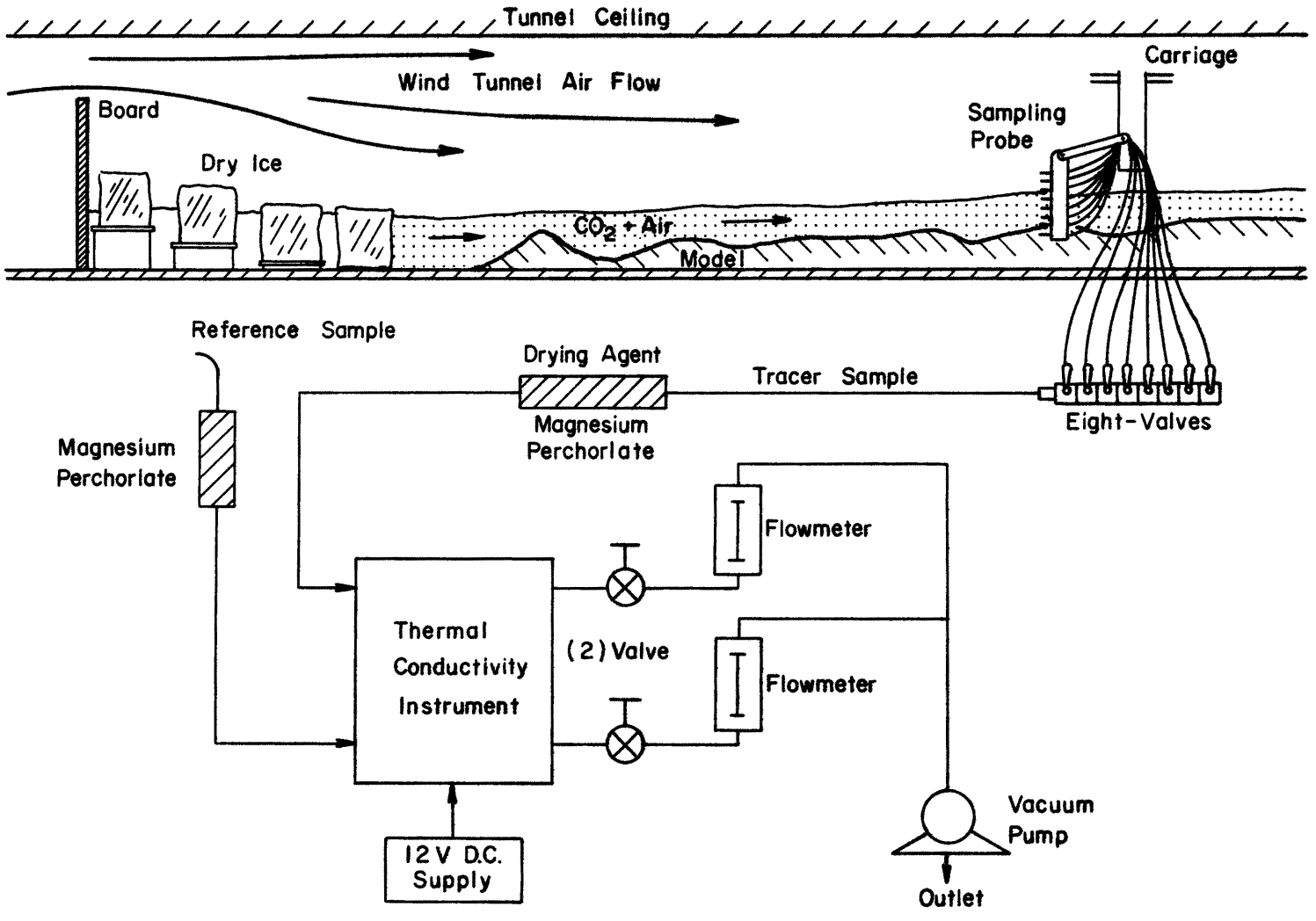

Fig. 78. Laboratory experimental arrangement for measuring concentration of carbon-dioxide for barostromatic airflow.

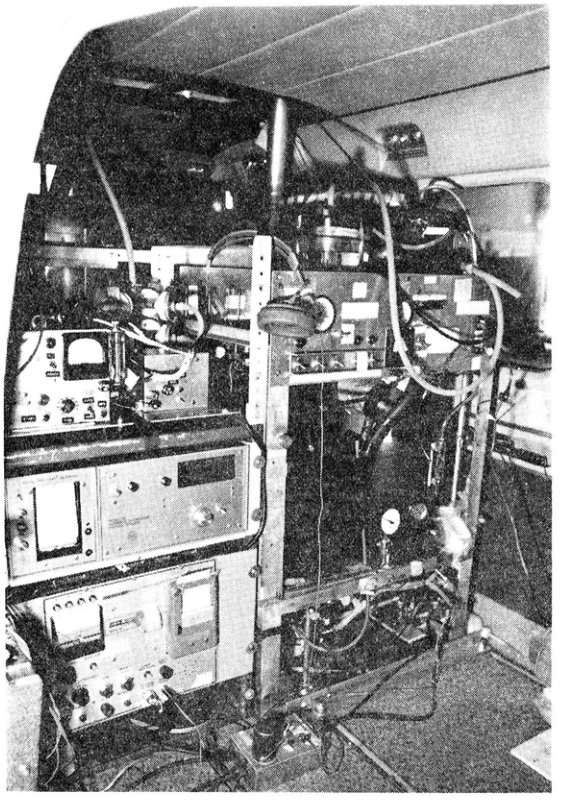

Fig. 79. Colorado State University's Aero Commander 500B and sampling equipment used for inflight sampling of silver iodide. Sampling equipment consisted of a NCAR Ice Nucleus Counter (right and left bottom) and a Millipore filter system (top left).

Fig. 80. Principal flight paths flown during aircraft sampling of silver iodide in the Eagle River Valley during 12, 13, 16 March and 1 May, 1970.